University of Southampton

Faculty of Engineering and Physical Sciences

Mechanical Engineering Department

Development of high fidelity imaging procedures to identify the relationship between the material microstructure and mechanical behaviour of friction stir welds

by

Saranarayanan Ramachandran

ORCID ID 0000-0002-6881-2940

Thesis for the degree of Doctor of Philosophy

May 2020

University of Southampton

Abstract

Faculty of Engineering and Physical Sciences

Mechanical Engineering Department

Thesis for the degree of Doctor of Philosophy

Development of high fidelity imaging procedures to identify the relationship between the material microstructure and mechanical behaviour of friction stir welds

by

Saranarayanan Ramachandran

A procedure to evaluate the local post-yielding behaviour of similar and dissimilar weld combinations of copper (Cu) and stainless steel (SS) materials produced by the Friction Stir Welding (FSW) process is devised. Friction stir weld sub-regions such as the Heat Affected Zone (HAZ), Thermo-Mechanical Affected Zone (TMAZ), and Stir Zone (SZ)/weld nugget located on the advancing (AS) and retreating sides (RS) of the weld are characterised using a range of microscopy techniques. The microstructural characterisation is linked to the local stress-strain behaviour through the development of a novel High Resolution (HR) Digital Image Correlation (DIC) methodology. The overarching aim is to provide a holistic understanding of the weld mechanical behaviour linked directly to the material microstructure and composition generated by the FSW process.

During FSW a thickness reduction occurs local to the weld zone as a result of the plastic deformation that is produced during the FSW process, hence a procedure is developed that accounts for the reduction in test specimen thickness and removes the need for post-weld machining to produce a specimen of uniform thickness. A high-resolution (HR) 2D-digital image correlation (DIC) methodology is developed to assess the local strain response across the weld surfaces and the cross-section in both elastic and plastic loading regimes. The HR-DIC methodology includes the stitching of multiple images, as it is only possible to partially cover the FSW region using a single camera with the high-resolution optical set-up. An image processing procedure is developed to stitch the strain maps as well as strain data sets that allows the full-field strain to be visualised and interrogated over the entire FSW region in the materials' elastic range. As the loading was in the material elastic range it meant the load step necessary for the DIC could be applied repeatedly so that images could be gathered from different positions across the weld region from the same specimen. An alternative to the stereo-DIC method has been devised, which is particularly applicable where high magnification and small stand-off distances are used. The parasitic effect of the out-of-plane displacements evolved from the reduced thickness of the weld was eliminated using a correction procedure as well as the geometry of the weld nugget. The procedure is initially validated in the materials' elastic loading range in FSW similar weld combinations by showing that the elastic

modulus could be obtained accurately in the weld nugget region if the geometry of the weld nugget is known. This provides the important first step in enabling accurate HR-DIC strain measurements on dissimilar FSW welds in the elastic loading range.

The microscopy results showed that the microstructure was not homogeneous through the thickness of the FSW region, hence the yielding would occur in a non-uniform fashion. Therefore, it was not possible to apply the methodology devised to account for the deformation resulting from thickness reduction post-yield. Instead, it was assumed that a welded material would yield homogenously in the through-thickness plane (i.e., across the width of the weld). Therefore, the 2D-DIC experimental methodology was applied to the weld cross-section so that the local strain gradients across the weld sub-regions were observed. Likewise, it was not possible to repeatedly load the specimen and collect several images across the weld. So instead of the image stitching, the procedure was modified so that the entire through-thickness view of the FSW region was captured by a sequence of single images during the plastic deformation. HR-DIC strain maps obtained during plastic deformation of the FSW weld cross-section are correlated with micrographs and microhardness measurements, and the local yielding characteristics of the different weld sub-regions are extracted.

Finally, X-ray CT characterisation is used to study the influence of FSW tool wear on the local material response and also to trace the complex solid-state material flow across the FSW welds. In both similar and dissimilar FSW welds, materials characterisation results achieved from microscopy, HR-DIC, and X-ray CT techniques are spatially correlated to establish the microstructure-mechanical property relationships from the heterogeneous FSW weld sub-regions.

Table of Contents

Contents

Table of Tables

Table of Figures

Research Thesis: Declaration of Authorship

Print name:	Saranarayanan Ramachandran
Title of thesis:	Development of high fidelity imaging procedures to identify the relationship between the material microstructure and mechanical behaviour of friction stir welds

I declare that this thesis and the work presented in it are my own and has been generated by me as the result of my own original research.

I confirm that:

1. This work was done wholly or mainly while in candidature for a research degree at this University;
2. Where any part of this thesis has previously been submitted for a degree or any other qualification at this University or any other institution, this has been clearly stated;
3. Where I have consulted the published work of others, this is always clearly attributed;
4. Where I have quoted from the work of others, the source is always given. With the exception of such quotations, this thesis is entirely my own work;
5. I have acknowledged all main sources of help;
6. Where the thesis is based on work done by myself jointly with others, I have made clear exactly what was done by others and what I have contributed myself;
7. Parts of this work have been published as: Please see Appendix E for references

Signature: Date: 24/05/2020

Acknowledgements

Firstly, I like to thank the University of Southampton for the unconditional offer (covering my international tuition fees and research stipend for three years) to pursue my PhD research in the Engineering Materials Research group. I would like to express my utmost sincere gratitude to my supervisors Professor Janice Barton and Professor Philippa Reed from the University of Bristol and the University of Southampton respectively for giving me the valuable opportunity to pursue my PhD at the University of Southampton. During my PhD, I have felt several times that I have been blessed with outstanding PhD supervisors. I have learned a wide range of research skills from my supervisors that include a fundamental approach to a research problem, performing a thorough literature review and critical thinking, conducting high fidelity experiments and post-processing, and writing high-quality scientific research articles. Janice's clear insights into the full field techniques as well as Philippa's strong research excellence in microscopy techniques have significantly enhanced my PhD research to correlate the valuable findings offered by these techniques on the Friction Stir Welding (FSW). Although they are extremely strict during their supervision, I strongly claim that the quality of research produced through their guidance will be well paid off at the end of PhD. Both their critical as well as very kind characteristics aided me a lot to effectively battle with the research and personal challenges evolved during my PhD. I really appreciate their valuable time spent for my progress meetings, supervision, peer-review (One-month report, Nine-month report, Eighteen-month report, Journal articles, and Final thesis draft), and continuous mentoring my research activities during my PhD. I profoundly thank my supervisors for my PhD stipend extension for 6 months with an additional enhancement from the actual funding cut-off date. This helped me a lot to come out of financial constraints and focus well on my PhD thesis writing. I am always thankful throughout my life for their support, motivation and always looking forward to collaborating with them in the future. Furthermore, I also thank my examiners Dr Brian Mellor and Dr Frances Davis for their valuable comments and feedback provided during my nine-month and upgrade project reviews. I would also like to extend my sincere thanks to my colleague Dr.A.K.Lakshminarayanan from SSN College of Engineering, Tamilnadu, India for his kind support and collaboration in supplying the FSW joints within the time frame for this PhD investigation. I like to thank my current line managers Professor Sarah Haigh and Dr Wajira Mirihanage from the University of Manchester for their continuous motivation to finalise my PhD thesis.

I would like to thank the Testing Structures and Research Laboratory (TSRL) Principal Experimental Officer Dr Andrew Robinson and my research colleagues' Dr Andreu Laborda, Dr Somsubhro Chaudhuri, Dr Angelos Evangelou, Dr Daoyun Chen, Dr James Thatcher, Dr Geoffrey Howell, Dr Daniel Bull, Mr Alvaro Sanchez, Mr Tobias Laux, Mr Geir Olafsson, Mr Jack Callaghan, Mr Timothy Harrell, Ms Irene Jimenez Fortunato for their support in conducting the experiments in the TSRL. I also thank Dr Pedro Rodrigues and Dr Shuncai Wang for their help to get trained in Electron

Backscattered Diffraction (EBSD) characterisation at the Electron Microscopy centre. I also like to thank Dr Terry Harvey for his technical support in the Nanometrology lab. My thanks also go to Dr Mark Mavrogordato, Dr Kathryn Rankin, and Dr Sebastian Rosini for their support to perform X-ray CT scan as well as CT data processing in the μ-VIS centre. I would like to thank the Mechanical Engineering Department Admin team Sue Berger, Katherine Day, Fiona Haigh, and Heather for their hard work in responding to all queries related to administration.

My thanks go to my parents Ramachandran Seenuvasan (Late) and Sivamani Ramachandran for their blessings and motivation to pursue my higher education in abroad. Without my mom's continuous support, patience and love, I would not be in the position where I am now. I also thank all my family members Manju Ramachandran, Vijay Viswanathan, Tamilmani Sundaram, Sundaram Natarajan, Valli Sundaram, Shanmugam Thyagarajan, Durga Sundaram, Elangovan Pandurangan for their full support since my undergraduate to PhD studies. I really proud to have these people as my family members, without having these fantastic people in my life I won't have had any success throughout my life. I also welcome a new member in my family as my cute fiancée Vidhyalakshmi Anbalagan for her love and mental support during my PhD thesis writing. I also thank my teachers Dr P Elangovan from IBRI college of Technology Oman, Dr M S Alphin from SSN College of Engineering, India and Dr P. Ramkumar from IIT Madras, India as well as good colleagues in India Karthee Krishnmoorthi, Yeshwant Raj, and Dr M Ananth Kumar for their motivation during my PhD research. Finally, my sincere thanks goes to my external examiner Professor David Nowell from Imperial College London and internal examiner Dr Andrew Hamilton from the University of Southampton for their valuable comments to enhance the quality of my thesis.

Definitions and Abbreviations

AE	All Euler angles
AISI	American Iron and Steel Institute
AS	Advancing side
ASTM	American Society for Testing and Materials
BM	Base material
BSE	Back-Scattered Electron Imaging
CCD	Charged couple device
CS-1	Weld cross-section (Front)
CS-2	Weld cross-section (Rear)
CT	Computer Tomography
Cu	Copper
d	Grain size diameter
DIC	Digital Image Correlation
DRX	Dynamic recrystallisation
DSS	Duplex stainless steel
E	Young's Modulus
EBSD	Electron Back Scattered Diffraction
EDS	Energy Dispersive Spectroscopy
E_t	Tangent modulus
ε_p	Plastic strain
ε_{XX}	Strain along X-axis
ε_{xy}	Shear Strain
ε_{yy}	Strain along Y-axis
Fe	Iron
FSW	Friction Stir Welding
HAGBs	High angle grain boundaries
HAZ	Heat Affected Zone
HR	High-resolution
HV	Vickers microhardness
IMC	Intermetallic compounds
IPF	Inverse Pole Figure
ISO	International organisation for standardisation
K	Strength coefficient
l	Distance between the grips

LAGBs	Low angle grain boundaries
M	Bending moment
ND	Normal direction
P_t	Transverse load
RD	Rolling direction
ROI	Region of interest
RPM	Rotation per minute
RS	Retreating Side
S1	Specimen used for HR-DIC measurements on WF and WR
S2	Specimen used for HR-DIC measurements on CS-1 and CS-2
SEI	Secondary Electron Imaging
SEM	Scanning Electron Microscopy
SS	Stainless Steel
SZ	Stir Zone
t	Specimen thickness
TD	Transverse direction
TEM	Transmission Electron Microscopy
TMAZ	Thermomechanical affected zone
UTS	Ultimate tensile strength
W	Tungsten
w	Specimen width
WF	Weld Face
WN	Weld nugget
WR	Weld Root
YS	Yield strength
Z	Atomic number
σ_a	Axial stress
σ_b	Bending stress
σ_i	Intrinsic yield strength
σ_{xx}	Stress along X axis
σ_y	Yield strength
σ_{yy}	Stress along Y axis

Chapter 1 Introduction

1.1 Project background and motivation

Dissimilar welded joints have received much attention in a wide range of structural applications as they combine the core advantages received from two different base materials [1-18]. For example, a dissimilar weld between copper and stainless steel materials would offer both high thermal/electrical conductivity and exceptional corrosion resistance properties for structural applications that need both these properties [19]. Copper to stainless steel joints are required in the nuclear power generating industries as one of the crucial components in the vacuum chambers for particle accelerators [20] and also in cryogenics [21] to utilise the high electrical conductivity of copper and high mechanical strength of the steel. It is highly challenging to produce strong fusion weld combinations of copper (Cu) and stainless steel (SS) materials due to the vast difference in their melting point (Cu-1085^{o}C, SS-1400-1500^{o}C). Additionally, the copper can conduct heat energy several times faster than steel which tends to dissipate the heat rapidly away from the weld zone making it difficult to achieve the melting point during fusion welding. Copper also has minimal solubility with steel in the liquid state and also the penetration of copper along the heat-affected zone (HAZ) of the steel may lead to hot cracking [22]. Therefore, fusion welding processes are intrinsically handicapped by the necessity of melting both copper and stainless steel. The selection of an appropriate welding process that avoids melting the base materials is the crucial element to produce a weld with good structural integrity between copper and stainless steel.

In contrast to the fusion welding processes, solid-state welding processes can produce a weld by the application of heat and pressure instead of heating the base materials to their melting points. The heat generated in the solid-state welding process due to friction is below the melting points of the base materials. All solid-state welding process are inherently autogenous and therefore do not require the usage of a filler material. Due to the absence of melting and filler materials, solid-state welding processes have been identified as suitable candidates to join dissimilar materials [5, 23]. Furthermore, the ability to produce dissimilar welds without the weld defects that commonly occur in fusion welding processes have increased the application range of solid-state welding processes in the field of dissimilar welding.

Friction stir welding (FSW) is a solid-state welding process, where the joining is achieved by the frictional heat and plastic work rate produced by a rotating and traversing non-consumable tool. This high plastic deformation and frictional heat produce a high density of submicron grains in the weld nugget, making the FSW weld nugget much stronger compared to the base materials [5]. On the other hand, the intense plastic deformation of FSW also produces a slight thickness reduction across the weld nugget. FSW involves lower heat input which enables dissimilar materials to be joined without

any bulk melting; therefore, it completely eliminates the solidification drawbacks associated with the fusion welding process [23]. There are well-documented investigations where the FSW has been successfully applied to a range of dissimilar materials that are considered to be extremely difficult to weld using the traditional fusion welding process [24]. The combined stirring action and plastic deformation of the FSW process usually causes a wide turbulence in the material flow which results in extensive microstructural changes in the vicinity of the weld nugget [23]. Hence, FSW on any base material combination produces various sub-regions along both the base materials. The FSW weld sub-regions are commonly classified as the weld nugget (stir zone), Thermo-mechanical affected zone (TMAZ), Heat affected zone (HAZ), and Base metal (BM). These weld sub-regions possess distinctive microstructural features due to the thermo-mechanical effects of the FSW process. The relationship between grain size and its corresponding yield strength of a material is defined by the well-known Hall-Petch equation:

$$\sigma_y = \sigma_i + \frac{K}{\sqrt{d}} \qquad (1.1)$$

where σ_y is the yield strength, σ_i is the intrinsic yield strength, K is the materials constant, and d is the grain diameter

According to Equation (1.1), the yield strength of a material is related to its grain size. Thus it is expected that the FSW weld sub-regions will plastically deform at different stresses corresponding to their grain size, and also may have different hardening characteristics. This heterogeneous material behaviour of the weld sub-regions is responsible for local material property variations across the FSW weld that control the global response of the joint [25]. Evaluating the locally varying yield strength of the FSW weld sub-regions will lead to a holistic understanding of the whole material behaviour of the weld. Furthermore, this information is also vital from a design perspective in determining the load-carrying capability of welded structures. Several methods have been attempted for measuring local mechanical property variations in welds, which include testing of micro-tensile specimens machined from various weld zones [1] and instrumented ball indentation methods [26]. But these methods are destructive, hard to interpret in the context of the overall mechanical response of the weld and extremely time-consuming. In addition to this, the spatial resolution achieved by these techniques is often insufficient to isolate the heterogeneities between the weld sub-regions. To characterise the varying plastic response of the FSW weld sub-regions at a high spatial resolution, there is a definite need for a full-field optical technique with high-resolution optics.

DIC (Digital Image Correlation) is a well-established technique that has been used for measuring full-field displacement and strain fields in welds [27, 28]. DIC has been used in FSW joints with the focus to assess the local material behaviour of weld zones [29, 30]. In DIC, the spatial resolution and displacement precision are limited by the number of pixels occupied in the image and size of the subsets [31]. The scale of a typical FSW welded region is small, and therefore there is a need for

high-resolution (HR) DIC to accurately resolve the local material behaviour of the FSW weld sub-regions. To date, HR-DIC has not been extensively used on friction stir welded dissimilar joints and also, a clear experimental methodology has not yet been proposed for evaluating the full-field strain data from the weld sub-regions by thoroughly accounting for the actual geometry of the weld.

In FSW (Cu-SS) welded joints, to date, only one investigation that uses DIC to study the local strain distribution across the weld has been reported [32]. However, this investigation did not correlate the DIC results with the microscopy findings, and therefore, the local material response of the individual FSW (Cu-SS) weld sub-regions was not determined. The current PhD investigation focusses on developing a novel HR-DIC experimental methodology to perform high-fidelity strain measurements on dissimilar FSW (Cu-SS) welds to evaluate the degree of heterogeneity in the mechanical response across various sub-regions of FSW (Cu-SS) welds. To achieve structure-property relationships of FSW (Cu-SS) weld sub-regions, the investigation employs a range of microscopy techniques such as optical and electron microscopy to locate the distinct microstructural features of the weld sub-regions. The findings from which are correlated with the DIC measurements to establish the relationships between the microstructure and mechanical strength of the FSW weld sub-regions with a high degree of confidence. Dissimilar FSW welds are extremely challenging for both microstructural and mechanical characterisation due to the extensive non-homogeneous materials mixture stirred in the weld nugget. Therefore, to systematically approach the objectives of this PhD investigation, FSW weld between similar materials such as FSW (SS-SS) and FSW (Cu-Cu) welds are also included for the preliminary investigations. It is noteworthy that these similar FSW welds were manufactured from the same base materials that were used to manufacture FSW (Cu-SS) welds and therefore the characterisation results received from the similar weld combinations inform the experimental approach for FSW (Cu-SS) welds. Overall, this PhD investigation is focussed on a comparative analysis of the local mechanical/microstructural properties of similar and dissimilar FSW welds.

1.2 Aim and objectives

The overarching aim of this PhD work is to critically understand the local microstructure-property relationships of FSW similar and dissimilar copper and stainless steel joints at a high spatial resolution using HR-DIC and a range of microscopy techniques. The full-field data-rich approach will be complemented with microstructural assessments to understand how microstructure governs local yielding of the FSW weld sub-regions. However, due to a non-uniform weld geometry of the actual FSW welds, resulting from the pressure applied during the welding, there are several challenges to be overcome before achieving accurate HR-DIC measurements. Thus there is a strong need to also investigate the effect of FSW geometry on strain measurements. To achieve the overarching aim and also to address the experimental challenges involved in the PhD investigation, the following objectives must be satisfied:

1. Establish the whole FSW weld geometry with a particular emphasis on accurately measuring the inherent reduced thickness across the weld nugget.
2. Classify the distinct microstructural features of the FSW weld sub-regions such as weld nugget, TMAZ, and HAZ as well as the boundaries between these weld sub-regions through optical and electron microscopy techniques such as SEM and SEM-EBSD.
3. Determine the microhardness variations between the weld sub-regions through spatial microhardness measurements across the weld cross-section, which consists of all major weld sub-regions.
4. Devise and validate a novel experimental methodology to perform HR-DIC strain measurements on similar FSW welds such as FSW (SS-SS) and FSW (Cu-Cu), and on dissimilar FSW (Cu-SS), in the material elastic regime.
5. Adapt the validated methodology to be used beyond the elastic regime to identify the heterogeneous local strain response of the weld sub-regions during plastic deformation.
6. Establish the FSW weld geometry as well as solid-state material flow across the weld nugget through X-ray CT.
7. Link the HR-DIC findings with micrographs (Optical, SEM, and X-ray CT) to establish the reason for the post-yielding behaviour.

1.3 Novelty

As the actual FSW welds have thickness reduction across the weld nugget, there is a definite necessity to account for the local geometry effects on the DIC strain measurements. However, most previous DIC studies on FSWs utilised specimens that were machined to the reduced thickness of the weld nugget to avoid any out of plane deformation and bending during loading [29, 30, 33]. Although these approaches enable accurate DIC strain measurements, they neglect the influence of the post-weld machining on the material microstructure and also its effect on the local strain distributions. Therefore, developing a new high-fidelity DIC experimental approach for the actual FSW similar/dissimilar welds with an assessment of weld geometry is novel. This can be achieved through HR-DIC data aided with X-ray CT and Alicona focus variation microscopy measurements.

The microstructural changes occurring during the FSW process cause variation in the mechanical properties of the weld sub-regions. This difference in the mechanical properties of the FSW sub-regions constrains the total strength of the joint. Many earlier studies have been attempted to establish the local material behaviour of FSW welds [29, 30]. These studies were attempted in a low-resolution DIC system in determining the local strain distributions along the weld. However, measuring the full-field strain at a high spatial resolution is vital for evaluating the local properties; this has not been previously reported. Correlating the HR-DIC measurements with microscopy findings is also new, as the full range of optical microscopy, SEM images, EBSD and associated material characterisations have not been mapped to the strain response across the weld. All the material

characterisation techniques will help to establish the relationship between global performance of the joint and local property variation along the vicinity of the weld.

Due to the complex thermo-mechanical cycle that occurs in the FSW process, the microstructures produced on the surface and cross-section of the FSW are distinct [34]. Therefore, the local mechanical behaviour of the FSW weld surfaces will be different from the through-thickness cross-section. This phenomenon is even more exaggerated for a dissimilar FSW weld, where the material response of both weld surface and cross-section regions during plastic deformation are totally dependent on the population density of dissimilar elements located in these regions. For a complete understanding of the whole behaviour of the FSW weld, a clear microstructure-property relationship of both surface and through-thickness cross-section must be established. However, the majority of DIC studies attempted to date on the FSW welds have been traditionally focused only on the weld cross-section instead of the weld surface. To fill this research gap, the microstructural features and strain distribution on the weld surfaces as well as weld cross-section regions are studied to obtain a complete understanding of the local thermo-mechanical effects of the FSW process in these regions.

1.4 Thesis structure

Excluding the introduction chapter (Chapter 1), this PhD thesis is constructed with eight main chapters that include literature review, experimental methodology, experimental results and validation, and conclusions. The main focus of each chapter is described as follows:

Chapter 2 offers a theoretical background of the FSW process alongside with advantages and limitations associated with the process. To achieve the primary objectives of this PhD investigation, this chapter critically reviews the recent investigations performed on the FSW of similar and dissimilar weld combinations of copper and stainless steel. Furthermore, the key findings derived from the previous investigations are also summarised at the end of this chapter.

Chapter 3 focuses on the theory behind DIC and also it reviews the recent DIC investigations performed on FSWs. This chapter also provides a brief literature background for high-resolution DIC applications.

Chapter 4 briefly describes the selection of FSW process parameters for manufacturing relatively defect-free FSW (SS-SS, Cu-Cu, and Cu-SS) joints for highly reliable experimental investigations. Additionally, this chapter explains the test specimen preparation and arrangements required for HR-DIC measurements.

Chapter 5 presents the specimen preparation procedures for a wide range of microscopy techniques followed by microstructural characterisation results derived from the three FSW (SS-SS, Cu-Cu, and Cu-SS) weld combinations. This chapter also includes the microhardness results obtained from these

weld combinations. A brief summary of the key findings achieved through a range of materials characterisation techniques is also included in this chapter.

Chapter 6 describes the development of a high fidelity full-field imaging procedures and validation methods developed for high-resolution strain measurements in the elastic loading range of the FSW welds. This chapter also highlights the experimental challenges involved in HR-DIC strain measurements on the FSW welds.

Chapter 7 demonstrates the application of high fidelity imaging procedures in the plastic loading range of FSW welds. Most importantly, this chapter establishes microstructure-property relationships of FSW weld sub-regions by correlating their local material behaviour achieved through HR-DIC with the corresponding microscopy findings (Chapter 5).

Chapter 8 presents the X-ray CT results obtained from the FSW welds, and also it correlates the X-ray CT findings with HR-DIC measurements (Chapter 7) and micrographs (Chapter 5) to achieve a holistic understanding of the structure-property relationships of the FSW weld sub-regions with more information about the FSW weld geometry.

Chapter 9 presents the main conclusions drawn from the PhD investigation. In addition to this, this chapter also offers the author's recommendations for future work to gain further insight into the research questions evolving from the findings of this PhD investigation.

Chapter 2 Introduction to Friction Stir Welding (FSW) process and material characterisations

2.1 Introduction

This literature review chapter briefly explains the theoretical background of the friction stir welding (FSW) process and also previous investigations of the FSW process found in the literature. The main focus of this chapter is on reviewing previous investigations on the performance of similar and dissimilar friction stir welds between copper and stainless steel. Investigations reviewed in this chapter are organised under three sections:

i) Theory of FSW process

ii) FSW of similar materials

iii) FSW of dissimilar materials

The first section describes the theory of the FSW process, which comprises significant FSW process parameters, advantages, applications, and limitations involved in FSW. The second section presents the key investigations performed in FSW of similar materials focused mainly on stainless steel to stainless steel and copper to copper material combinations. The third section explains the key investigations performed in FSW of dissimilar materials focused mainly on copper to stainless steel combinations. Both the second and third sections mainly review the microstructural evolution and mechanical properties achieved from the FSW welds. The review of these sections then informs the appropriate design of experiments and material characterisations required for this PhD research. This PhD investigation deals only with FSW joints manufactured between copper and stainless steel base materials in both similar and dissimilar material combinations. Therefore, investigations which deal with the FSW of a wide range of similar/dissimilar materials are not addressed in this review. However, a few key investigations related to the evaluation of the local material properties in FSW welds using DIC have been discussed in the next chapter.

2.2 Introduction to Friction Stir Welding (FSW)-a solid-state welding process

2.2.1 Theory of Friction Stir Welding (FSW)

Friction Stir Welding (FSW) was invented at The Welding Institute (TWI) in the UK in 1991 [35] as a solid-state joining technique, and it was initially attempted to weld aluminium alloys. FSW involves

a rotating tool with a shoulder and profiled pin traverse along the butting surfaces of two rigidly clamped plates. The parts need to be clamped onto a backing plate in a manner that prevents the abutting joint faces from being forced apart. The heat generated by friction between the non-consumable FSW tool and the material being welded causes the material to soften without reaching the melting point. The combined severe plastic deformation and frictional heat generation produced by the FSW tool leads to plastic flow of the material as the tool is translated along the welding direction. The formation of thermal energy (frictional heat) and mechanical energy (tool rotation and translation) from this process causes the movement of material from the leading to the trailing edge of the tool, and it gets consolidated into a weld. As a result of this mechanism, a weld is produced in the 'solid-state' that avoids most of the solidification issues associated with the fusion welding processes. The different terminologies involved in the FSW process are shown in Figure 2.1. The side of the weld where the direction of the rotating tool is same as that of welding direction is called the advancing side (AS) and the converse is designated as the retreating side (RS).

Figure 2.2 illustrates various weld sub-regions across the cross-section of a typical FSW. Each zone (A, B, C, D) and its corresponding boundaries are commonly classified based on their distinct microstructural features and grain size. The description of each weld sub-region is as follows:

Sub-region A: the base material (BM) or parent metal is the region distant from the weld, which has the same set of properties as the as-received conditions of the plates or sheets that have been joined.

Sub-region B: the Heat affected zone (HAZ) is close to the weld so it experiences thermal effects from the FSW process and therefore the average grain size of this zone is slightly larger than the base material (due to grain growth processes). However, the HAZ is unaffected by any plastic deformation from the FSW process.

Sub-region C: the thermo-mechanically affected zone (TMAZ) which lies between the HAZ and the weld nugget. In the TMAZ, the FSW tool has plastically deformed and heated the material, but it does not undergo complete recrystallisation process. The TMAZ zone is often categorised by elongated grains or grains which have an extremely low aspect ratio [23]. The formation of the elongated grains is mainly due to the intense plastic deformation experienced in this region.

Sub-region D: represents the dynamically recrystallised (DRX) zone, often referred to as the weld nugget/stir zone. The weld nugget of a typical FSW has an "onion-ring" structure, and it is the result of the intense stirring action of the FSW tool [23]. The weld nuggets produced by the FSW process have ultra-fine recrystallised grains compared to the base material. Because of this fine grain size, the mechanical strength of the weld nugget (as per the Hall-Petch relationship) is usually superior to its base material.

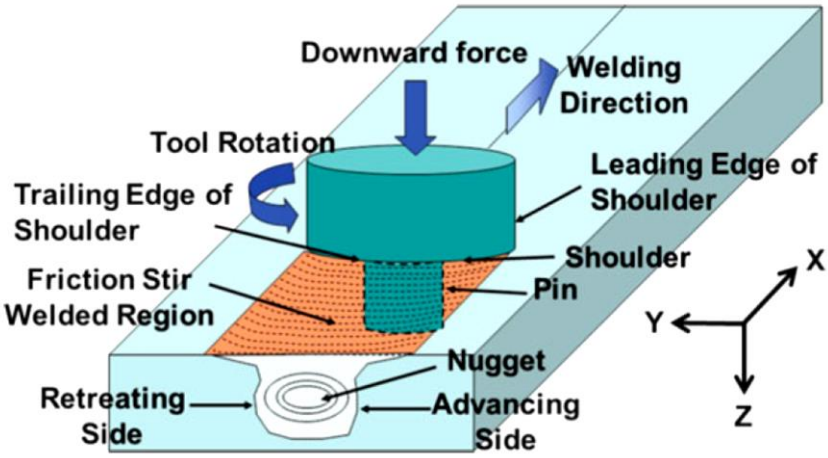

Figure 2.1 Schematic illustration of the FSW process [23]

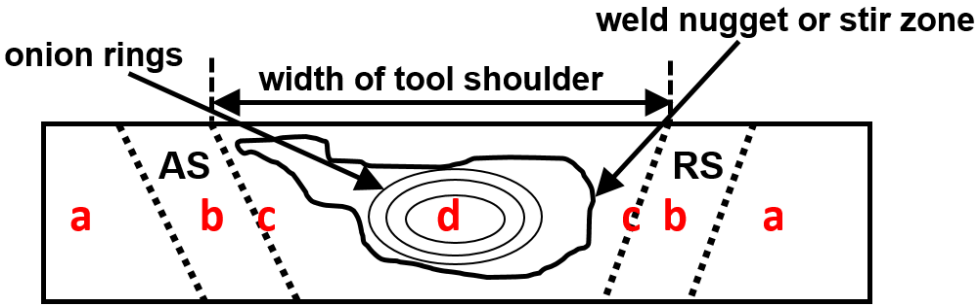

Figure 2.2 Schematic illustration of FSW weld cross-section shows different weld sub-regions: A-BM; B- HAZ; C-TMAZ; and D- Weld Nugget (Stir Zone)

2.2.2 Advantages of FSW over fusion welding processes

Advantages of FSW over fusion welding processes can be classified from four major perspectives as follows: (a) Microstructural, (b) Mechanical, (c) Environmental, and (d) Energy [23].

Microstructural advantages include:

i) FSW process improves the weldability of a wide range of dissimilar alloys with reduced distortion.

ii) FSW welds are mostly free from porosity, solidification cracking, and other major weld defects compared to the fusion welds.

iii) As the base materials do not achieve their melting point, no loss of alloying elements during the FSW process.

iv) FSW welds have excellent microstructural characteristics due to fine recrystallised grains produced by the severe plastic deformation of the FSW tool.

Mechanical advantages include:

i) The FSW weld nugget achieves superior mechanical strength, ductility, and fatigue resistance than the corresponding base materials due to its ultrafine microstructural features.

ii) FSW process also enhances the microhardness of the weld nugget in some similar/dissimilar material combinations.

Environmental advantages include:

i) FSW does not require any shielding gas as in the conventional fusion welding process.

ii) FSW needs only minimal surface preparation for joining (such as degreasing, milling the joint surface of the plate).

iii) No harmful fumes released during FSW as there is no bulk melting.

iv) No radiant energy is emitted during the FSW process.

Energy advantages include:

i) FSW process often requires a single welding pass compared to multiple passes for fusion welding processes.

ii) In FSW, there is a wide range of scope to weld materials with different combinations and thicknesses that reduces material wastage.

iii) FSW energy consumption is several times less than higher energy fusion welding process such as Electron Beam Welding and Laser Beam Welding.

2.2.3 Limitations of the FSW process

Despite these advantages, the FSW process also has limitations as follows:

- FSW process commonly produces welds with a reduced thickness across the stir zone due to the substantial axial force and severe plastic deformation involved in the FSW process.
- FSW involves highly expensive tool materials such as Polycrystalline Cubic Boron Nitride (PCBN) and refractory metals based tools for welding high-temperature materials such as stainless steel, nickel, and titanium.
- Although the majority of the FSW tool materials have wear-resistant properties, there is some evidence reported about the possibility of tool wear during the FSW process on high-

temperature materials [36, 37]. This FSW tool wear may significantly modify the material compositions locally across the region affected by the tool.

- FSW process usually generates an exit hole at the end of welding as a result of the tool retraction. The material near the region of the exit hole is generally considered as scrap and therefore not suitable for further material characterisations in this study.
- FSW can be somewhat limited in the orientations of welds possible (given the tooling required) and in terms of the thicknesses of sheet that can be joined.

2.2.4 FSW of Stainless steel (SS) to Stainless steel (SS)

FSW has been extensively used to join a wide grade of steels as a consequence of the advancements made in developing high strength FSW tool materials [38]. Although the temperature generated during the FSW process when used on steels is below their melting point, both plastic deformation and severe friction during the process create different microstructural features in the form of weld sub-regions. The FSW weld sub-regions therefore have a different material response in line with their grain size. As a result, there is a strong need to characterise the weld sub-regions using material characterisation techniques including microscopy and localised mechanical characterisation using DIC to understand the structure-property relationships of the weld sub-regions. A few fundamental investigations [37, 39-42] have been attempted on the FSW of steels and the crucial findings derived from these previous investigations are reviewed in the following sections of this chapter.

2.2.4.1 Microstructural evolution across the FSW (SS-SS) weld sub-regions

Li et al. [37] studied the microstructural evolution of friction stir welded super-austenitic stainless steel S32654 at a constant welding speed of 100 mm/min and different rotational speeds of 300 and 400 rpm. Figure 2.3 (a) and (b) show the low magnification optical micrograph obtained from the weld manufactured at 300 rpm and 400 rpm respectively. Both micrographs show complete weld penetration without any weld defects. The authors coined the description of the shape of the stir zone as a “basin-shape” structure and the weld sub-regions such as SZ, TMAZ-AS, TMAZ-RS, and BM are classified according to their grain size. A sharp transition between the TMAZ and stir zone is clearly observed along the advancing (AS) and retreating sides (RS). It is reported that no significant grain growth was achieved in the vicinity of the weld at both welding conditions which proves the absence of high temperatures and thus limited formation of HAZs during the FSW process. The size of the stir zone is consistent with the width of the shoulder. Optical micrographs captured from the individual weld sub-regions at two different welding conditions are displayed in Figure 2.4. BM (Figure 2.4a and f) exhibits typical austenitic microstructural features with a dense population of annealing twins. As expected, the stir zone (SZ) has achieved equiaxed ultrafine grains from the resultant of dynamic recrystallisation (DRX) mechanism offered by the frictional heat and plastic deformation as shown in (Figure 2.4c and h). Due to the lower heat input, the HAZ (Figure 2.4b and

g) has not shown any abnormal grain growth. Although the micrographs observed at two different welding conditions look similar to each other, the authors reported that the formation of band structures on the AS (Figure 2.4i) is evident only at 400 rpm. This is because of the intense stirring action offered by the FSW tool at 400 rpm compared to 300 rpm. To investigate the band structures further, the authors have performed SEM/EDS analysis on the locations shown in Figure 2.5a and confirmed the existence of tungsten (W) and rhenium (Re) elements. These elements are marked as A and C in Figure 2.5d and Figure 2.5e, respectively. In addition to the AS of SZ, the authors also reported the presence of W particles on the upper surface of SZ (Figure 2.5c). Tool wear produced by the high strain rate and frictional heat at 400 rpm rotational speed is the key reason offered by this investigation for the presence of W in the weld nugget.

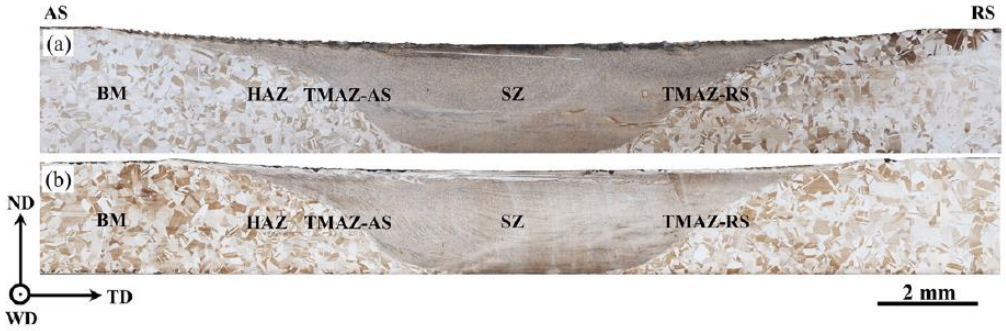

Figure 2.3 Low magnification optical micrograph of friction-stir welded super-austenitic stainless steel S32654 joint manufactured at different rotational speeds: (a) 300 rpm and (b) 400 rpm [37]

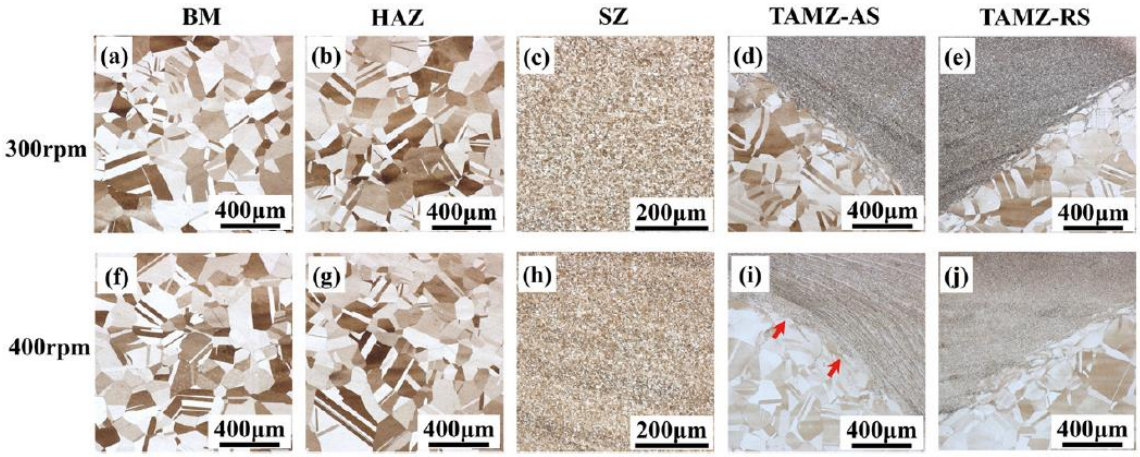

Figure 2.4 High magnification optical micrographs of FSW weld sub-regions captured at 300 rpm and 400 rpm: (a) (f) BM; (b) (g) HAZ; (c) (h) Stir Zone; (d) (i) TMAZ-AS; (e) (j) TMAZ-RS [37]

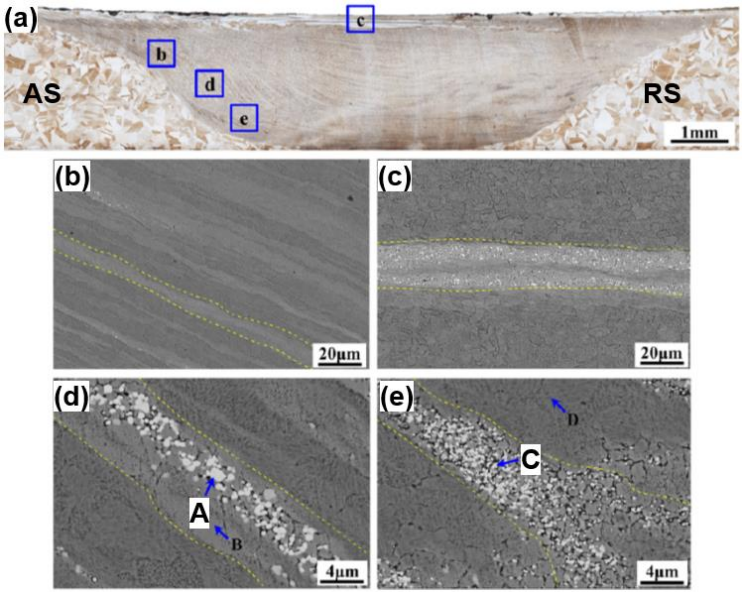

Figure 2.5 Micrographs of weld cross-section at a rotational speed of 400 rpm: (a) Optical micrograph; (b)-(e) SEM micrographs corresponding to different regions of the macrostructure marked b, c, d and e included in (a) [37]

Park et al. [39] examined the microstructural formation processes in friction stir welded 304 austenitic stainless steel. Figure 2.6a shows a low magnification optical macrograph of the weld cross-section, where the weld nugget does not achieve complete weld penetration as the length of the pin used was shorter than the 2 mm sheet thickness. The authors reported the presence of tunnel type defects in the interface between the SZ and TMAZ on the AS. However, the authors did not report any reason for the formation of this defect. Optical micrographs captured from the major weld sub-regions such as the stir zone and TMAZ (AS and RS) are displayed in Figure 2.6b-d. The stir zone (Figure 2.6b) has achieved fine recrystallized grains. It is noteworthy that the TMAZ-AS (Figure 2.6c) possess a mixture of coarse and fine grains. However, the TMAZ-RS (Figure 2.6d) sub-region mostly consists of coarse grains. This shows that both these regions had experienced a different scale of thermo-mechanical deformation effects during the FSW process. Although this investigation partially resolved the weld sub-regions, the existence of a HAZ is not confirmed. In contrast to the results achieved by Li et al. [37], the optical micrographs of TMAZ (AS and RS) characterised in this investigation did not show a sharp interface between TMAZ and weld nugget regions. Additionally, the TMAZ micrographs have failed to confirm the presence of elongated and deformed grains achieved by the plastic deformation.

Guo et al. [40] investigated the microstructures of friction stir welded 304 stainless steel joints and found the basin shape structure achieved by the weld cross-section similar to the investigation reported by Li et al. [37]. The authors described that extreme plastic deformation and frictional heat of the FSW process are responsible for the formation of this structure. Figure 2.7 shows the optical

micrograph obtained from this investigation, where the material flow in the form of onion rings is evident. Additionally, this figure displays the spatial locations of the weld sub-regions such as SZ, TMAZ, HAZ and BM. However, these regions are not clearly observed through high magnification optical or SEM micrographs of this investigation.

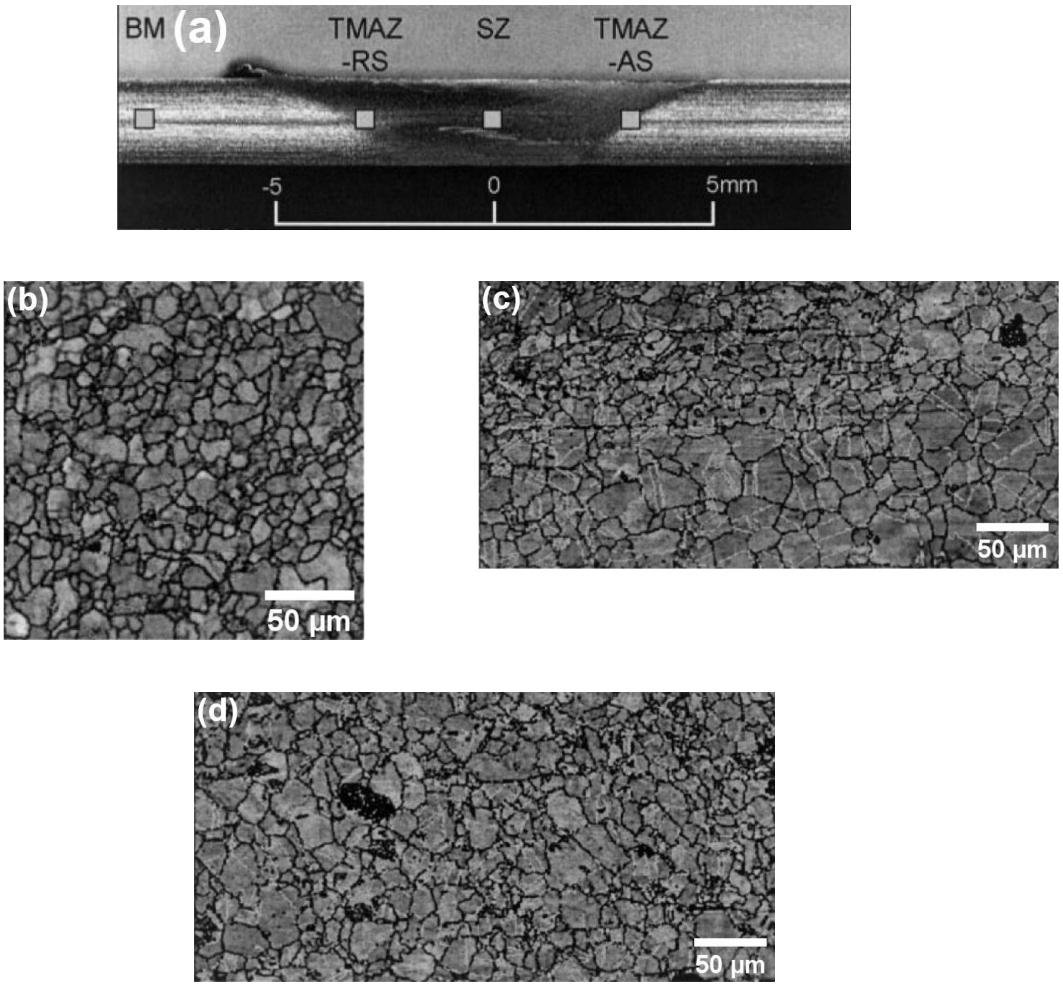

Figure 2.6 Optical micrographs of FSW (SS-SS) weld cross-section: (a) Low magnification optical micrograph; (b) Stir zone; (c) TMAZ-AS; (d) TMAZ-RS [39]

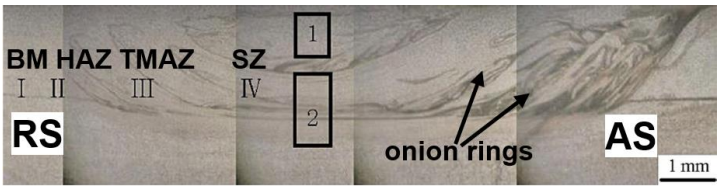

Figure 2.7 optical micrograph of FSW (SS-SS) weld cross-section [40]

Mironov et al. [41] characterised the microstructure of friction stir welded TRIP steel. Figure 2.8 shows the low magnification optical micrograph of the weld cross-section, where the reduced thickness across the stir zone is noticed. The authors confirmed the evidence of bending achieved by the joint due to the residual stresses. In contrast to the findings advocated by Li et al. [37], this investigation has found the existence of a significant HAZ (Zone-1) located between the TMAZ (Zone-2) and BM.

Figure 2.8 Low magnification optical micrograph of friction-stir welded TRIP steel [41]

Lakshminarayanan [42] determined the microstructural properties of friction stir welded 304 stainless steel joints manufactured via multi-criteria optimization. Figure 2.9 displays the optical micrographs of the weld sub-regions characterised from the joint manufactured from the optimised process parameters. A step change in the grain size is observed at the TMAZ/HAZ interface located on the AS (Figure 2.9a). In addition to this, TMAZ (AS) achieved the band structures with vortex layers of different grains size (Figure 2.9d). Li et al. [37] also supported this claim in their investigation. The stir zone has a dense population of equiaxed sub-micron grains (Figure 2.9b), and the BM shows coarse austenite grains with annealing twins (Figure 2.9c).

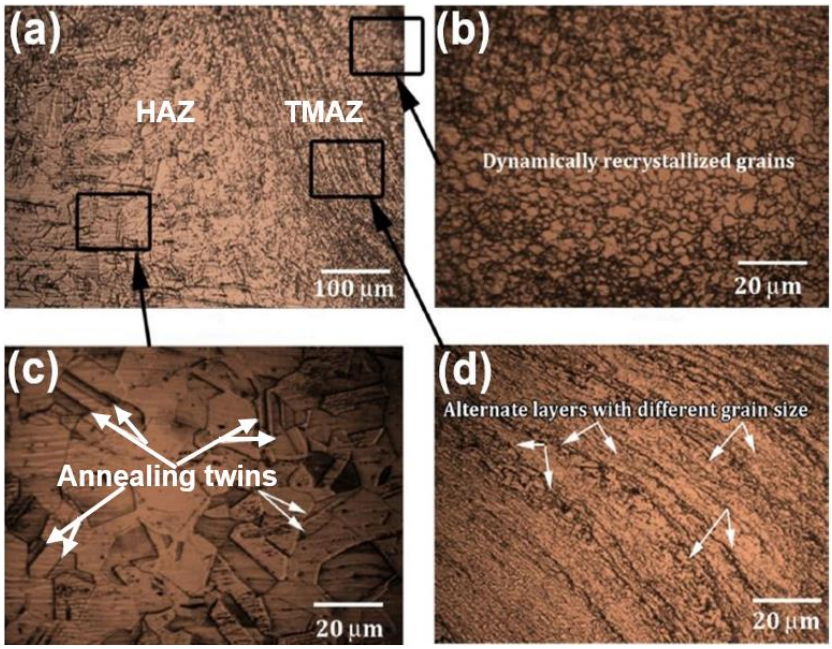

Figure 2.9 Optical micrographs of FSW (SS-SS) weld sub-regions: (a) TMAZ/HAZ interface (AS); (b) Stir Zone; (c) Base metal; (d) Band structure [42]

2.2.4.2 Mechanical properties of FSW (SS-SS) joints

2.2.4.2.1 Microhardness properties of FSW (SS-SS) welds

Li et al. [37] studied the microhardness properties of friction stir welded super-austenitic stainless steel S32654 manufactured at a constant welding speed of 100 mm/min and different rotational speeds of 300 and 400 rpm. Figure 2.10a shows the hardness profiles obtained at two different welding conditions. It is reported that the average hardness value of the stir zone at 300 rpm and 400 rpm are 363.3 HV and 378 HV respectively. Both these values of SZ are higher than the average hardness of the BM (290.7 HV). The authors emphasised that the high degree of grain refinement is the crucial factor for the hardness enhancement in the stir zone. It is also mentioned that both dislocation density and sub-structure formation usually increase with tool rotation speed. Because of this reason, the hardness achieved at 400 rpm is comparatively higher than the 300 rpm.

Park et al. [39] examined the microhardness distributions in friction stir welded 304 austenitic stainless steel. Figure 2.10b exhibits the hardness profiles derived from this investigation. From this figure, it is clear that hardness achieved in the SZ (200 HV) is higher than in the BM (180 HV). This finding corroborates the microhardness results obtained in the investigation performed by Li et al. [37]. However, it is noticed that the hardness of the SZ is slightly lesser than the TMAZ. To clarify this finding, the authors argued that the hardness achieved by the FSW weld sub-regions is not entirely governed by the grain size alone; instead, both dislocation density and the population of sub-grains also have an impact on the hardness distributions. Therefore, the authors indirectly mentioned that a simplistic version of the Hall-Petch relationship is not fully satisfied in their investigation.

Miyazawa et al.[43] measured the microhardness distribution on the friction stir welded 304 stainless steel manufactured using an Ir based tool under different process parameters. Figure 2.10c displays the hardness profiles of the weld manufactured using two different tool rotating speeds and a range of welding speeds. Both the hardness profiles (18 rev/sec and 22.2 rev/sec) demonstrate the higher hardness of the SZ than other weld sub-regions. The authors agree with the claim offered by Li et al. [37] by saying that both ultrafine grains and high deformation resistance associated with the SZ are the principal reasons for the maximum hardness observed.

Guo et al. [40] investigated the microhardness properties of friction stir welded 304 stainless steel joints. Figure 2.10d shows the hardness values measured on the FSW weld sub-regions including SZ, TMAZ, HAZ, and BM. It is reported that the hardness of the BM is 224 HV and for the SZ, it varies from 270 to 335 HV. In contrast to the observation made by Park et al. [39], this investigation has confirmed that the SZ has achieved the maximum hardness rather than the TMAZ. The authors cited the traditional Hall-Petch relationship was the reason for the maximum hardness recorded in the SZ. Furthermore, it is mentioned that the deformation resistance offered by the high volume of grain boundaries located in the SZ is the crucial phenomenon for the hardness increment in the SZ.

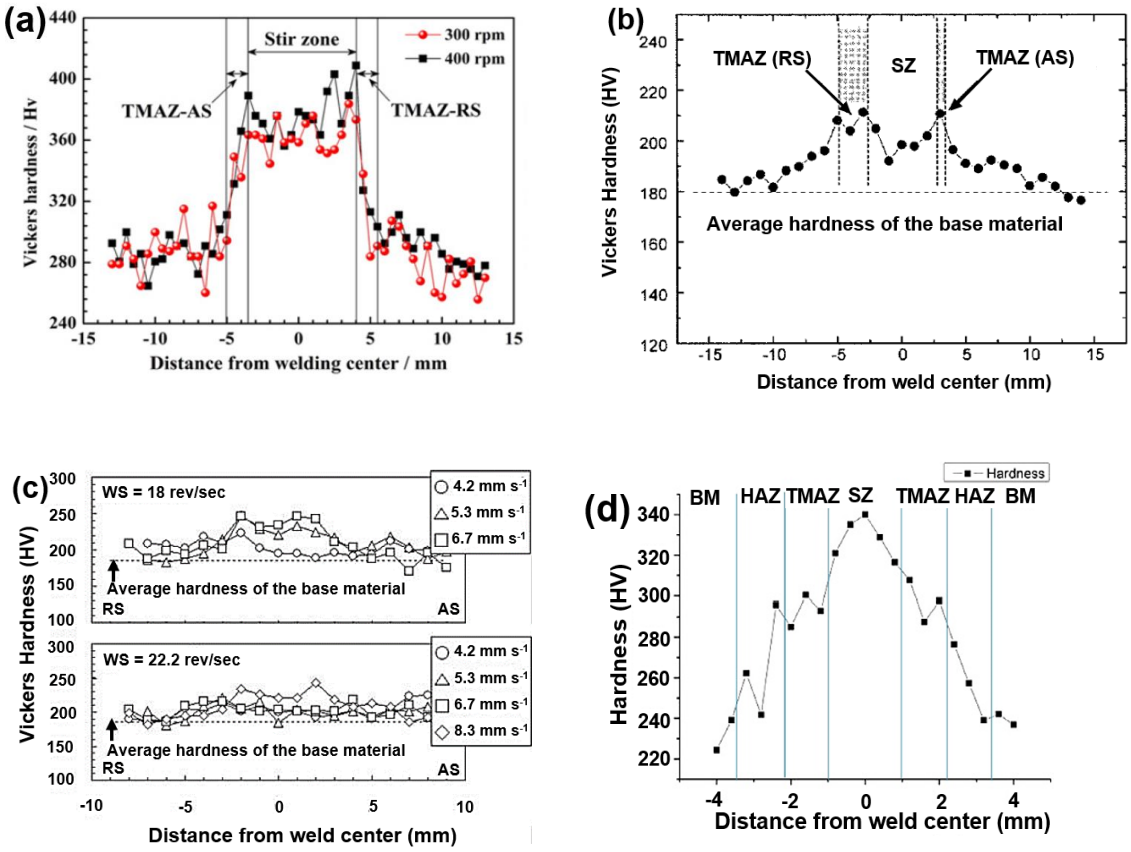

Figure 2.10 Microhardness maps along the centre line of FSW (SS-SS) weld cross-section reported from previous investigations: (a) Li et al. [37]; (b) Park et al. [39]; (c) Miyazawa et al. [43]; (d) Guo et al. [40]

2.2.4.2.2 Tensile properties of FSW (SS-SS) joints

Li et al. [37] also characterised the tensile properties of their friction stir welded super-austenitic stainless steel S32654 manufactured at a constant welding speed of 100 mm/min and different rotational speeds of 300 and 400 rpm. Figure 2.11a displays the stress-strain curves derived from the welded joints and the BM. It is clearly noticeable that both the welded joints have achieved superior ultimate tensile strength (UTS) and yield strength than the BM. From Figure 2.11b, it is observed that both UTS and YS values achieved at the two different rotational speeds are very similar. However, both the welded joints had a more reduced elongation % than the BM. The authors stated that the high-density dislocations and substructures produced in the SZ are the primary sources for reducing the ductility of these joints. Additionally, they reported the possibility that the fine grain size of the SZ generally accelerates dislocation accumulation against grain boundaries which leads to a reduction in the plastic deformation. The authors emphasised that the ultrafine grains produced in the weld nugget are the key element in improving the strength of FSW samples. Low magnification and high magnification fractographs observed from the fractured tensile specimen are shown in Figure 2.11c and Figure 2.11d, respectively. High magnification fractograph (Figure 2.11d) exhibits

dimples and microvoid coalescence features that indicate the nature of the tensile failure is ductile. The major limitation of this investigation is that only single tests were performed on the individual tensile specimens which were manufactured with different process parameters, so no estimate of scatter is made.

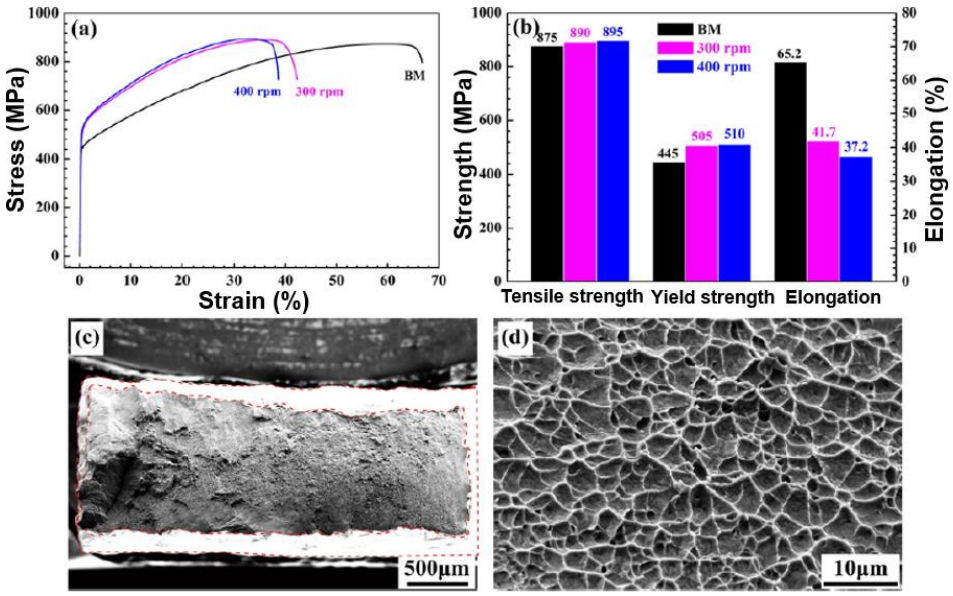

Figure 2.11 Tensile properties of FSW S32654 weld : (a) stress-strain curves ; (b) results of tensile test; (c) Fracture morphologies at low magnification; (d) Fracture morphologies at high magnification [37]

Miyazawa et al.[43] derived the tensile properties of friction stir welded 304 stainless steel manufactured using an Ir based tool under different process parameters, as shown in Figure 2.12. It is reported that the joint manufactured with the rotation speed of 18 rev/sec alongside with the welding speed of 5.3 mm/sec was fractured in the base metal and achieved sounder tensile properties than other welded joints. The authors claim that under these process parameters, the stir zone had reduced heat input due to the increase in welding speed and the decrease in rotation speed, and therefore more fine grains produced in the weld nugget compared to when other welding parameters were applied. A high density of fine grains located in the stir zone usually favour more strain hardening during the tensile tests and the result is exceptional tensile properties. However, it is noteworthy that the elongation% achieved using the same process parameters is less than the base metal. This finding is in agreement with the tensile results reported by Li et al. [37]. The authors further reported that due to the reduced thickness across the stir zone, the joints manufactured with other welding parameters have fractured in the stir zone instead of base metal. But this claim is wholly contradicted by the previous claim offered by the authors, where the weld manufactured with the rotation speed of 18 rev/sec alongside with the welding speed of 5.3 mm/sec also had reduced thickness across the stir zone but fractured in the base metal.

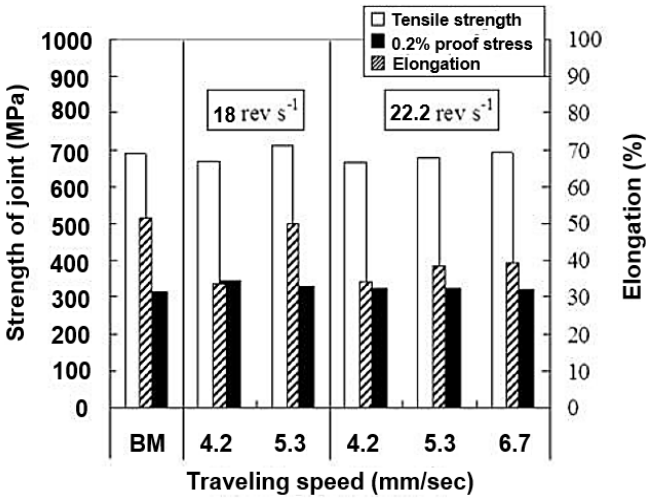

Figure 2.12 Tensile properties of FSW (SS-SS) joints under various welding conditions [43]

2.2.5 FSW of Copper (Cu) to Copper (Cu)

Welding of copper using fusion welding processes is challenging due to its high thermal conductivity properties. However, FSW has achieved a significant growth in popularity in joining high thermal conductivity materials, such as copper alloys, due to its better capability to mitigate the issues related to the extensive heat dissipation characteristics of copper than fusion welding processes [23]. Additionally, due to the solid-state welding mechanism of FSW, there is more possibility that common defects such as solidification and incomplete penetration can be completely avoided while joining copper alloys through the FSW process. However, FSW of copper alloys profoundly modifies the microstructures across the weld due to the frictional heat and plastic deformation involved in the FSW process. This results in the formation of weld sub-regions with different microstructural features across the FSW weld nugget. As the mechanical performance of a material is directly related to the grain size and prior deformation structures, there is a definite requirement to characterise the weld sub-regions using material characterisation techniques to achieve a clear insight into the structure-property relationships there. To date many feasibility studies have been made on the FSW of copper alloys [44-48], and these studies were mainly attempted to characterise the microstructural and mechanical properties achieved in the welds. However, only the key findings derived from the previous investigations are reviewed in the following sections of this chapter.

2.2.5.1 Microstructural evolution across the FSW (Cu-Cu) weld sub-regions

Heidarzadeh et al. [44] characterised the microstructural evolution of friction stir welded pure copper. Figure 2.13a and Figure 2.13b show the optical micrographs of friction stir welded copper along advancing (AS) and retreating sides (RS) respectively. All the weld sub-regions such as weld nugget, TMAZ, HAZ, and BM are classified based on their distinct microstructural features. BMs possess

equiaxed coarse copper grains; TMAZs show elongated grains in both the advancing and retreating sides; weld nugget has very fine grains due to the dynamic recrystallization mechanism offered by the FSW process. From the optical micrographs, the authors claimed the absence of any HAZ. However, the existence of grain growth (HAZ) is evident in the region between the BM and TMAZ sub-regions located on the RS (Figure 2.13a).

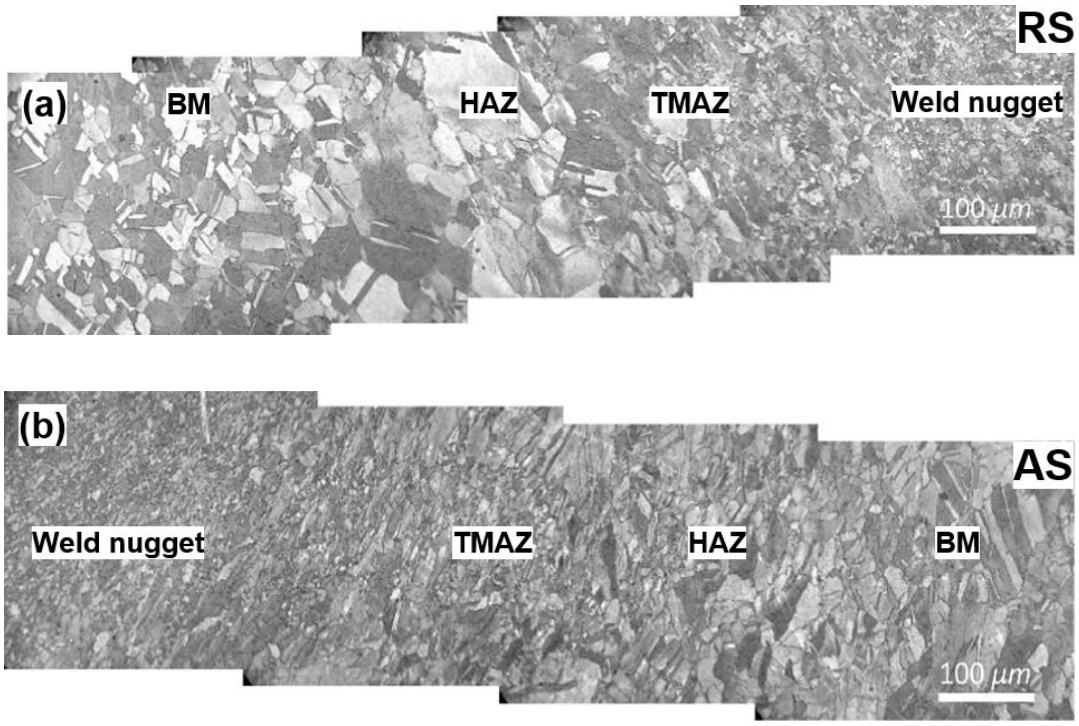

Figure 2.13 Optical micrographs of friction stir welded copper alloys: (a) Retreating side; (b) Advancing side [44]

Xu et al. [49] investigated the microstructural formations in a friction stir welded Cu-30Zn brass joint. Figure 2.14a displays an optical micrograph of the weld sub-regions captured on the advancing side. A sharp transition in the grain size is clearly observed at both BM/TMAZ and TMAZ/SZ interfaces. In this investigation, it is mentioned that the HAZ was absent in this weld. To observe the grains located in the weld sub-regions at a high spatial resolution, the authors attempted an EBSD characterisation. EBSD micrographs of the BM and SZ regions are shown in Figure 2.14b and Figure 2.14c, respectively. Cu BM has coarse grains with annealing twins, and the SZ is occupied with extremely fine recrystallized grains. From the EBSD micrographs, the average grain size of the BM and SZ are reported as 21.4 μm and 0.5 μm, respectively. In addition to this, it is also reported that the SZ is highly populated with high angle grain boundaries. This is because of the large number of equiaxed fine recrystallized grains produced by the severe plastic deformation of the FSW process. Although this investigation has characterised the microstructural heterogeneities between the FSW weld sub-regions, the microstructural features observed on the retreating side of the weld are not reported in this investigation.

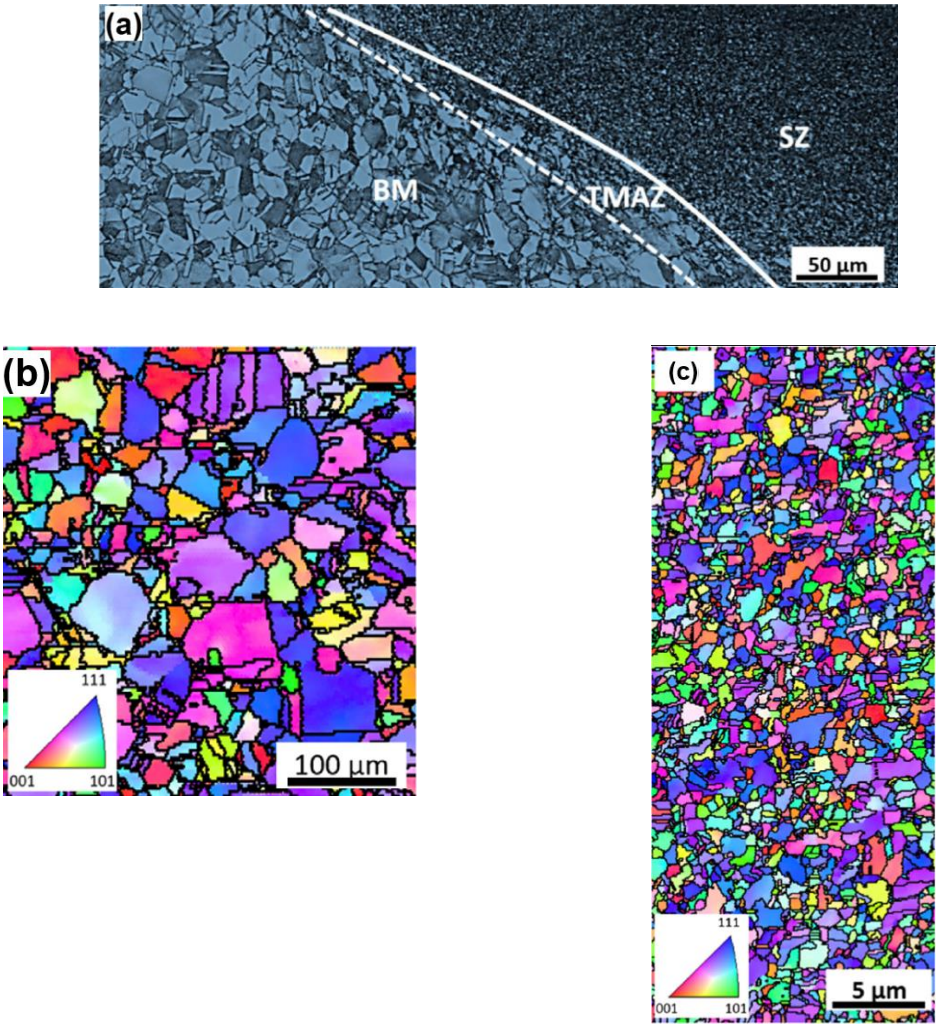

Figure 2.14 Micrographs of the FSW Cu-30Zn brass joint: (a) Optical micrograph of the transition zone of the advancing side; (b) EBSD micrograph of BM; (c) EBSD micrograph of stir zone [49]

2.2.5.2 Mechanical properties of FSW (Cu-Cu) welds

2.2.5.2.1 Microhardness properties

Xu et al. [49] also studied the microhardness properties of the friction stir welded Cu-30Zn brass joint. Figure 2.15a displays the hardness map measured along the centre line of the weld. The hardness map clearly shows that the weld nugget has achieved higher hardness than the BM. In this investigation, it is reported that the average hardness value measured on the BM and SZ are 111 HV and 152 HV, respectively. Even though the authors have failed to offer an explanation for the hardness enhancement in the weld nugget, it is likely that the grain refinement which occurred in the weld nugget was responsible for achieving the higher hardness than in the BM.

Shen et al. [45] investigated the effect of welding speed on the microhardness properties of the friction stir welded copper. Figure 2.15b shows the microhardness profiles measured on the welds which were manufactured at different welding speeds from 25 mm/min to 200 mm/min. From this

figure, it is observed that the average hardness of the weld nugget initially decreases and then increases with the increase in the welding speed; the weld nugget achieved its highest hardness at the maximum welding speed of 200 mm/min. To investigate this finding further, the authors correlated the microhardness map with the optical micrographs and found a high degree of grain refinement occurred at this welding speed. By using the findings offered by the micrographs and microhardness measurements on the FSW (Cu-Cu) welds obtained at different welding speeds, the authors confirmed the significant impact of welding speed on microstructural and microhardness properties. Additionally, the authors concluded that except in the weld nugget region, the hardness value of other weld sub-regions were equivalent to the base material. However, clear hardness fluctuations are observed at the location between the BM and weld nugget along both AS and RS (Figure 2.15b). This investigation failed to clarify/investigate the microhardness gradients observed between the FSW weld sub-regions.

Sun et al. [46] examined the effect of FSW process parameters on the microhardness properties of friction stir welded pure copper. Figure 2.15c presents the microhardness profiles derived from the welds which were manufactured using a constant welding speed of 650 mm/min alongside different tool axial force and rotational speeds. From this figure, it is observed that hardness of the weld nugget gradually increases with respect to the increase in the tool axial force. Additionally, the HAZ shows reduced hardness, and the TMAZ exhibits higher hardness under same welding conditions. In contrast to the previous investigations offered by Xu et al. [49] and Shen et al. [45], the authors have found the hardness of the weld nugget is lower than in the other weld sub-regions under all welding conditions investigated. Although the FSW weld nugget had very fine grains in this investigation, the weld nugget did not have the maximum hardness compared to the other weld sub-regions. The authors explained this by proposing that the FSW process produces an “annealing soft” condition across the stir zone, leading to the hardness reduction observed across the stir zone. Furthermore, the authors also cited other investigations where a similar phenomenon has been confirmed [50]. Overall, this investigation has revealed that an important relationship exists between the tool axial force and the corresponding hardness properties achieved in FSW welds (in addition to deformation imparted by the welding tool speed).

Hwang et al. [47] demonstrated a feasibility study on the friction stir welding of copper metals and measured the microhardness on welds which were manufactured at two different welding conditions, as shown in Figure 2.15d. As confirmed by Sun et al. [46], this investigation also noted that the hardness achieved by the weld nugget is comparatively lower than in the base material. The authors argued here that both dynamic recovery and dynamic recrystallization mechanisms are responsible for the reduced microhardness properties achieved in the weld nugget. However, it is noteworthy that this investigation has determined the hardness properties of the major weld sub-regions (Weld nugget, TMAZ, and BM) by using just seven hardness data points positioned at a distance of 4 mm. It is noteworthy that the distance between the weld sub-regions is a few microns, and therefore, the

hardness values of the weld sub-regions reported in this investigation are both somewhat qualitative and questionable.

Xue et al. [48] determined the effect of heat input on the hardness properties of friction stir welded copper joints which were manufactured under two different welding conditions shown in Figure 2.15e. In the first welding condition, the welding speed was maintained constant at 50 mm/min, and the tool rotational speed was varied from 400 to 800 rpm. In the second welding condition, the tool rotation speed was fixed at 800 rpm, and the welding speed was varied from 50 mm/min to 200 mm/min. From the hardness profiles derived at these two different welding conditions, it is noticed that hardness of the weld nugget is directly proportional to the welding speed and inversely proportional to the tool rotation speed. In this investigation, the authors have failed to report any concrete reason for the relationship between the FSW process parameters and hardness properties. However, this investigation demonstrates the effect of welding speed and tool rotation speed on the hardness values of the FSW (Cu-Cu) weld sub-regions.

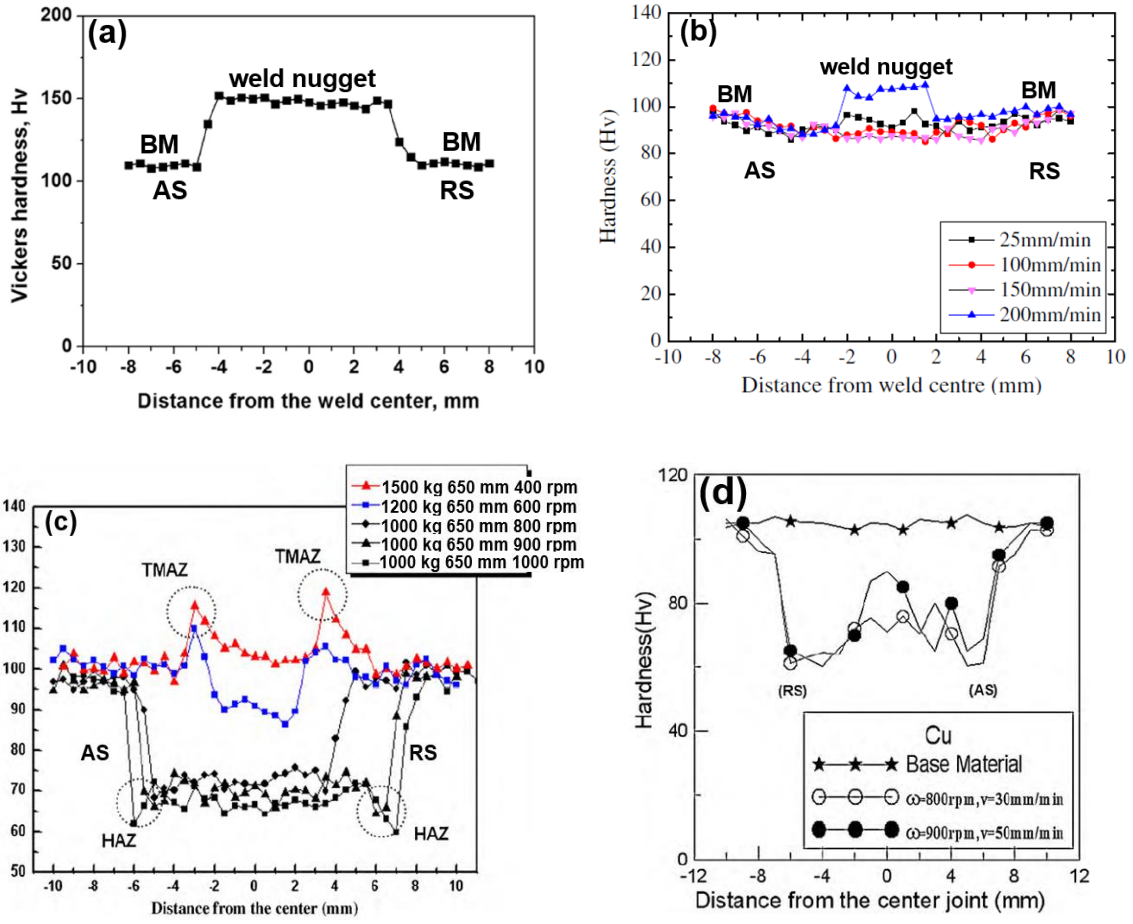

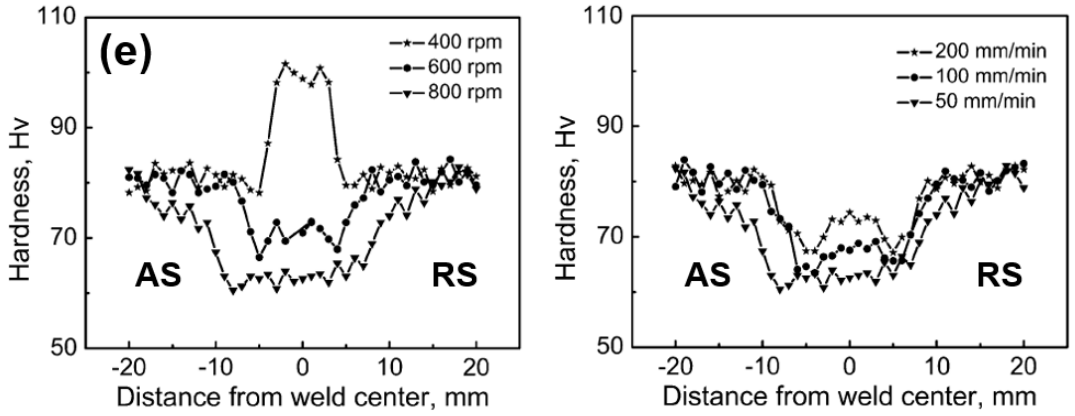

Figure 2.15 Microhardness maps along the centre line of FSW (Cu-Cu) weld cross-section reported from previous investigations: (a) Xu et al. [49]; (b) Shen et al. [45]; (c) Sun et al. [46]; (d) Hwang et al. [47]; (e) Xue et al. [48]

2.2.5.2.2 Tensile properties

Xu et al. [49] also characterised the tensile properties of the friction stir welded Cu-30Zn brass joint and reported that the FSW joint exhibited a yield strength and tensile strength of 437 MPa and 589 MPa. The stress-strain curves extracted from the base material and welded joint are shown in Figure 2.16a. It is important to note that the tensile properties achieved by the weld are higher than the corresponding BM. Thus this investigation proves the capability of the FSW process in manufacturing joints with superior mechanical properties. However, this investigation has failed to study the average tensile properties achieved by the FSW joints (or indeed the scatter), which is a clear gap found in this investigation.

Shen et al. [45] assessed the effect of welding speed on the tensile properties of the friction stir welded copper and found that both tensile strength and elongation% initially increased with an increase in the welding speed and then decreased as shown in Figure 2.16b. But this investigation has not correlated the tensile properties of the welded joints with the base material and therefore, it is difficult to confirm the origin of this variation in tensile properties achieved by the FSW joints.

Hwang et al. [47] derived the tensile properties of the friction stir welded copper joints which were manufactured under two different welding conditions. The stress-strain curves obtained from this investigation are shown in Figure 2.16c. This figure demonstrates that the tensile strength of the weld achieved under two different welding conditions is less than that achieved in the base material. However, both the joints have achieved a significantly higher plastic deformation than the base material. The authors stated that the dynamic recrystallization mechanism was responsible for achieving the high levels of plastic deformation in the FSW welds. It is also reported that the tensile specimen manufactured at two different welding conditions (Rotational speed = 800 rpm, Welding speed= 30 mm/min and Rotational speed = 900 rpm, Welding speed= 50 mm/min) failed at the centre of the weld and at the HAZ respectively.

Liu et al. [51] investigated the effect of tool rotation rate on the tensile properties of friction stir welded copper. In this investigation, the FSW was conducted with a constant welding speed of 100 mm/min together with different rotation rates of 300, 400, 600, 800, and 1000 rev/min. The tensile properties obtained from these process parameters are displayed in Figure 2.16d. From this figure, it can be seen that both tensile strength and elongation% have shown the same trends at all rotation speeds. However, this figure does not include the tensile properties derived from the base material and failed to offer an opportunity to correlate with the tensile properties of welds. It is reported that the majority of joints failed in the region close to the weld nugget, which indirectly demonstrates that the strength of the FSW joints were lesser than the BM.

Xue et al. [48] determined the effect of heat input on the tensile properties of friction stir welded copper joints which were manufactured under two different welding conditions, as shown in Figure 2.16e. From this figure, the authors have made three major observations. Firstly, the reduction in the heat input either by decreasing the rotation rate or increasing the traverse speed led to an increase in the yield strength of the welds. Secondly, only a small increase in the UTS was observed in the reduced heat input condition. Thirdly, the elongation% of the joints were decreased by reducing the heat input. It is noteworthy that all the FSW joints of this investigation failed at the HAZ, which shows the nature of the tensile failure is ductile and also the tensile properties of the welded joints are very close to that of the base metal. It is important to note that all the tensile results reported in the literature above have neglected the effect of reduced cross-sectional area of FSW weld nugget in the tensile specimens.

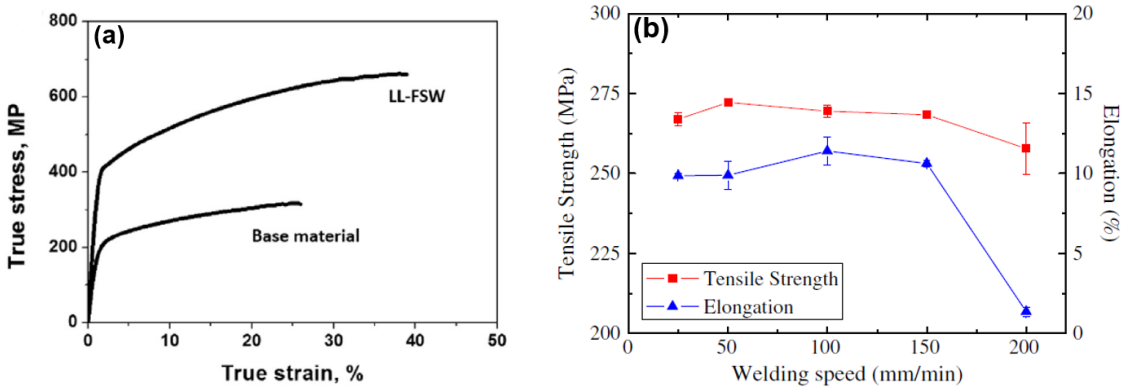

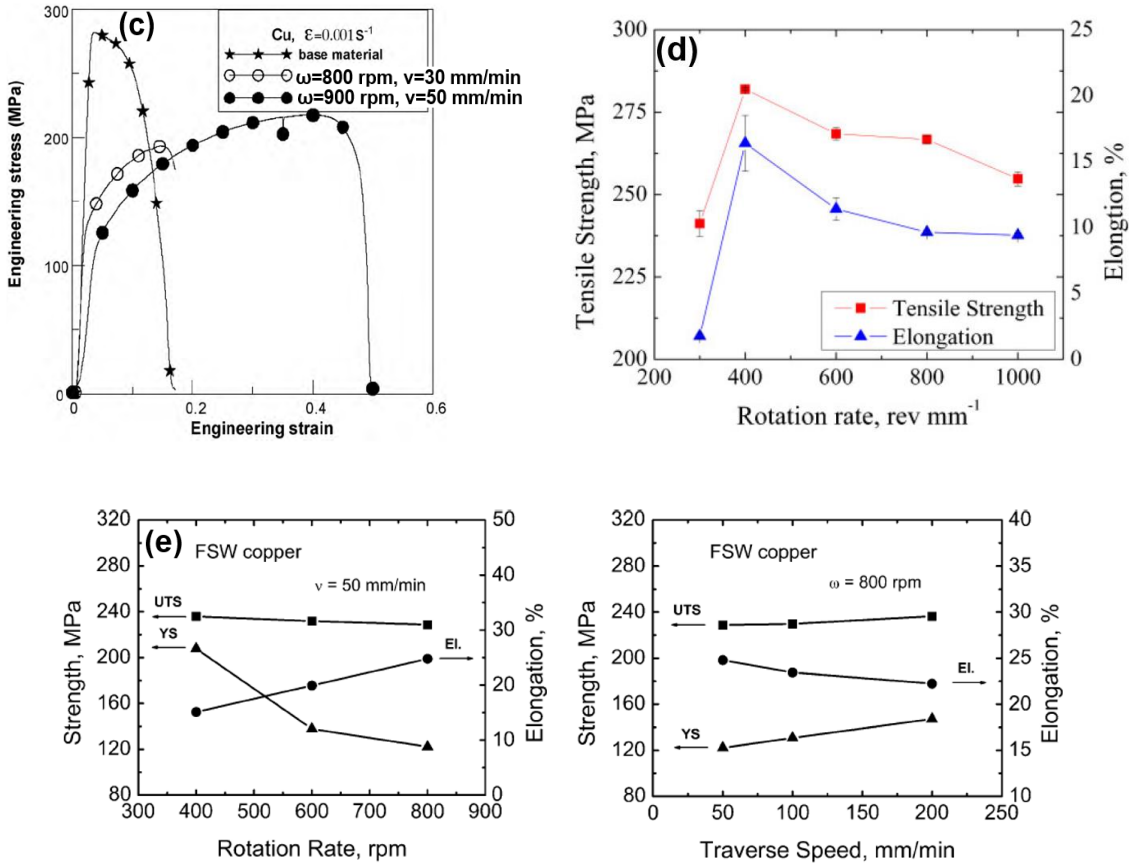

Figure 2.16 Transverse tensile properties of FSW (Cu-Cu) joints reported from previous investigations: (a) Xu et al. [49]; (b) Shen et al. [45]; (c) Hwang et al. [47]; (d) Liu et al. [51]; (e) Xue et al. [48]

2.3 Friction stir welding of dissimilar materials

2.3.1 Challenges in the Friction stir welding of dissimilar materials

The key elements involved during the FSW process are frictional heat generation and the plasticized flow of material that determines the thermal profile and the resultant microstructure of the weld. Therefore, an exhaustive understanding of the FSW process requires establishing the connection between the input process variables (tool rotation rate, tool traverse speed, position of tool on AS or RS, tool offsets) and the output process variables (frictional heat generation, flow stress, and local mechanical properties). In the FSW of dissimilar materials, in addition to the major FSW process parameters, other challenging factors are also encountered due to the different thermo-mechanical properties of the two materials. In addition, as the FSW tool involved in a dissimilar material system generates a complex material flow from the AS to the RS of the weld, therefore, it is more challenging to accurately classify the various weld sub-regions and their boundaries across the weld nugget [20, 24].

Furthermore, the issues that need to be addressed in the FSW of dissimilar materials compared to FSW of similar materials includes:

i) A wide difference in the melting point of the two materials has to be addressed by plunging the FSW tool a few mm away from the joint-line, i.e. offsetting the FSW tool from the joint line. Optimum tool offsets and the corresponding directions for welding various combinations of dissimilar materials via the FSW process are discussed elsewhere [20, 24, 52]. From those studies [20, 24, 52], it is shown that the tool needs to be plunged towards the low melting-point and high thermal-conductivity materials, as demonstrated in an example shown in Figure 2.17. This example illustrates a different material combination consists of copper and stainless steel where the tool is plunged more towards the copper side. This is because of the following two primary reasons: (1) to reduce the wear rate of the tool, and (2) to eliminate the pre-heating procedure currently required for high thermal-conductivity materials such as copper [1, 53].

ii) In dissimilar material FSW, the weld nugget will develop different composition levels contributed from both the parent materials. This is because of the rotating/traversing action of the FSW tool usually shears the material from the advancing side and transports it towards the retreating side of the tool [3, 52]. Therefore, the position (AS, RS) of the dissimilar materials has a severe impact on modifying the compositions of the weld nugget. As the temperature generated on the advancing side of the weld is usually much higher than on the retreating side of the weld [52, 54], the higher melting temperature materials are generally preferred on the advancing side position. This phenomenon is schematically represented in an example shown in Figure 2.17 where the high-temperature material (stainless steel) and low-temperature material (copper) are positioned on the advancing and retreating sides, respectively. Thus in any dissimilar material friction stir welds, the offset of the tool and position of the base materials (AS or RS) are considered as significant process variables.

The core findings observed in the previous investigations [17, 20, 32, 54-56] carried out on friction stir welded copper to stainless steel joints are briefly reviewed in the following sections of this chapter. The review is mainly focussed on the experimental set-up, microstructural evolution, elemental analysis, and mechanical properties of FSW welds reported in these investigations.

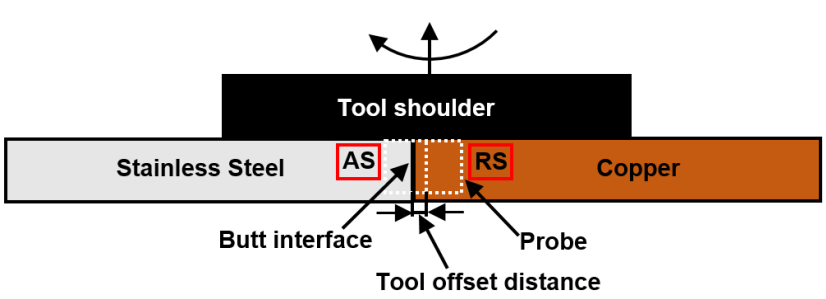

Figure 2.17 A schematic illustration of probe offset distance in a typical FSW (Cu-SS) joint

2.3.2 Experimental set-up

Shokri et al. [54] analysed the effect of FSW parameters on microstructure and mechanical properties of duplex stainless steel (DSS)-copper joints. In this study, the effect of three FSW parameters on microstructure and mechanical properties of DSS/Cu-alloy joints were investigated. The three parameters are (1) Travel speed (20 and 30 mm/min), (b) rotation speed (1000, 1200 and 1400 rpm) and (3) tool offset (0, 0.5 and 1 mm). Maximum offset of 1 was selected based on the fact that at offsets greater than 1, significant pin wear occurred. In DSS, there is more possibility for the formation of intermetallic phases (IMC) such as σ-phase (Fe-Cr) and the presence of this phase has adverse effects on the mechanical properties of the joints. Hence, this study focussed on measuring the thickness of IMC through SEM-BSE and establishing the relationship between the IMC thickness and mechanical properties of the joints. The experiment was performed on 4 mm thickness duplex-stainless steel and copper sheets using a standard tungsten carbide tool. The FSW (Cu-SS) joint manufactured and the experimental matrix used in this investigation are shown in Figure 2.18a and Figure 2.19, respectively. From Figure 2.18a, it can be seen that the DSS was on the advancing side and copper was on the retreating side. The authors reported that the FSW tool was plunged into the copper alloy with different offset conditions for all the samples to prevent tool wear rate and to avoid local melting of copper.

Ramirez and Benati [20] investigated the effect of tool offset on 2 mm thick dissimilar Cu-AISI 316 friction stir welded joints. The study was carried out in three different offset conditions (0, 0.6, 1.6 mm) as shown in Figure 2.18b with varying process parameter (Table 2.1). The tool used in the investigation is made up of a convex shoulder ceramic composite with shoulder and pin diameters of 25 mm and 5.5 mm respectively. As noticed in the investigation performed by Shokri et al. [54], this investigation also adopted the tool offset more towards copper; Copper and stainless steel were kept on the retreating and advancing sides of the weld respectively.

Aval [56] characterised the microstructural evolution and mechanical properties of friction stir welded 2 mm thick C71000 copper-nickel alloy and 304 austenitic stainless steel sheets. Figure 2.18c illustrates the base materials set-up and tool offset condition adopted in the investigation. A tungsten carbide tool with 1.8 mm height cylindrical pin was used for welding. Welding parameters reported in the investigation are listed in

Table 2.2. It is mentioned that copper−nickel alloy was on the retreating side, and the stainless steel alloy was on the advancing side; FSW tool was offset by 0.75 mm to the copper alloy with respect to the joint interface.

Wang et al. [32] attempted an investigation to obtain sound butt joints between 6 mm thick pure copper and 316 stainless steel sheets through friction stir welding. Figure 2.18d shows the schematic representation of the Cu and SS base materials set-up used in this investigation. A W-Re tool was used for FSW, and the welding parameters adopted are shown in Table 2.3. The authors specified that the copper sheet was placed on the retreating side, and the SS sheet was placed on the advancing side during the FSW process. Additionally, the tool was offset towards the copper sheet by 2 mm from the butt interface.

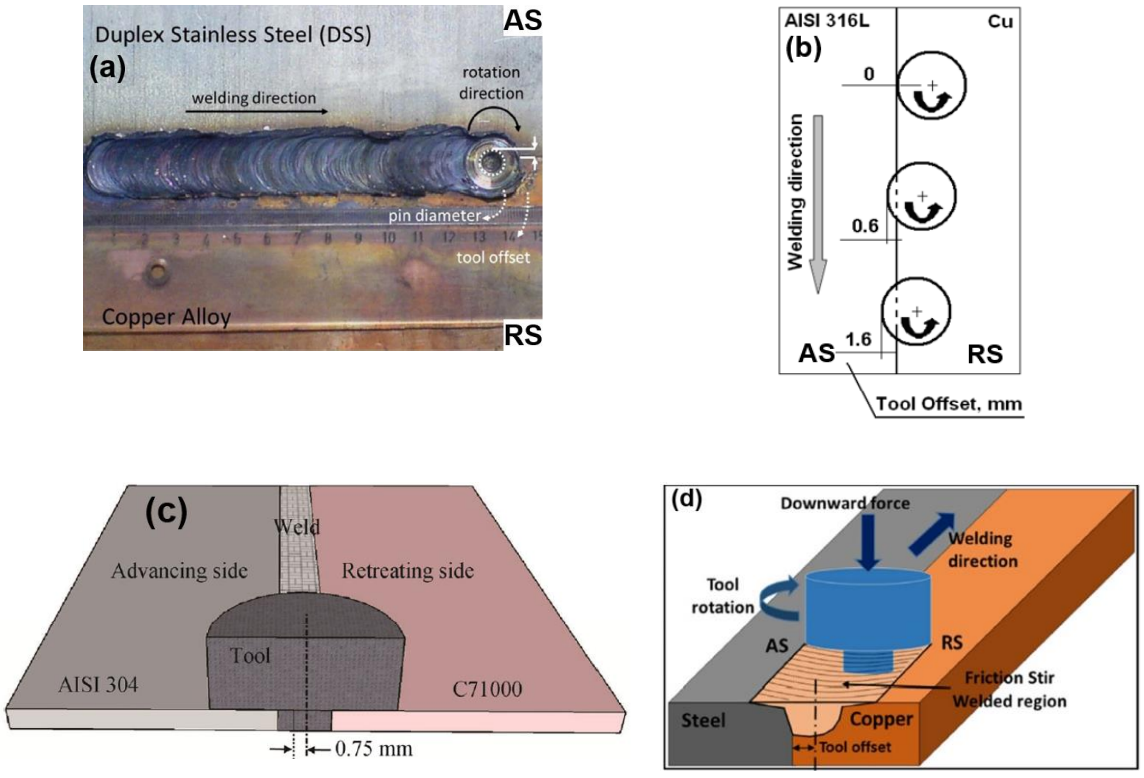

Figure 2.18 Tool offset conditions reported from previous investigations on FSW (Cu-SS) joints: (a) Shokri et al. [54]; (b) Ramirez et al. [20]; (c) Aval et al. [56]; (d) Wang et al. [32]

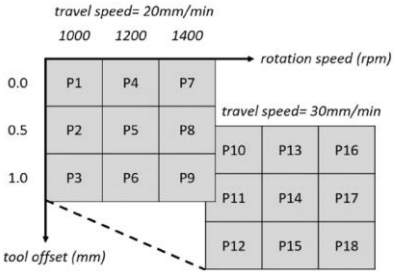

Figure 2.19 Experimental matrix used in the investigation P1 to P18 respective codes for Samples 1 to 18 [54]

Table 2.1 Welding parameters used in the investigation [20]

Spindle speed (rpm)	Welding speed (mm/min)	Ratio (mm/rev)	Sample designation (spindle speed/ welding speed/penetration)		
	Tool offset (mm)		0	0.6	1.6
1000	100	0.1	1000/100/0	1000/100/0.6	1000/100/1.6
	200	0.2	1000/200/0	1000/200/0.6	1000/200/1.6
	300	0.3	1000/300/0	1000/300/0.6	1000/300/1.6
1500	350	0.23	1500/350/0	1500/350/0.6	1500/350/1.6
	450	0.3	1500/450/0	1500/450/0.6	1500/450/1.6
	550	0.36	1500/550/0	1500/550/0.6	1500/550/1.6

Table 2.2 Welding parameters used in the investigation [56]

Sample No	Rotational speed (rpm)	Traverse speed (mm/min)	Rotational to linear speed ration (rev/mm)
1	800	40	20
2	800	60	13.33
3	800	80	10
4	1000	40	25
5	1000	60	16.65
6	1000	80	12.50

2.3.3 Microstructural evolution across the FSW (Cu-SS) weld sub-regions

Shokri et al. [54] analysed the effect of FSW parameters on the microstructure evolution of duplex stainless steel (DSS) to copper joints. The authors performed the microstructure analysis on the weld sample P9, which was manufactured using 1400 rpm rotational speed, 20 mm/min welding speed and 1 mm tool offset distance. Figure 2.20a shows the optical macrograph observed from the region of the weld sample where it clearly demonstrates the migration of DSS from the AS to RS at the weld

nugget. Additionally, some DSS fragments were sheared from the base material through the stirring action of the tool and deposited on the weld nugget (Figure 2.20b). This figure further highlights the series of vortex rings in the weld nugget and the authors stated that these vortex layers usually improve the tensile properties of the joints. Both TMAZ and weld nugget regions of the DSS are distinguished by elongated grains and ultra-fine recrystallized grains, respectively (Figure 2.20c). It is interesting to observe that the weld nugget on the copper side also achieved fine recrystallized grains due to the high strain rate and low heat input offered by the FSW (Figure 2.20d). It is significant to note that this investigation has claimed the presence of HAZ only on the Cu side and no such HAZ evidenced on the DSS side. To clarify this finding further, the authors reported that the major alloying elements of DSS effectively controlled the grain growth during the FSW process, which led to the absence of any HAZ along the DSS.

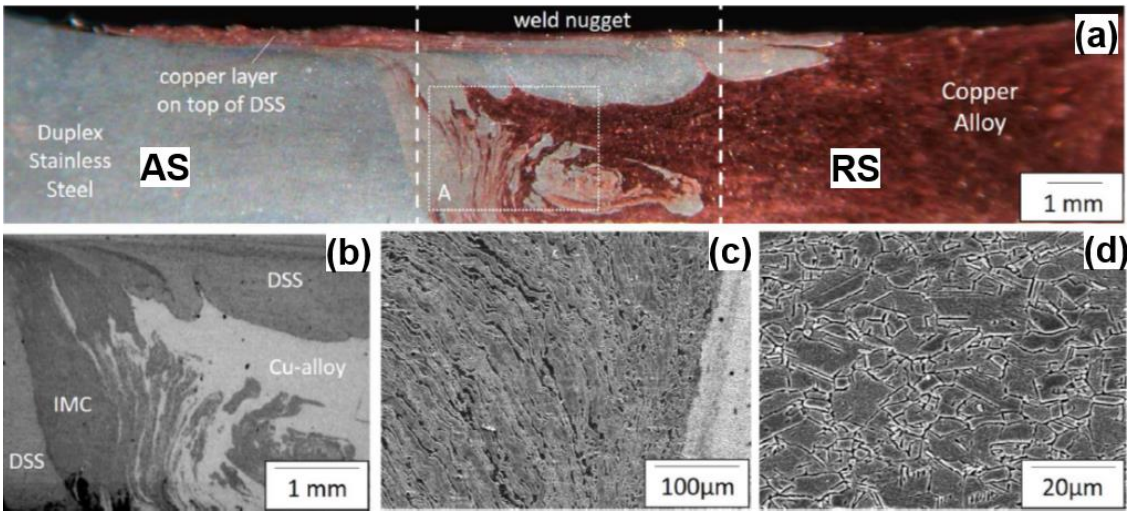

Figure 2.20 Optical images of FSW (Cu-SS) weld: (a) optical macrograph of the sample P9 (rotation speed: 1400 rpm, travel speed: 20 mm/min and tool offset: 1 mm) and SEM micrographs of (b) the weld nugget (labelled as A in a) (c) TMAZ (DSS) (d) DRX (Cu) [54]

Ramirez and Benati [20] studied the effect of tool offset on the microstructure formation in the dissimilar Cu-AISI 316 friction stir welded joints. Six different weld sub-regions were observed using an optical microscopy, as shown in Figure 2.21a. The authors indicated that an independent TMAZ along the copper side was not found in this study as the copper has completely recrystallized. The microstructure of the joint interface obtained using the process parameters that include 1000 rpm spindle speed, 100 mm/min, and 0.6 mm tool offset distance are shown in Figure 2.21b. TMAZ of 316L exhibits partially recrystallized deformation bands due to the low temperature and lower plastic deformation imparted from the FSW process. The stir zone was subjected to severe plastic deformation which has led to the formation of fine grains. Wide variations in the grain size were observed in the weld nugget because of the differences in the thermo-mechanical properties of the dissimilar elements causing different recrystallization and grain growth mechanisms.

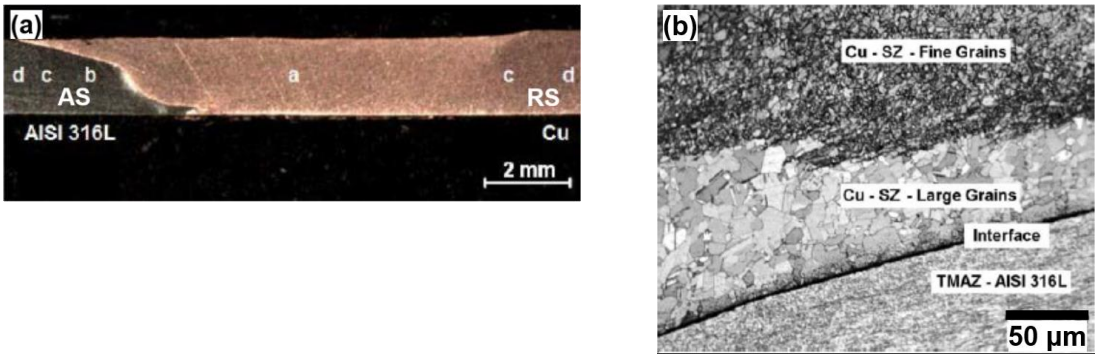

Figure 2.21 Optical images of FSW (Cu-SS) weld cross-section: (a) Macrostructure; (b) Optical micrograph [20]

Jafari et al. [17] classified the weld sub-regions of the friction stir welded 304L stainless steel and copper joints through their microstructural features as displayed in Figure 2.22. The authors captured the optical micrographs of the weld sub-regions based on the locations shown on the macrograph Figure 2.22a. A clear distinction between the BM (Figure 2.22 b and h) and its corresponding HAZ (Figure 2.22 c and g) is noted along the copper and stainless steel base materials, respectively. Both stainless steel (Figure 2.22e) and copper (Figure 2.22f) weld nugget regions have ultrafine grains. Figure 2.22f also represents the heterogeneous characteristics of the FSW weld nugget where the distribution of fine stainless fragments located on the copper matrix. In contrast to the finding made by Ramirez and Benati [20], the authors confirmed the presence of TMAZ along the copper, as shown in Figure 2.22d. But this figure does not show any elongated grains of TMAZ, and therefore this evidence is not sufficient to confirm the existence of TMAZ.

Aval [56] examined the microstructural evolution of friction stir welded C71000 copper (Cu)-nickel alloy and 304 austenitic stainless steel (SS) sheets and presented the optical micrographs derived from the weld sub-regions as shown in Figure 2.23. Figure 2.23a displays the macrostructure of the dissimilar weld cross-section, where a sharp interface between Cu and SS is observed at the centre of the stir zone. Cu base metal (Figure 2.23c) has coarse grains compared to the SS (Figure 2.23b). Figure 2.23f clearly represents the TMAZ of Cu with elongated and partially recrystallized grains. However, the same feature is not visible in Figure 2.23d, although the authors have considered this optical micrograph as representing the TMAZ of the SS. The stir zone observed on the SS side has very fine grains obtained from the severe plastic deformation imparted by the FSW process (Figure 2.23e).

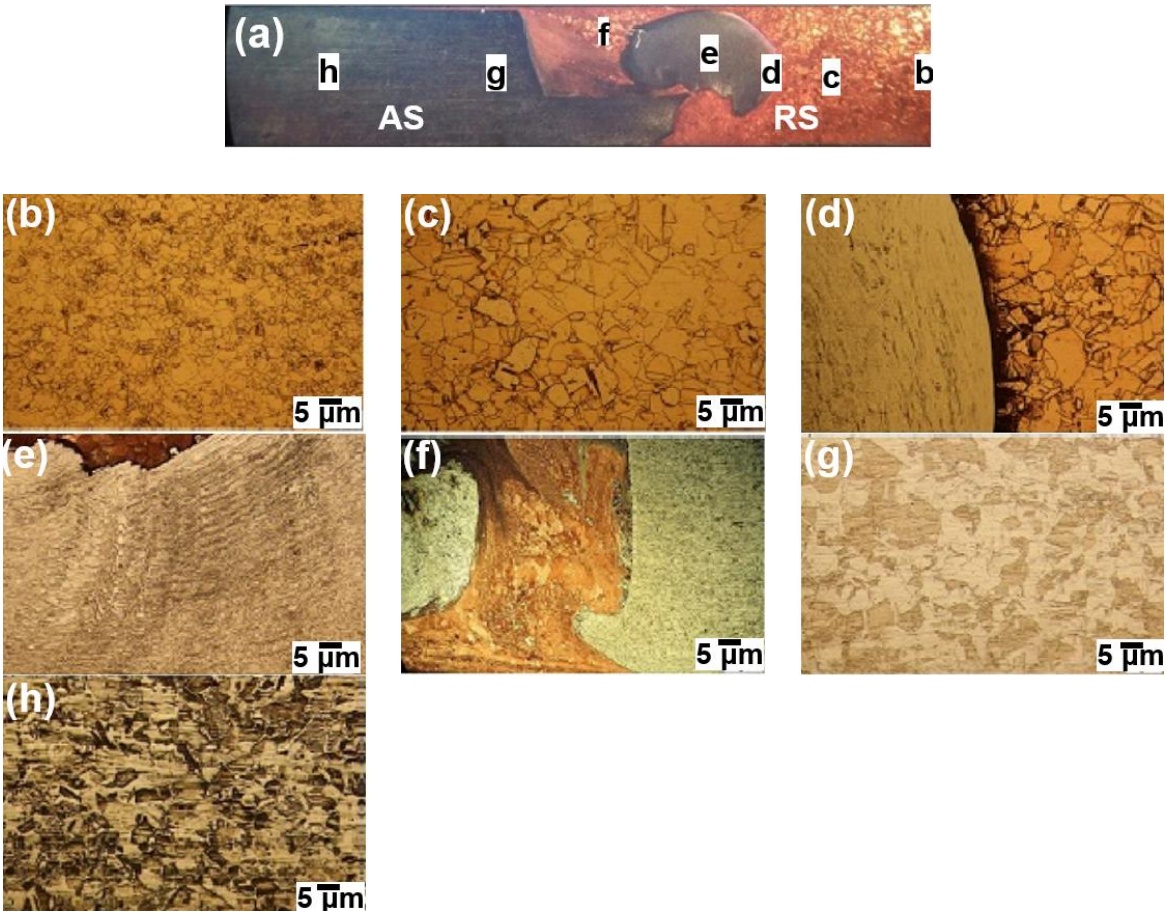

Figure 2.22 Optical images of FSW (Cu-SS) weld cross-section: (a) Macrostructure; (b)-(h) Optical micrographs of the weld sub-regions correspond to the locations shown in (a) [17]

Wang et al. [32] attempted to characterise the microstructural features in the friction stir welded 110 copper alloy and 316 stainless steel sheets under different welding conditions listed in Table 2.3. Figure 2.24 displays the optical micrographs obtained at these welding conditions. All the optical micrographs show the presence of steel fragments in the stir zone. This observation agrees with the claim made by Shokri et al. [54] and Jafari et al. [17] in their investigations. This investigation has studied only the effect of process parameters, mainly tool rotating speed and welding speed on the microstructural development across the weld. However, the microstructural information about the individual weld sub-regions along the copper and stainless steel are not resolved.

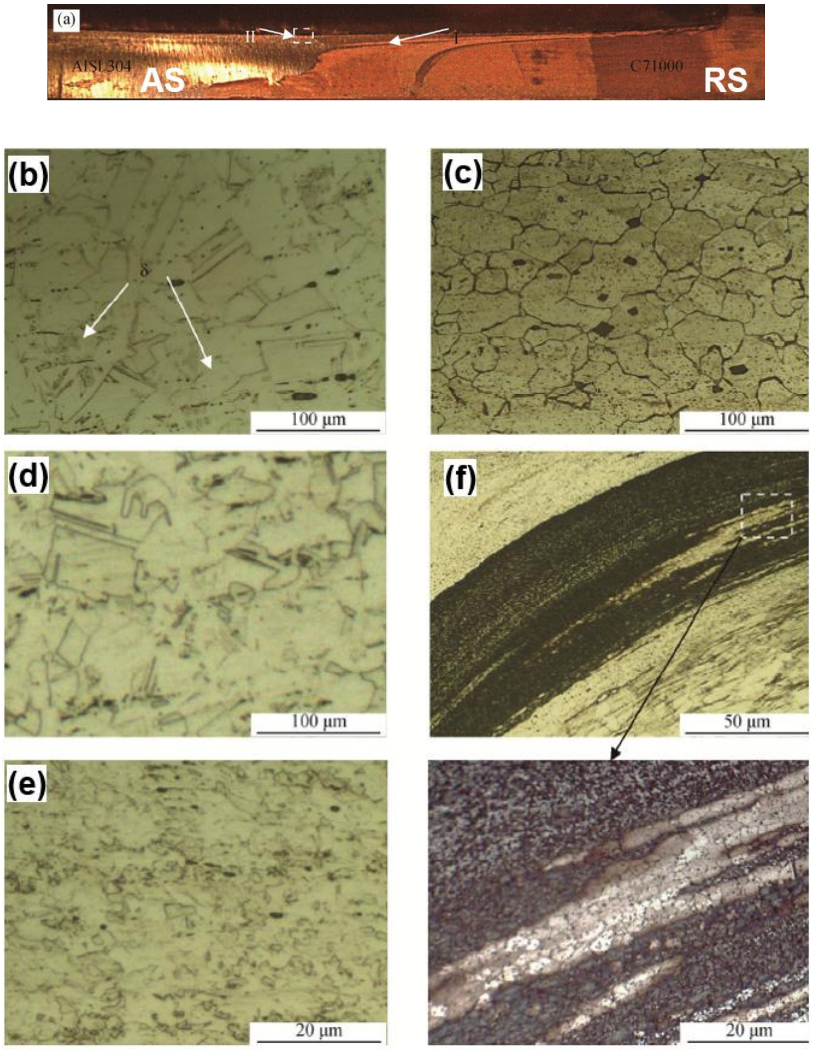

Figure 2.23 Optical images of different zones of sample No. 4: (a) macrostructure of welded sample No. 4; (b) base metal of AISI 304; (c) base metal of C71000; (d) TMAZ in AISI 304 side; (e) SZ in AISI304 side; (f) TMAZ in C71000 side as marked by zone I in (a) [56]

Table 2.3 Welding parameters used in the investigation [32]

Weld number	Rotational speed (rpm)	Traverse speed (mm/min)	Plunge depth (mm)	Tool offset in copper (mm)	Tilt angle (degree)
W1	400	25	4.75	2.0	2.5
W2	400	50	4.75	2.0	2.5
W3	500	25	4.75	2.0	2.5
W4	500	50	4.75	2.0	2.5

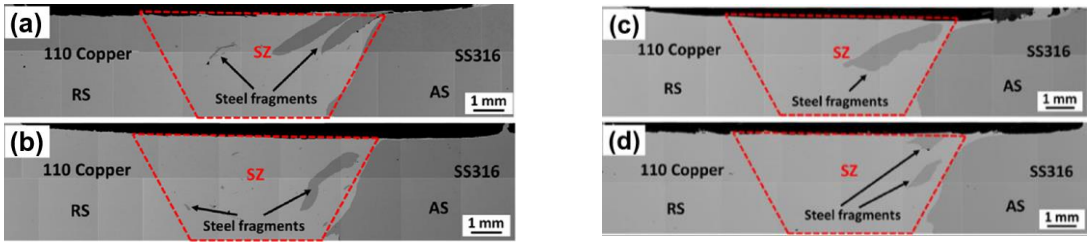

Figure 2.24 Optical micrographs of the weld cross-sections: (a) W1; (b) W2; (c) W3; (d) W4 [32]

2.3.4 SEM/EDS analysis across the FSW (Cu-SS) weld

Shokri et al. [54] also performed SEM-BSE (backscattered electron) analysis on the weld cross-section of friction stir welded duplex stainless steel (DSS) and copper (Cu) joints. Figure 2.25a shows the SEM-BSE micrograph where the SS and Cu elements are clearly differentiated through their dark and bright features, respectively. It is observed that both these elements are severely mixed in the weld nugget which confirms the heterogeneous characteristics of the weld nugget. Additionally, the SEM-BSE image also evidenced the SS fragments scattered across the weld nugget due to the stirring action of the FSW tool. But this investigation does not quantify the amount (weight %) of copper and stainless steel elements located in the weld nugget. Therefore, from this investigation, it is difficult to estimate the population density of Cu and SS base materials located in the weld nugget.

Jafari et al. [17] also conducted an SEM-EDS line scan analysis across the weld cross-section of friction stir welded 304L stainless steel and copper joints. Figure 2.25b shows the results obtained from the EDS line scan which confirmed that the weld nugget reported in this investigation has a higher intensity of copper than iron. Although the weld nugget has a mixture of copper and iron, the authors clarified that both iron and copper elements were not thoroughly mixed in the FSW weld nugget. This is because the iron has low solubility in copper as per the copper-iron phase diagram [57].

Wang et al. [32] also characterised the elemental distribution in the weld interface of the friction stir welded 110 copper alloy and 316 stainless steel sheets. Figure 2.25c displays the EDS maps of Cu and Fe captured on the dissimilar weld interface. This figure represents the sharp weld interface where there is no migration of Fe elements noticed on the Cu side as the Fe is not entirely soluble in Cu. It is noteworthy that this investigation confirmed the presence of steel fragments located in the weld nugget, as shown in Figure 2.24. However, the same steel fragments are not evident in the EDS maps shown in Figure 2.25.

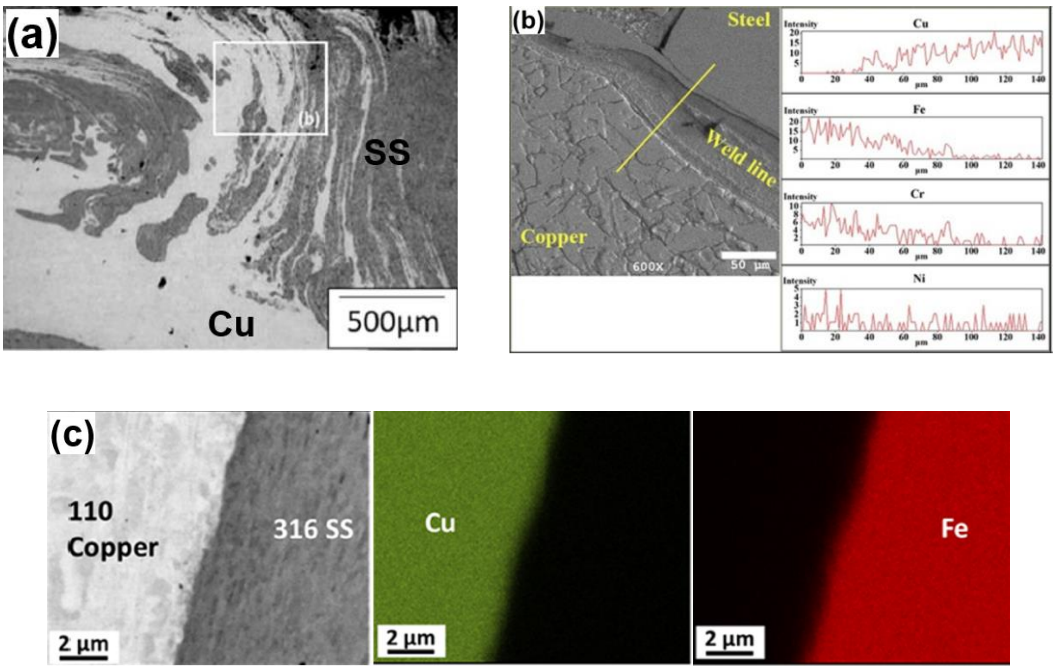

Figure 2.25 SEM-EDS analysis on FSW (Cu-SS) weld cross-section reported from previous investigations: (a) Shokri et al. [54]; (b) Jafari et al. [17]; (c) Wang et al. [32]

2.3.5 Mechanical properties of FSW (Cu-SS) welds

2.3.5.1 Microhardness properties

Shokri et al. [54] performed microhardness measurements on the weld cross-section of friction stir welded duplex stainless steel (DSS) and copper (Cu) joints. The microhardness line profile measured is shown in Figure 2.26a, and it can be seen that the hardness is decreasing in the stir zone compared to DSS. This indicates that the FSW weld nugget contains more copper than DSS. Generally, a FSW weld nugget is expected to have higher hardness compared to the base material [23] due to the recrystallized fine grains produced by the process. However in the case of dissimilar material FSW, even though the weld nugget has fine grains, the hardness of the weld nugget will depend on the proportions and hardnesses of the two dissimilar materials stirred into the weld nugget. The lowest hardness is found at the HAZ of the copper because of the coarsening of precipitates and grain growth caused by the FSW thermal cycle.

Ramirez and Benati [20] measured the hardness variations across the weld cross-section of dissimilar Cu-AISI 316 friction stir welded joints. Figure 2.26b shows the microhardness map obtained from the weld manufactured using 1000 rpm spindle speed, 300 mm/min, and 0.6 mm tool offset distance. It is reported that the maximum hardness is located at the TMAZ of 316 stainless steel. The authors justified this by saying that the FSW tool produced a severe deformation in the TMAZ which led to enhancement in the microhardness. Additionally, the hardness of the stir zone is closely aligned with the hardness range of Cu BM, as the stir zone consists of a major volume of copper. It is important

to note that although the SZ has achieved ultrafine grains in this investigation, the dynamic recrystallization phenomenon associated with the FSW process does not have much impact in increasing the hardness of the dissimilar FSW weld nugget.

Imani et al. [55] examined the hardness properties of friction stir welded Cu-304L stainless steel joints. Microhardness was measured on the joints fabricated with three different welding speeds (40, 56, 28 mm/min) as shown in Figure 2.26c. In all three joints, the higher hardness was recorded in the weld nugget due to the expected occurrence of fine dynamic recrystallized grains in the stir zone. The authors claimed that the formation of intermetallic compounds was responsible for increasing the hardness in the weld nugget. However, from the Fe-Cu phase diagram [57], there is no possibility for the formation of intermetallics between Fe and Cu; therefore any increase in the hardness values should be attributed to the expected fine recrystallized grains.

Jafari et al. [17] investigated the hardness properties of friction stir welded 304L stainless steel and copper joints. In this investigation, all the hardness data points measured from the individual weld sub-regions are plotted as a line profile, as shown in Figure 2.26d. From this figure, it is more visible that the weld nugget has a maximum hardness compared to other weld sub-regions. This agrees with the finding reported by Imani et al. [41]. Even though this investigation has failed to analyse the distribution of Fe and Cu elements located in the weld nugget, the higher hardness of weld nugget clearly links with the dense population of stainless steel located in the weld nugget.

Aval [56] characterised the microhardness variations on the mid-thickness weld cross-section of the friction stir welded C71000 copper (Cu)-nickel alloy and 304 austenitic stainless steel (SS) sheets. Figure 2.26e presents the hardness line profile obtained in this investigation. From this hardness profile, it is observed that the hardness of the weld increases by moving from the SS base metal to the centre region of the stir zone. It is noteworthy that some portion of the stir zone has attained a hardness close to the Cu base metal. This indicates that the stir zone has attained an equivalent mixture of SS and Cu in addition to the production of fine grains as an outcome of the FSW process.

Wang et al. [32] studied the microhardness properties of the friction stir welded 110 copper alloy (Cu) and 316 stainless steel (SS) specimens (W1, W2, W3, and W4) manufactured under different welding conditions as listed in Table 2.3. This investigation has revealed the hardness gradients between the weld sub-regions, as shown in Figure 2.26f. Both SS BM and its HAZ have achieved similar hardness. However, on the copper side, there is a small reduction in the hardness observed due to thermal softening. The stir zone shows clear hardness fluctuations produced by the mixture of Cu and Fe elements. The authors reported that the hardness increment in the SZ at all welding conditions is due to the presence of steel fragments as well as recrystallized fine grains. Additionally, they also mentioned that the welds which were manufactured at high traverse speed (W2 and W4) have achieved higher hardness in the stir zone than the welds which were manufactured at low traverse speed (W1 and W3). To explain this phenomenon further, the authors stated that an increase

in traverse speed usually leads to a high degree of grain refinement in the FSW. However, this investigation has failed to submit any microstructural evidence to justify this claim.

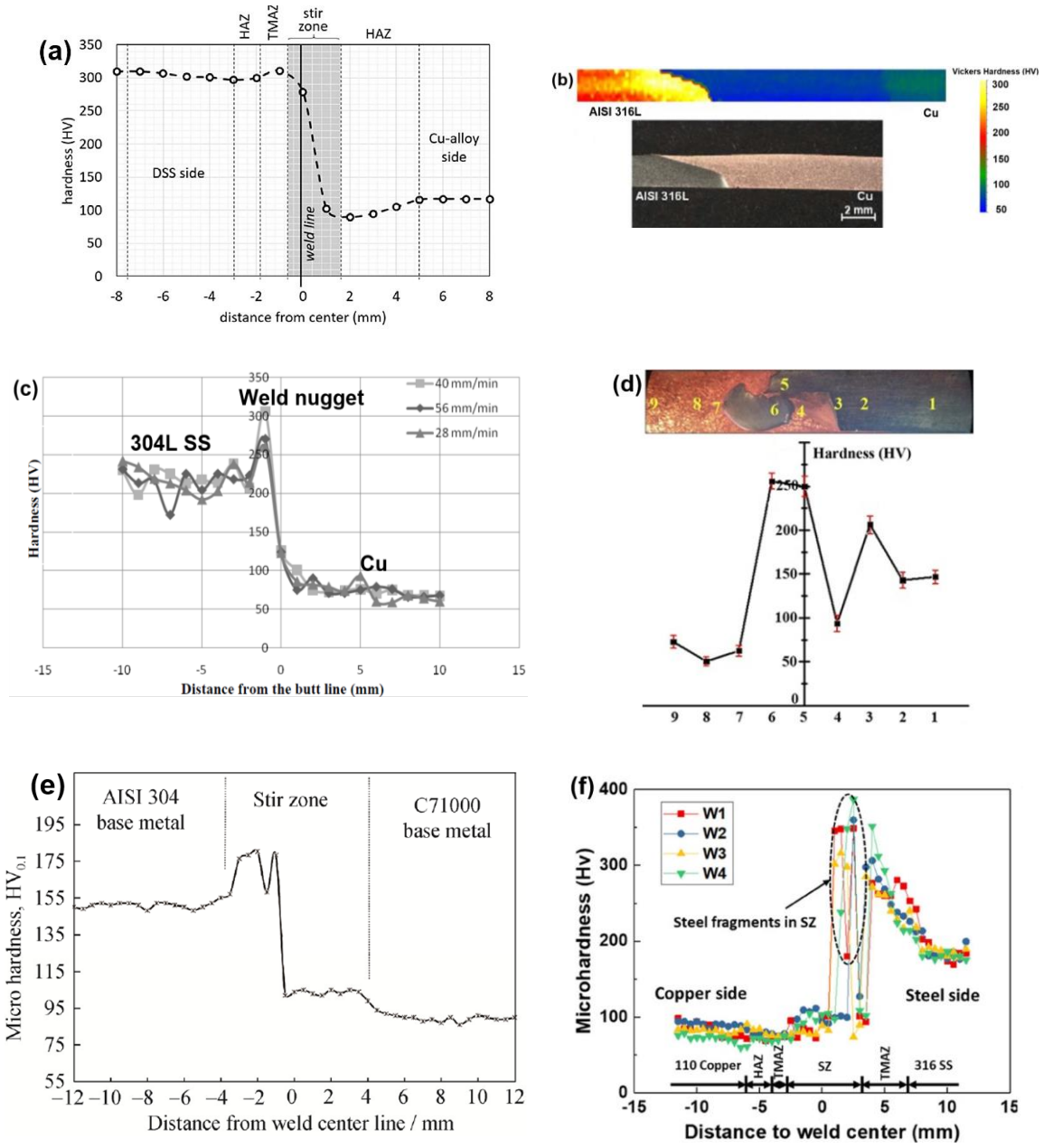

Figure 2.26 Microhardness results of FSW (Cu-SS) weld cross-section reported from previous investigations: (a) Shokri et al. [54]; (b) Ramirez et al. [20]; (c) Imani et al. [55]; (d) Jafari et al. [17]; (e) Aval et al. [56]; (f) Wang et al. [32]

2.3.5.2 Tensile properties

Shokri et al. [54] derived the tensile properties from the friction stir welded duplex stainless steel (DSS) and copper (Cu) joints. The ultimate tensile strength of all samples (P1-P18) were determined and were related to the observed intermetallic compound (IMC) thickness, as shown in Figure 2.27a. From this figure, it can be seen that the maximum tensile strength was achieved in the joints (P2, P3, P14) which were manufactured with high tool offsets (P2, P14= 0.5 mm, and P3= 1 mm) and these joints have failed in the Cu-HAZ. Additionally, IMC thickness also has an impact on the tensile properties of the joints. High and low IMC thickness causes the joints to fail at the weld interface and weld nugget respectively, but intermediate IMC thickness joints have failed at the Cu-HAZ. In this investigation, the authors concluded that tool offset, travel speed, rotational speed, and thickness of IMC are the critical process parameters that control the tensile properties of the joints. To date the majority of FSW investigations attempted to join Cu with SS had austenitic stainless steel (304, 304L, 316L) as the base material along with Cu. All these investigations clearly confirmed the absence of IMC between the austenitic stainless steel and Cu. However, Shokri et al. [54] evidenced the IMC formation during the FSW of DSS with copper. It is important to note that the chemical composition of the DSS (50% austenite and 50% ferrite) is completely different from a typical austenitic stainless steel as it contains a significant amount of ferrite. Therefore, the authors claim about the IMC formation needs further investigation as there is no literature currently available to support this claim.

Imani et al. [55] extracted the tensile properties of friction stir welded Cu-304L stainless steel joints at three different welding speeds (40, 56, 28 mm/min) as shown in Figure 2.27b. It can be seen that very high welding speed (56 mm/min) and very low welding speed (28 mm/min) have decreased the tensile properties of the joints because of insufficient frictional heat input and abnormal frictional heat generation respectively. The authors further reported that the nature of failure for the weld that was manufactured at 28 mm/min and 56 mm/min were brittle and ductile, respectively. However, this claim is not evidenced through the fractographs that correspond to these failures.

Ramirez and Benati [20] identified the tensile strength and elongation% of dissimilar Cu to AISI 316 friction stir welded joints. Figure 2.27c shows the tensile properties achieved by the joints under different process conditions. It is important to note that increasing the tool offset resulted in reduced tensile properties, and this result agrees with the findings of Imani et al. [55]. The authors observed that the welds made with the smaller tool offset (0 and 0.6 mm) fractured in the HAZ of the copper and the welds made with a larger 1.6 mm tool offset failed at the weld interface. The authors explained this by indicating that high tool offsets (1.6 mm) lead to weld defects which affected the tensile properties of the joints and the joints apparently failed at the weld interface. However, the authors have failed to evidence the fractographs observed on the failed tensile joints to confirm the nature of failure (Ductile or Brittle). Although this investigation has indicated the better tensile properties obtained from low tool offsets, no repeats of the tensile tests were carried out to reveal the

scatter. Furthermore, the effects of tool offsets (0, 0.6, 1.6 mm) on the composition of the weld nugget was also not reported.

Jafari et al. [17] investigated the effect of welding pass number on the tensile properties of friction stir welded 304L stainless steel (SS) and copper (Cu) joints. The authors have performed three different welding pass numbers while manufacturing the FSW (Cu-SS) joints, and the stress-strain curves derived from these specimens are shown in Figure 2.27d. The stress-strain curves show that an increase in the pass number decreases both tensile strength and ductility. But this investigation has failed to clearly explain the structure-property relationship between the welding pass number and tensile properties by offering any suitable microstructural evidence. The authors mentioned that all the specimens fractured at the HAZ of the copper. However, no evidence was submitted to support this claim (or to explain why it had occurred).

Aval [56] characterised the tensile properties of the friction stir welded C71000 copper (Cu)-nickel alloy and 304 austenitic stainless steel (SS) sheets, as shown in Figure 2.27e. The yield strength and tensile strength achieved by the joint are 103 MPa, and 285 MPa, respectively, and the elongation is 21%. It is significant to note that these values are less than the tensile properties of both base materials. To assess the joint efficiency of a typical dissimilar joint, the joint strength needs to be correlated with the properties of the weaker base material in the particular dissimilar combination. Therefore, in the case of Cu to SS joint, the tensile strength of the weld has to be compared with the properties of the copper base material. A sound FSW (Cu-SS) joint should have tensile properties superior to the Cu base material. However, the tensile strength of the weld achieved in this investigation is slightly less than in the Cu base material. This shows that the weld nugget had major defects during the FSW process which significantly reduced the overall tensile strength of the joint.

Wang et al. [32] studied the tensile properties of the friction stir welded 110 copper alloy (Cu) and 316 stainless steel (SS) specimens (W1, W2, W3, and W4) manufactured under different welding conditions as listed in Table 2.3. Figure 2.27f shows the tensile strength of these specimens along with the base materials. Although this investigation has reported that the failure location of all the tensile specimens were in the stir zone, the tensile strength achieved by the welds is close to the tensile strength of copper. The authors justified their claim through the fractograph captured on the failure location where the failure type of the tensile specimen is clearly evident as ductile.

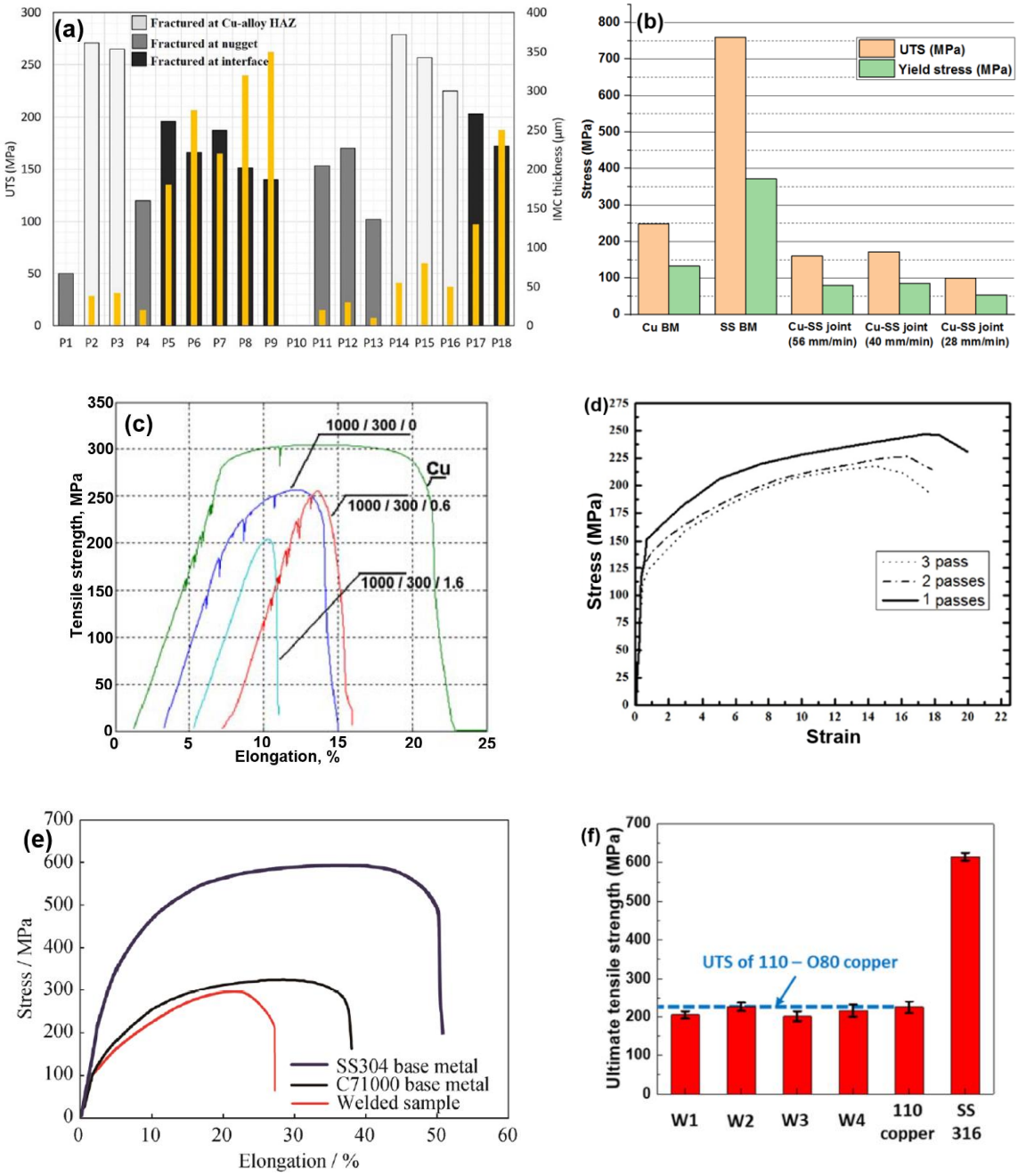

Figure 2.27 Tensile results of FSW (Cu-SS) joints reported from previous investigations: (a) Shokri et al. [54]; (b) Imani et al. [55]; (c) Ramirez et al. [20]; (d) Jafari et al. [17]; (e) Aval et al. [56] (f) Wang et al. [32]

2.4 Summary

- **FSW of similar materials (SS-SS, Cu-Cu):** The literature review discussed in section 2.2 of this chapter identifies the local effects of FSW process on the microstructure evolution and mechanical properties of friction stir welded SS-SS and Cu-Cu joints. To summarise, both these welds have highly heterogeneous weld sub-regions such as weld nugget and TMAZ. The weld nugget typically comprises equiaxed fine recrystallized grains. Due to the high thermal conductivity of copper, HAZ is visible only in the FSW (Cu-Cu) welds, and is absent in the FSW (SS-SS) welds. W distribution from FSW tool wear is reported in the weld nugget of FSW (SS-SS) joints [37]. It is confirmed that the fine grains achieved by the weld nugget improved the microhardness and tensile properties of the FSW (SS-SS), FSW (Cu-Cu) welds compared to their corresponding base materials. But the investigations reported in the FSW (SS-SS) and FSW (Cu-Cu) welds to date have only characterised the microstructural characteristics of the weld sub-regions. Therefore, the local mechanical properties associated with the weld sub-regions need to also be characterised to assess the structure-property relationships of the individual weld sub-regions. Even though Mironov et al. [41] have attempted to investigate the local strain response of the friction stir welded duplex stainless steel through DIC, the investigation did not address the local stress-strain properties of the weld sub-regions. The other two significant limitations noticed in the previous investigations attempted in FSW (SS-SS), and FSW (Cu-Cu) welds are: Firstly, all the investigations have focussed their characterisation techniques only on the weld cross-section. However, the FSW process clearly affects the microstructure of the material both on the surface and weld cross-section [34]. Therefore, there is a strong need to understand the microstructural and mechanical property variations in both these regions. Secondly, the majority of investigations have not considered the effect of actual FSW weld geometry especially the reduced thickness across the FSW weld on the subsequent tensile properties. These limitations are still recognised as a significant gap in developing our knowledge and understanding of the FSW process structure-property relationships.

- **FSW of dissimilar materials (Cu-SS):** The literature review presented in section 2.3 of this chapter discusses the effects of FSW process parameters (tool rotation speed, welding speed, and tool offset distance) on the mechanical/microstructural properties of friction stir welded Cu-SS joints. From the thorough literature review on the FSW (Cu-SS) welds, it is evident that only six highly relevant investigations [17, 20, 32, 54-56] have been attempted to date. To summarise their findings, it is extremely challenging to resolve the weld sub-regions located along the Cu and SS sides due to the heterogeneous material flow across the weld. But some studies have made an effort to observe the heterogeneous zones; however an individual TMAZ for copper was not detected in most of the studies [20, 32] due to its ease

of recrystallization. Although the FSW (Cu-SS) weld nugget has a mixture of Cu and SS elements, the FSW (Cu-SS) weld nugget clearly demonstrates higher hardness than both the base materials due to the fine recrystallized grains. In most investigations, the tensile strength achieved by the FSW (Cu-SS) joint is closer to the strength of the Cu base material. The key limitation noticed in all the investigations is the lack of evidence to establish the structure-property relationships of the dissimilar weld sub-regions. Studies attempted in the FSW Cu-SS joints have not thoroughly correlated the microstructural information with the local mechanical performance under plastic deformation. Cu to SS joints have a broad scope within many critical structural applications, and the global mechanical response of the joints depends on the mechanical properties of the various zones (HAZ, TMAZ and weld nugget) produced in the vicinity of the weld [29]. Correlating the local property changes across the FSW (Cu-SS) weld sub-regions with their corresponding microstructures is needed to achieve a clear insight into the entire material performance of the FSW (Cu-SS) joint. Understanding the evolution of local strain across the FSW joints could involve the use of a high-resolution full-field technique such as Digital Image Correlation (DIC) to characterise the local strain responses linked to the mechanical properties of the weld sub-regions. A brief review of the fundamental basis of DIC and a few key investigations related to the DIC applications in FSW welds are presented in the next chapter of the PhD thesis.

Chapter 3 Theory of Digital Image Correlation (DIC) and its application to FSW welds

3.1 Introduction

The purpose of the current chapter is to provide background in the following areas related to DIC:

i) DIC overview

ii) High-resolution (HR)-DIC

iii) DIC applications in FSW welds

iv) HR-DIC applications in welds/joints

The first section provides an overview of the DIC technique including the underlining principles involved in this technique. Its purpose is to familiarise the reader with DIC and highlight aspects of the technique relevant to the PhD. DIC is now a well-established technique with several detailed descriptions of the algorithms used for processing and uncertainties in the measurement provided in the literature [58, 59]. The section finalises with a brief overview of the experimental set-up required for HR-DIC and describes the state of the art in the application of HR-DIC, which informs the development of the techniques described in the thesis.

The second section of the chapter discusses the key results obtained from the DIC investigations on FSW, to define the findings from other researchers and identify where gaps exist in the literature, justifying the developments of the technique described in the later sections of the thesis. The section ends by focusing on investigations where HR-DIC was attempted on welds/joints, clearly identifying the limitations of the techniques carried out to date. Although, several detailed investigations have been carried out using DIC on fusion-welded specimens, e.g. [60-64], in the interests of brevity the literature review focuses only on DIC applied to FSWs. The literature review, therefore provides the basis to devise a new HR-DIC experimental procedure for FSW.

3.2 Digital Image Correlation (DIC)-Theory and Experimental set-up

DIC is a well-known full-field optical technique, and the theory behind DIC has been described thoroughly in the literature [59, 65]. In brief, DIC is a non-contact full-field imaging technique that has been used as a reliable analytical tool for measuring full-field displacement and strain fields. This technique is based on white light image correlation of a specimen that has undergone deformation with the corresponding undeformed image (usually a reference image-Image captured at zero load). Figure 3.1 shows the typical 2D-DIC experimental set-up. The main components of a DIC system are a sturdy tripod mounted with a monochrome digital camera fitted with high-quality lens, a

computer system with application software for digital image acquisition and processing, and monochromatic lights for illumination. A DIC system involves scientific-grade digital cameras to capture high-resolution images on the sensor plane. Both the charge-coupled device (CCD) camera and complementary metal-oxide-semiconductor (CMOS) have been used in a wide range of DIC applications. The CCD cameras have been dominant in the field of DIC due to high image quality and more flexible function than the CMOS cameras [66]. High-quality lenses involved in DIC imaging usually have the focal lengths ranging from 17 to 200 mm. Monochromatic lights (LED) are highly recommended for constant and continuous illumination during DIC measurements. Many commercial DIC software packages (DaVis from LaVision, VIC-2D from correlated Solutions, GOM correlate from GOM, and MatchID) are available to perform image acquisition, detailed post-processing and analysis. The strain resolution of a DIC hardware system depends on the spatial resolution and size of the digital camera and also the lens magnification used to capture greyscale images. The standard deviation of the strain calculated from the DIC measurements captured at zero load (no deformation) condition is the strain resolution of the DIC system. It is noteworthy that the standard deviation should be higher than the average strain for any reliable strain measurements performed at no-load condition.

DIC is a surface strain measurement technique, therefore, for any reliable DIC measurements, the specimen used for DIC should have a random grey scale distribution pattern on its surface to deform along with the specimen during the test. Thus the DIC specimen surface generally coated with a random speckle pattern (e.g. random black dots sprayed over the white background painted with aerosol spray paints). It is noteworthy that for high-resolution DIC, speckle pattern produced using an airbrush has been preferred to generate more fine speckle pattern than aerosol spray paints [67]. The specimen surface should be parallel to the camera sensor during uniaxial tensile loading to maximise the reduction of any out-of-plane motion of the specimen. Therefore, the out-of-plane displacement should be avoided to achieve more precise DIC measurements.

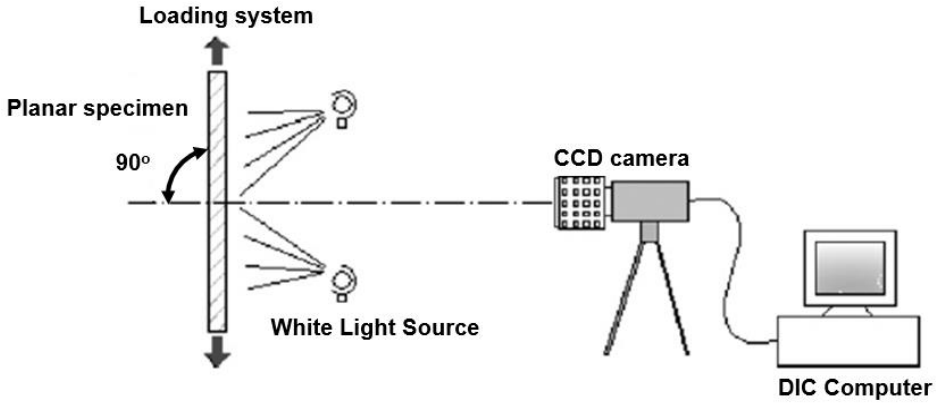

Figure 3.1 A typical 2D-DIC experimental set-up [59]

The primary principle of 2D-DIC is the correlation of the data points (pixels with greyscale value) between the deformed and undeformed image as schematically shown in Figure 3.2. To determine the displacements of point P in the deformed image, a reference subset of (2M + 1) x (2M + 1) pixels centred at point P(X_0, Y_0) in the reference image can be used to track its corresponding location in the deformed image. As it is not feasible to correlate each pixel in the image, a small area which has multiple pixels (called subsets) is chosen for the correlation. To achieve an accurate correlation, the subset chosen for correlation should contain adequate light intensity variations to ensure that the chosen subset can be uniquely identified in the subsequent deformed images. The speckle pattern is matched using the maximum correlation between the subsets of the images captured under deformed and undeformed states of the specimen. The speckle pattern of the undeformed image is correlated with images captured at various load steps using a correlation algorithm, and the corresponding displacement field and strains are evaluated (as shown in Figure 3.3).

It is important to note that numerical differentiation amplifies noise, but the HR-DIC set up is designed to minimise noise; this is because the small displacements experienced are large in comparison to the subset size, hence smoothing is unnecessary [31]. Any smoothing of the data would be undesirable because the large strain gradients experienced in the vicinity of the changes in microstructure require a high spatial resolution to be identified and smoothing would effectively reduce the spatial resolution and mask the peaks in the data. The strain is calculated using the usual formulation:

$$\varepsilon_x = \frac{du}{dx} \dots 3.1$$

$$\varepsilon_y = \frac{dv}{dy} \dots 3.2$$

$$\varepsilon_{xy} = \frac{du}{dy} + \frac{dv}{dx} \dots 3.3$$

where *du* and *dv* is the difference between adjacent displacement vectors in the longitudinal and transverse directions, *dy* and *dx* are the distances between the centres of two adjacent subsets and the engineering shear strain (γ_{xy}) = 2 ε_{xy}. In the DaVis software used throughout the thesis, a central difference algorithm is used to compute the horizontal strain (ε_{xx}) values, as shown in the below equation:

$$\varepsilon_{xx}(m,n) = \frac{dv_x\,(m,n)}{dx} = \frac{\left(V_x(m+1,n) - V_x(m,n)\right) + \left(V_x(m,n) - V_x(m-1,n)\right)}{2g} \dots 3.4$$

where ε_{xx}(m, n) is the transverse strain at grid position (*m*, *n*), v_x (*m*, *n*) is the *x* component of the displacement vector for the cell located at grid location (*m*,*n*) and *g* is the step size. Hence in the version of DaVis used throughout the thesis the strain window is fixed at 3 x 3 steps.

In a 2D DIC experimental setup, one camera is used to capture the image and this system is then capable of measuring only in-plane surface displacements and the corresponding strain components (ε_{xx}, ε_{yy}, ε_{xy}). Thus in 2D-DIC, the effect of out of plane displacements could not be separated from the in-plane strain measurements. However, a 3D or stereo DIC experimental setup has two cameras at an oblique angle to one another. The images from the two cameras are aligned using a calibration procedure that utilises a plate with an array of markers, so that all three displacement components can be obtained and the out-of-plane displacements integrated into the in-plane strains.

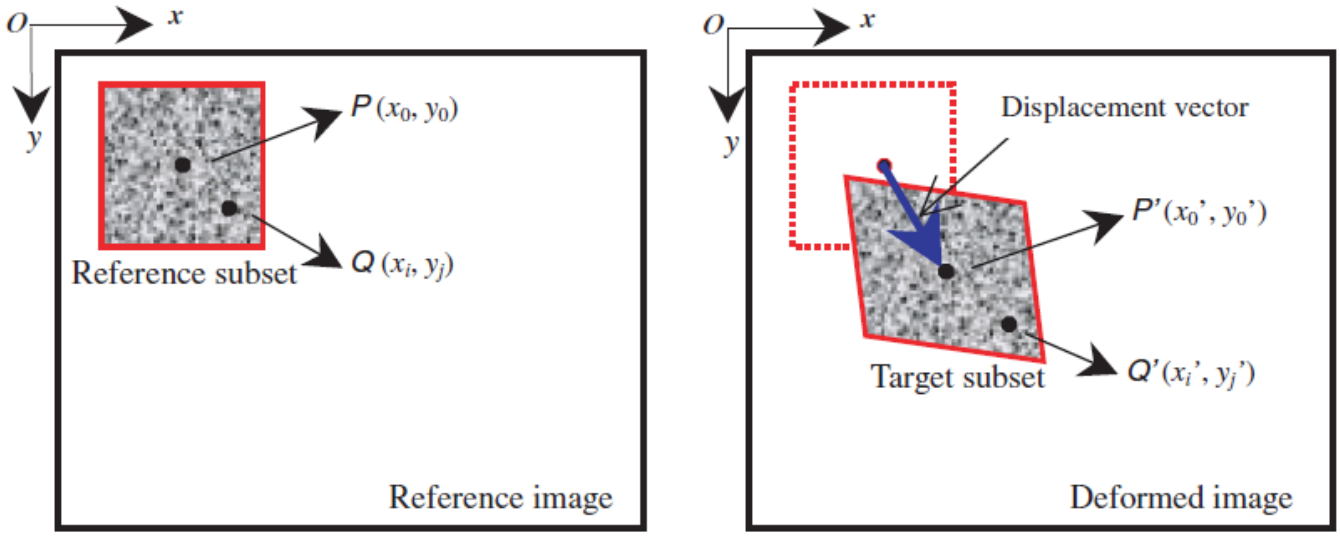

Figure 3.2 Schematic illustration of a reference square subset before deformation and a target (or deformed) subset after deformation [59]

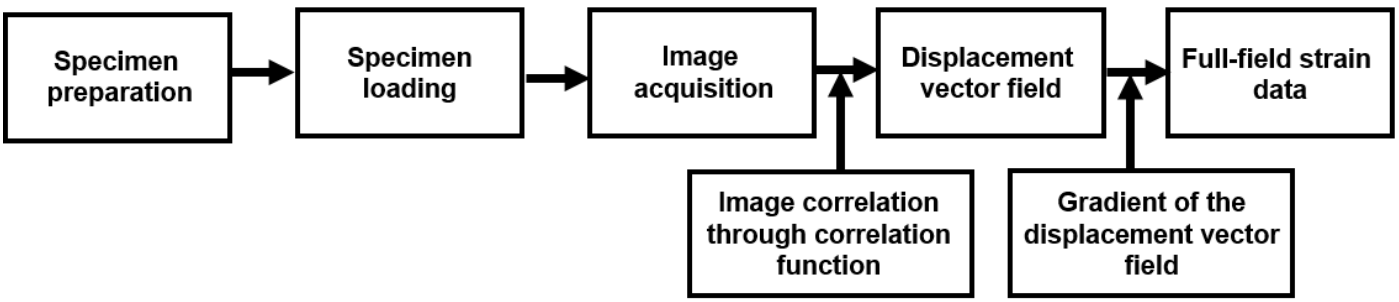

Figure 3.3 Process sequence in 2D-DIC

The accuracy of DIC measurements is highly influenced by various error sources that can be classified under two major categories such as measurement space (specimen, loading and imaging) and correlation algorithm (as listed in Table 3.1).

Table 3.1 2D-DIC error sources

Errors related to loading	Test machine misalignment
	Out of plane displacement
	External vibrations
	Calibration
Errors related to specimen preparation (Speckle pattern)	Size
	Shape
	Contrast
	Illumination
Errors related to Sensor (Camera)	Resolution
	Dynamic range
	Noise
	Lens
Errors related to correlation algorithm	Subset size
	Correlation function
	Sub-pixel algorithm
	Shape function
	Interpolation scheme

The detailed description of these errors has been discussed in the literature [59, 65]. From the 2D-DIC perspective, the errors due to out-of-plane displacement can cause serious impact on the DIC measurements. In general, the out-of-plane motion produces a change in magnification of the recorded image sequence and it will generate parasitic strains on the actual DIC measurements due to the additional in-plane displacements. Any camera misalignment in a DIC system produces a uniform in-plane strain after correlation due to the difference in lens magnification achieved across the width of the specimen. This will generate a significant error in DIC measurements. For achieving highly reliable DIC measurements, it is vital to capture high-quality images without any artefacts to avoid the chance of decorrelation. The artefacts include lens contamination, reflection on the specimen surface, sensor saturation and variations in lighting levels across the image [59]. It is highly recommended to use the maximum image contrast by using the full dynamic range of the camera sensor. Speckle size highly influences the optimum subset sizes required for DIC. Large size speckles can occupy an entire subset and produce decorrelation. On the other hand, speckles less than 2 pixels

diameter are more likely to produce the pixel locking effect, where displacement vectors become biased toward integer pixel values. To achieve accurate subset matching during DIC, it is recommended that each subset should have approximately 9 speckles. The digital camera sensors may generate errors in the image as a result of random noise. However, this can be reduced by sensor cooling. Dead pixels produced in a sensor array can cause a decrease in image similarity after correlation. To avoid this, digital cameras with low dead pixel counts are highly preferred for any DIC system. The spatial resolution and precision of the displacements calculated using DIC are limited by the number of pixels contained in the image and the subset size. Choosing a larger subset size during correlation will produce lower spatial resolution and less noise, while a smaller subset size will yield higher spatial resolution and more noise in the strain maps. Therefore, there is always a trade-off between spatial resolution and strain resolution in DIC. It is noteworthy that DIC has many applications in the field of experimental mechanics in characterising the local deformation/strain information for a range of materials where strain gauges cannot be applied. However, this chapter is focussed on reviewing the particular investigations where DIC was utilised as an optical tool for evaluating the local material response of FSW joints.

High resolution (HR) DIC is a variant of DIC technique that involves high-resolution digital camera interfaced with a high magnification macro lens. Thus, the stand-off distance between the specimen and HR-DIC optics will be very narrow during a typical HR-DIC experimental set-up, and therefore it enables strain measurements at a high spatial resolution with a minimum field of view. Despite experimental challenges associated with the application of HR-DIC [31, 34], HR-DIC has been successfully attempted to achieve high fidelity strain measurements on joints. Two key investigations [31, 33] which have attempted the HR-DIC strain measurements on joints are also reviewed in the chapter. One of the first applications of HR-DIC was conducted by Crammond et al. [31], where the localised through-thickness load transfer and damage initiation in a composite adhesive joint were evaluated. A double butt strap joint (DBSJ) was constructed from chopped strand mat (CSM) glass fibre with outer and inner adherends having a width of 25 mm as shown in Figure 3.4. An epoxy adhesive was used to bond the outer and inner adherends together. Initially, a 3D-DIC trial experiment was performed on glass fibre reinforced composite adhesive joint, and the authors reported that the recorded strain values were due to rigid displacement of the adherends and not the actual straining of the material, as shown in Figure 3.5. To address this limitation and to increase the spatial resolution, high-resolution 2D-DIC was attempted using a 5MP 12 bit monochromatic CCD camera coupled with high magnification Canon MP-e65 macro lens to derive the local strain values in the region of the discontinuity in the joint with a spatial resolution of 726 pixels/mm. To avoid out of plane displacements during high-resolution 2D-DIC, an initial pre-load of 50 N and a reduced loading rate of 1 mm/min was applied before testing in the servo-mechanical machine. Figure 3.6 (a) (b) (c) shows the full-field plots of the axial, peel, and shear strains, respectively in the principal directions evaluated at 13 kN. These strain maps show the complex strain distributions within the joint better than Figure 3.5.

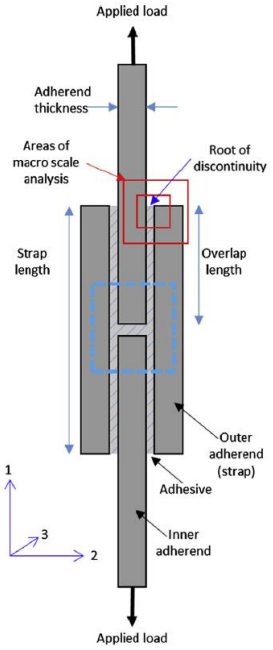

Figure 3.4 Schematic configuration of Double butt strap joint [31]

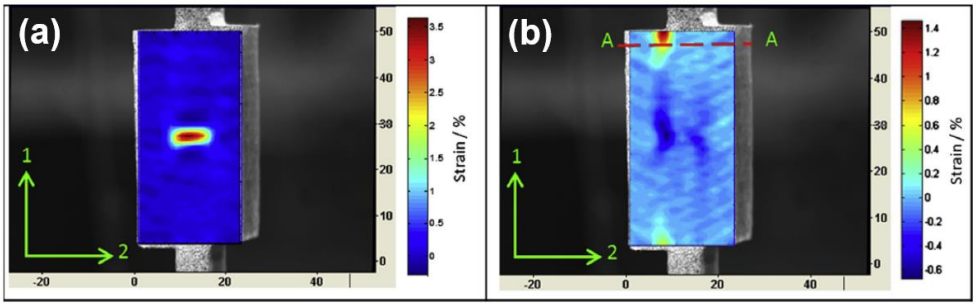

Figure 3.5 Strain distribution in the joint loaded at 16 kN, (a) axial (ε_1) and (b) through-thickness (ε_2) [31]

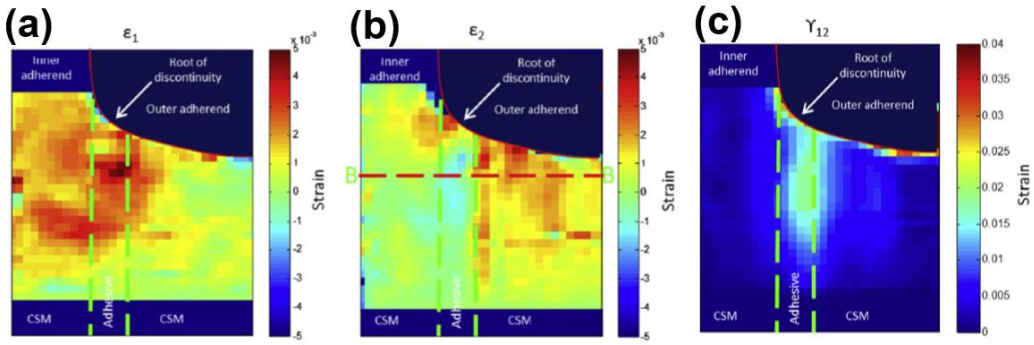

Figure 3.6 Strain distributions around joint discontinuity at 13 kN, (a) axial (ε_1) strain field, (b) through-thickness (ε_2) strain field, (c) shear strain (γ_{12}) [31]

However the resolution is low, and by employing higher resolution cameras, not available at the time of writing [31], greater fidelity can be achieved to resolve the FSW sub-regions. The investigation in [31] has served to inspire the current work, and the set-up forms the basis of the HR-DIC approach

used in the thesis described in detail in Chapter 6. The difference is that two cameras are used in the investigations and a servo-hydraulic test machine is used as the hydraulic grips are more robust in operation compared to the mechanical grips used in [31].

3.3 DIC applications to FSW welds

Local properties in welds have been previously determined by testing miniature tensile specimens (called "weld coupons") machined from various zones of the weld [68]. But in practice, the preparation of micro-tensile specimens is a time-consuming task, and the accuracy achievable is also limited in terms of the variation in microstructure across even the small volume of a microtensile sample. DIC has revolutionised research in the field of welding through its full-field approach in determining the full-field displacement/strain from a single tensile test. DIC was successfully applied in evaluating the local strain distribution across FSW welds [29, 30, 32, 33, 41, 69, 70]. Reynolds [30] first used the DIC technique in friction stir welds and conducted a feasibility study to determine the local mechanical behaviour of the weld and the base metal in two similar material combinations (5454-O, 5454-H32 aluminium alloys) FSWs. In this investigation, optical micrographs were used to identify the FSW sub-regions and to measure the length of the weld sub-regions, as shown in Figure 3.7a. A 2D-DIC system consisting of a single 8-bit digital camera having 768 x 484 pixel sensor array attached with a 200 mm telephoto lens was used. To extract the local stress-strain curves of the weld sub-regions, optical microscopy was used to identify the weld regions corresponding pixel positions in the DIC strain maps. The local stress-strain curves of the weld sub-regions were extracted from the DIC, as shown in Figure 3.7b. It can be seen that the stress-strain response in the weld nugget, i.e., DRZ (Dynamically recrystallized zone) is close to the 5454-O base material, but with reduced yield and reduced ductility. Additionally, both the HAZ's (Recrystallized and Recovered) have larger strains to failure and smaller yield strengths compared to weld nugget and align with the results for the tempered base material. Although, this investigation identified the importance of identifying the FSW weld sub-regions through microstructural analysis and to link the local DIC data with the respective FSW sub-regions. However, the FSW weld sub-regions are not clearly connected to their microstructural features and also the approach used to correlate the microstructural information with the DIC results is not described in the paper. The approach is clearly limited by the low-resolution equipment used, nevertheless the different mechanical characteristics of the weld sub-regions are identified and correspond to the expected results with respect to the different conditions of the materials. Furthermore, the scatter received from the average strain of the weld sub-regions at different stress level was not reported in this study.

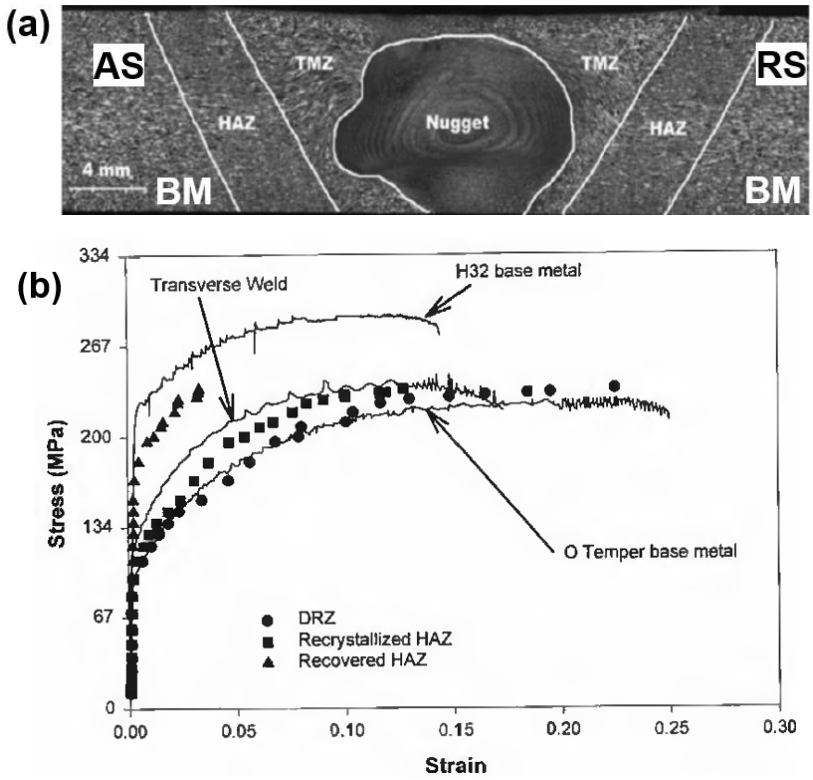

Figure 3.7 Structure-property relationships of FSW weld sub-regions: (a) Macrograph of the FSW weld cross-section; (b) Local stress-strain curves of the FSW weld sub-regions determined via DIC [30]

Leitão et al. [29] studied the local properties of the FSW similar/dissimilar material welds and computed the local stress fields in the ROI by considering both local thickness variations and the local strain fields obtained from DIC. The DIC system used was Aramis 3D 6M (Camera resolution: 2752 x 2200) optical system (GOM GmbH). In this investigation, both similar and dissimilar material welds were made between the aluminium alloys AA5182 and AA6016. The process parameters involved in making these joints and the corresponding metallography analysis were also discussed by the same authors in [71, 72]. Throughout this investigation, similar material FSW welds of AA5182, AA6016 were coded as S55, S66 respectively and dissimilar material welds between AA5182 and AA6016 were coded as D56. Both longitudinal and transverse tensile specimens were machined from the weld for the experiments as schematically shown in Figure 3.8. The strain maps derived from S55, S66, and D56 welds and their hardness profiles are shown in a, b and c, respectively in Figure 3.9. From these strain maps, it is observed that the strain distribution across the FSW weld nugget is highly heterogeneous. Furthermore, the local stress-strain curves extracted from the locations close to the weld nugget show the heterogeneous material response. Comparison of the hardness line profiles with the stress-strain curves links the observed local property variations with the relevant microhardness distribution. The local stress-strain curves for all the welds (S55, S66, and D56) obtained from transverse tensile specimens and the global stress-strain curves obtained by testing longitudinal tensile specimens (LONG5, LONG6, and LONG56) are shown in

Figure 3.10. From this figure, it can be inferred that even though there is a significant difference between the strain levels between the longitudinal (LONG5, LONG6, and LONG56) and transverse specimens (S5, S6, and S56) of a particular weld, the local stress-strain curves follow the respective trends expected from the longitudinal samples. This is because all the longitudinal specimens (LONG5, LONG6, and LONG56) have only the weld nugget as the sub-region exactly where the local DIC strain data of the weld nugget was extracted in the respective transverse specimens (S5, S6, and S56).

Although this study has provided insight in evaluating stress from local DIC strain measurements by taking into account geometrical variations across the weld nugget, the precise location of the FSW weld sub-regions were approximated. Previous work [2, 3, 52] confirms that FSWs (for both similar and dissimilar materials) have highly heterogeneous microstructural features and determination of the weld sub-regions and their boundaries should be linked to the relevant microstructural features. Another major limitation of this study is that the local stress-strain curves were derived only for the weld nugget and properties of other (surrounding) zones of the FSW such as HAZ, TMAZ along the advancing and retreating sides were completely neglected, but clearly will influence the overall mechanical response of the joint.

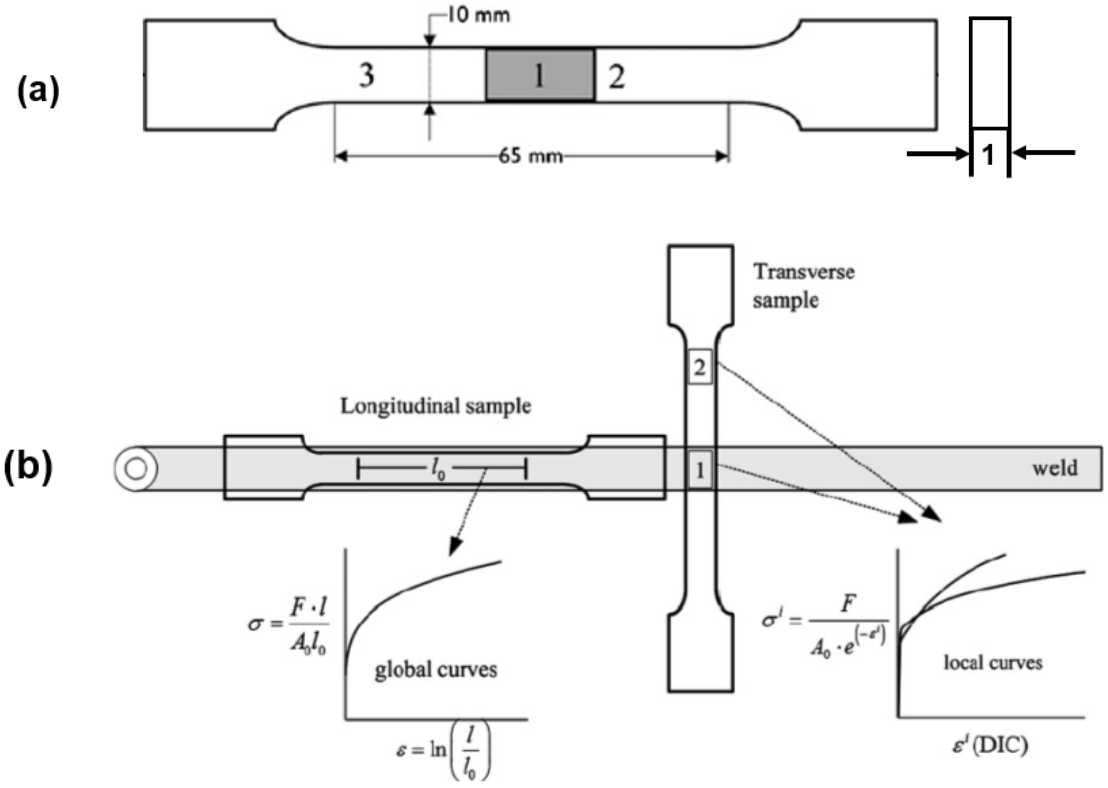

Figure 3.8 (a) Tensile specimen with dimensions for DIC measurements; (b) Longitudinal and transverse tensile specimen scheme used in the study [29]

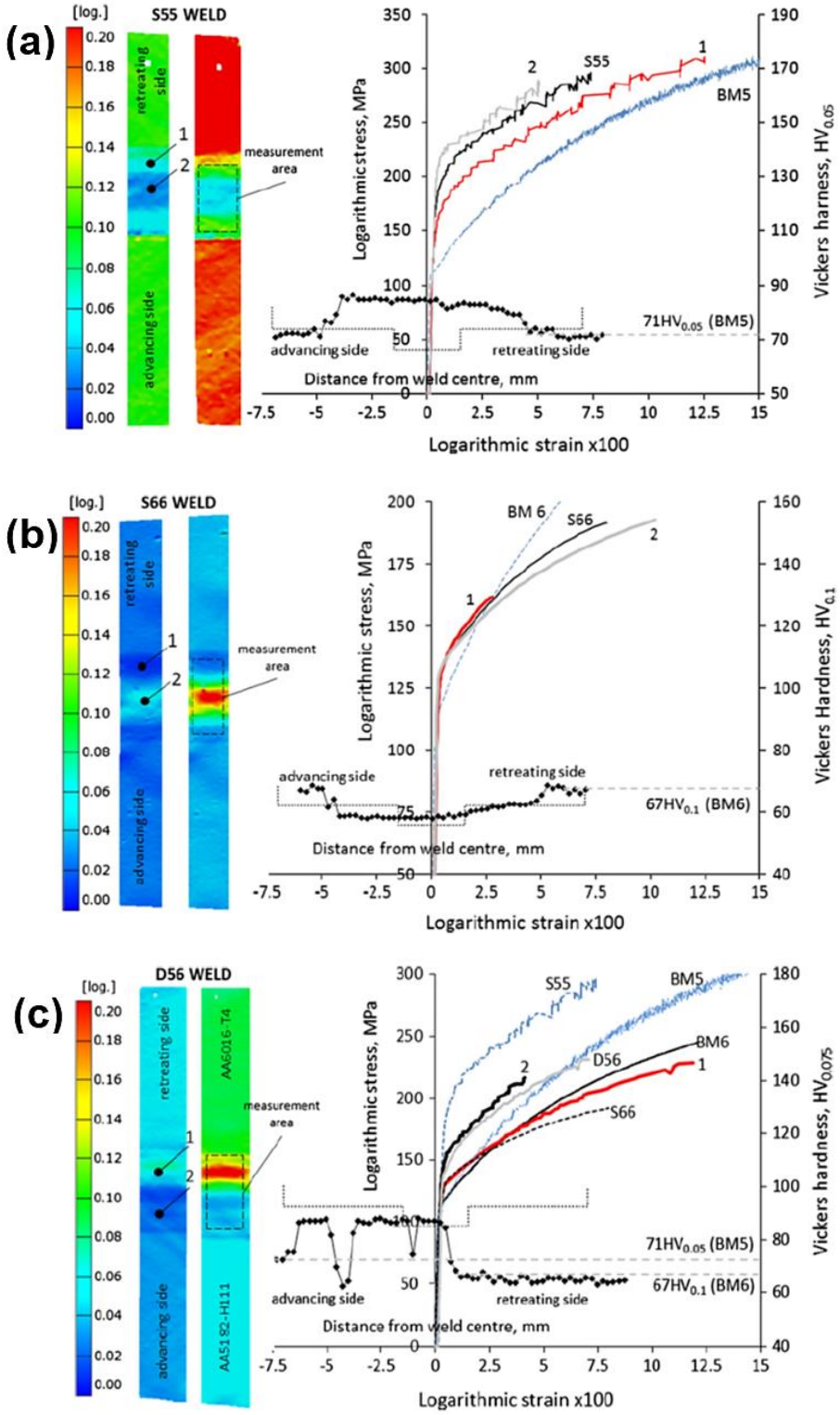

Figure 3.9 Local stress-strain curves: (a) Strain maps and hardness profile for S55 weld; (b) Strain maps and hardness profile for S66 weld; (c) Strain maps and hardness profile for D56 weld (Left strain map was captured at 50% Elongation, and right strain map was captured at maximum load) [29]

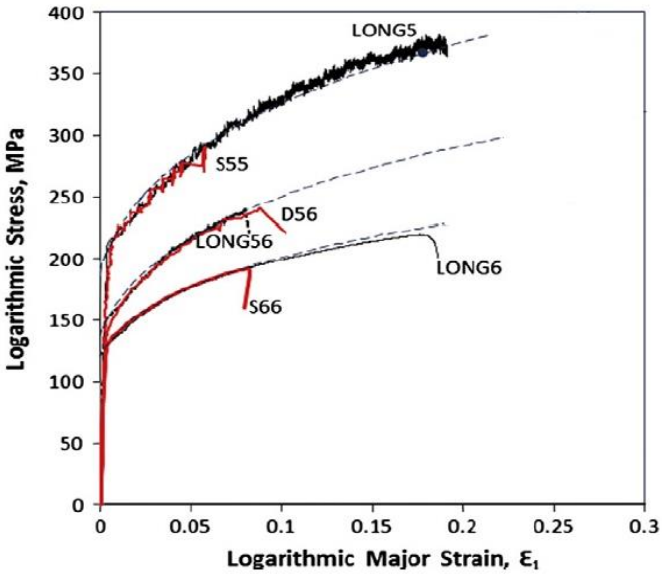

Figure 3.10 Comparison of weld local stress-strain curves obtained by DIC and those corresponding to the longitudinal specimens [29]

Li et al. [70] studied the heterogeneity in the mechanical response of FSW 6082 aluminium joints with DIC. Butt welds were created on 5 mm thickness Al alloy plate with a tool rotating speed of 1800 rpm and a welding speed of 200 mm/min. As any FSW weld has steep microstructural gradients along both the surface and through-thickness cross-sections, it is essential to derive the local DIC strains along both the surface and the through-thickness cross-sections of the weld to fully assess the heterogeneous characteristics. In this investigation, the authors considered three surfaces of the specimen (Front, rear, and one side surface) for this analysis. Five different locations were selected approximately along the centre axis of the specimen, representing BM/HAZ on the Advancing side (AS) and nugget, BM/HAZ on the Retreating side (RS) as shown in Figure 3.11. It is reported that the TMAZ was not considered in this investigation due to the difficulties in resolving the boundaries between the weld nugget and TMAZ through optical microscopy. Figure 3.12 shows the tensile specimen dimensions in line with ISO 4136-2001 standards for 2D-DIC measurements. It is reported that the upper and lower surfaces of the welded specimen were milled on a plane to achieve a uniform thickness. The details of the DIC system (camera resolution and Focal length of the lens) used in the investigation was not reported in the paper. From the 2D-DIC strain maps obtained along the three surfaces (Figure 3.13), it was observed that the strain distribution on the side surface is more homogeneous than on the front and rear surfaces. This finding raises more questions on the reliability of the DIC data. This is because, strain gradients are highly expected at plastic deformation of the joint as the weld sub-regions of the FSW usually have different microstructural features. Therefore, the DIC finding obtained from the side surface is not aligned with this expected outcome and highly subjected for further investigation especially on the post-processing procedures (such as data smoothing) adopted in the study. The local stress-strain curves obtained through these strain maps

are shown in Figure 3.14. Figure 3.14a confirms a sharp transition between the properties of the weld nugget and the HAZ in the front surface. However, more homogeneous local stress-strain curves were obtained on the side surface of the specimen (Figure 3.14b), showing the uniformity in the distribution of mechanical property across various zones.

Figure 3.11 Macrostructure of 6082 aluminium alloy FSW weld cross-section [70]

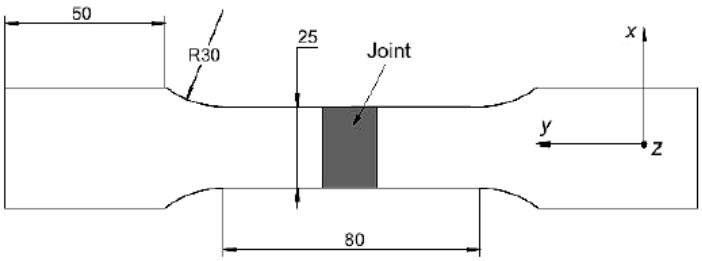

Figure 3.12 Tensile specimen dimension used in the investigation [70]

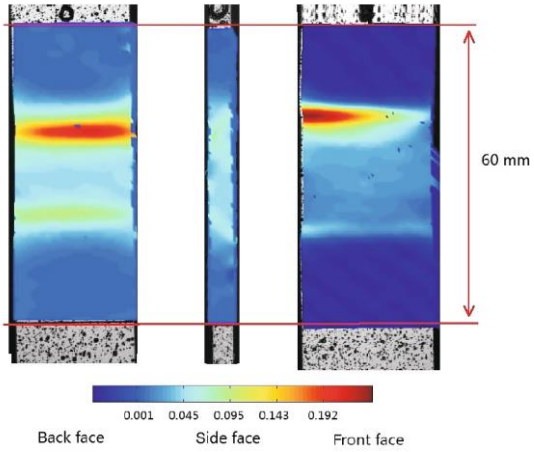

Figure 3.13 DIC strain maps obtained from the different surfaces of FSW at 0.5 sec before cracking [70]

Figure 3.14 also shows that the strain achieved by the base material regions (BM-AS and BM-RS) are close to zero in both elastic and plastic deformation of the specimen. Furthermore, the local strain-strain response extracted from the aluminium base material regions (AS and RS) do not correspond with the elastic modulus of aluminium (70 GPa approx). Therefore, the quality of the experimental set-up and the DIC data used to extract the local stress-strain curves is in question, and the indications are that the 2D single camera set-up has correlated parasitic strains caused by out of plane displacements. Although this study demonstrates the strain gradients distributed along the different surfaces of the FSW weld specimen, the position of the FSW zones were again approximated, and the strategy applied in linking the local DIC strains with the specific FSW zones is not explained.

Thus this study has not unequivocally established the structure-property relationships of the specific FSW zones. The mechanical interactions between the different zones and the associated effects on the overall joint response require a clear identification of the different zones.

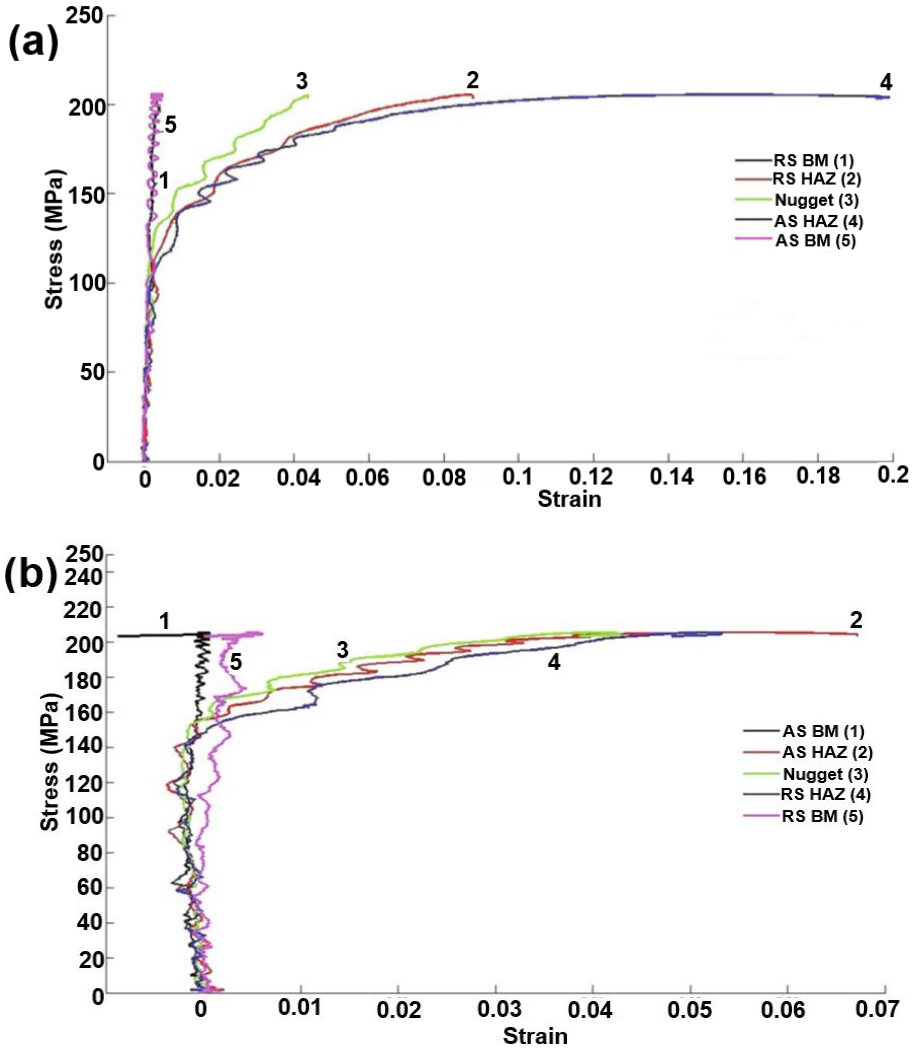

Figure 3.14 Local stress-strain curves: (a) Front surface; (b) Side surface [70]

Mironov et al. [41] employed the DIC technique to evaluate strain distributions during tensile tests on the friction stir welded TRIP steel. Before conducting the test, the specimen was mechanically polished to achieve a uniform weld thickness across the weld nugget. The 2D-DIC system used in the investigation was a high-speed digital camera (camera resolution was not reported) equipped with a Nikon AI AF Micro-Nikkor 200 mm f/4D IF-ED lens; the spatial resolution (pixels/mm) of the measurements was not reported. Figure 3.15 shows the strain maps obtained from the weld surface at different strain levels. In the elastic region (Figure 3.15a), the strain concentration is observed on the outer boundary of the stir zone. The authors claimed that the strain concentration is located in the HAZ, which is attributed to material softening effects. After yielding, it is very significant to note that the plastic strain is more concentrated on the retreating side (RS) of the weld (Figure 3.15b-d). Additionally, the stir zone exhibits very low strain compared to other weld sub-regions at all strain levels. It is reported that before failure the strain was concentrated in the HAZ and finally led to

fracture in the same region. Even though this investigation did not identify the exact reason behind the greater strain on the RS, the DIC results clearly evidenced different strains across the weld nugget. Furthermore, the full-field DIC data was not used to extract the local stress-strain response of the FSW sub-regions.

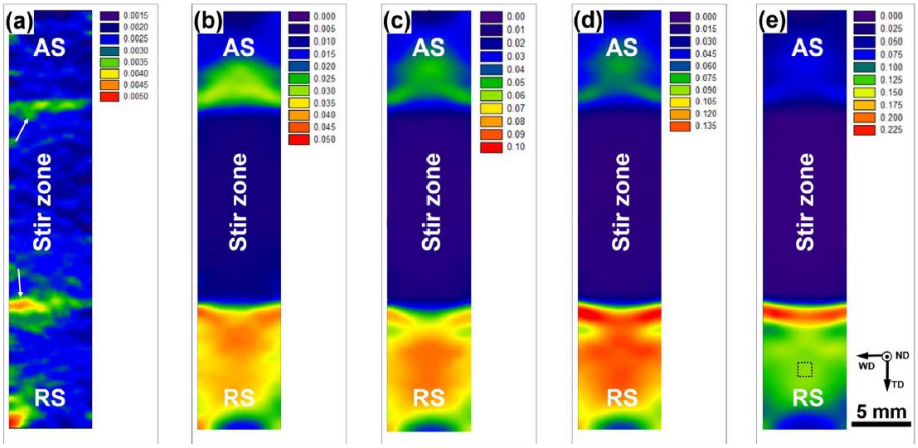

Figure 3.15 The distribution of true extensional strain in the upper surface of weld after (a) elastic loading, and global plastic strain at (b) 0.2%, (c) 1.5%, (d) 3.2% (i.e., peak load), and (e) 3.6% (i.e., immediately before fracture) [41]

Wang et al. [32] studied the local tensile properties of friction stir welded 110 copper alloy (Cu) and 316 stainless steel (SS) specimens using 2D-DIC; the details of the DIC system (camera resolution and Focal length of the lens) was not reported. Figure 3.16 shows the strain maps captured on the weld cross-section at different stages of deformation. Figure 3.16b shows the strain map captured during elastic deformation where the strain distribution along copper and steel sides are entirely different due to their difference in their elastic modulus. Figure 3.16c and d shows the crack initiation and crack propagation, respectively at the steel/weld interface during the plastic deformation. The hardness difference noted at the steel/weld interface were given as the principal reason for the strain localisation at this region during the uniaxial tensile testing. The local DIC strain information was not used to derive the stress-strain response of the dissimilar weld sub-regions. Additionally, the microstructural features of the weld sub-regions such as TMAZ, HAZ along the stainless steel and copper sides were not characterised in this investigation. FSW process between the dissimilar materials usually produces wide microstructural and composition gradients in the vicinity of the weld [5]. Due to this reason, there should be a significant variation in yield strength of the weld nugget. Therefore, to fully understand the local strain response with respect to the microstructure and compositional variations across the dissimilar weld nugget it is necessary to correlate the stress-strain behaviour over the FSW region with microscopy, which is a clear objective of the work presented in the thesis.

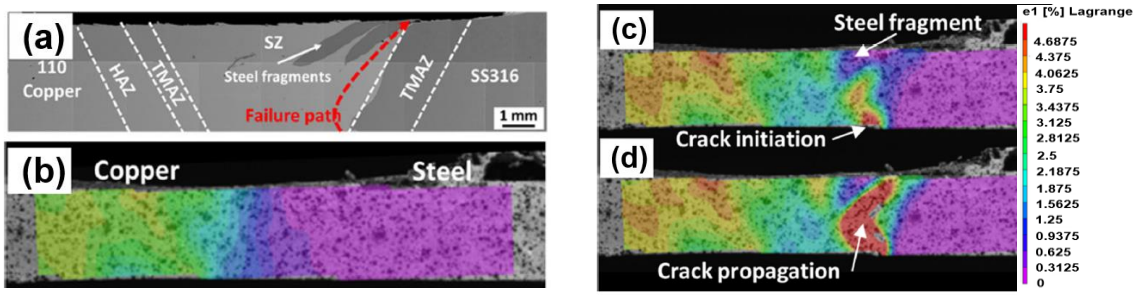

Figure 3.16 2D-DIC results: (a) schematic of failure location on the cross-section of butt-welded copper/steel during tensile testing; (b) DIC measurements during elastic deformation; (c) DIC measurements during crack initiation; (d) DIC measurements during crack propagation [32]

Texier et al.[33] attempted to measure the local mechanical properties of friction stir welded dissimilar aluminium alloys (AA-2024-T3/AA-2198-T3) using the HR 2D-DIC. In this investigation, a 150 µm-thick layer of material was machined from the tensile specimen surface to eliminate the thickness reduction caused by the FSW process; the specimen is shown in Figure 3.17a. The HR-DIC used comprised of a single digital camera (3594 x 3594 pixels) with a macro lens at 5x magnification, and the image resolution achieved was 1.13 µm/pixel. Figure 3.17b shows the DIC strain maps (ε_{xx}, ε_{yy}, ε_{xy}) captured at five sequential loading steps on the region of interest shown in Figure 3.17a.

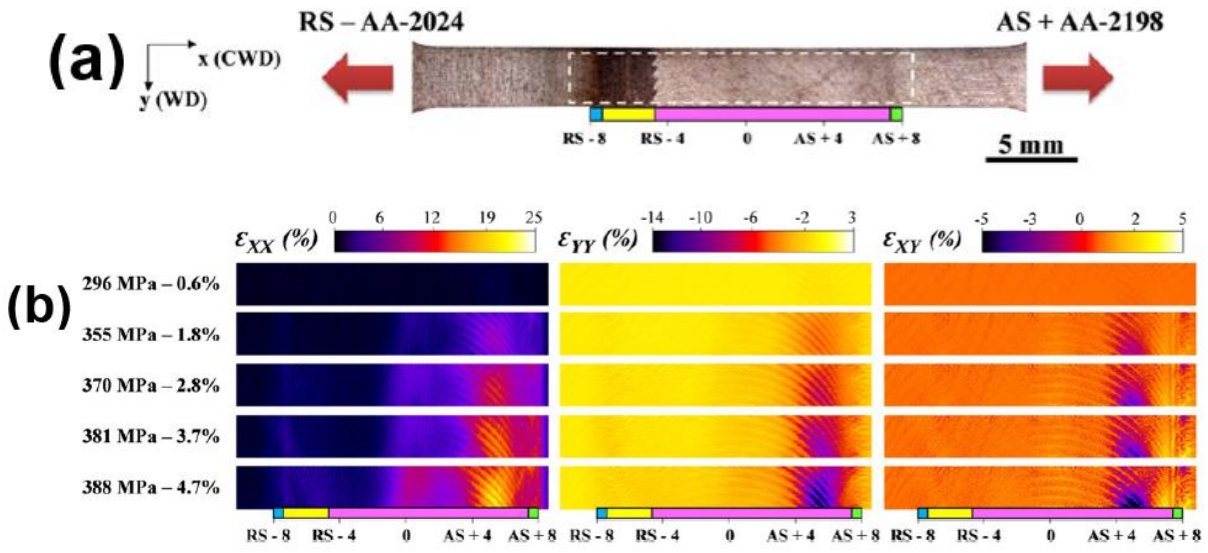

Figure 3.17 DIC results: (a) Area of interest of the joint used for DIC measurements; (b) Local in-plane strain distribution obtained with DIC corresponding to various macroscopic strains (based on a 30 mm gauge length [33]

The strain maps show a non-uniform strain distribution along the advancing and retreating sides with the strain localisation due to the stirring evident only on the advancing side and completely no strain localisation observed on the retreating side; this may be due to the scaling of the images. It is noteworthy that Ɛyy/ Ɛxx does not appear to be in correspond to a Poisson's ratio of around 0.3; Ɛxx appears to be small and indicates some out of plane bending in the specimen. Likewise, the shear strain is non-zero. To determine the heterogeneous mechanical response, the DIC results were correlated with EBSD micrographs, and it was postulated that the heterogeneous microstructure of the weld especially the differences in crystallographic orientations had an influence on the behaviour of the strains. Microhardness measurements were also correlated with DIC results, which showed that the HR-DIC results were more aligned with the microstructure than the microhardness measurements. Even though this detailed investigation has characterised the structure-property relationship of the dissimilar FSW weld, the authors did not consider the possibilities of parasitic strain caused by out-of-plane displacements and made no attempt to classifying the stress-strain behaviour in the different weld sub-regions.

3.4 Conclusion and research questions

The fundamental background to DIC and various investigations which have involved DIC were discussed in this chapter. It can be seen that most of the DIC investigations attempted in FSWs were performed along the cross-section of the weld and also in low spatial resolution; however, one key investigation [70] clearly showed that FSWs have different material response along the thickness cross-section and the surface. To identify the local weld sub-regions across the weld and also to link the DIC local strains to the individual weld sub-regions, the majority of studies have used micrographs and microhardness measurements. Many investigations have confirmed the superior mechanical properties achieved in the FSW weld nugget due to the fine recrystallized grains produced in the weld nugget. It is clear that only a few researchers have employed both DIC and microscopy techniques to establish the structure-property relationships of FSW welds. However, such work has not effectively utilized the full-field DIC data and material microstructure to match the local DIC strain data that corresponds to various microstructural features across the weld sub-regions. Thus a clear gap in the literature is to devise a means of connecting the microstructure of the different weld sub-regions to the stress-strain behaviour obtained from the DIC. Most DIC studies on FSW welds have masked the actual FSW weld geometry by machining the gauge section of the tensile specimen down to the reduced thickness produced across the weld nugget. In the present thesis, procedures are developed so that the weld nugget of FSW is not modified by machining or further processing to facilitate DIC. A means of eliminating the effect of parasitic strains resulting from out-of-plane displacement of the weld region cause by offset loading is devised. Hence the region in the vicinity of the change in weld geometry can be evaluated and its effects during plastic

deformation are established for the first time. To date only a few DIC investigations have been attempted on dissimilar FSW welds. This is because of the lack of high fidelity DIC experimental methodology as well as correlation approaches to establish the relationship between the DIC results and micrographs. The HR-DIC approach developed in the thesis allows a detailed investigation of the dissimilar weld region enabled by the ability to correlate the DIC results with micrographs and microhardness measurements.

Combining the application of high-resolution DIC with a range of microscopy characterisations in the similar and dissimilar friction stir weld in copper and stainless steel are identified as the core research areas available for investigation. The main objective of the PhD is to understand the locally varying post-yielding characteristics of FSW welds and also to achieve the microstructure-material property relationship of the FSW weld sub-regions through high-resolution DIC and a range of microscopy techniques. Hence, in this PhD investigation, a systematic high-fidelity materials characterisation approach is planned to evaluate the microstructural and local material response of the FSW weld sub-regions. For the first time, the FSW weld geometry is investigated in 3D by using X-ray CT and also evaluate the influence of non-homogeneous weld geometry on the mechanical response of joints. By combining the insights received from the various material characterisation techniques, the outcome of the PhD investigation provides a micromechanical assessment of the overall FSW joint, which could be feedback into defining optimised FSW characteristics for various structural applications. Therefore, there are three key research questions that will be addressed in the remainder of the thesis:

- Can a HR 2D-DIC methodology be developed and validated that enables the different microstructure regions in the FSWs to be related to the stress-strain behaviour of an actual FSW?
- Can the procedure be applied to a range of FSW joints after the material has yielded?
- Is it possible to identify the strain concentrations and link these to defects and features identified in by X-ray CT?

Chapter 4 Manufacturing of FSW (SS-SS, Cu-Cu, Cu-SS) joints, process-parameters selection and test specimen preparations for HR-DIC

4.1 Introduction

This chapter discusses the FSW process parameters selection for manufacturing (SS-SS, Cu-Cu, and Cu-SS) joints. All the joints were manufactured using a 50 kN maximum downward force capacity numerical controlled FSW equipment facility available with the collaborator at the SSN College of Engineering, Tamilnadu, India (Figure 4.1). It should be note that the author was not present during the manufacturing process at the FSW facility in India. All the dimensions of the base materials were fixed based on the maximum capability of the FSW equipment. This chapter also presents the test specimen preparation and arrangements required for HR-DIC measurements. Most importantly, this chapter addresses the effect of in-plane bending produced by thin FSW specimens on the HR-DIC measurements.

4.2 Manufacturing of FSW (Cu-SS), FSW (SS-SS) and FSW (Cu-Cu) Joints

The base materials used in this study are rolled sheets of AISI 304 austenitic stainless steel and C21000 copper alloy. The manufacturer's quoted chemical compositions, thermo-physical and the mechanical properties of the base materials are shown in

Table 4.1, Table 4.2, and Table 4.3, respectively. In manufacturing the FSW (SS-SS), FSW (Cu-Cu) and FSW (Cu-SS) joints, the dimensions of the base materials were maintained as (143 x 139 x 2), (143 x 119 x 2) and (131 x 127 x 2) mm respectively. Before welding, the adjoining surfaces of the Cu and SS sheets were machined using a vertical milling machine to produce a uniform surface to weld. The surfaces of the sheets were degreased using 200 grit SiC emery paper followed by cleaning with acetone and then dried with a hair dryer. The base materials were mounted on a 50 mm thick steel backing plate to prevent the abutting joint faces from being forced apart during the welding process. The specimen pairs of (SS-SS, Cu-Cu) sheets were friction stir welded along the joint line (parallel to the rolling direction of the sheets) in a butt weld geometry. However, while joining the Cu to SS, the FSW tool was slightly offset from the joint line. The FSW tool is made up of a tungsten carbide (Chemical compositions: W-90%, Ni-3%, Mo-1%, and Co-1%, Fe-balance) doped with 1% Lanthanum alloy (La_2O_3) to increase the creep resistance and surface energy capability of the tool. The FSW tool (as shown in Figure 4.1b) employed in this study has a convex shoulder with a tapered

right-hand threaded cylindrical pin to facilitate the effective mixing of materials from the advancing side (AS) to the retreating side (RS) or vice-versa.

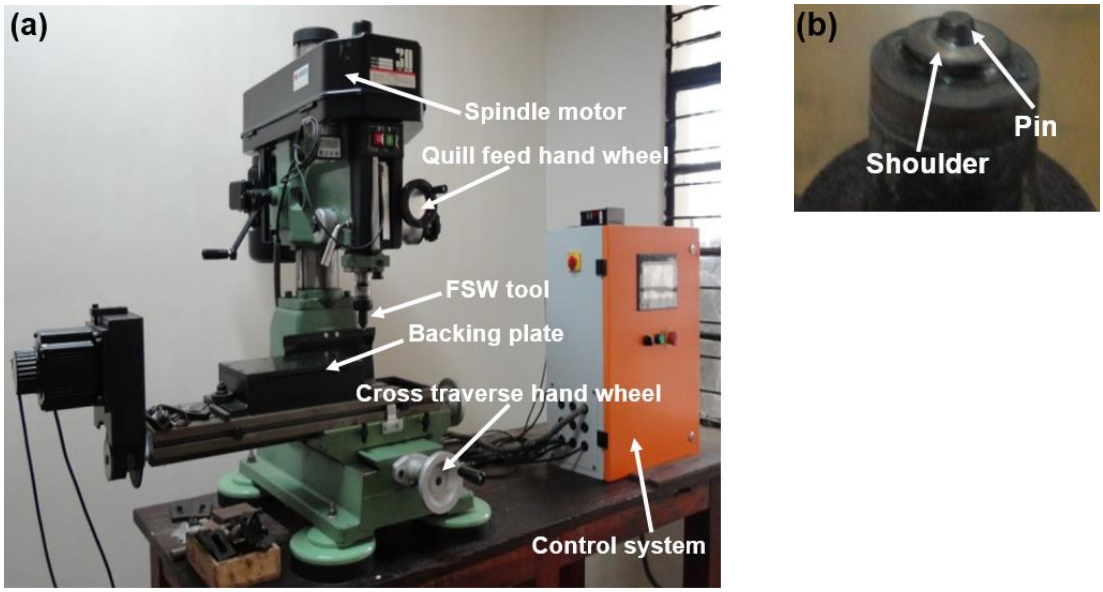

Figure 4.1 (a) A numerical controlled FSW machine; (b) W-1% Lanthanum alloy tool

Table 4.1 Chemical compositions of the base materials

Materials	**Chemical composition (wt%)**									
	C	**Zn**	**Ni**	**Cr**	**Mn**	**Si**	**P**	**S**	**Fe**	**Cu**
304 SS	0.068	-	8.135	18.142	0.945	0.302	0.036	0.003	Bal	-
C21000 Cu	-	6.320	0.023	0.006	0.002	0.003	0.006	0.009	0.010	93.591

Table 4.2 Thermo-physical Properties of the base materials [45] [49]

Materials	**Density (Kg/m^3) @25°C**	**Coefficient of thermal expansion ($(m/mK)x10^{-6}$)**	**Heat Capacity (J/K-kg) @25°C**	**Thermal Conductivity (W/mK) @25°C**	**Melting Point (°C)**
C21000 Cu	8860	18.1	385	401	1085°C
304 SS	8000	17.3	500	16.2	1400-1455°C

Table 4.3 Mechanical Properties of the base materials

Material Property	**C21000 Cu**	**304 SS**
Tensile Strength (MPa)	255	505
0.2%Yield Strength (MPa)	145	215
%Elongation @ 25 mm gauge length	35	55
Young ’s Modulus (GPa)	115 [45]	193 [49]
Poisson ratio	0.307 [45]	0.29 [49]
Rockwell Hardness B (HRB)	48	80

As the copper and stainless steel have significant differences in their thermo-physical properties, there is a possibility of formation of an asymmetric temperature distribution across the weld nugget. This can lead to defects in the root region of a dissimilar weld nugget [5]. To avoid this asymmetric temperature distribution and also to compensate for the heat dissipated by the high thermal conductivity copper during the FSW process, it has been found to be necessary to pre-heat the copper base material [22]. In this study, the FSW of Cu-SS was attempted with and without preheating of the copper base material. For pre-heating, the gas torch was used to pre-heat the copper base material to 200^{o}C. A typical FSW experimental set-up for joining Cu and SS (without and with a preheating arrangement) is shown in Figure 4.2a and Figure 4.2b respectively. To manufacture Cu-Cu and Cu-SS joints without external visible defects, a number of trials were run (as shown in Figure 4.3 and Figure 4.4) to select the process parameters.

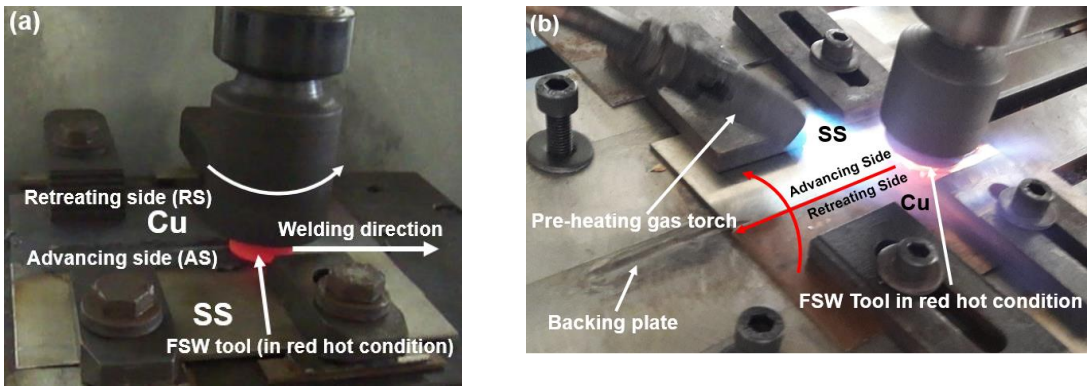

Figure 4.2 Manufacturing of FSW (Cu-SS) joints: (a) without pre-heating; (b) with pre-heating

4.3 FSW process-parameter selection

4.3.1 FSW (SS-SS)

i) As the collaborators (SSN College of Engineering, India) producing the FSW samples had prior experience in manufacturing different grades of stainless steel joints via the FSW process [42]. The FSW (SS-SS) joint as shown in Figure 4.6a was manufactured using previously determined optimised process parameters as follows, Welding Speed: 118 mm/min, Tool Rotation speed: 441 RPM and the FSW tool was plunged on the butt line. No welding defects were observed.

4.3.2 FSW (Cu-Cu)

i) In joining copper to copper via the FSW process, it is noted that the tool rotation speed has a more serious impact than the tool traverse speed in producing defect-free FSW (Cu-Cu) joints. Using process parameters such as very high rotation speed (1300 RPM) or low rotation speed (900 RPM) during the FSW process resulted in defects such as hot cracking and groove defects as shown in Figure 4.3. This is because the amount of frictional heat generation that drives the FSW process is mainly dependent on the tool rotation speed [23]. The low rotation speed (900 RPM) has failed to generate sufficient friction heat between the FSW tool and the base materials, hence the stirring action was not sufficient to transport the materials effectively from the AS to RS which leads to defects.

ii) To successfully weld a material using the FSW process, it is necessary for the material to flow at elevated temperatures. Flow stress as a function of temperature can be used to determine the flow characteristics of a material [5]. In general, the flow stress drops more rapidly with an increasing temperature. Thus a very high spindle speed (1300 RPM) creates an excessive amount of frictional heat and severe plastic deformation which can detach large Cu particles from the base materials. However, the detached particles were not fully consolidated to form the joint and resulted in defects such as hot cracking and voids, as shown in Figure 4.3b [73]. An externally defect-free FSW (Cu-Cu) joint as shown in Figure 4.6b was manufactured using the optimised process parameters as follows: Welding Speed: 30 mm/min, Tool Rotation speed: 1200 RPM and the FSW tool was plunged on the butt line.

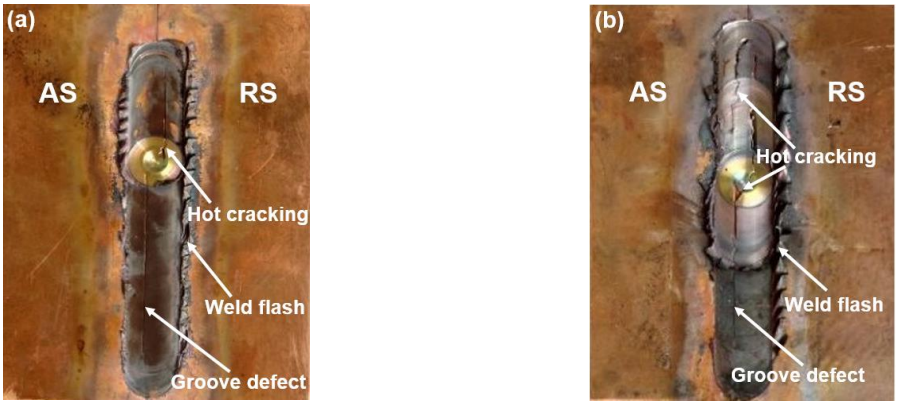

Figure 4.3 Manufactured FSW (Cu-Cu) joints using different process parameters: (a) Rotation speed: 900 RPM and Traverse speed: 40 mm/min; (b) Rotation speed: 1300 RPM and Traverse speed: 40 mm/min

4.3.3 FSW (Cu-SS)

i) When the FSW process is performed by offsetting the tool towards the copper and also positioning the Cu and SS on the AS and RS respectively results in major defects such as porosity and groove defects (Figure 4.4a). This is because the high frictional heat generated on the AS of the FSW process causes the low melting point material (Cu) to melt locally [5, 54]. This phase transformation from the solid-state to the liquid-state of the copper then loses effective frictional contact with the tool, and the dissimilar material was not effectively stirred across the weld interface. Ensuring the position of the lower temperature base material is towards the RS is a key controlling factor in manufacturing a defect-free FSW (Cu-SS) joint.

ii) The FSW process performed after pre-heating the Cu base material and positioning the Cu and SS on the RS and AS respectively has effectively controlled the scale of defects as shown in Figure 4.4b compared to Figure 4.4a. As copper is a very high thermal conductivity material, it can dissipate heat several times faster than the stainless steel. Hence, pre-heating the copper base material to 150-200^{o}C before the welding process can minimise the heat dissipation rate of the copper and facilitate the stirring mechanism of the FSW process. This together with ensuring the higher melting point material (SS) is on the AS are considered as the major influencing FSW process-parameters in the FSW of Cu and SS. However, the impact of traditional FSW process parameters such as tool rotation speed, traverse speed and tool axial force in the quality of the FSW (Cu-SS) joint were also assessed. The external defect-free FSW (Cu-SS) joint shown in Figure 4.6c was manufactured using the process parameters as follows: Welding Speed:

35 mm/min, Tool Rotation speed: 1200 RPM, Tool offset: 0.2 mm towards copper, AS: Stainless steel and RS: Copper.

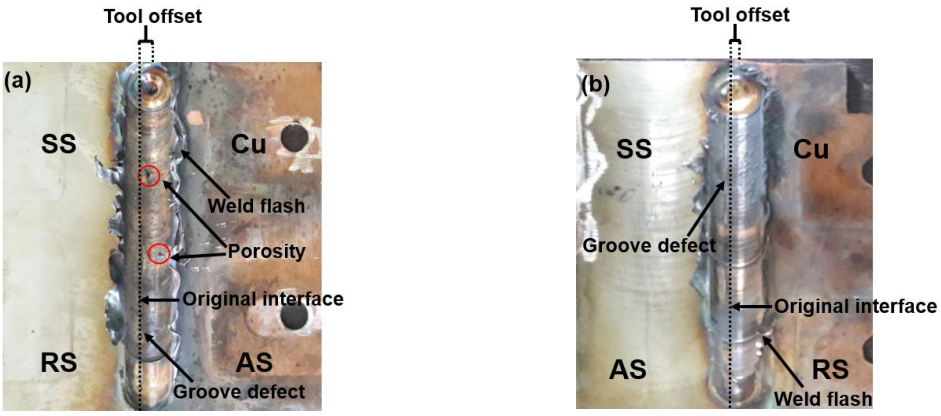

Figure 4.4 Manufactured FSW (Cu-SS) joints using different process parameters: (a) Without pre-heating the Cu and also Cu and SS were on the AS and RS respectively; (b) Without pre-heating the Cu and also Cu and SS were on the RS and AS respectively

Table 4.4 The selection of FSW Process parameters

Process Parameters	**FSW (Cu-SS)**	**FSW (SS-SS)**	**FSW (Cu-Cu)**
Tool rotation speed (RPM)	1200	441	1200
Tool traverse speed (mm/min)	35	118	30
Advancing side	Stainless steel	Stainless steel	Copper
Retreating side	Copper	Stainless steel	Copper
Tool offset (mm)	0.2 (Cu)	-	-
Shoulder diameter (mm)	20	17.5	13.5
Pin major diameter (mm)	9	8	3.5
Pin minor diameter (mm)	3	5	2
Pin length (mm)	1.8	1.8	1.8

In a typical FSW process, the magnitude of rotation of the tool (R_V) and feed (F_V) velocities are the same. This means that in the AS and RS regions the velocities act in the opposite direction as clearly illustrated in the figure shown below.

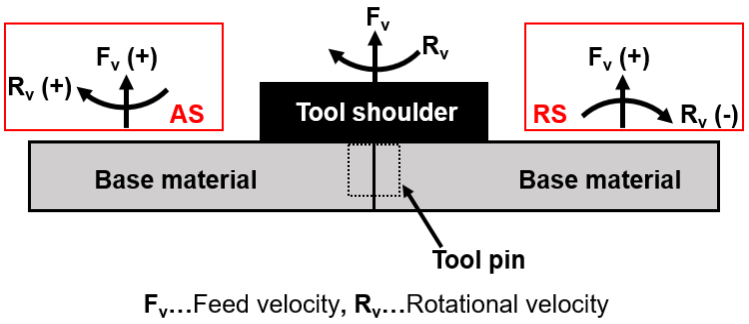

Figure 4.5 A schematic representation of FSW process alongside with the direction of Feed (F_v) and Rotational velocities (R_v) along the AS and RS

From the above figure, the total velocity of the FSW tool along the AS and RS can be calculated as follows:

Total velocity of the FSW tool (AS) = FV + RV…..4.1

Total velocity of the FSW tool (RS) = FV - RV…...4.2

From equation 4.1 and 4.2, it is determined that the total velocity of the FSW tool along the AS is comparatively higher than the RS as both the velocities are acting in the same direction. Therefore, the AS usually achieves larger frictional heat and increased plastic deformation compared to the RS and this will generate distinct microstructural features as well as variable material flow along the AS and RS [74]. The above statement has been added to Page 68 in Chapter 4.

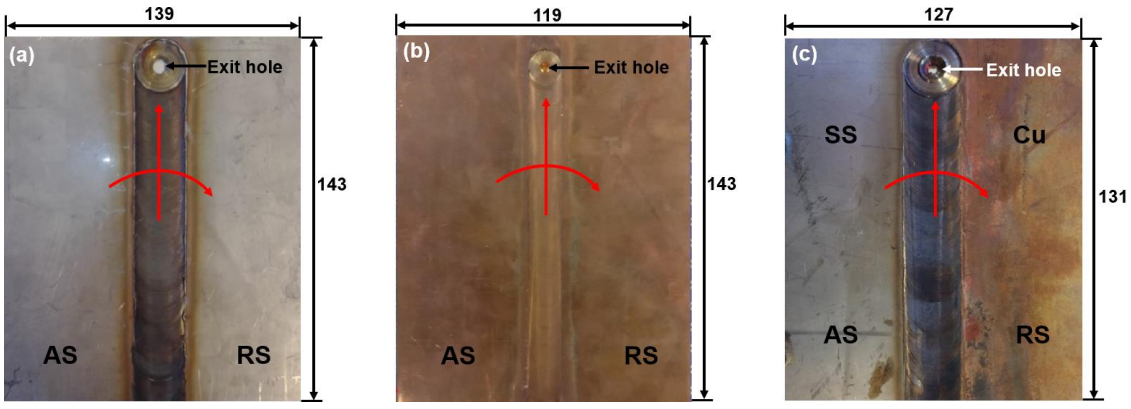

All dimensions are in mm
Tolerance: ± 0.2 mm

Figure 4.6 FSW joints manufactured using the optimised process parameters: (a) FSW (SS-SS) joint; (b) FSW (Cu-Cu) joint; (c) FSW (Cu-SS) joint

4.4 Test specimen preparation and arrangements for HR-DIC measurements

For HR-DIC measurements, the FSW (SS-SS, Cu-Cu, Cu-SS) transverse tensile specimens (length perpendicular to the welding direction) were produced by water jet cutting to the dimensions shown in Figure 4.7. Figure 4.8 presents a schematic representation of the ASTM: E8/E8M-16a [75] standard sub-size tensile specimen with dimensions. It is important to note that the dimensions of the FSW tensile specimens adopted in this investigation are not entirely aligned with the ASTM: E8/E8M-16a [75] standard sub-size tensile specimen as summarised in Table 4.5. This is because of various limitations involved in the dimensions of the manufactured FSW sheets. It should be noted that in order to conduct the DIC it was necessary to maximise the region of interest for the DIC and hence making specimens of a more compact nature that would avoid the in-plane bending would not be practical.

As the specimens have to be of the geometry given in Figure 4.6 results in some limitations when mounting the specimen in the test machine. Small misalignments will cause both in-plane and out of plane bending to the specimen and great care is required to mount the specimen directly in the machine grips. It should also be noted that the use of a universal joint is not possible as this would require drilling of a hole in the specimen and possibly lead to premature failure. Therefore the only option is to mount the tensile specimen in the grips of the servo-hydraulic test machine. The Instron 8501 test machine used in this work has a fixture that allows for accurate alignment of the grips hence out of plane bending due to grip misalignment was minimised. However, it is still possible to cause in-plane bending by gripping the specimen at an angle to the line of action of the applied load. This is dependent on the operator and although an inclinometer was used to monitor this some small misalignment is inevitable either from mounting the specimen, uneven gripping across the width of the specimen even though hydraulic grips were used and possible misalignment of the actuator. Hence a consideration of the effect of misalignment with the line of action of the applied load is necessary.

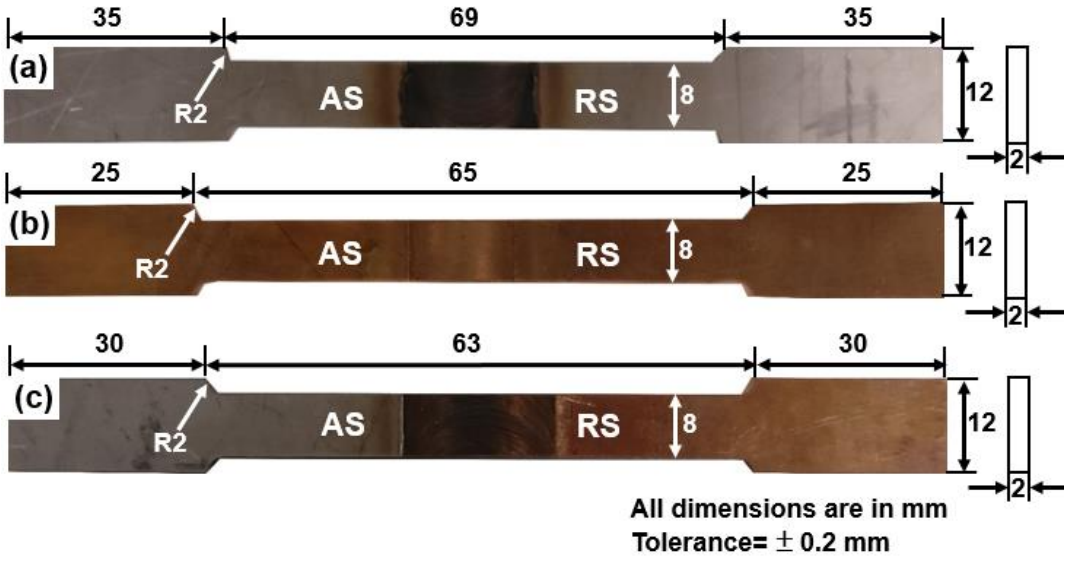

Figure 4.7 Water jet machined transverse FSW tensile specimens: (a) FSW (SS-SS) specimen; (b) FSW (Cu-Cu) specimen; (c) FSW (Cu-SS) specimen

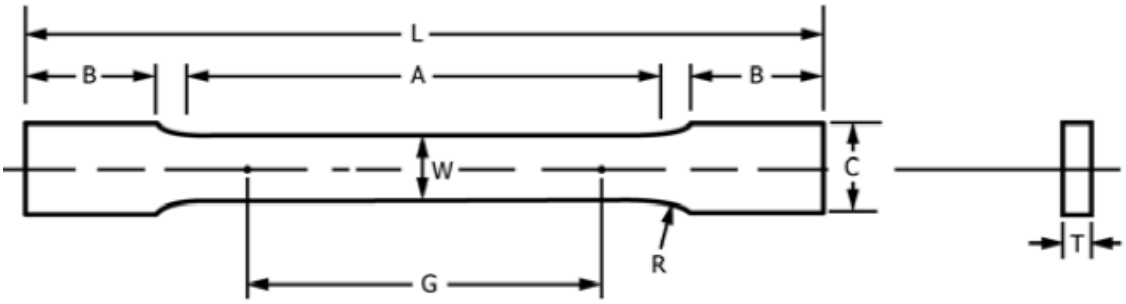

G…Gauge length = **25 ± 0.1 mm**
W…Width = **6.0 ± 0.1 mm**
T…Thickness = **Thickness of test specimen (mm)**
R…Radius of fillet= **6 mm (minimum)**
L…Overall length of specimen = **100 mm (minimum)**
A…Length of reduced parallel section = **32 mm (minimum)**
B…Length of grip section = **30 mm (minimum)**
C…Width of grip section = **10 mm (approx)**

Figure 4.8 Schematic representation of the ASTM E8/E8M-16a standard sub-size tensile specimen with recommended dimensions [75]

Table 4.5 Comparison of ASTM E8/E8M-16a standard sub-size tensile specimen dimension with the FSW specimens used in the investigation

Specimen dimension (mm)	ASTM E8/E8M-16a standard sub-size tensile specimen (mm)	FSW (SS-SS) tensile specimen (mm)	FSW (Cu-Cu) tensile specimen (mm)	FSW (Cu-SS) tensile specimen (mm)
W	6.0 ± 0.1	8	8	8
T	Thickness of material	2	2	2
R	6 (min)	2	2	2
L	100 (min)	139	115	123
A	32(min)	65	61	59
B	30 (min)	35	25	30
C	10 (approx)	12	12	12

As the FSW (SS-SS, Cu-Cu, and Cu-SS) tensile specimens have a small cross-section of 8 x 2 mm as well as reduced thickness across the weld nugget, and are relatively long, a minor misalignment will produce in-plane bending. This may lead to a substantial parasitic strains in HR-DIC measurements as a result of additional bending stresses caused by the misalignment. To assess the impact of in-plane bending by specimen rotation, a set-up, as shown in Figure 4.9a is considered. Figure 4.9b shows the free body diagram of Figure 4.9a under equilibrium condition.

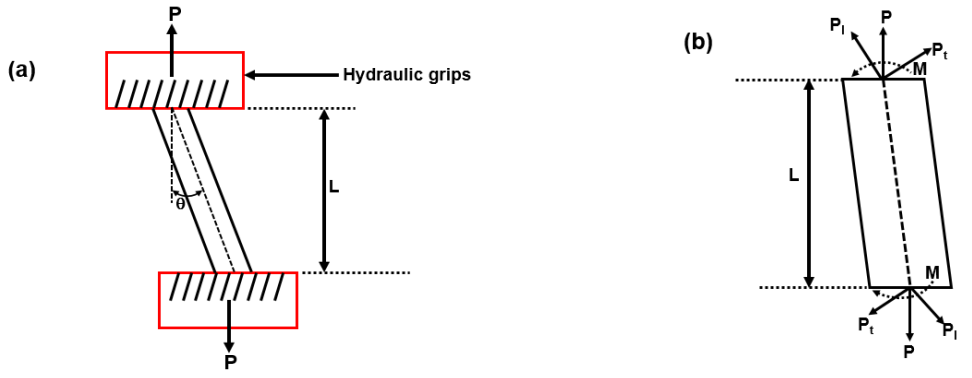

Figure 4.9 (a) Schematic representation of In-plane bending caused by specimen rotation in the test machine grips; (b) Free body diagram with respect to (a) under equilibrium condition

From the free body diagram, the load (P) resultant can be resolved along the longitudinal (P_l) and transverse (P_t) direction as follows:

$$cos\theta = \frac{P_l}{P} \qquad P_l = Pcos\theta \qquad (4.1)$$

$$sin\theta = \frac{P_t}{P} \qquad P_t = Psin\theta \qquad (4.2)$$

where θ is the angle of the specimen to the line of action of the load. The transverse load (P_t) causes a fixing moment to be developed at each end of the specimen. This produces a constant applied moment (M) on the specimen is:

$$M = P_t l = P sin\theta l \qquad (4.3)$$

where l is the distance between grips. Therefore, at the outer edges of the specimen, the stress is a combination of axial (σ_a) and bending stress (σ_b) is:

$$\sigma = \sigma_a \pm \sigma_b = \frac{P\cos\theta}{wt} \pm P\sin\theta l \frac{w}{2} \frac{12}{tw^3} \qquad (4.4)$$

The above equation can be further simplified as shown below:

$$\sigma = \sigma_a \pm \sigma_b = \frac{P\cos\theta}{wt} \pm \frac{6P\sin\theta l}{tw^2} \qquad (4.5)$$

From Equation 4.5, it is understood that the actual DIC strain measurements (as shown in Equation 4.6) on the FSW tensile specimen in the materials elastic regime will be the outcome of both axial and bending stress received by the specimen:

$$\varepsilon = \frac{\sigma}{E} \text{ (uniaxial condition)} \qquad (4.6)$$

To theoretically demonstrate the influence of bending stress due to specimen misalignment in the FSW (SS-SS) tensile specimen, Equation. 4.5 and Equation. 4.6 were used to derive the stress-strain plots, as shown in Figure 4.10 by varying the angle of misalignment (θ) from -0.5° to 0.5° at 2 kN load.

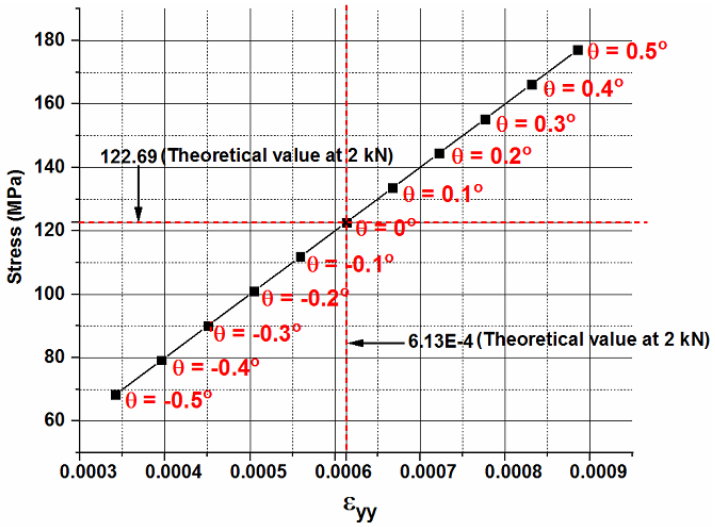

Figure 4.10 Stress-strain plots at various angle of rotation determined using Equation 4.5 and Equation 4.6 for the FSW (SS-SS) specimen at 2kN

The distance between the grips (l) is considered as 69 mm. From Figure 4.10, it is clearly understood that even a small degree of misalignment achieved by the FSW (SS-SS) tensile specimen can produce a significant parasitic strains in the HR-DIC measurements caused by the in-plane bending stresses. Therefore, a robust DIC experimental set-up incorporating cameras observing the front and back of the specimens as well as high fidelity experimental methodology are essential to achieve reliable HR-DIC measurements on thin cross-section FSW welds. The use of two cameras will allow any effect of both in-plane and out of plane bending to be observed and accounted for in the HR DIC measurements.

4.5 Summary

The selection approach adopted to weld the similar and dissimilar combinations of copper and stainless steel through FSW process is briefly discussed in this chapter. The key FSW process parameters for joining both similar and dissimilar materials were identified as welding speed and tool rotating speed. In addition to these parameters, the FSW tool offset distance, AS and RS position of dissimilar materials and also the pre-heating of high thermal conductivity material were also determined as the most important process parameters for manufacturing sound dissimilar FSW joints. Furthermore, this chapter also clearly highlighted the influence of bending stress caused by specimen misalignment during the DIC strain measurements on thin FSW tensile specimens.

Chapter 5 Materials characterisation results from the FSW (SS-SS), FSW (Cu-Cu) and FSW (Cu-SS) joints

5.1 Introduction

This chapter discusses the experimental techniques and the corresponding test specimen preparation procedures involved in performing materials characterisation on FSW (SS-SS, Cu-Cu, and Cu-SS) welds. The materials characterisation results obtained from these FSW weld combinations are briefly discussed, and future approaches for further characterisation are also proposed.

5.2 Test specimen preparation and experimental techniques

5.2.1 Microstructural Characterisation

To investigate the properties of the FSW joints at the micro scale and to correlate their microstructural characteristics with the mechanical response of the joints, several microscopy techniques were employed in this investigation. All the specimens for the microstructural examination have been prepared from the cross-section as well as the surface of the welds using the polishing routes displayed in Table 5.1. For the FSW (Cu-SS) joint, both the weld face and weld root have been considered in addition to the weld cross-section for the optical microscopy. An ASTM E3-11 standard [76] was followed for the preparation of metallographic specimens. The following stages were involved in the preparation of metallographic specimens: i) Cutting of metallographic specimens, ii) Mounting of specimens, iii) Grinding and polishing, and iv) Chemical etching. All the metallography specimens were characterised using a range of microscopy techniques as follows: i) Optical Microscopy (OM), ii) Scanning Electron Microscopy (SEM- under SEI and BSE), iii) SEM-EDS (Energy Dispersive Spectroscopy), and iv) EBSD- Electron Back Scattered Diffraction.

5.2.1.1 Cutting of Metallographic Specimens

An abrasive cut-off wheel (Al_2O_3) was used to slice the FSW (Cu-SS), FSW (SS-SS) and FSW (Cu-Cu) joints along the transverse direction of the weld in a precision cutting machine (Make: Presi, Model: Mecatome T210). The spindle speed and feed rate were maintained at 3000 RPM and 0.1 mm/s, respectively. During the cutting operation, an appropriate cutting fluid (oil + water emulsion) was supplied as a coolant to reduce the heat generation on the cutting surface and also to minimise the microstructural changes in the materials.

Table 5.1 Polishing routes for the FSW(SS-SS), FSW (Cu-Cu), and FSW (Cu-SS) Specimens

Steps	Polishing Cloth	Abrasive	Lubricant	Polishing grinder speed (RPM)	Time duration
1	-	SiC-800 grit	Water	300	2 min
2	-	SiC-1200 grit	Water	300	2 min
3	MD-Mol*	DP-Paste* 6µm	Blue	150	15 min
4	MD-Mol*	3µm**	Diamond Suspension	150	15 min
5	MD-Nap*	DP-Paste* 1µm	Blue*	150	15 min

5.2.1.2 Mounting of Specimens

Sliced specimens were treated with ethanol and distilled water to eliminate surface contaminants and then dried with a hair dryer. For mounting, a hot compression versatile hydraulic press (Make: Buehler, Model: Simplimet 2000) loaded with a conductive Bakelite powder called KonductoMet (a conductive phenolic compound exclusively for SEM characterization) was used. The process parameters utilised for the hot mounting were: Temperature=180^{o}C, Pressure= 5 bar for the duration of 4 min, and a cooling time of 5 min. As both copper (Melting point: 1050^{o}C) and stainless steel (Melting point: 1400^{o}-1455^{o}C) are considered as high-temperature materials, it is strongly believed that the temperature and time involved during the compression moulding process will not significantly alter the microstructures of the base materials.

5.2.1.3 Grinding and Polishing

Mounted specimens were ground in turn on 800, 1200, and 4000 silicon carbide abrasive papers with water as a lubricant in the polishing grinder machine (Make: Struers, Model: Tegrapol-15). At the end of each grinding stage, all the ground specimens were rinsed with the distilled water followed by ethanol and dried with a hair dryer. For the FSW (Cu-SS) joint, appropriate common polishing routes needed to be defined for both copper and stainless steel to get an adequate polish across the dissimilar weld nugget. By a lengthy trial and error method and using the Struers Metalog guide [77] as a guidance, the polishing routes were defined for the FSW (Cu-SS) specimens, as shown in Table 5.1. These same polishing routes were used for the FSW (SS-SS), and the FSW (Cu-Cu) specimens and a fine quality polish (mirror finish) was achieved in all these specimens. Mounted specimens were polished manually without using the automatic features of the Tegrapol-15 to carefully control the force acting on the surface of the specimens during the polishing stage.

5.2.1.4 Chemical etching

An ASTM E407-07 standard [78] was followed to etch the FSW (Cu-SS), FSW (SS-SS), and FSW (Cu-Cu) specimens. For the FSW (Cu-SS) specimens, the etching was attempted with different chemical solutions such as Aqua Regia (20 ml HNO_3 + 60 ml HCL), Glyceregia (10 ml HNO_3 + 20-50 ml HCL + 30 ml glycerol) for 10 sec in the certified fume hood and these resulted in non-uniform etching. This is because both the copper and stainless steel have somewhat different etching rates in these chemical solutions, with the copper etching faster than the stainless steel and resulting in non-uniform etching. So an appropriate etchant was needed that would etch both copper and stainless steel in a dissimilar weld at the same etching rate. To achieve this, a solution of 20 ml $FeCl_3$ mixed with 20 ml HCL (ASTM E407-07 Etchant No: 36) was prepared in a petri dish, and the specimen was immersed for 10 sec followed by rinsing with the ethanol and distilled water and finally dried with a hair dryer. This allowed good optical and SEM analysis along the cross-sections of the FSW (Cu-SS) and FSW (SS-SS) specimens. To etch the FSW (Cu-Cu) specimens, Aqua Regia (ASTM E407-07 Etchant No: 12) was used.

5.2.1.5 Specimen preparation for the EBSD characterisation

EBSD is a surface-sensitive characterisation technique where the diffracted electrons escape from within a few nanometers depth from the crystal lattice during the EBSD analysis [79]. Thus the specimen surface should be as free as possible from deformation, oxide layers, and other surface contaminants. The specimen preparation is the critical challenging element to achieve a strong Kikuchi pattern and high indexing rates during the EBSD analysis. In contrast to the aforementioned polishing routes, a slightly different polishing route has been followed in preparing the specimens for the EBSD analysis as shown in Table 5.2. To eliminate any remaining deformation acquired from the polishing stages and also to achieve a slight etching, all the EBSD specimens were finally polished with a 0.04 µm colloidal silica solution for 90 minutes. As the freshly prepared specimen surface suffered some subsequent oxidisation in ambient environmental conditions, the final polished EBSD specimen was immediately examined in the SEM to perform the EBSD analysis.

5.2.1.6 Microscopy

To observe the macrostructure of the etched specimens, a stereo zoom microscope (Make: Nikon macroscope, Model: M420) under a low magnification of 25x was utilized to reveal the width and depth of the welded region. An optical microscope (Make: Olympus, Model: BX51) integrated with an image analyzing software (stream essentials) was used at magnifications from 50x to 200x to observe the microstructural features at various locations of the friction stir welded specimens. In addition to the weld cross-section, both the front (WF) and rear face (WR) of the weld regions were also considered for microstructural characterisations. All the macrographs and optical micrographs captured in the same magnification were stitched in sequential order using Fiji/ImageJ software to

accommodate all the weld sub-regions (BM, HAZ, TMAZ, and WN) in the final stitched macrographs/micrographs. For more detailed microstructural characterisation, the Field-emission gun scanning electron microscope (FEG-SEM) (Make: JEOL, Model: 6500F) was used at different magnifications in Secondary and Backscattered electron mode (SEI and BEI). This SEM characterization has provided high spatial resolution micrographs (SEI) and compositional contrast (BEI) information from various sub-regions of the welded samples. An Energy Dispersive X-ray Spectroscopy (EDS) integrated with the SEM was used to map the elemental composition distributed in the vicinity of welds. However, the above-mentioned characterisation techniques have not been able to reveal the ultrafine grains in the weld nugget and also the apparent boundary between TMAZ and the weld nugget [80]. Therefore, the SEM was also operated in an Electron Back Scattered Diffraction (EBSD) mode to analyse the grain orientations at a high spatial resolution across the weld nugget. An EBSD (HKL Nordlys Detector with HKL channel 5 Flamenco software) characterisation was carried out at an accelerating voltage of 20 kV, Probe current of 17 nA, 15 mm working distance to measure the grain size as well as their relative orientations. For the EBSD analysis, the sample was tilted at 60^{o} to receive the diffracted electrons emitted from the crystal lattices and to record these diffraction patterns through the EBSD detector.

Table 5.2 Polishing routes for the FSW(SS-SS), FSW (Cu-Cu), and FSW (Cu-SS) EBSD Specimens

Steps	**Polishing Cloth**	**Abrasive**	**Lubricant**	**Polishing grinder speed (RPM)**	**Time duration**
1	-	SiC-800 grit	Water	300	2 min
2	-	SiC-1200 grit	Water	300	2 min
3	MD-Mol*	DP-Paste* 6µm	Blue	150	20 min
4	MD-Mol*	3µm**	Diamond Suspension	150	20 min
5	MD-Nap*	DP-Paste* 1µm	Blue*	150	15 min
6	MD-Nap*	OPUS Non-crystalline colloidal silica*** 0.04 µm	-	150	90 min

*Polishing consumables (SiC, MD-Mol, MD-Nap, DP-Paste) of various grades and blue lubricant as supplied by Struers Inc [77]
**Polishing consumable (3µm-diamond suspension) supplied by Buehler Inc [81]
***Polishing consumable (OPUS 0.04 µm) supplied by Metprep Inc

An FSW weld nugget was reported to contain ultrafine recrystallized grains due to the extensive plastic deformation, and the average grain size of those recrystallized grains could be less than 1 µm [80]. To resolve those fine grains, a range of step-sizes such as 0.25, 0.5, and 1 µm were used to achieve the best spatial resolution during the EBSD analysis. All the EBSD scanned datasets were post-processed by the Tango Map software for further quantitative analysis such as grain misorientation distributions, and the proportion of High Angle Grain boundaries (HABs) and Low Angle Grain Boundaries (LABs).

5.2.2 Microhardness measurements

Microhardness distribution across the FSW weld sub-regions was measured to establish a relationship between microhardness variations in various weld sub-regions with their corresponding microstructural characteristics. The microhardness variations were measured across the cross-section of the weld in the fine polished specimen using a digital microhardness tester (Make: Future tech, Model: FM-300). All the indents were placed at a load of 50 g with a dwell time of 15 sec. Before placing the indents, the surface of the polished specimen was cleaned with acetone to degrease the surface. Furthermore, the microhardness equipment was calibrated by placing the indent at a load of 500 g with a dwell time of 15 sec on the calibration plate, and the average hardness values obtained from this calibration test were correlated with the known standard values. ASTM E384-17 [82] standard was followed while preparing the weld specimens for microhardness measurements. As the weld nugget of the FSW (Cu-SS) contains a considerable amount of copper and stainless steel due to the stirring action of the FSW tool, a wide fluctuation in the hardness values is expected in the weld nugget. To accurately map these hardness variations, a specific region in the specimen that covers all the weld zones was screened for indentation. An indentation experiment matrix of dimensions (5 x 60), (5 x 80), (5 x 150) was defined for the placement of the indents in the FSW (Cu-SS), FSW (SS-SS) and FSW (Cu-Cu) weld specimens respectively. The distance maintained between each indent in both row and column directions was 0.1 mm. This value was determined as per the ASTM standard by calculating the average diagonal length of a group of indents (d), and therefore the distance between the indents was maintained at greater than 2.5d by choosing this consistent spacing. All the microhardness values recorded in the excel sheet were imported through Origin 2017 graphical software to map the hardness values in a 2D contour plot. Additionally, the indents positioned on the weld nugget and weld interfaces were also observed by OM at a high magnification (200x) to examine the hardness gradients (based on the indent sizes) in these locations.

5.3 Materials characterisation results

Figure 5.1 shows the schematic representation for extracting the specimens from the FSW (SS-SS, Cu-Cu, and Cu-SS) joints for various microscopy techniques and microhardness measurements. The key results obtained from these techniques are presented in the following sections.

5.3.1 FSW (SS-SS)

5.3.1.1 Optical macro/micrographs

Optical micrographs correspond to the locations such as the weld cross-section and weld face of the FSW (SS-SS) joint are displayed in Figure 5.2 and Figure 5.3, respectively. Figure 5.2a shows the

macrograph of the FSW (SS-SS) weld cross-section with the weld sub-regions located along the advancing and retreating sides.

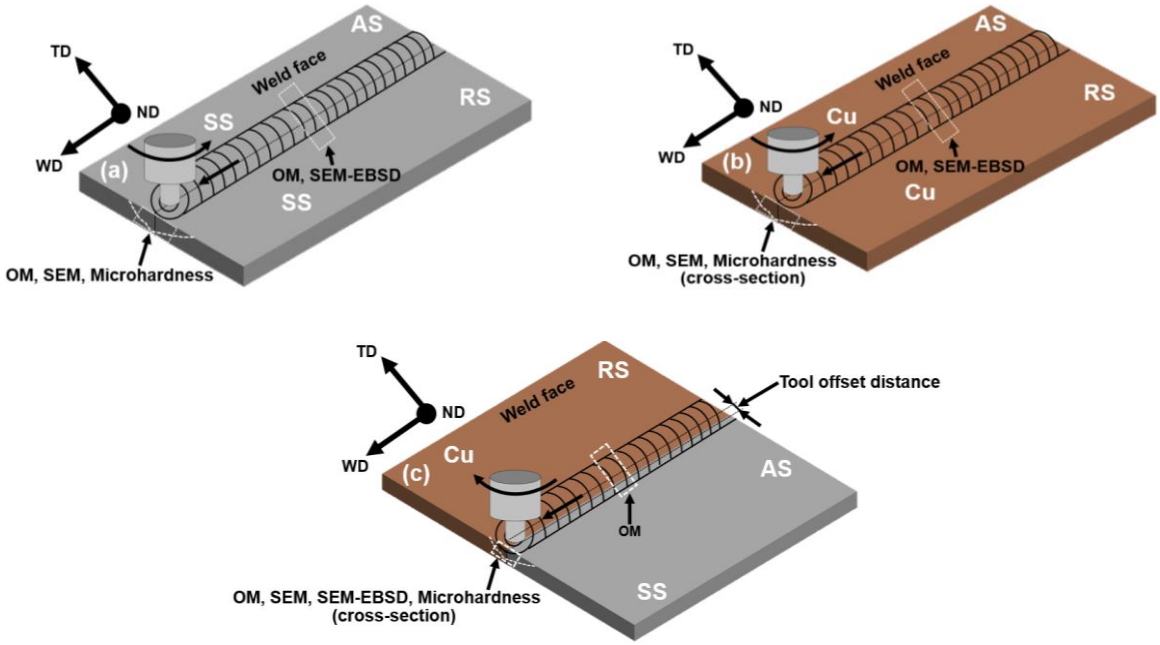

Figure 5.1 Schematic representation for extracting the specimens for various material characterisations (AS-Advancing side; RS-Retreating side): a) FSW (SS-SS) joint; b) FSW (Cu-Cu) joint; c) FSW (Cu-SS) joint

Figure 5.2b shows the sequentially stitched optical micrographs correspond to the location shown in Figure 5.2a. From both Figure 5.2 and Figure 5.3, it can be observed that the weld nugget (both surface and cross-section) does not have any major observable surface defects such as cracks, pores, or incomplete penetration. Base metal (BM) exhibits typical coarse austenite grains with annealing twins. Due to the reduced heat input and high cooling rate of the FSW process [3], the narrow HAZ of the FSW weld located between the TMAZ and BM regions is not clearly observed in the optical micrographs. Because of this, both the HAZ and BM sub-regions together are considered as the HAZ/BM in all the optical micrographs. Figure 5.2b reveals the weld nugget in the form of intercalated plastic flow of the material generally called as onion rings [83] in the FSW terminology. This standard onion ring pattern has been considered as a common feature of a typical FSW weld, and the shape of the weld nugget is usually in line with the FSW tool geometry as well as the FSW process parameters [84]. Figure 5.2b also represents the direction of plastic material flow, where the material flow is from the AS to RS. It is noteworthy that the fine grains (Figure 5.2b) distributed on the tool shoulder affected region are much coarser than the grains located on the weld nugget.

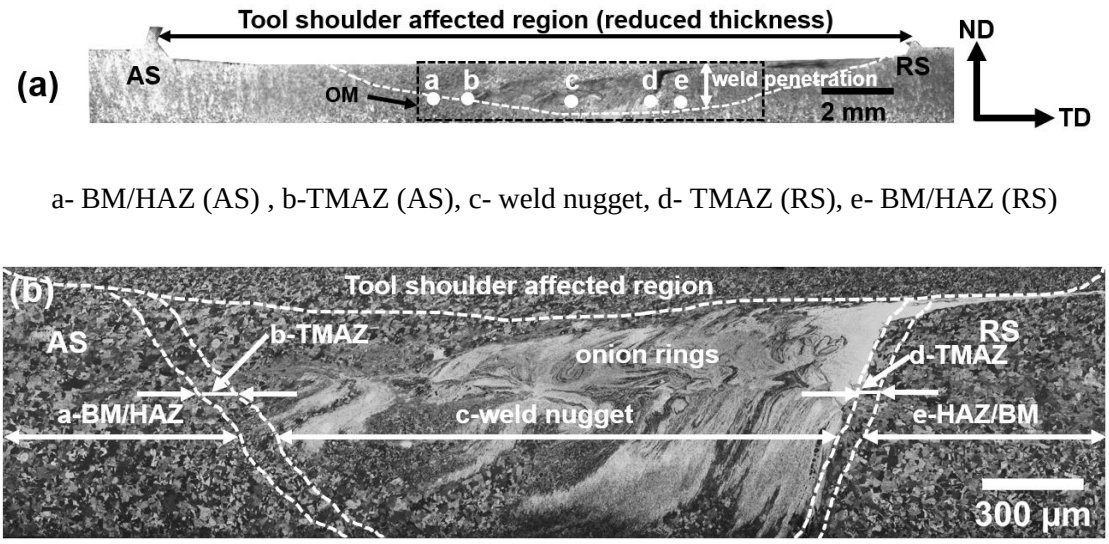

a- BM/HAZ (AS) , b-TMAZ (AS), c- weld nugget, d- TMAZ (RS), e- BM/HAZ (RS)

Figure 5.2 Optical microscopy observations on the FSW (SS-SS) weld cross-section: (a) Low magnification macrograph with the locations marked for optical microscopy; (b) Sequentially stitched optical micrographs correspond to the locations shown in (a)

Both Figure 5.3b and Figure 5.3c show the sharp interface between the weld nugget and TMAZ regions. In these figures, both the TMAZ regions (AS and RS) have a mixture of deformed elongated grains along the welding direction as well as partially recrystallized fine grains. However, the TMAZ located on the RS has a larger proportion of recrystallized fine grains compared to the TMAZ-AS. The FSW weld nugget is completely populated with the ultrafine recrystallized grains due to the dynamic recrystallization (DRX) mechanism offered by the frictional heat and intense plastic deformation effects associated with the FSW. This proves that both the TMAZ regions (along both the AS and RS) have only partially experienced the DRX process due to the lack of frictional heat and plastic deformation. In contrast to the microstructural features observed on the weld face, there is no obvious TMAZ with elongated and deformed grains located along the weld cross-section. This is due to the high degree of grain refinement produced at the TMAZ/weld nugget interface of the weld cross-section alongside with the limitations involved in the resolution and magnification range of an optical microscopy. In addition to this, the TMAZ/weld nugget interface also possesses a wide range of grains, and therefore the distinct TMAZ cannot be classified accurately. Thus, both TMAZ locations (along AS and RS) are approximated on the outer boundary of the weld nugget, as shown in Figure 5.2b. From the optical micrographs (Figure 5.2 and Figure 5.3), it is clear that both the weld face and cross-section of the FSW (SS-SS) have significantly different grain morphologies developed during the FSW process.

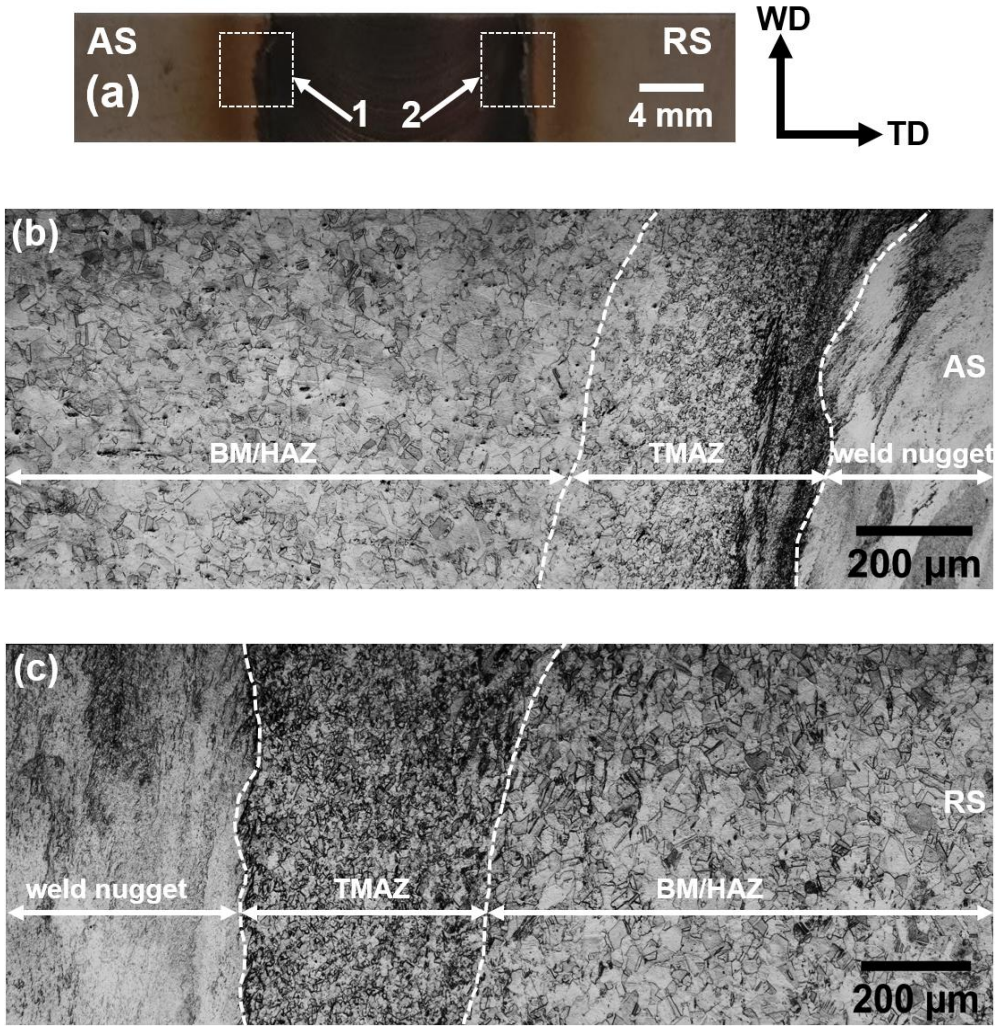

Figure 5.3 Optical microscopy observations on the FSW (SS-SS) weld face: (a) Image shows the ROI for optical microscopy; (b) Sequentially stitched optical micrographs correspond to the location 1 shown in (a); (c) Sequentially stitched optical micrographs correspond to the location 2 shown in (a)

5.3.1.2 SEM micrographs

Figure 5.4 presents the SEM micrographs of the FSW (SS-SS) weld sub-regions observed along the weld cross-section at a higher magnification than optical micrographs. The SS-BM (Figure 5.4a) clearly shows coarse austenite grains with the average grain size of 40-50 µm. In contrast to the optical microscopy observations, the SEM micrograph of SS-HAZ (Figure 5.4b) shows a sharp difference in the grain size with the corresponding SS-BM. It appears that the SS-HAZ has achieved some grain growth, which confirms the presence of a minor heat affected zone due to the frictional heat generated from the FSW process. Figure 5.4c shows the clear interface between the weld nugget and TMAZ as well as TMAZ and HAZ regions along the RS of the weld cross-section. The plastically deformed grains located in the TMAZ have elongated along the direction of shear stress produced by the stirring effects of FSW tool. The plastic deformation caused by the FSW process severely

compressed the pre-deformed coarse grains and produces very fine recrystallized equiaxed grains in the weld nugget (Figure 5.4d). In addition to this, the dynamic recrystallization (DRX) phenomenon which is expected to have been triggered by the adsorption of dislocations by subgrain boundaries may also have facilitated the nucleation and growth of ultrafine grains in the FSW weld nugget [83]. High magnification SEM micrography of the weld nugget (Figure 5.4e) has evidenced the deformed microstructure with several networks of submicron grains in the form of thin fragments. From Figure 5.4e, it is significant to note that both the size and orientation of the microstructure networks formed by the grouping of sub-micron grains are clearly distinct due to the differences in their plastic deformation rate gained from the FSW process. It has been reported that the FSW process parameters, tool geometry, and axial force will have a significant impact on the size of recrystallized grains generated in the weld nugget [32]. As per the Hall-Petch relationship, it is expected that the grain refinement achieved in the FSW weld nugget will often enhance the weld strength. Figure 5.4f shows a series of closely spaced horizontal deformation bands in the form of the classical onion ring pattern adjacent to the weld nugget. The turbulence produced by the FSW parameters (tool rotation and welding speed) on the solid-state material leads to this intercalated material flow from the advancing to the retreating side.

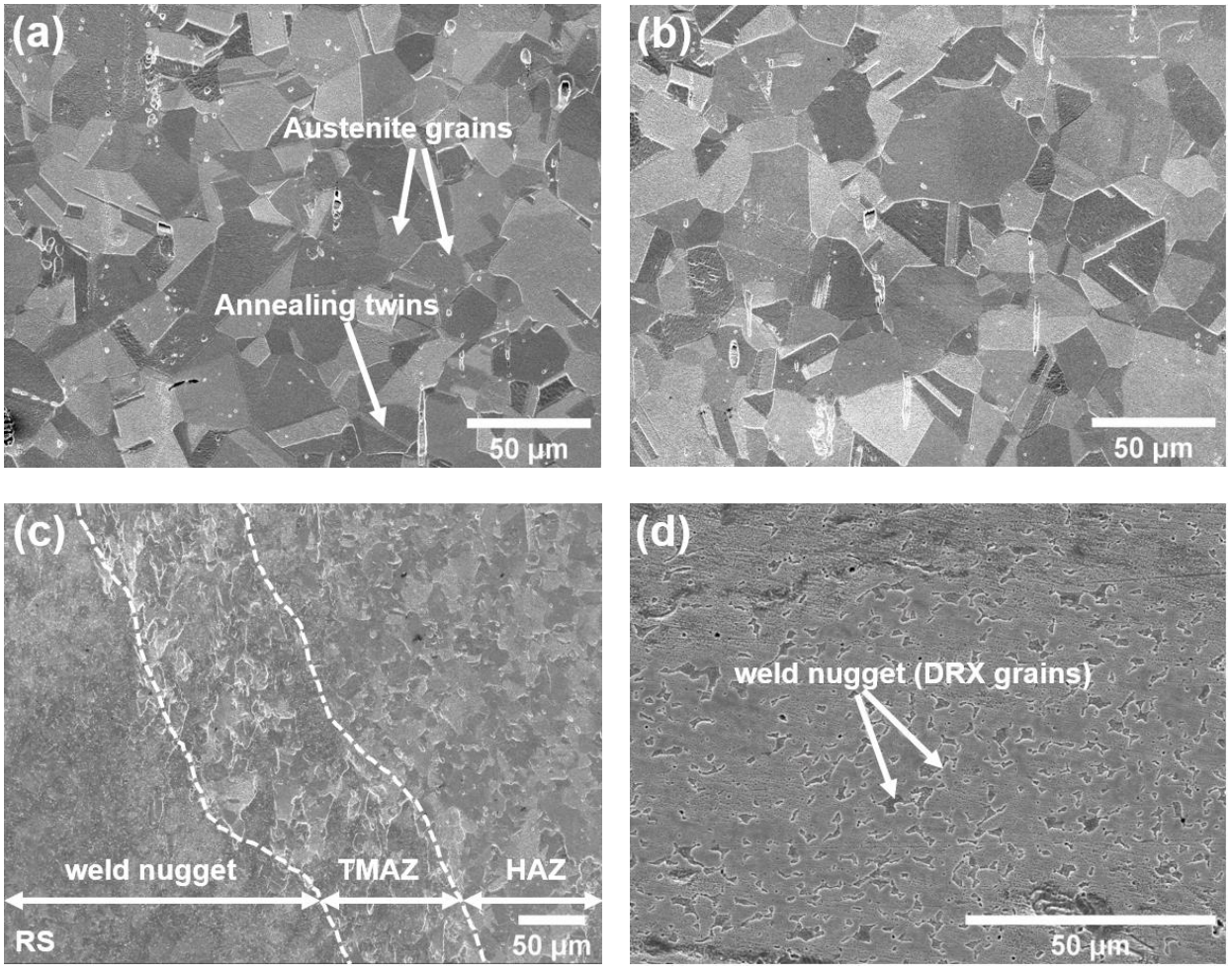

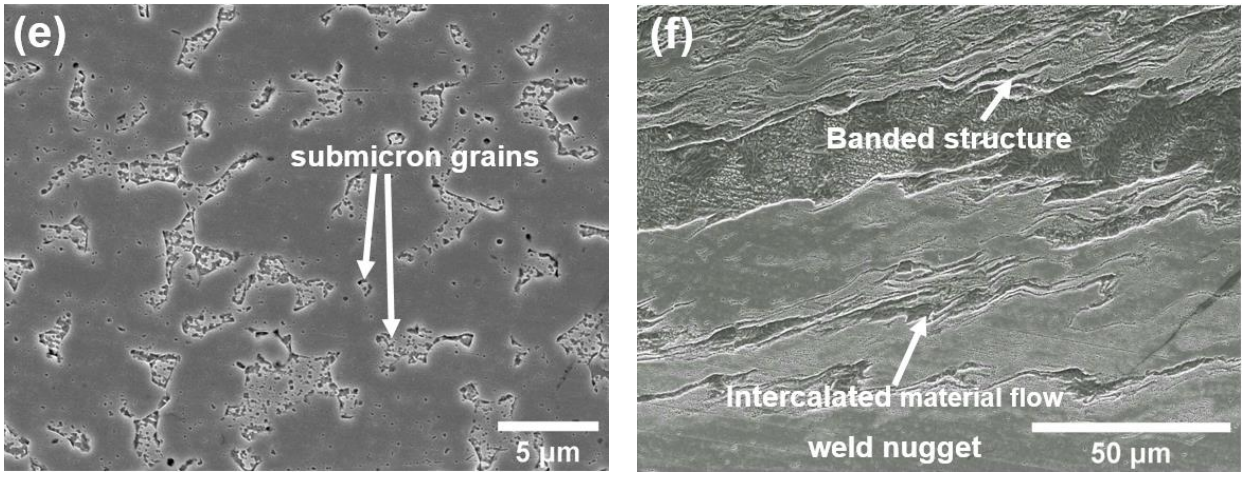

Figure 5.4 SEM Micrographs of the FSW (SS-SS) weld sub regions along cross-section: (a) SS-BM; (b) SS-HAZ; (c) Weld nugget/TMAZ/HAZ interface; (d) Weld nugget; (e) Weld nugget (at high magnification); (f) Intercalated material flow pattern

5.3.1.3 SEM-EDS micrographs

The SEM-EDS analysis on the FSW (SS-SS) weld has only considered major elements, such as Iron (Fe) and Tungsten (W) distributed on the FSW (SS-SS) weld interface. Figure 5.5a shows the SEM-BSE (backscattered electron mode) image captured at the TMAZ/weld nugget interface (weld face) with the corresponding EDS elemental maps of Fe and W represented in green and red colours respectively. SEM-BSE micrographs have revealed the heterogeneous elemental composition of the weld nugget through contrast variations mapped with respect to the atomic number of the heterogeneous elements. The backscattered electrons (BSE) are high energy electrons, which are usually produced by the elastic collisions with atoms. By Heinrich's empirical relationship [85], the intensity of high energy backscattered electron coefficient of an element is directly related to its atomic number (Z) as shown in Equation. (5.1),

$$\eta_{BSE} = 0.025 + 0.016Z - 1.86 * 10^{-4}Z^2 + 8.3 * 10^{-7}Z^3 \qquad (5.1)$$

By applying the above polynomial relationship, the BSE coefficients of Fe (Z=26) and W (Z=74) elements are calculated as 0.28 and 0.48, respectively. Due to this major difference between their BSE coefficients, a wide compositional contrast variation between the Fe and W elements is evident in all the SEM-BSE micrographs. The results obtained from the EDS horizontal line scans across the weld interface are also shown in Figure 5.5. In both line scans (Figure 5.5a and Figure 5.5b), a sharp increase in the tungsten level is evident across the weld nugget. From the EDS maps of the weld face (Figure 5.5a), it is noticed that the Fe is well mixed throughout the weld nugget; but tungsten distribution is highly concentrated only in the weld nugget. This dense population of tungsten present in the weld nugget is likely to be due to tool wear. The FSW tool material used in this study was manufactured from the tungsten-1% lanthanum alloy material; therefore, it is clear that tungsten particles removed from the tool material were deposited in the weld nugget during the FSW process.

The scattered tungsten particles worn from the tool due to the high strain rates experienced during FSW were diffused into the weld nugget during the stirring action of the FSW process. Thus the whole weld nugget contains a mixture of both Fe and W elements. It is also noticeable that the distribution of tungsten is very consistent within the weld nugget region where the influence of the tool was most pronounced. A similar observation is also evidenced along the weld cross-section (Figure 5.5b), where tungsten is clearly spotted only in the weld nugget (onion ring pattern). By correlating the SEM-BSE micrographs of weld face (Figure 5.5a) and weld cross-section (Figure 5.5b), the weld cross-section shows much better contrast where the weld nugget appears much brighter than the other weld sub-regions. This indicates that the weld cross-section has a higher intensity of tungsten particles compared to the weld face due to a severe frictional impact. Tungsten has been found in the FSW weld nugget of high-temperature materials, such as stainless steels, because of their high melting point and extreme mechanical strength [47]. Additionally, the FSW process in high-temperature materials always involves high rotational speeds as well as axial force to generate sufficient frictional heat to plasticize the material in the solid-state without forming any defects [70]. Because of these reasons, the FSW tool has been subjected to considerable wear while joining high-temperature materials. It is noteworthy that Zhang et al.[36] have found in their investigation that such tool wear can be minimised by applying external water cooling agents during the FSW process. The presence of tungsten particles in the weld nugget as exposed by the SEM-EDS results may have an effect on the mechanical properties of the weld nugget region, which is discussed in more detail in the next chapter.

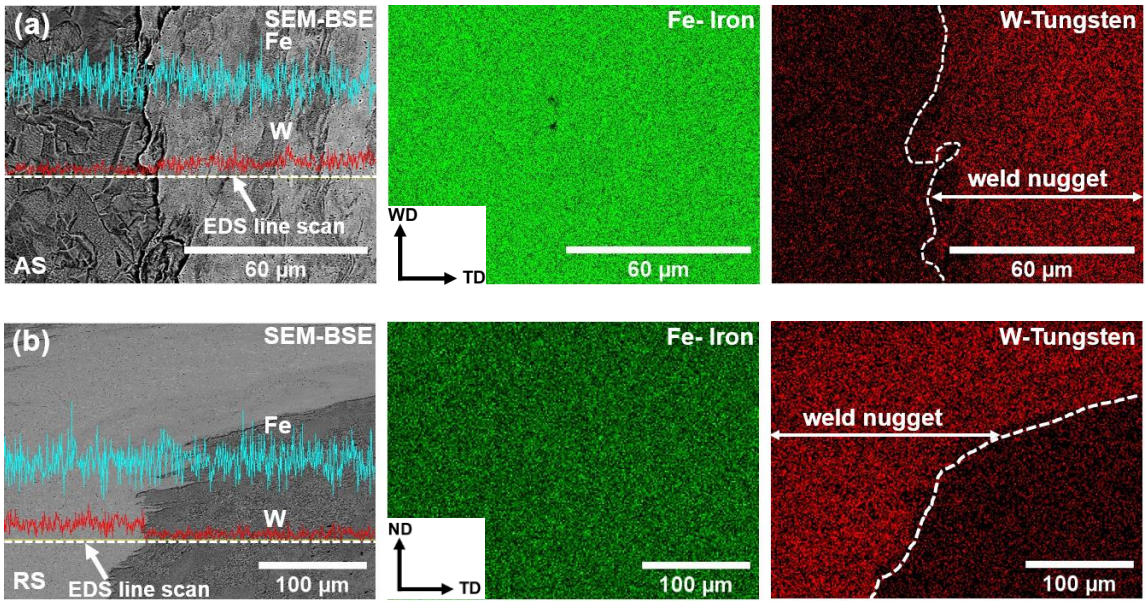

Figure 5.5 SEM-EDS line profiles/micrographs captured at TMAZ/weld nugget interface of the FSW (SS-SS) weld: (a) along the weld face; (b) along the weld cross-section

5.3.1.4 SEM-EBSD analysis

Due to the complex recrystallization process involved in a FSW, a large number of ultrafine grains will be generated in the weld nugget. From an EBSD grain orientation map, more quantitative information about the grain distribution (average grain size, grain misorientation angle, and recrystallized fraction) can be derived. Although the SEM characterisations have resolved the microstructure of the FSW (SS-SS) weld sub-regions, the grain boundaries of the sub-regions such as the weld nugget and TMAZ are not very clearly observed or easily distinguishable in the SEM micrographs. Determining the average grain size of the different weld sub-regions can therefore be challenging to measure from the SEM observations. To characterise the grain size of the FSW weld nugget and also to image the microstructural gradients in the region vicinity to the weld nugget, an EBSD characterisation was attempted with a very low step size to achieve the best resolution EBSD micrographs.

5.3.1.4.1 Grain orientations-Inverse Pole Figure (IPF)

A typical EBSD experimental setup is shown in Figure 5.6a. As the specimen is usually tilted at 70^{o} during the EBSD analysis, the specimen coordinate system (X-Rolling direction, Y- Transverse direction, and Z-Normal direction) is not always aligned with the crystal coordinate system [100], [010], [001] patterns recorded in the EBSD detector. Therefore, the EBSD post-processing software has been programmed to align these coordinate systems by several transformations usually performed through the Euler angles as shown in Figure 5.6b. Hence, the crystallographic orientation of crystals is usually represented by the EBSD component called All-Euler (AE). Euler angles (φ_1, φ, φ_2) are a set of three angles and the value of each Euler angle with respect to the plane normal is represented by a colour scale (red, green, and blue for Euler angles φ_1, φ, φ_2 respectively) as shown in Figure 5.6c. In general, similar colour Euler grains have similar orientations. As all Euler grains are coded by the mixture of RGB colour, therefore the relationship between the grain orientations cannot be inferred clearly through the AE component [79]. Because of this primary reason, the grain orientation is usually represented by its direction of the orientations with respect to the plane normal using an Inverse pole figure (IPF). Inverse pole figure (IPF) orientation components of the EBSD maps represent the direction of the grain orientations such as <100>, <110>, <111> with respect to the plane normal as schematically shown in Figure 5.7a. The rolling direction (RD) of a specimen can be assigned based on the rolling direction of the grains. Since it is not always possible to correctly assign the rolling (RD) and transverse planes (TD) of the specimen during the EBSD analysis, all the EBSD results are processed with respect to the plane normal (Z-ND). For cubic crystalline systems, grain orientations such as <100>, <110>, <111> are represented by the red, green, and blue colour coding scheme, respectively, as shown in Figure 5.7a. All the intermediate orientations of grains are then coded by the mixture of RGB colouring scheme. The main limitation of the IPF component is that the colouring of each pixel of grains is only related to the crystallographic axis and the sample

projection direction irrespective of grain misorientation about the axis as schematically shown in Figure 5.7b.

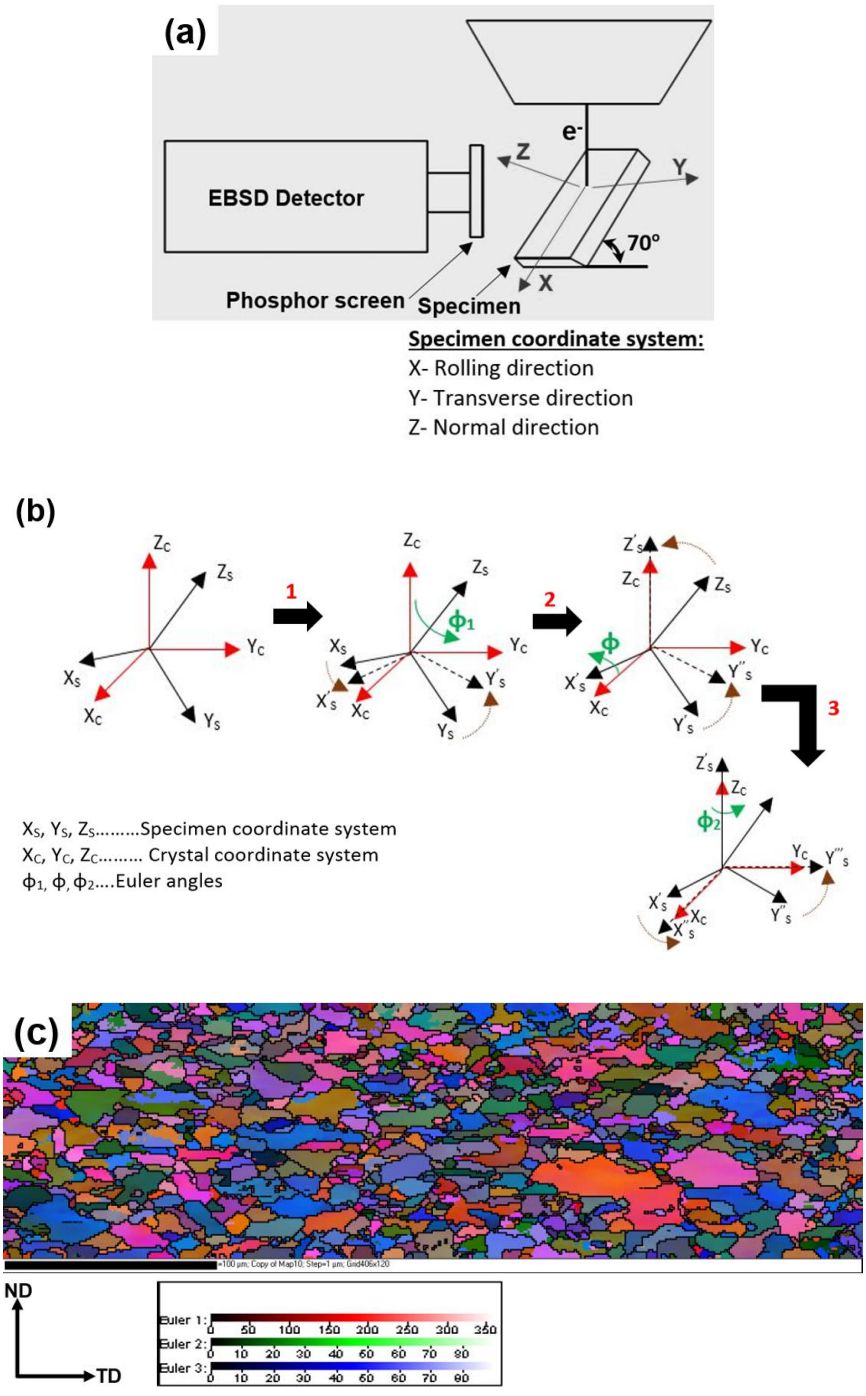

Figure 5.6 SEM-EBSD characterisation: (a) EBSD experimental set-up, (b) Euler transformations, (c) Euler grain orientation maps with respect to the plane normal

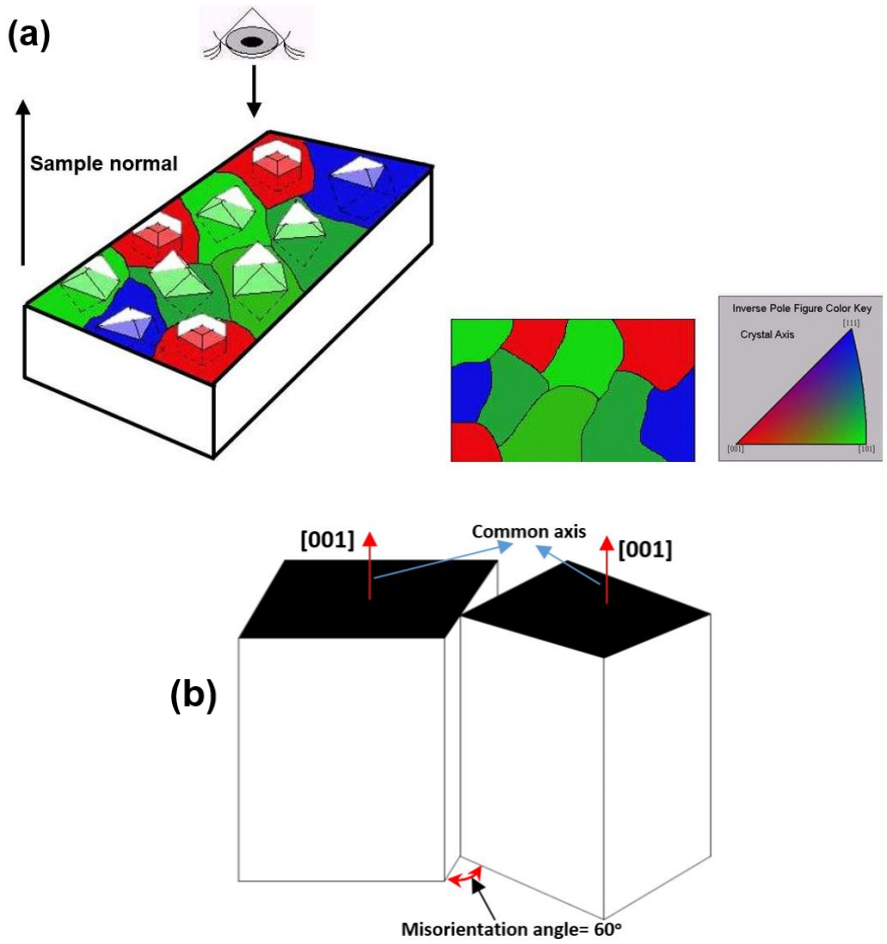

Figure 5.7 SEM-EBSD grain orientation map: (a) Schematic representation of grain orientations through IPF [86], (b) Schematic representation of misorientation between grains

5.3.1.4.2 Grain misorientations

To evaluate the grain misorientation angle from the EBSD map, a pixel to pixel misorientation angle from the grain is calculated through the EBSD post-processing software. This misorientation data was used to calculate the proportion of Low angle grain boundaries (LAGBs) and High angle grain boundaries (HAGBs) in the grain map. Generally, LAGBs are generated between a large size grain and with its corresponding interior grains (or sub-grains), but the formation of HAGBs are usually between two-grain boundaries [87]. To calculate this proportion from the EBSD scanned datasets, a cut-off angle of 2° was applied to eliminate spurious grain boundaries and to minimise the grain orientation noise in the misorientation distributions. From the statistics data obtained from the grain maps, a general misorientation criterion was applied to differentiate the low angle grain boundaries (LAGBs) from the High angle grain boundaries (HAGBs). All grains with a misorientation angle in the range of (2°-15°) were mapped as the low angle grain boundaries (LAGBs), and the remaining grains (>15°) were mapped as the high angle grain boundaries (HAGBs) [83].

5.3.1.4.3 SEM-EBSD analysis

Figure 5.8 (a, b) and Figure 5.8 (c, d) show the post-processed SEM-EBSD grain maps of the FSW (SS-SS) weld face captured on the AS and RS, respectively. Figure 5.8a and Figure 5.8c are Inverse pole figures (IPF) of the weld face along the AS and RS, respectively. From the IPF, it is observed that all the weld sub-regions (along AS and RS) have achieved more random orientations. Figure 5.8b and Figure 5.8d are band contrast grain maps plotted with low angle grain boundaries (LAGBs) and high angle grain boundaries (HAGBs). All grains with a misorientation angle in the range of (2^o-15^o) were mapped as the LAGBs (shown in white colour), and the remaining grains (>15^o-shown in red colour) were mapped as the HAGBs [41].

Figure 5.8a shows a wide range of grain distributions with a sharp spatial transition in grain size across the weld sub-regions. From the IPF, although the locations of weld sub-regions can be approximated based on their grain size, the exact boundary between the weld sub-regions cannot be resolved. Therefore, in this study, the weld sub-regions such as weld nugget, TMAZ, and HAZ are classified with a high degree of confidence based on the change in population density of LAGBs and HAGBs as displayed in Figure 5.8b. All the boundaries between the weld sub-regions as located in Figure 5.8b have a step-change in the population density of HAGBs and LAGBs as well as the change in grain size. From Figure 5.8b, it is noticed that the FSW weld nugget on the AS has equiaxed sub-micron grains with a large number of grain boundaries. In addition to this, the weld nugget has an equal proportion of HAGBs and LAGBs. In theory, these fine HAGBs located in the weld nugget will act as barriers for dislocation movements, and therefore will enable the weld nugget to achieve superior mechanical properties (higher strength and toughness). The high strain rate of the FSW process has effectively produced many dislocations within the grains in the weld nugget, which has in turn led to the growth of a high density of fine recrystallized grains. It is expected that the weld nugget will initially contain a significant number of sub-grain boundaries (misorientation<2^o) due to the intense plastic deformation. However, due to the extensive absorption of dislocations and the frictional heat, many sub-grain boundaries within the weld nugget will transform into LABs at the end of the DRX regime [37]. From the outer boundary of the weld nugget to TMAZ (Figure 5.8b), it is seen that the misorientation angles of grain boundaries are progressively increasing and turning to HAGBs. The TMAZ on the AS consists of deformed and compressed elongated grains facing towards the shear (welding) direction; all the deformed grains have large segments of HAGBs. It can be seen that the majority of LAGBs distributed in the TMAZ have not completely developed into complete grain boundaries (Figure 5.8b), which indicate that the TMAZ experienced a lower intensity of plastic deformation and did not experience sufficient thermal energy for extensive recrystallization to occur. The HAZ can be differentiated by its coarse grains and significantly higher number of HAGBs than LAGBs. It is noteworthy that the TMAZ on the AS has only a very few LAGBs than the weld nugget and the HAZ. However, the TMAZ located on the RS (Figure 5.8d) contains a high fraction of LAGBs. Additionally, the grains located in the TMAZ-RS are much

coarser than in the TMAZ-AS. It is clear that the RS has a narrow HAZ of about 40 µm compared to the AS. LAGBs and HAGBs distribution patterns for the other weld sub-regions such as weld nugget, HAZ, and BM of the RS are similar to that of the AS. Furthermore, on the RS, the population of LAGBs is steadily increasing towards the direction of the weld nugget from the BM region. The above findings confirm that both the AS and RS regions of the weld face had completely different scales of plastic deformation and frictional heat during the FSW process.

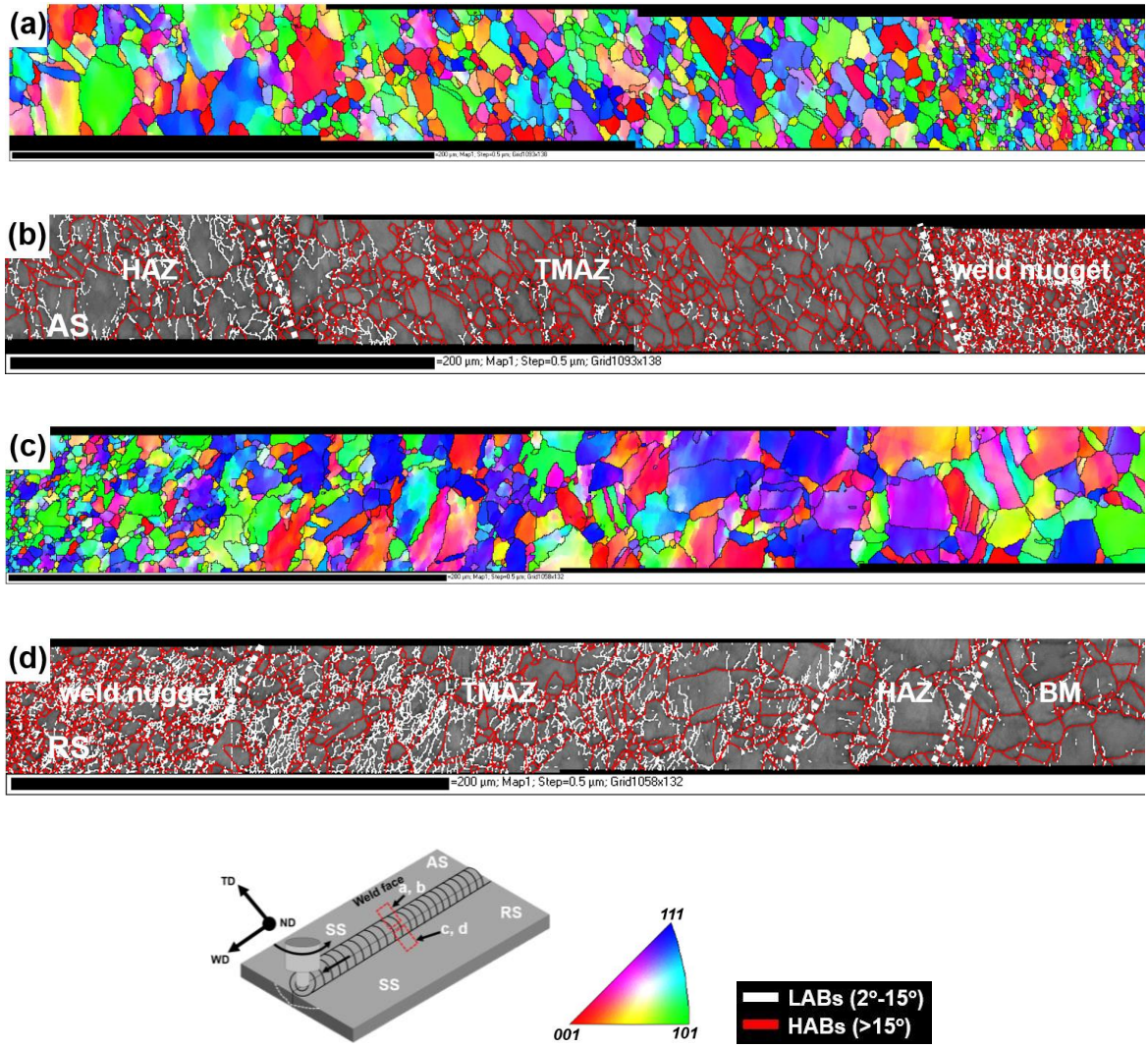

Figure 5.8 SEM-EBSD post-processed micrographs of the FSW (SS-SS) weld face: (a) SEM-EBSD Inverse Pole Figure (IPF)- Weld Face (AS); (b) SEM-EBSD band contrast image mapped with LABs and HABs- Weld Face (AS); (c) SEM-EBSD Inverse Pole Figure (IPF)- Weld Face (RS); (d) SEM-EBSD band contrast image mapped with LABs and HABs- Weld Face (RS)

5.3.1.5 Microhardness measurements

Figure 5.9a shows the optical micrograph of the FSW (SS-SS) weld cross-section with the region of interest (ROI) located for microhardness measurements. All the hardness data points measured were plotted as line profiles shown in Figure 5.9b. From the whole hardness line profiles, it is noticeable

that the hardness distribution pattern along the AS and RS regions are asymmetric due to the non-uniform distribution of heat input and plastic deformation. The hardness profiles further show that both BM and HAZ regions located on the AS have a relatively similar hardness with an average of 226 ± 0.7 HV. Along the RS, except in the weld nugget, there is more scatter observed in the hardness measurements across the weld sub-regions; the hardness measured on the BM/HAZ is 222 ± 5 HV. This finding again confirms that both AS and RS of the weld cross-section had significantly different thermal and deformation histories during the FSW process. As the FSW process usually generates a very narrow HAZ in contrast to the fusion welding process with a small region of grain growth, therefore, a significant difference between the hardness values of BM and HAZ is not clearly detected through the microhardness measurements. Li et al. [37] had this same observation in their study. A moderate increase in hardness is noticed in the outer boundary of the weld nugget, i.e. the TMAZ due to the mixture of deformed and partially recrystallized grains located in this zone. It is evident that the hardness increases rapidly in the region close to the weld nugget. Among other weld sub-regions, the weld nugget has achieved the highest hardness of 281 ± 2.8 HV. All the hardness spikes observed on the weld nugget region are associated with the high degree of grain refinement reflecting the major resistance to plastic flow induced by the ultrafine grain boundaries in forming the microhardness indentations. Furthermore, the high expected density of dislocations and observed sub-grain boundaries in the weld nugget also contribute to the hardness elevation [39]. The microhardness findings, are in good agreement with the expected structure-property relationships in the weld nugget and TMAZ regions.

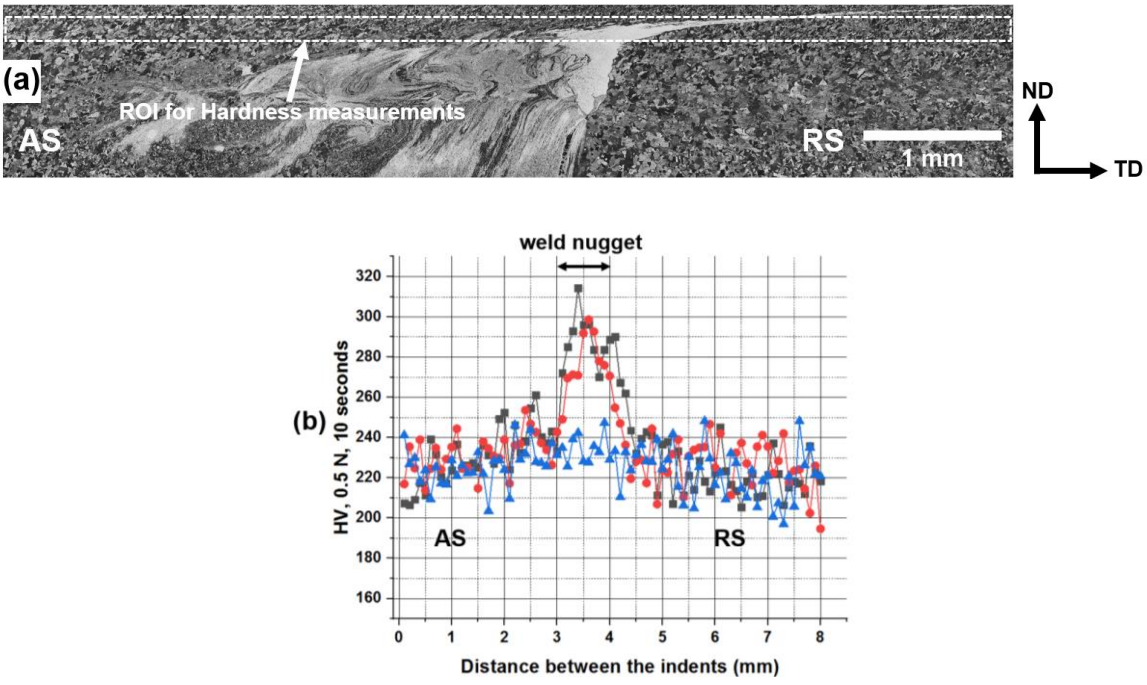

Figure 5.9 Microhardness measurements of the FSW (SS-SS) weld cross-section: (a) Region of interest (ROI) located for microhardness measurements on the FSW (SS-SS) weld cross-section; (b) Microhardness line profiles of the FSW (SS-SS) weld cross-section

5.3.2 FSW (Cu-Cu)

5.3.2.1 Optical macro/micrographs

Figure 5.10a shows the macrograph of the FSW (Cu-Cu) weld cross-section with the locations (1 and 2) marked for optical microscopy observations. From the macrograph, it is observed that the weld cross-section does not have any major FSW weld defects. Four distinct weld sub-regions are located in the macrograph, namely: (a) Base metal/Heat affected zone (HAZ), (b) Thermo-mechanical Heat affected zone (TMAZ)-AS, and (c) weld nugget along the advancing (AS) and retreating sides (RS), (d) TMAZ-RS. The entire shape of the weld nugget (c) is similar to a typical basin shape structure, as reported by Sun and Fujii [46]. It is noteworthy that a sharp interface between the TMAZ (b) and weld nugget (c) is clearly noticed. The weld penetration was measured as ~1.7 mm from the surface, which is coincident with the length of the pin used during the FSW process. A minor thickness reduction is observed across the weld nugget due to the severe frictional contact produced between the FSW tool shoulder and workpiece during the FSW process. Figure 5.10b displays the sequentially stitched optical micrographs captured from location 1, as shown in Figure 5.10a. In this figure, the FSW (Cu-Cu) weld sub-regions are recognised and classified based on their microstructural features. The copper base metal exhibits equiaxed coarse copper grains and also there is no distinction observed between the base metal and HAZ. This is due to the low frictional heat input offered by the FSW process as well as the high thermal conductivity of copper [44]. The TMAZ (b) located on the AS has both plastically deformed grains and a minor quantity of fine grains due to the expected partial recrystallization effect resulting from the dynamic recrystallization mechanism. Along the AS, the boundary between the TMAZ and weld nugget regions is very gradual and therefore not very clearly recognised. However, the TMAZ on the RS has a sharp boundary with the weld nugget, and also the zone is densely packed with elongated grains (Figure 5.10c). This is due to the difference in the material flow rate between the AS and RS sides of FSW process. Liu et al. [51] also confirmed this observation in their investigation. As mentioned by Liu et al. [51], during the FSW process the material flow on the AS is usually similar to the rolling direction of the sheet, and therefore the AS has a smooth interface between the TMAZ and weld nugget. However, this condition is exactly opposite on the RS which leads to the formation of a distinct interface between these regions.

As expected, the entire FSW (Cu-Cu) weld nugget (c) possesses ultrafine grains produced as an outcome of the severe plastic deformation imparted by the FSW process. In addition to this, both the weld nugget (AS and RS) have a gradient in grain refinement due to the spatial variation in the thermo-mechanical input offered by the FSW process. The grains located in the shoulder affected region as shown in Figure 5.10c are much finer than the weld nugget grains due to the impact of both tool shoulder and pin. It is important to note that the onion ring pattern is found very close to the weld nugget associated with the RS (Figure 5.10c). This confirms the clear signs of material

transportation from the AS to the RS during the FSW process which led to the accumulation of multi-layer plasticized material on the RS. The spacing between the onion rings was directly related to the ratio of welding speed (r) to the tool rotational speed (ω) [46]. Except in the TMAZ, both the AS and RS weld sub-regions have almost similar microstructural features.

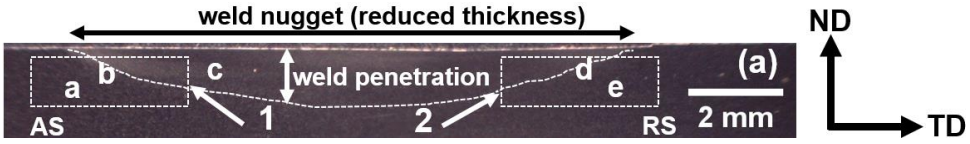

a- BM/HAZ (AS) , b-TMAZ (AS), c- weld nugget, d- TMAZ (RS), e- BM/HAZ (RS)

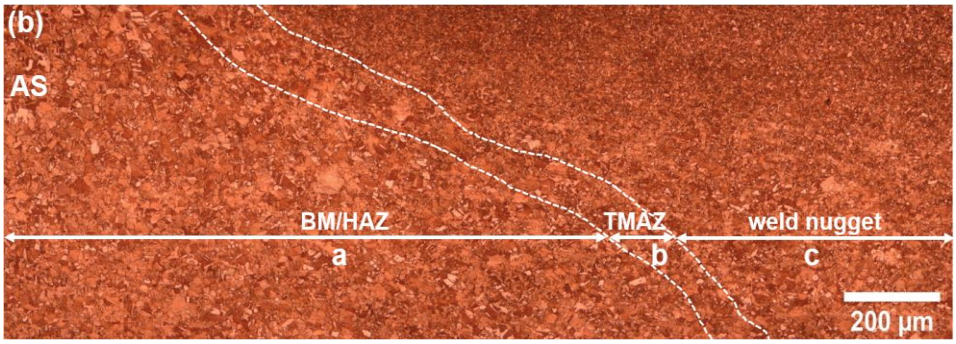

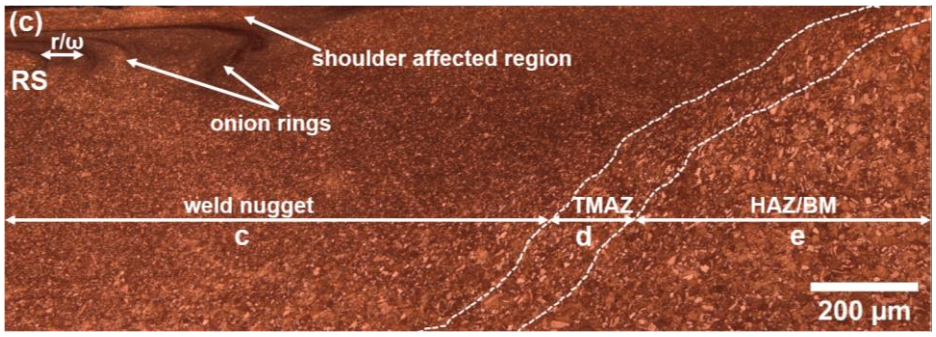

Figure 5.10 Optical microscopy observations on the FSW (Cu-Cu) weld cross-section: (a) Low magnification macrograph of the FSW (Cu-Cu) weld cross-section with the locations marked for optical microscopy; (b) Sequentially stitched optical micrographs correspond to the location 1 shown in (a); (c) Sequentially stitched optical micrographs correspond to the location 2 shown in (a)

Figure 5.11b and Figure 5.11c show the optical micrographs captured from the respective location 1 and 2, as shown on the FSW (Cu-Cu) weld face (Figure 5.11a). Both these micrographs clearly show the distinct boundary between the weld nugget and TMAZ, as well as the TMAZ and BM/HAZ regions. The entire TMAZ of the weld face has achieved more elongated and deformed grains along the shear direction (WD) compared to the weld cross-section. Furthermore, it is evident that the scale of grain refinement produced in the weld face is much stronger than the weld cross-section. The above-mentioned findings clearly represent the complex microstructural heterogeneities between the weld face and cross-section of the FSW (Cu-Cu) joint. Because of this reason, the expected

mechanical behaviour of these regions under globally applied plastic deformation will also be quite varied.

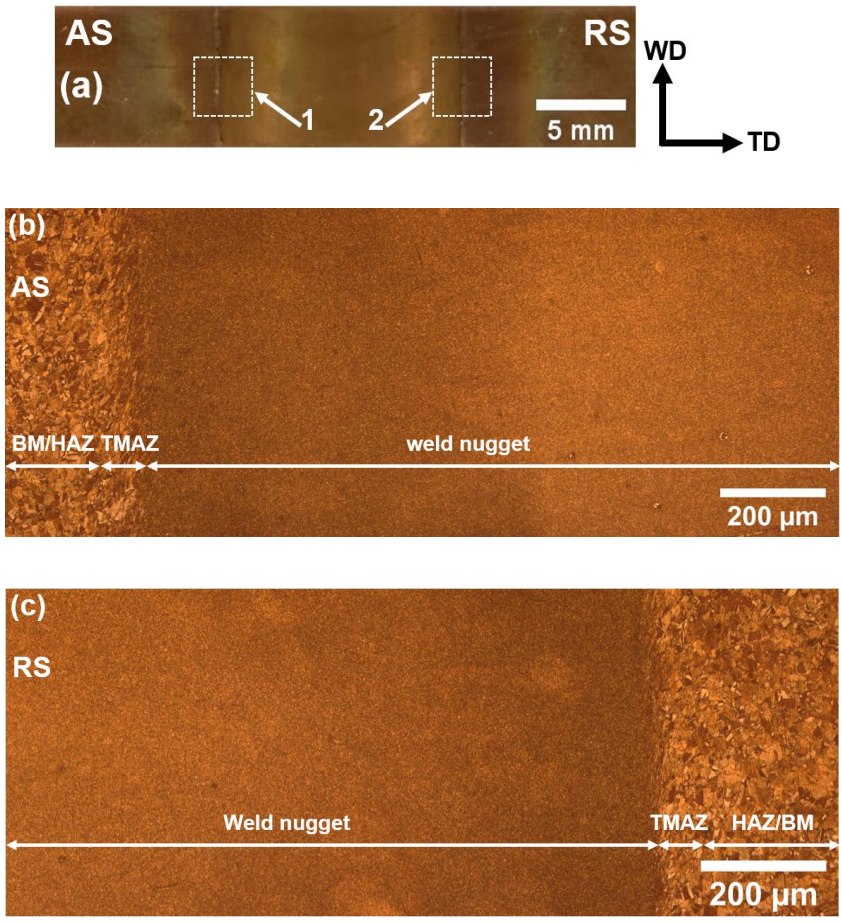

Figure 5.11 Optical microscopy observations on the FSW (Cu-Cu) weld face: (a) Image shows the ROI for optical microscopy; (b) Sequentially stitched optical micrographs correspond to the location 1 shown in (a); (c) Sequentially stitched optical micrographs correspond to the location 2 shown in (a)

5.3.2.2 SEM micrographs

FSW (Cu-Cu) weld sub-regions, especially the weld nugget and the TMAZ/weld nugget interface of the weld cross-section are not clearly resolved through optical microscopy techniques due to the limitations involved in the magnification and spatial resolution. Therefore, high-resolution SEM micrographs were captured at different locations close to the TMAZ and weld nugget regions to achieve a clearer insight into the microstructural features of these regions (as shown in Figure 5.12). Figure 5.12a displays the gradual interface between the TMAZ and weld nugget regions at a higher spatial resolution than the optical micrograph. Figure 5.12b shows the micrograph of the TMAZ located on the AS where the elongated grains along the welding direction are observed. In addition to this, a sharp boundary that separates the fine and coarse elongated grains populated regions is also evident in this Figure. All recrystallized ultrafine grains in the weld nugget are spatially resolved

through the SEM. Due to a vast difference in the thermo-mechanical input during the FSW process, the weld nugget shows a range of equiaxed ultrafine recrystallized grains (Figure 5.12c), and also demonstrates that the majority of the grains located the weld nugget are less than one micron. To further understand the grain morphology of the weld nugget, a few SEM micrographs were captured exclusively on the weld nugget at different magnifications, as shown in Figure 5.12d-e.

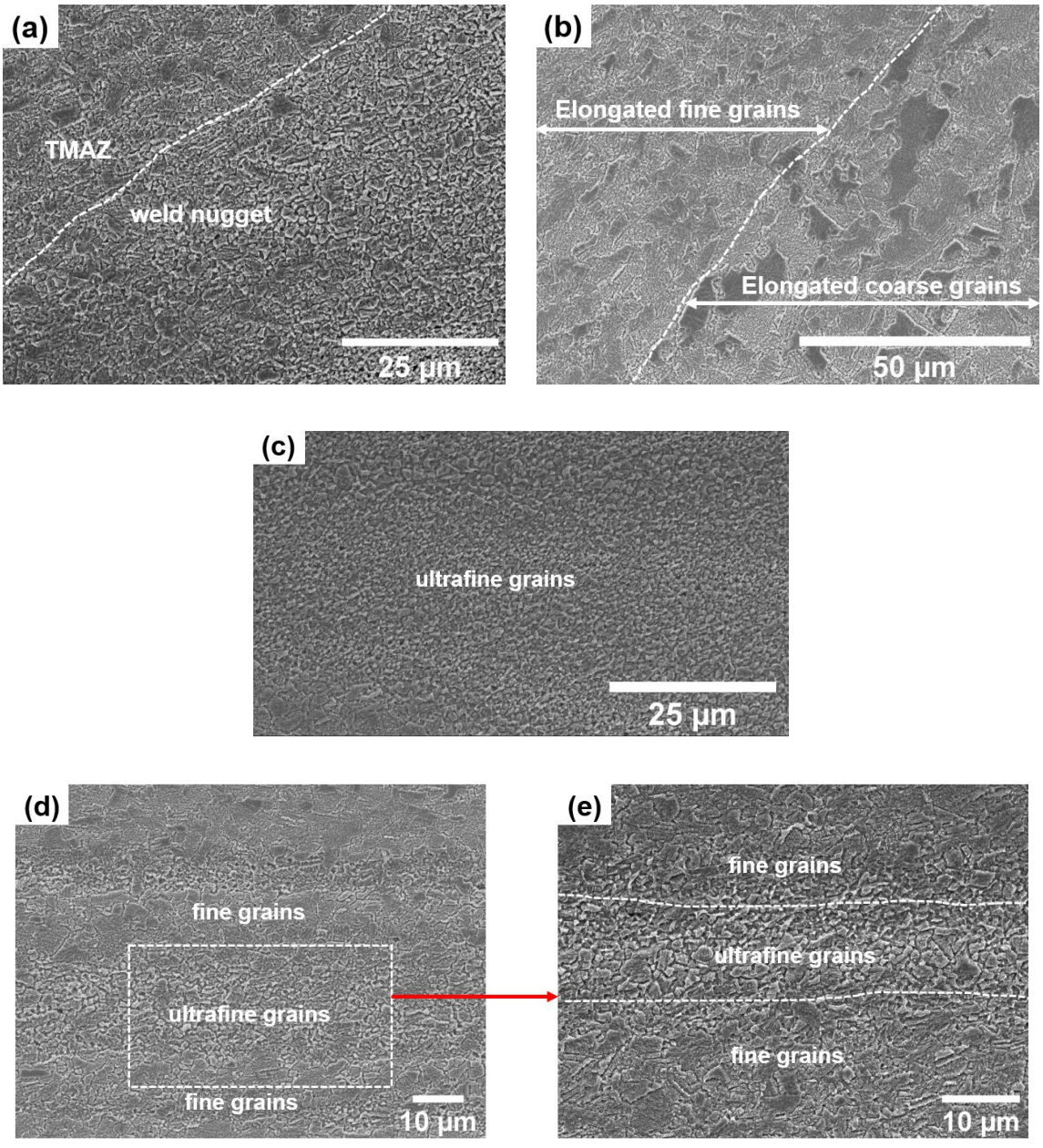

Figure 5.12 SEM Micrographs of the FSW (Cu-Cu) weld sub-regions along the cross-section: (a) Weld nugget/TMAZ interface (RS); (b) TMAZ (AS); (c)-(e) Weld nugget

These micrographs evidenced the high-density mixture of both ultrafine and fine grains located in the weld nugget, which shows the non-homogeneous grain size distributions achieved from the FSW process. It is understood that both annealing effects of the welding heat and peak temperature of the FSW thermal cycle are the crucial factors that determine recrystallized grain size [45, 47]. Therefore,

from the microstructural evidence in the weld nugget, it is confirmed that the degree of plastic deformation, as well as the intensity of the frictional heat during the FSW process, are not uniform along the advancing and retreating sides. The above SEM findings highlight the necessity to involve high-resolution full-field strain measurements on the weld nugget to achieve high-fidelity microstructure-mechanical property relationships for the heterogeneous microstructures of the FSW (Cu-Cu) weld.

5.3.2.3 SEM-EBSD analysis

Figure 5.13 displays the IPF figure of the major weld sub-regions of the weld face and its corresponding band contrast grain maps plotted with low angle grain boundaries (LAGBs) and high angle grain boundaries (HAGBs). Figure 5.13a shows the EBSD micrograph captured on the AS where the weld sub-regions BM/HAZ, TMAZ, and weld nugget regions are located based on the distribution of LAGBs and HAGBs. This EBSD micrograph clearly demonstrates the gradual transition of microstructure from the BM to weld nugget along the AS. As confirmed in the optical/SEM microscopy findings, there is no significant difference observed between the microstructure of BM and HAZ. The BM/HAZ region has coarse copper grains with annealing twins. A sharp boundary between the BM and TMAZ as well as TMAZ and weld nugget regions are also evident. On the AS (Figure 5.13b), the proportion of LAGBs gradually increases from the BM to TMAZ and then decreases while moving towards the weld nugget from TMAZ. The copper BM has more LAGBs compared to the weld nugget. As the BM was unlikely to experience any plastic deformation during the FSW process, then the BM was expected to have more LABs compared to HAGBs. But note that the copper BM is generally also processed through various stages of sheet manufacturing processes, and these original manufacturing processes may have already generated a substantial shear strain in the material and thus led to more HAGBs than LAGBs. Due to the partial dynamic recrystallization effects attained from the FSW process, all low aspect ratio oriented (elongated) grains of TMAZ exhibit more LABs than HAGBs. In contrast to this finding, the majority of the equiaxed fine grains of the weld nugget have HAGBs. Figure 5.13d shows the obvious grain refinement achieved in the FSW weld nugget with no significant distribution of LAGBs. This is because the FSW weld nugget has attained a high strain level due to the heavy axial force induced by the FSW tool which leads to a dynamic recrystallization. Because of this severe plastic deformation, a significant population of coarse grains have been sheared down into the ultrafine equiaxed grains in the weld nugget. As a result of this recrystallization effect, a formation of high density of sub-grains generally occurs in the weld nugget, and these sub-grain boundaries can absorb the dislocations caused by the FSW process and become HAGBs [88]. In addition to this, the generation of HAGBs is also associated with the thermal cycle of the welding process and the flow behaviour of the plastic material [87]. Song et al. [89] reported that any high frictional heat input welding process would significantly reduce the work hardening and viscosity capability of the plasticized material. Hence, this will result in a high degree of material plasticity and significant

migration of HAGBs. A similar effect has been reported by Wang et al. [90]. Figure 5.13e shows the EBSD micrograph captured on the TMAZ located on the RS. The TMAZ experiences far less deformation and frictional heat than the weld nugget because of the absence of the pin effect, therefore this partial deformation zone does not promote any significant recrystallization behaviour of grains.

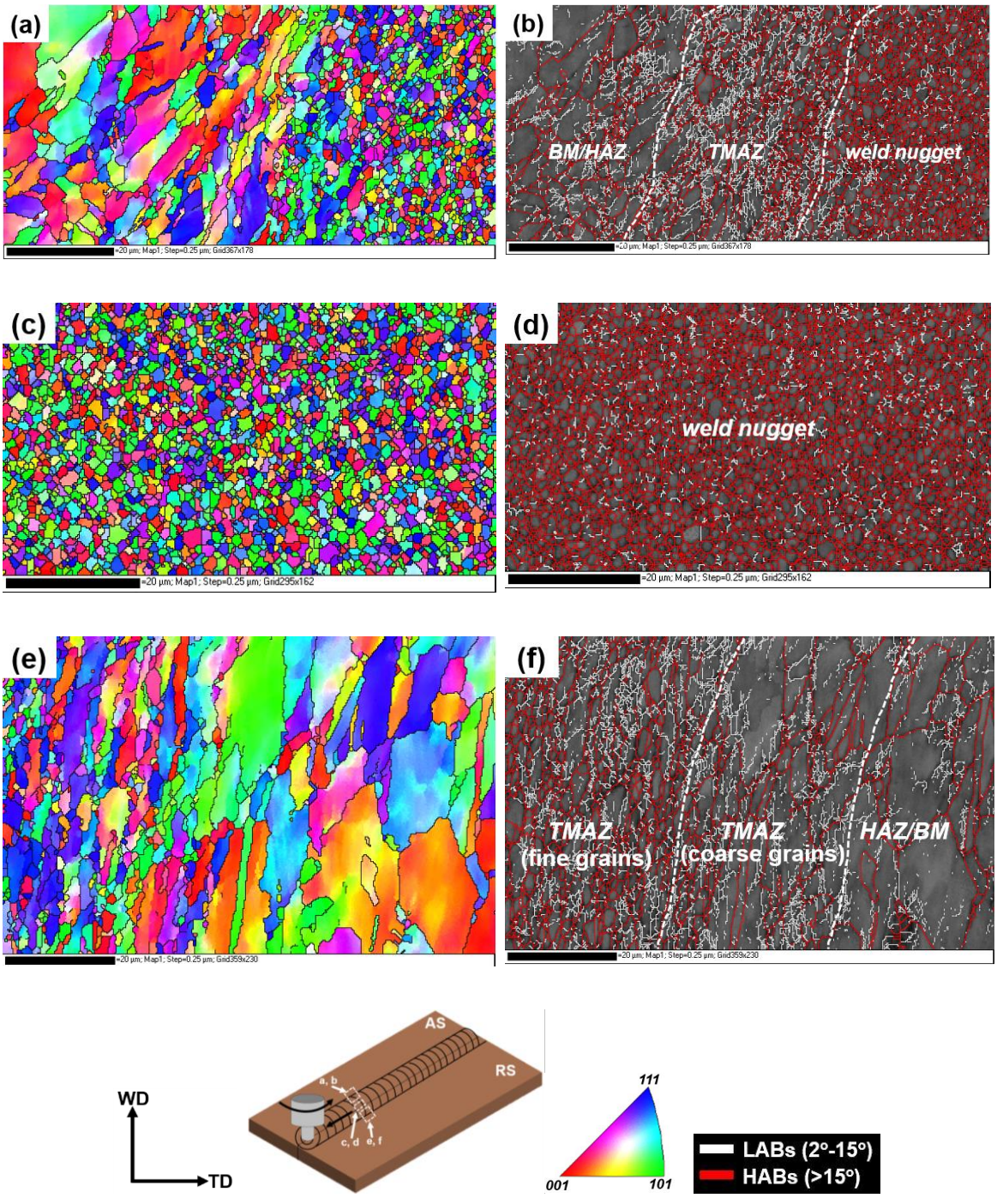

Figure 5.13 SEM-EBSD post-processed micrographs of the FSW (Cu-Cu) weld face: SEM-EBSD Inverse Pole Figure (IPF): (a) TMAZ/weld nugget interface (AS), (c) Weld nugget, (e) TMAZ (RS); SEM-EBSD band contrast image mapped with LABs and HABs: (b) TMAZ/weld nugget interface (AS), (d) Weld nugget, (f) TMAZ (RS)

The TMAZ has therefore been identified by its elongated grains and fewer HAGBs than in the weld nugget. It is noteworthy that the TMAZ on the RS has a completely different grain morphology than the AS where it has a mixture of fine and coarse elongated grains along the shear direction of the FSW process. Furthermore, there is a clear boundary located between the fine and coarse elongated grains as noticed in the SEM micrograph shown in Figure 5.12b. In addition to this, the grains located in the TMAZ-RS are much coarser than the TMAZ-AS. All these findings again highlight the non-uniform thermo-mechanical deformation generated by the FSW process on the advancing and retreating sides.

5.3.2.4 Microhardness measurements

For microhardness measurements, a suitable ROI, as shown in Figure 5.14a was chosen on the FSW (Cu-Cu) weld cross-section. Figure 5.14b shows the optical micrographs captured from the ROI used for microhardness measurements. From the microhardness contour map shown in Figure 5.14e, it is found that a range of maximum hardness distributed across the weld nugget. The hardness gradient of the weld nugget is due to the distribution of a wide range of fine grains produced from the non-uniform thermo-mechanical deformation of the FSW process. The hardness increment pattern in the weld nugget is aligned with the shape of the weld nugget. The weld nugget has achieved the higher hardness (105 ± 0.6 HV) than the BM (94 ± 0.2 HV) due to the distribution of fine recrystallized grains and higher density of sub-grain boundaries. Both Nan et al. [49] and Nakata [91] also had the same results in their investigation. Thus the hardening resulting from severe plastic strain and grain refinement during the FSW process have made the weld nugget much stronger than the BM. From the microhardness map, there is no clear distinction noted between the hardness of TMAZ and BM regions. Even though the SEM-EBSD micrographs have evidenced the completely different microstructural features produced along the AS and RS, the hardness distribution is more homogeneous in both these regions. Although all the micrographs have indicated the absence of a HAZ, a sharp hardness dip is observed along the RS in the region close to the Cu-BM. To observe these hardness variations via micrographs, the intended area was etched and observed in the OM under the bright-field mode, as shown in Figure 5.14b-c. But due to the bright background, the variation between the indents positioned in the stir-zone (weld nugget) and non-stir zone is not observed. Hence the OM was operated under the dark field mode where the differences between the indents is clearly observed in the dark background as shown in Figure 5.14d. All the indents located in the stir zone have a smaller diagonal length, i.e., higher hardness compared to the indents located in the non-stir zone. This is due to the strong resistance to the microhardness indentation produced by the densely populated sub-grain boundaries of the stir zone. From this it can be seen that the microstructural-mechanical property relationship is directly confirmed only in the weld nugget region where there is a significant observable difference in the grain size compared to the base metal.

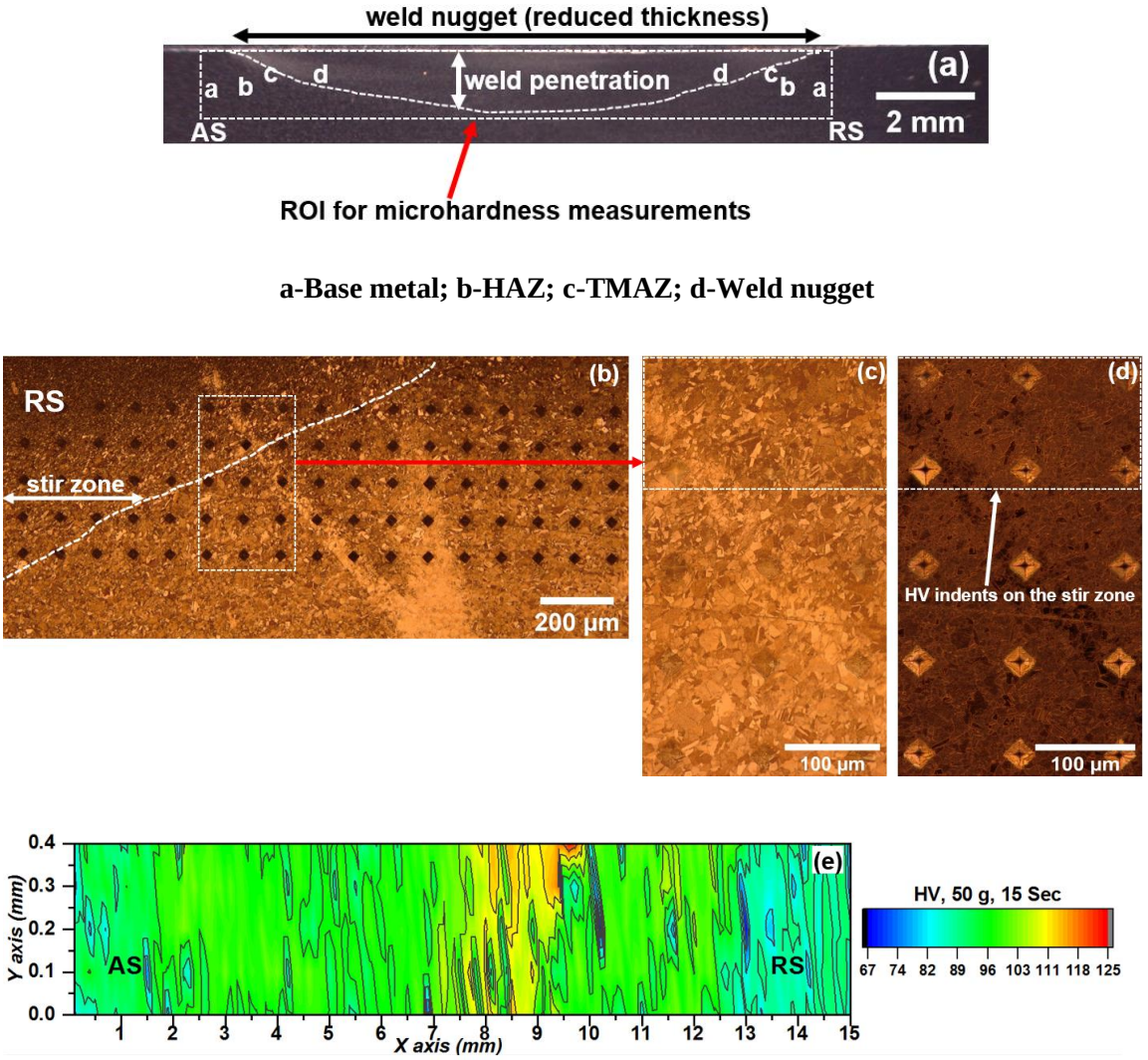

Figure 5.14 Microhardness results of the FSW (Cu-Cu) joint: (a) Region of interest located for microhardness measurements on the FSW (Cu-Cu) weld cross-section; (b) OM of the indent region at 100x; (c) Magnified OM (Bright field mode) of the region as shown in (b); (d) OM (Dark field mode) of the region as shown in (c); (e) Microhardness contour map

5.3.3 FSW (Cu-SS)

5.3.3.1 Optical Microscopy

5.3.3.1.1 Macrostructure

In contrast to the FSW of similar materials, it is extremely challenging to accurately locate the weld sub-regions in typical cross-sections of dissimilar material FSW joints. This is because of the highly heterogeneous dissimilar material flow stirred across the FSW weld nugget. Additionally, due to the tool offset condition involved during the FSW of dissimilar materials, some of the weld sub-region especially the TMAZ can be masked due to a strong overlap with an adjacent zone such as the weld nugget [20]. These masked weld sub-regions cannot be easily resolved by the OM and it requires a

higher resolution characterisation technique such as EBSD to observe the gradients in the grain size characteristics. Figure 5.15a shows the macrostructure along the cross-section of the FSW (Cu-SS) weld. The dissimilar FSW (Cu-SS) weld exhibits seven local weld sub-regions such as: (b) Base metal-Cu, (c) Heat affected zone (HAZ) in the Cu, (d) TMAZ/Cu-weld interface, (e) weld nugget/stir zone on the retreating side (RS). On the advancing side (AS) it includes: (f) TMAZ/SS-weld interface, (g) Heat affected zone (HAZ) in the SS, and (h) Base metal-SS. As the TMAZ of Cu and SS sides are not clearly observed in Figure 5.15a, therefore, the Cu-weld interface and SS-weld interface are considered as their respective TMAZs. The stir zone exhibits a mixture of copper and stainless steel elements due to the forging and stirring action of the FSW tool. As the tool was offset towards the copper, the stir zone had a composite structure of a copper matrix reinforced with the stainless steel fragments. The classical "onion ring structure" is observed in the centre of the weld nugget, and the area of the onion ring is wider in the centre and becomes narrower when travelling from the AS to the RS of the weld. A swirl like pattern has appeared near the copper interface due to the complex intercalated material flow rising from the weld nugget and heading towards the copper base material. The FSW parameters such as tool rotation speed and welding speed combined with the FSW stirring mechanism are responsible for these turbulence activities in the vicinity of the dissimilar weld nugget and the formation of the "onion ring structure" [5]. Although a wide scale of dissimilar metals mixed in the weld nugget, a sharp weld interface along the stainless steel is clearly observed.

5.3.3.1.2 Microstructure of the FSW (Cu-SS) weld cross-section

Optical micrographs of the FSW (Cu-SS) weld sub-regions identified in the macrograph (Figure 5.15a) are displayed in Figure 5.15 b-g. Figure 5.15b shows the microstructure of the copper base material which exhibits equiaxed grains with annealing twins. Significant grain growth is observed in the HAZ of the copper (Figure 5.15c) due to the absorption of frictional heat generated from the FSW process. Although the tool was offset towards the copper side and it occupied the majority of the weld nugget as shown in Figure 5.15a, an independent copper TMAZ which is generally distinguished by elongated grains is not evident. This finding agrees with the investigation performed by Ramirez, A.J et al. [20]. A defect-free interface (Figure 5.15d) is clearly evident between the copper and the weld nugget confirming the integrity of the joint and indicating the potential and reliability of the FSW process in joining dissimilar metals. However, the stainless steel has a sharp weld interface (Figure 5.15e) in contrast to the copper interface which raises concern about adequate bonding of the joint towards the stainless steel side. The intercalated solid-state flow of the stainless steel is observed near the copper interface (Figure 5.15d). This is due to the heavy plastic deformation and stirring action produced in the weld nugget which lead to mass transportation of material from the advancing side (SS) to the retreating side (Cu). As a consequence of this mechanism offered by the FSW process, the weld nugget has a composite structure containing a rich mixture of both copper and stainless steel. The weld nugget has achieved a classical 'onion ring structure' in the form of

intercalated lamellae produced by the frictional heat interlinked with the tool traverse and rotating motion during the FSW process. Furthermore, the elliptical onion ring structure is the compilation of multiple vortex layers, and the size of these layers gradually increases from the centre to vertex. The ultrafine equiaxed recrystallized grains which densely populated the FSW weld nugget cannot be resolved in the OM due to the limitations in magnification and spatial resolution. Because of the turbulent solid-state migration of the stainless steel, a few stainless steel fragments detached from the base material are observed in the copper matrix (Figure 5.15e). Wang et al.[32] have also found this evidence in their investigation. The base material of 304 stainless steel shows typical austenite grains (Figure 5.15g), and its corresponding HAZ (Figure 5.15f) exhibits slightly larger size grains compared to the base material. As the tool was offset towards the copper side, the scale of plastic deformation was significantly higher in the copper than the stainless steel, therefore the TMAZ of the stainless steel completely overlaps the weld nugget. Hence a clear boundary between the weld nugget and the stainless steel TMAZ is not evident in the optical micrographs.

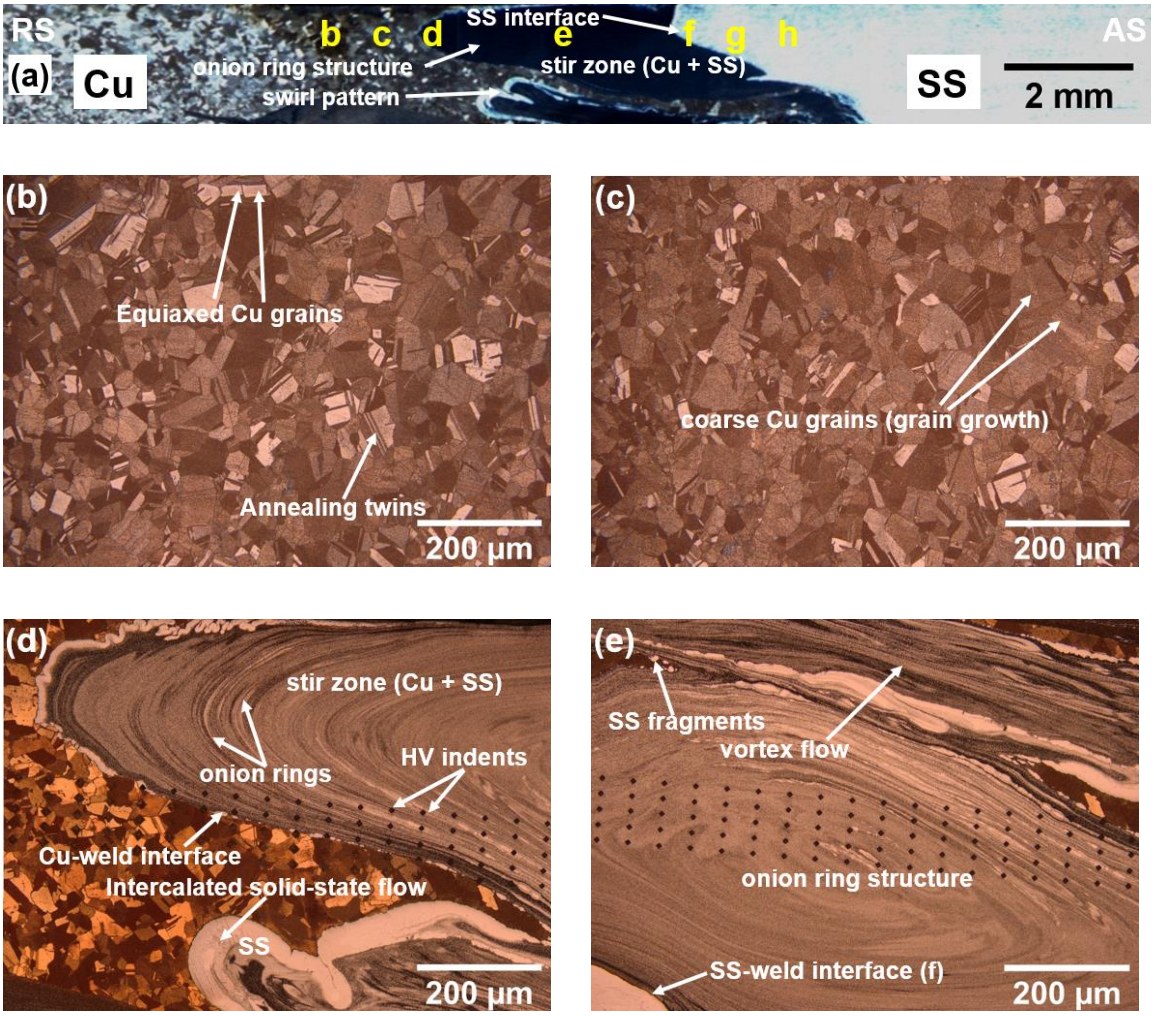

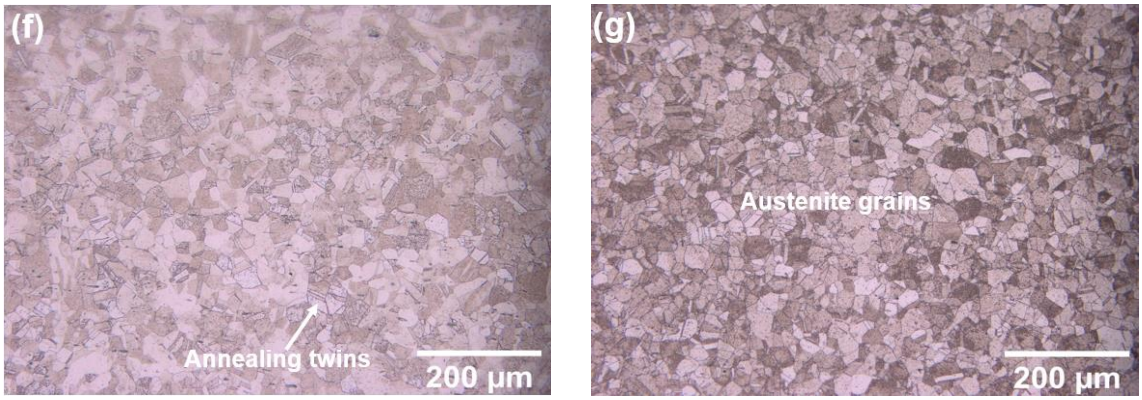

Figure 5.15 Optical Macro/Micrographs of the FSW (Cu-SS) Joint: (a) Macrostructure along the cross-section with the weld sub-regions marked for optical microscopy; Optical micrographs: (b) Cu-BM; (c) Cu-HAZ; (d) TMAZ/Cu-weld interface; (e) weld nugget/stir zone; (f) SS-HAZ; (g) SS-BM

5.3.3.1.3 Microstructure of the FSW (Cu-SS) weld- along the weld face

Many investigations have proved that a dissimilar material FSW joint has highly heterogeneous microstructures along its cross-section, and also this cross-sectional heterogeneity differs widely across the weld face and weld root of a joint [24, 70, 83]. The schematic sketch shown in Figure 5.16 illustrates that the frictional force acting on the weld face can be influenced by both shoulder and pin, however the weld cross-section can be influenced only by the pin during a typical FSW process [24]. Hence the frictional heat generation and the rate of plastic deformation do vary along the weld face, weld root, and through-thickness cross-sections during the FSW process. But these effects apparently do not produce any complex metallurgical incompatibilities in similar material FSW welds as the material properties are homogeneous. In a dissimilar material FSW process, the aforementioned effects exaggerate the chemical and mechanical incompatibilities across the dissimilar weld nugget and result in the intricate material flow pattern during a FSW process [2].

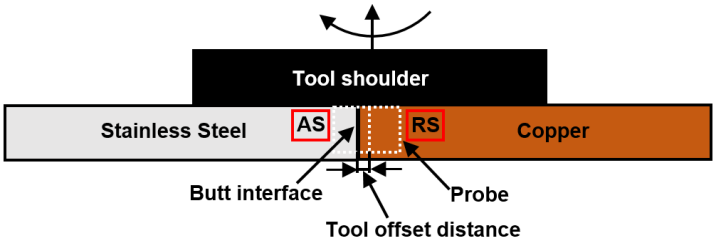

Figure 5.16 A schematic illustration of probe offset distance in a typical FSW (Cu-SS) joint

Although the standard protocol for characterising the FSW weld through microscopy techniques has usually been in the weld cross-section, dissimilar material FSW welds have to be characterized along the weld face, weld root, and through-thickness cross-sections. These characterisations will provide a significant insight into the material flow pattern and asymmetry transport of two dissimilar

plasticised alloys. Figure 5.17b-e show the sequentially stitched optical micrographs along the weld face from the corresponding locations shown in Figure 5.17a. The turbulent solid-state flow of stainless steel and copper is clearly observed in Figure 5.17b-c. Furthermore, some vortex layers of the stainless steel are completely overlapped with the layers of copper because of the asymmetric transportation of the material from the AS to RS (Figure 5.17c). Randomly distributed stainless steel fragments in the copper matrix are evidenced in Figure 5.17c, and again this confirms the migration of stainless steel towards the copper. As the weld face has been mostly influenced by the shoulder contact compared to the tool pin, all the onion ring layers generated in the weld face have semi-circular onion layers (as shown in Figure 5.17d) in contrast to elliptical structured onion rings seen along the weld cross-section. The SS-weld interface (Figure 5.17d) formed along the weld face is found to be a mixed interface instead of a sharp interface observed along the weld cross-section. Figure 5.17e shows the sequentially stitched optical micrographs along the stainless steel side of the weld face where the local weld sub-regions (SZ, TMAZ, HAZ, and BM) can be classified based on their grain size. As the tool was offset towards copper during the FSW process, a typical onion-ring pattern is missing across the weld nugget of the stainless steel. Nevertheless, the weld nugget of stainless steel has fine recrystallized grains, and the boundary between the nugget and the TMAZ is clearly defined. A series of cracks along the welding direction are observed within the weld nugget, as shown in Figure 5.17e.

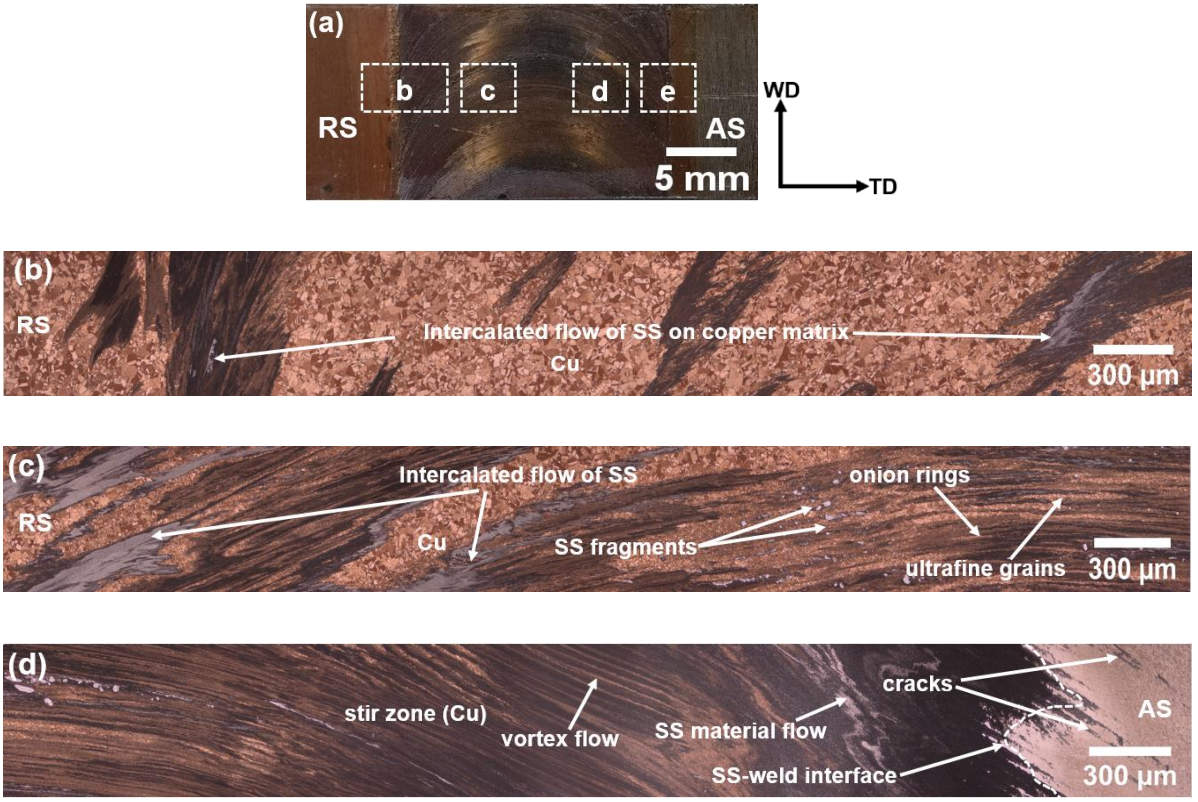

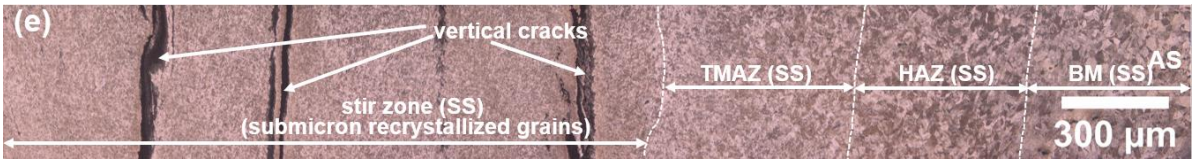

Figure 5.17 Optical micrographs of the FSW (Cu-SS) weld face: (a) Image shows the ROI for optical microscopy; (b)-(e) Sequentially stitched optical micrographs from the respective locations as shown in (a)

The formation of these cracks may be due to the effect of FSW process parameters (welding speed and tool rotating speed) and insufficient plunge depth of the tool during the FSW process [23]. As the tool was offset towards the copper, the frictional contact between the shoulder and stainless steel was apparently lower compared to the copper. Thus insufficient frictional heat has not produced the optimum solid-state flow and resulted in defects such as incomplete penetration and cracks. This kind of FSW weld defect can be avoided by further optimising the process parameters such as increasing the tool rotation speed and tool axial force while manufacturing the joints [23]. Although the FSW (Cu-SS) joint is free of macroscopic defects along the cross-section, the presence of defects in the weld face demonstrates the requirements for detailed material characterisations along the weld face and root of the joint. Hence these material characterisations will lead to a more holistic understanding of the microstructural heterogeneities in different planes of the dissimilar material FSW joints.

5.3.3.1.4 Microstructure of the FSW (Cu-SS) weld- along the weld root

Figure 5.18b shows the sequentially stitched optical micrographs obtained from the ROI shown in Figure 5.18a along the weld root, i.e. rear face of the FSW (Cu-SS) joint. The stitched optical micrograph represents a sharp weld interface between the copper and stainless steel. In contrast to the findings from the weld face and cross-section, all the micrographs captured along the weld root show less complex microstructural features, and all the weld sub-regions across the weld are easily classified by their corresponding grain size. Along the stainless steel side, the stir zone close to the weld interface has ultrafine recrystallized grains. Although the fine recrystallized grains extended a few µm distance from the sharp interface showing that the weld root had experienced plastic deformation, the scale of this deformation is not as severe as observed in the weld face and cross-section. It is noticed that the HAZ of SS has a mixture of coarse grains and fine grains. This is due to the gradient in the thermal heat input during the FSW process. The coarse grains located in the SS-HAZ are found to be slightly larger than grains located in the base material. Towards the copper side, fine copper grains are observed for a few µm distance from the interface, and beyond that the grain growth is evident due to the effects of frictional heat. Furthermore, there is no migration of SS towards the Cu in contrast to the findings achieved along the weld face and through-thickness cross-sections. From these observations, it is confirmed that the stirring mechanism of the FSW process

has not been conclusively demonstrated along the weld root as reported elsewhere [23, 24, 54]. This is believed to be because of the length of the tool pin used in any FSW process should be slightly less than the thickness of the plates to facilitate the stirring mechanism across the cross-sections [23]. Due to this, the weld microstructure along the weld root had less frictional heat and plastic deformation compared to the cross-section as well as the weld face. Thus the FSW weld root has no major effects from the tool shoulder and pin making the material flow from the AS to RS nearly homogeneous during the welding process. It is noteworthy that cracks are identified both in the copper and stainless steel stir zones indicating that the FSW process parameters adopted in this investigation were not perfectly optimised to produce a stronger FSW (Cu-SS) joint. These evaluations indicate the FSW process parameters have to be optimised further to coordinate the different flow characteristics of the copper and stainless steel and also to control the challenging effects due to the widely varying thermo-physical properties of the copper and stainless steel.

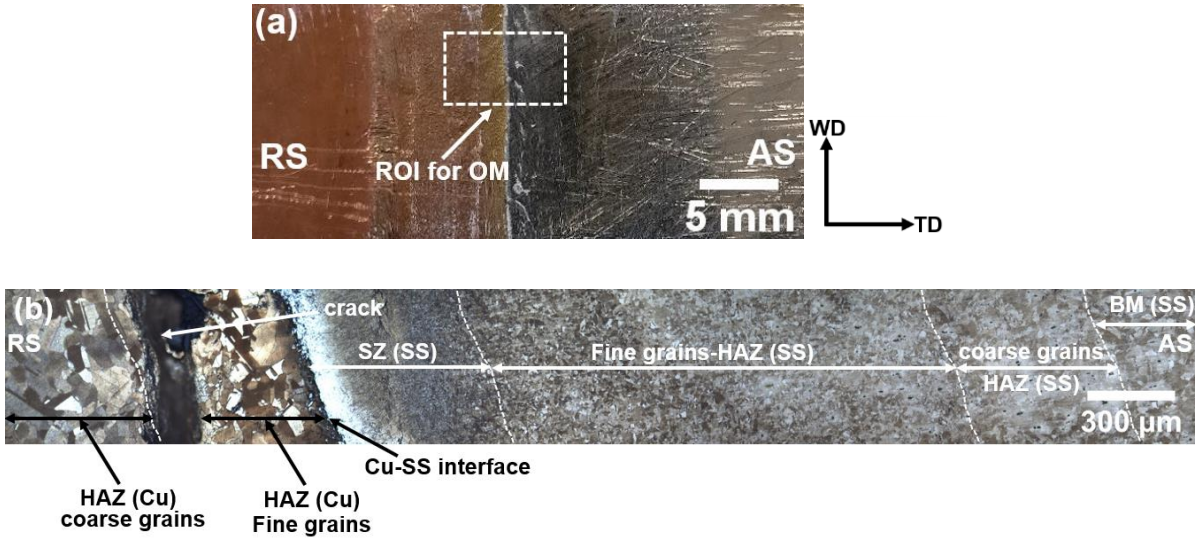

Figure 5.18 Optical micrographs of the FSW (Cu-SS) weld root: (a) Image shows the ROI for optical microscopy; (b) Sequentially stitched optical micrographs from the ROI shown in (a)

5.3.3.2 SEM

5.3.3.2.1 SEM-SEI Micrographs

Figure 5.19 shows the high-resolution SEM micrographs captured on the different sub-regions of the FSW (Cu-SS) weld cross-section under Secondary Electron Imaging (SEI) mode. Figure 5.19a displays the micrograph of the SS-weld interface region where the stir zone located towards the stainless steel side has achieved a wide range of fine grains. From this figure, it is noteworthy that some recrystallized fine grains also crossed the SS-weld interface and deposited in the region close to the SS-HAZ due to the strong stirring action of the FSW process. Figure 5.19b demonstrates the intercalated solid-state material flow produced in the stir zone close to the copper as a consequence of mass migration of stainless steel elements towards copper. The leading cause of this occurrence is

due to the advancing side position of stainless steel as the material flow direction is always from the advancing side to the retreating side during the FSW process [5]. Figure 5.19c displays the significant variation in the grain size in the region in the vicinity of the stir zone (Cu) which represents the heterogeneous characteristics of weld sub-regions in the copper side. A sharp interface between the copper and weld nugget is noticed (Figure 5.19d). Hence this sharp interface raises concern about the bonding strength of the joint towards the copper side that needs to be confirmed by a series of mechanical tests. Extremely refined recrystallized grains with an average grain size of (<1 μm) produced by the dynamic recrystallization mechanism are observed in the weld nugget (Figure 5.19d).

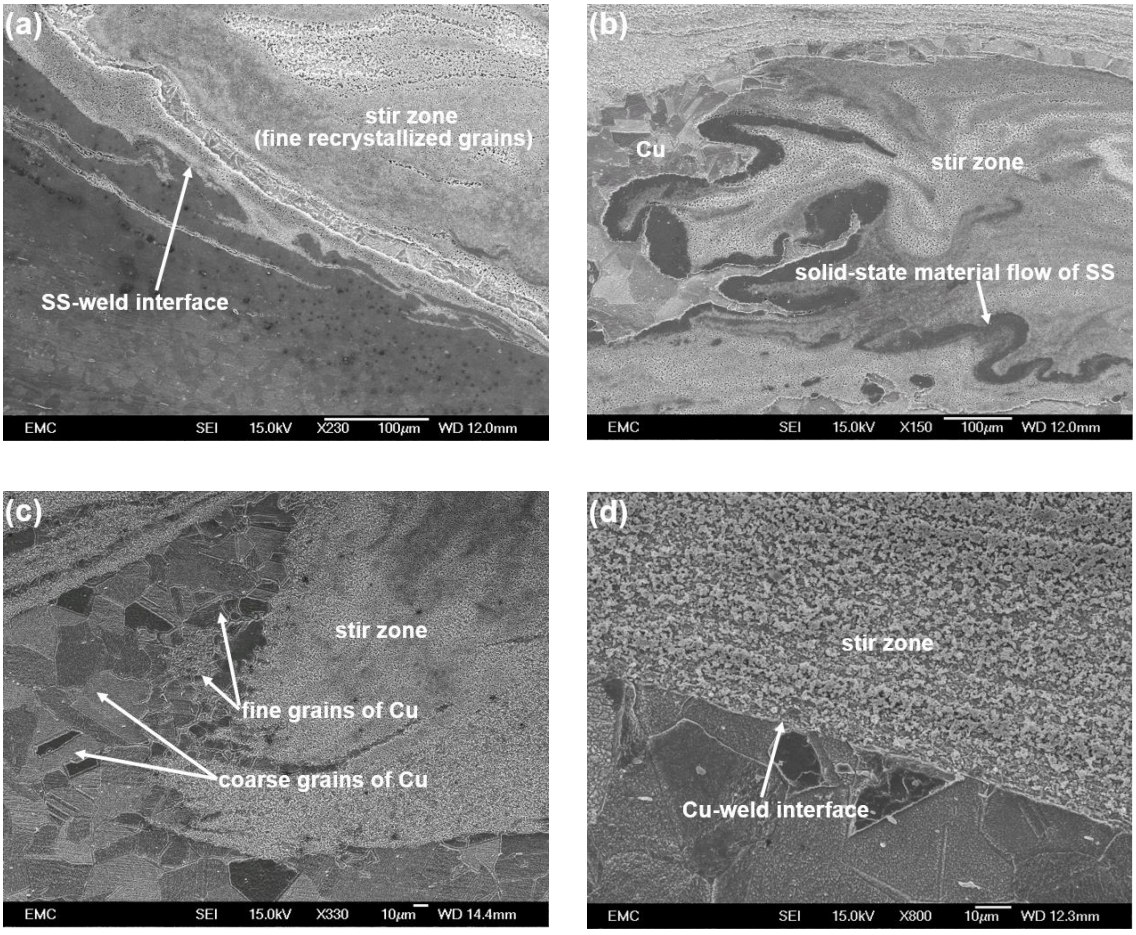

Figure 5.19 SEM micrographs of the FSW (Cu-SS) weld sub-regions: (a) SS-weld interface; (b) Stir zone (close to Cu); (c) Stir zone (close to Cu); (d) Cu-weld interface

The formation of the complex weld microstructures across the weld sub-regions could be due to the incompatibility in the thermophysical properties of the dissimilar base materials [5]. Although the SEM can characterise samples at a high spatial resolution, a distinct boundary between the weld nugget and the TMAZ in the dissimilar FSW (Cu-SS) weld is not resolved in the SEM.

5.3.3.2.2 SEM-BSE Micrographs

Figure 5.20 shows the SEM-BSE micrographs captured from the ROI located in the corresponding optical micrographs of the friction stir welded Fe/Cu joint. The SEM was operated under Back-Scattered Electron (BSE) mode to characterise the complex microstructural features of the dissimilar weld nugget alongside with the compositional information. Figure 5.20a shows several swirl and vortex patterns near the tool shoulder affected region. Large amounts of fine particles of Fe were dispersed in the Cu matrix, and dispersion of these Fe fragments was seen towards the Cu interface. These scattered Fe fragments in the Cu matrix have irregular shapes and sizes that make hybrid like structures. Similar observations were made by Tan et al. [92]. Figure 5.20b shows the stir zone where a highly intense stirring action of the FSW process can be clearly observed. Because of the plastic stirring mechanism associated with the FSW process, some Cu pieces have detached from the Cu bulk and become stirred into the Fe matrix giving rise to alternate lamella. High plastic deformation and friction heat generation are the primary reasons for the heterogeneous characteristics of the weld nugget. The SEM-BSE micrograph of the onion ring structure shown in Figure 5.20b offers an approximate insight into the density of Fe and Cu in weld nugget. The stir zone has a higher density of Fe than Cu, so there is a possibility that the weld nugget may attain some properties of Fe. There is no sign of an intermetallic layer in the joint interface from the BSE-SEM micrographs. However, the formation of an intermetallic layer in the dissimilar FSW process has been reported by many researchers [93-95], and intermetallics are generally responsible for degrading the mechanical performance of FSW joints. As per the Fe-Cu phase diagram shown in Figure 5.21, there is no thermodynamic driving force for the formation of intermetallics between Fe and Cu.

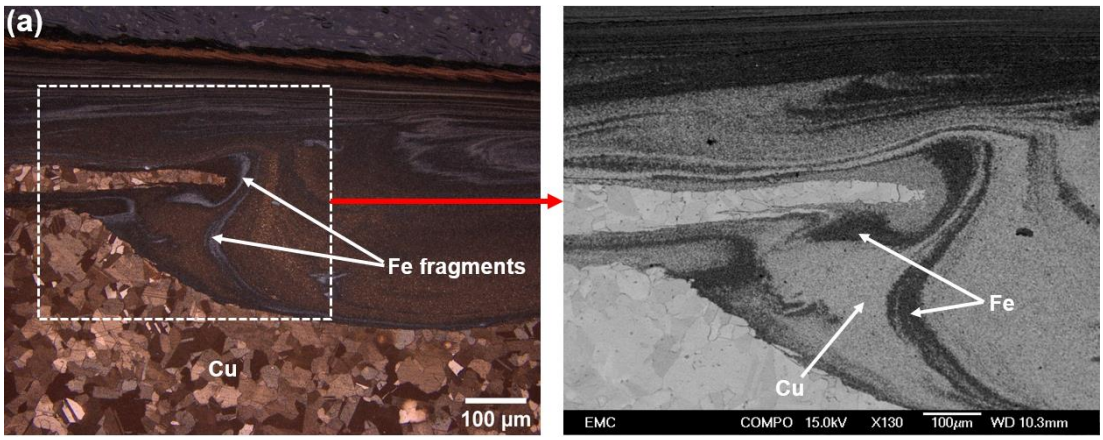

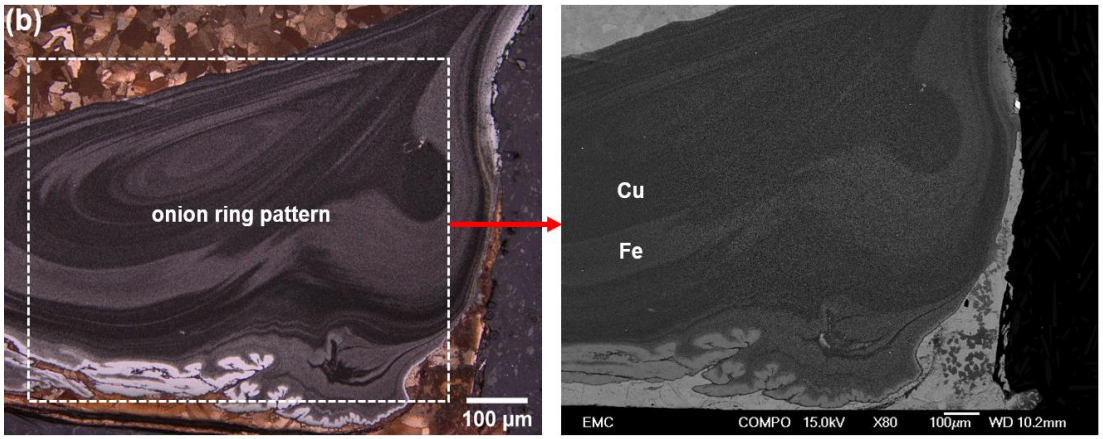

Figure 5.20 Backscattered electron (BSE) micrographs with respect to the ROI shown in the optical micrographs of the FSW (Cu-SS) weld: (a) Intercalated flow of SS on copper matrix; (b) onion ring pattern (weld nugget)

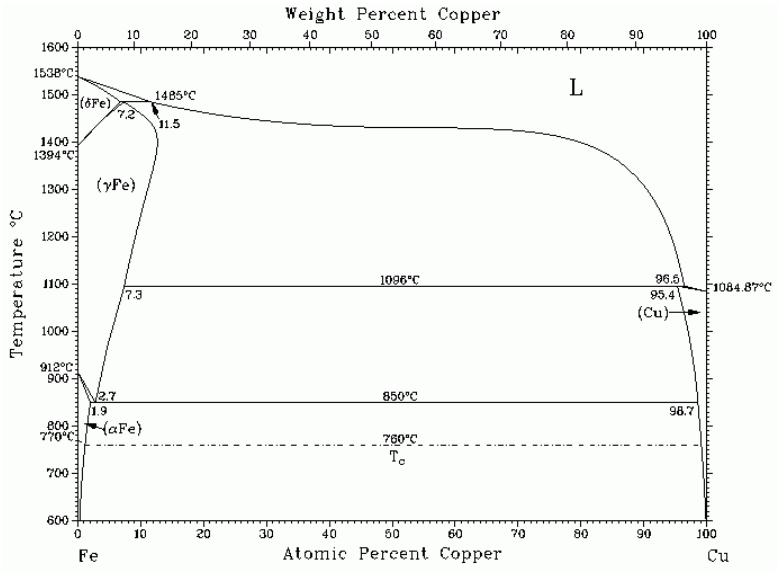

Figure 5.21 Phase diagram of Fe-Cu [57]

5.3.3.2.3 SEM-EDS micrographs

Elemental distribution maps along the base materials interface and the weld nugget are shown in Figure 5.22. EDS maps on the weld interface (Figure 5.22 a,b) clearly show the presence of a distinct interface between the weld nugget and dissimilar base materials (Fe and Cu). From Figure 5.22a, it is determined that some Cu particles were chipped from the Cu matrix and overlapped with Fe on the weld nugget. In addition to this, this figure also represents the vortex flow of stainless steel from the advancing side of weld to the retreating side of copper resulting from the thermomechanical reactions associated with the FSW process. This is due to the strong stirring action of the FSW tool

that facilitates better mixing between the base materials. Nevertheless, the weld nugget does not achieve the rich mixture of both Cu and Fe, as these elements have limited solubility with each other [22]. The EDS mapping of the weld nugget (Figure 5.22b) is in good agreement with the results obtained in SEM-BSE (Figure 5.20b). This exclusive EDS mapping performed at the weld nugget confirmed that the FSW (Cu-SS) joint was enriched with more Fe than Cu elements. This indicates the mechanical behaviour of the friction stir welded Cu-SS joint will be more closely aligned with the stainless steel properties. In contrast to this finding, Jafari et al. [17] evidenced the copper enriched weld nugget in their investigation as the tool was plunged exactly on the butt interface without any offset. Figure 5.22c represents the perfect bonding of Fe with the weld nugget as well as weld nugget with Cu without any major weld defects.

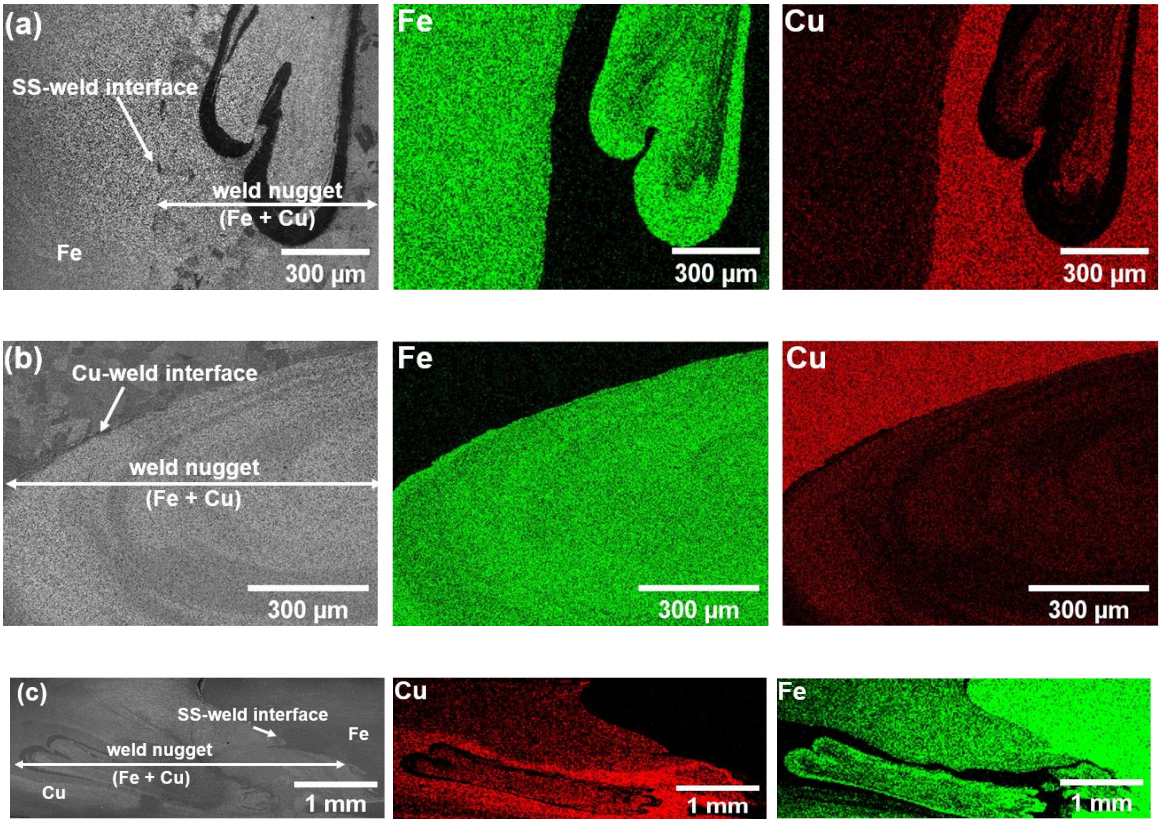

Figure 5.22 SEM-EDS elemental maps of the FSW (Cu-SS) weld sub-regions: (a) SS-weld interface; (b) Cu-weld interface; (c) Centre of the weld nugget

5.3.3.2.4 SEM-EBSD analysis

All friction stir welded joints typically have a sharp boundary between the weld nugget and the TMAZ. This sharp boundary has been recognised in the literature based on the differences in grain sizes between weld nugget and the TMAZ. The FSW weld nugget has been distinguished by its dynamic recrystallized fine grains, and the TMAZ has been identified by its elongated and partially recrystallized grains. However, in the dissimilar FSW process, the tool offset towards one base material will affect the process, so there is a possibility that the dissimilar TMAZ will turn into a

subset of the weld nugget. Simultaneously, a dissimilar FSW has the most recrystallized ultra-fine dissimilar grains in the weld nugget (<1μm) [80] where both optical and SEM techniques cannot resolve such fine grains due to limitations in their spatial resolution. In this investigation, it is important to classify the boundaries between TMAZ and the weld nugget through microstructural characterization techniques. This is because, identifying the correct boundaries between weld nugget and the TMAZ will help to correlate the full-field DIC strain data that correspond to these weld sub-regions, which leads to clarification of their local material stress-strain response. Therefore, an EBSD characterization technique was successfully attempted to classify the boundary between TMAZ and the weld nugget at a high spatial resolution.

Figure 5.23 shows the grain orientation maps of various sub-regions of the FSW (Cu-SS) weld using an orientation code triangle with respect to the plane normal. From Figure 5.23 (a-d) it is observed that a significant population of grains had a <111> direction (blue colour) as their preferential orientation [79]. As the base materials were remote from the weld nugget, many of the copper and stainless steel base material grains (Figure 5.23a and Figure 5.23b) have more random orientations. Figure 5.23a shows the equiaxed copper grains with annealing twins exhibited by the copper base material, and Figure 5.23b reveals the grain orientations of the stainless steel base material austenitic grains. All these base materials grain characteristics derived via EBSD are consistent with both optical and SEM micrographs presented in the previous section of this chapter. Figure 5.23c shows the TMAZ of SS where a few elongated grains are produced along the rolling direction by the plastic deformation and stirring action of the FSW process. As the TMAZ in the FSW was less affected by the plastic deformation and frictional heat compared to the weld nugget, the TMAZ is not expected to have been subjected to as much of a recrystallization effect as the weld nugget [87]. Hence the TMAZ is seen to be completely free from any ultra-fine recrystallized grains. Figure 5.23d shows the grain orientations of the TMAZ/weld nugget interface along the stainless steel side where the ultrafine recrystallized equiaxed grains are evidenced in the weld nugget. Furthermore, a clear boundary between TMAZ (elongated grains) and the weld nugget (fine grains) is evidenced in the EBSD map. The formation of these high-density sub-micron grains in the weld nugget is because of the expected dynamic recrystallization (DRX) effect during the FSW process. This dynamic recrystallization effect is achieved due to the intense plastic deformation and the thermal cycle during the FSW process. The abnormal grain rotation during the FSW process produces a huge volume of grains in the weld nugget (stir zone) which achieves more random orientations compared to other weld sub-regions. It is noteworthy that even using EBSD, some fine grains in the weld nugget cannot be resolved, and hence this needs to be addressed by increasing the magnification and reducing the step size (<0.5 μm) during the EBSD analysis [79]. Prangnell and Heason [83] attempted a detailed EBSD study in the FSW weld face instead of through-thickness cross-sections and successfully obtained grain orientation maps across the weld sub-regions at a high spatial resolution. The authors claim that weld sub-regions were clearly differentiated along the weld face as the dynamic recrystallization effects were much lower on the weld face than in the weld cross-section.

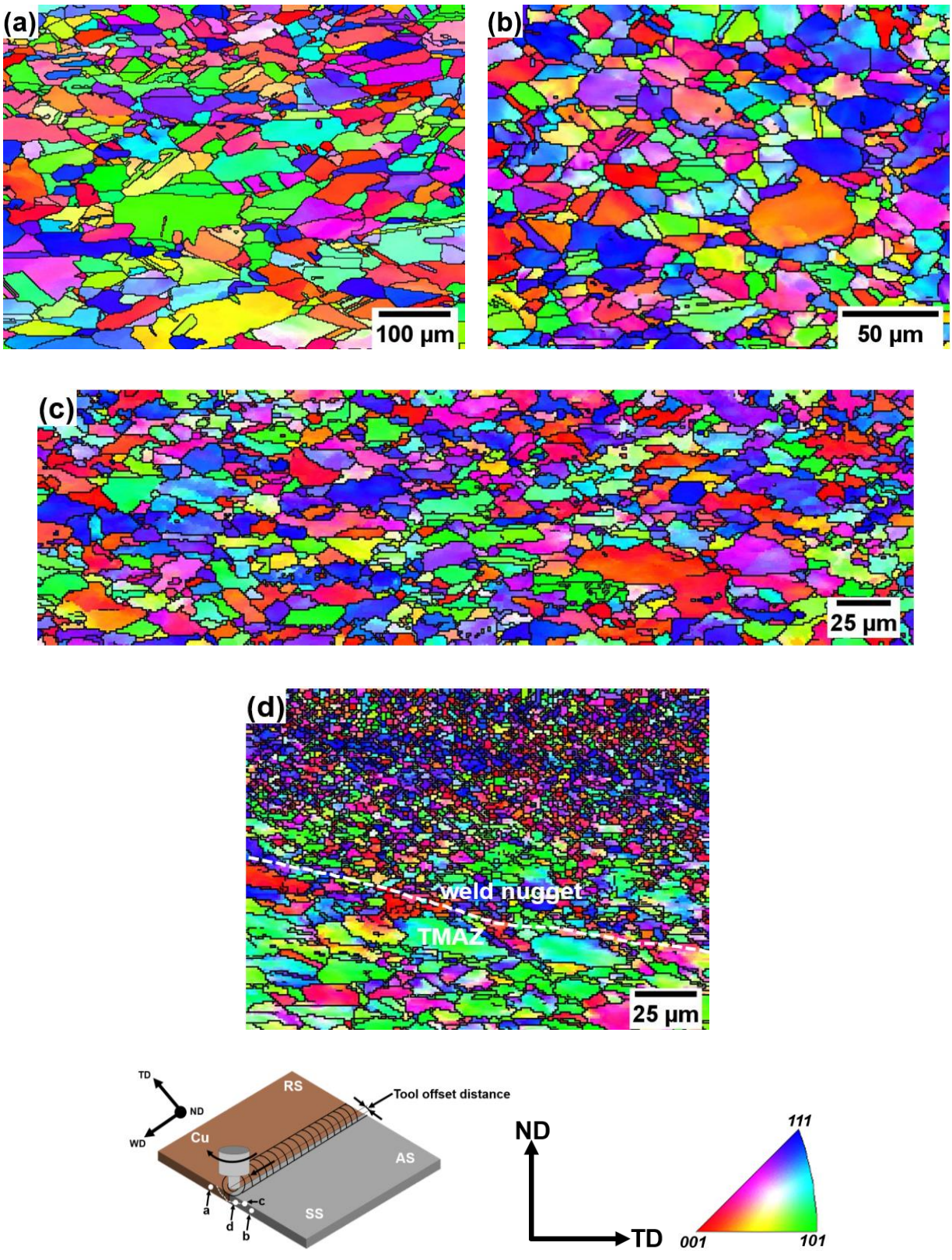

Figure 5.23 SEM-EBSD post-processed micrographs of the FSW (Cu-SS) weld cross-section: SEM-EBSD Inverse Pole Figure (IPF): (a) Cu-BM, (b) SS-BM, (c) TMAZ (SS), (d) TMAZ/weld nugget interface (SS)

5.3.3.3 Microhardness measurements

Microhardness measurements on the FSW (Cu-SS) weld cross-section has been represented by a normal line profile [17, 32, 54-56]. However, a simple microhardness line profile is not the best description for FSW joints, particularly considering the heterogeneous spatial characteristics of a dissimilar material FSW. In dissimilar material FSW joints, a wide fluctuation in the microhardness is expected due to the possible non-homogeneous mixture of dissimilar base materials in the weld nugget. To accurately map this microhardness distribution, a suitable ROI for the hardness measurements was identified, as shown in Figure 5.24a, and indents were positioned in a grid spacing at 0.1 mm intervals, as shown in Figure 5.24b. From Figure 5.24c, it is observed that the size of the hardness indents located on the stir zone are much smaller than the indents positioned at the same load on the copper base material. This immediately shows that the weld nugget is harder than the copper base material due to its possession of large amount of stainless steel fragments compared to the copper. The hardness value of these indents were digitally measured, and the microhardness contour map (Figure 5.24d) was plotted from the measured hardness values around the area (as opposed to a simple line) that covered all the local weld sub-regions. The hardness distribution was found to be entirely consistent in the base materials with average hardness values of 225.9 ± 1.743 HV and 78.05 ± 1.024 HV for stainless steel and copper respectively. These values were compared with the material certificate provided by the manufacturer and found to be within the acceptable limits (indicating that the base material had been unaffected away from the FSW). The transition of hardness from the stainless steel to the weld nugget is more gradual. A sharp fluctuation in the hardness values (121-260 HV) is observed throughout the stir zone because of the significant mixing of stainless steel (AS) and copper elements. This high hardness gradient at the weld nugget is strongly connected with the complex stirring action of the tool and also the thermomechanical aspects of the FSW process. Due to the transmission of stainless steel fragments across the copper boundary from the effect of tool offsets during the FSW process, a non-homogeneous hardness zone is created at the Cu interface.

Although the weld nugget of the FSW (Cu-SS) was dominated by the Fe compared to the Cu (from the EDS maps), the average value of microhardness (250.85 ± 1.53 HV) in the weld nugget is significantly higher than in the parent stainless steel due to the presence of fine recrystallized grains. This observation agrees with the findings reported by Imani et al.[55] and Aval et al.[56]. The varying microhardness distributions shown in the contour map clearly represent the heterogeneous characteristics of the FSW (Cu-SS) weld, and this finding also agrees with the SEM-BSE/SEM-EDS results. Nevertheless, the hardness properties of other weld sub-regions such as TMAZ and HAZ regions located along the copper and stainless steel sides cannot be clearly differentiated from the microhardness measurements. From the above findings offered by the microhardness measurements, it is apparent that the hardness properties of the FSW (Cu-SS) weld sub-regions are not simply correlated with their distinctive microstructural features. This is due to the limitations involved in

the spatial resolution of the microhardness measurements. Therefore to establish the hardness measurements as a key technique for determining the local weld sub-regions and also to compute the local mechanical property of the weld nugget such as elastic modulus, an instrumented nanoindentation technique is proposed in future work. As it is not feasible to determine the standard elastic modulus value for the FSW (Cu-SS) weld nugget from literature sources, the elastic modulus can be determined by the nano-indentation method, and this will be compared with the DIC strain measurements derived from the weld nugget.

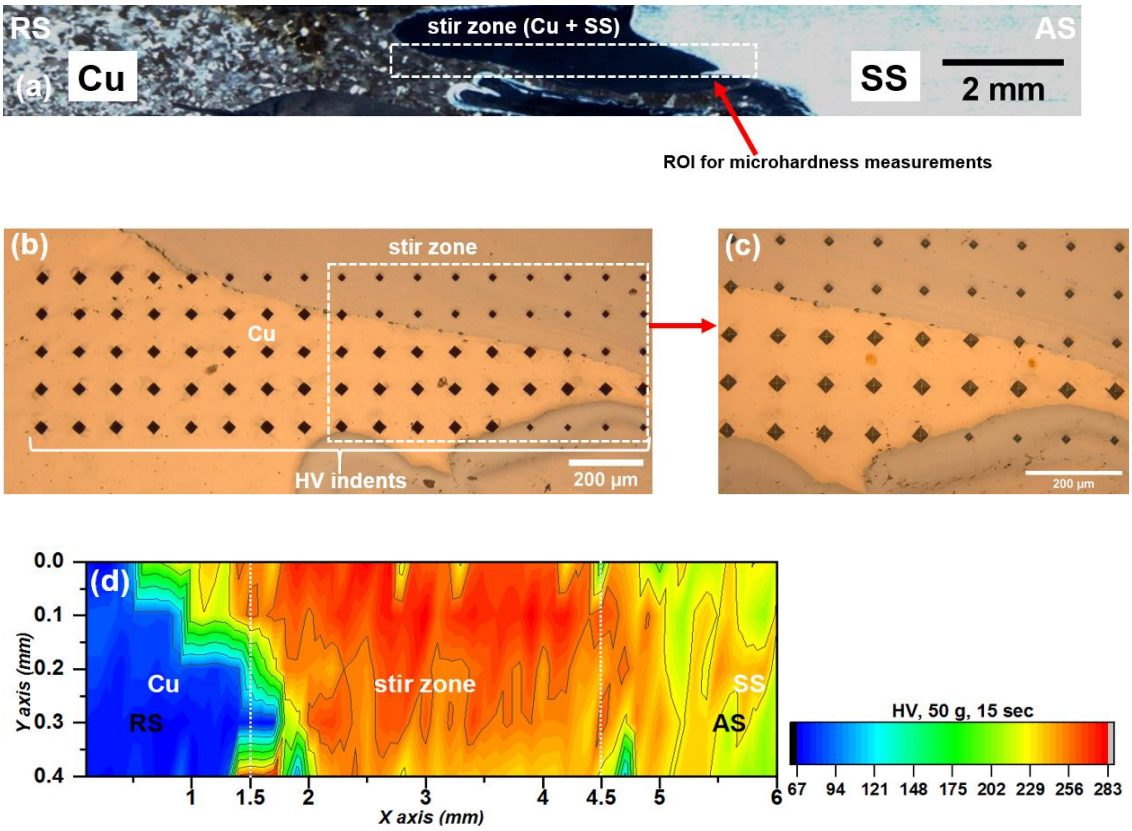

Figure 5.24 Microhardness results of the FSW (Cu-SS) weld cross-section: (a) Macrograph shows the ROI screened for microhardness measurements; (b) Optical micrograph shows the microhardness indents positioned across the weld; (c) Magnified Optical micrograph of the ROI shown in (b); (d) Microhardness contour map

5.4 Summary

The results obtained from the various materials characterisation techniques performed in the FSW (SS-SS), FSW (Cu-Cu) and FSW (Cu-SS) joints are presented and discussed in this section. These results clearly show that all the FSW joints have reduced thickness across the weld nugget as well as heterogeneous microstructures along the weld cross-section and weld surface. The FSW process produced ultrafine recrystallized grains in the weld nugget with a narrow HAZ. Both the AS and RS regions of the FSW (SS-SS) joint have achieved different microstructural features. However, the AS

and RS of the FSW (Cu-Cu) joint had similar microstructural features. The FSW (Cu-SS) joint has more complex microstructure than the similar FSW joints due to the non-homogenous material flow of copper and stainless steel in the weld nugget. The weld nugget of FSW (Cu-SS) joint has high density of SS than Cu. It is noteworthy that the FSW tool wear (presence of W particles) is evident only in the FSW (SS-SS) joint. The findings derived from the microhardness measurements on these welds are not completely aligned with the microstructure of the weld sub-regions due to limited spatial resolution. Therefore, to achieve microstructure-mechanical property relationships of the FSW welds, it is essential to involve a High-Resolution (HR) full-field technique such as Digital Image Correlation (DIC) to assess the post-yield behaviour of the highly heterogeneous microstructure of the FSW welds. Additionally, the complex geometry of the FSW weld should be established to identify the local geometry effects on the stress-strain material response. The results obtained from the HR-DIC measurements on the FSW (SS-SS), FSW (Cu-Cu) and FSW (Cu-SS) joints by accounting the FSW weld geometry are discussed in the next chapter of this PhD thesis.

Chapter 6 Validation of the high fidelity full-field imaging procedures for high-resolution strain measurements on FSW welds

6.1 Introduction

As described in detail in chapter-3, DIC has been used on FSW joints with the focus on attempting to assess the local material behaviour of weld zones [25, 30, 41, 96, 97]. However, the optics used in these studies produced low spatial resolution images and also focused the local region of interest (ROI) either across the surface or through the weld cross-section. Due to the complex thermo-mechanical cycle that occurs in the FSW process, the FSW weld nugget contains fine recrystallized grains alongside a slight thickness reduction produced by the plastic deformation experienced in the FSW process [29]. During tests in uniaxial tension, the local geometry variations at the weld produce an out-of-plane displacement, which can be removed from the measurement of the in-plane strains by using stereo DIC [98]. Nevertheless, most DIC studies on FSWs used specimens that were machined to the reduced thickness of the weld nugget to avoid any out-of-plane displacements [25, 29, 30, 41, 96, 97]. Although this approach enables a more accurate single-camera (2D) DIC, it neglects the effects that the post-weld machining procedure may have on the material microstructure and its effect on the local strain distributions. Notably, only [29] considered the local thickness variations of the FSW weld on the post-processed DIC results, but, in general, the FSW geometry and its effect on local strain distribution have not been considered [25, 30, 41, 96, 97]. Therefore, in this chapter, the development of a new high-fidelity HR-DIC methodology is described that enables high-resolution strain measurements on a typical joint without reducing the actual thickness of the joint. HR-DIC requires imaging at a very high magnification using a macro lens, which provides a narrow depth of field due to its short focal length [31] and a limited field of view. Therefore, in the process of developing the HR-DIC approach, the following significant experimental and post-processing challenges were addressed:

- The effect of the geometry of the test specimen in the region of the weld causes out-of-plane deformations and consequent parasitic in-plane strains. Executing stereo DIC at the short focal length necessary for the macro lens is practically impossible, so a means of identifying the out-of-plane displacement is developed which allows the parasitic strains to be removed from the in-plane strains obtained by the HR-DIC.

- The limited field of view of the macro lens means that the entire weld region cannot be captured by a single image. Hence, it is necessary to develop an experimental methodology

that enables sequential loading and the capture of multiple images across the weld region to fully exploit the full-field nature of DIC.

- The capture of the separate images requires that an image stitching procedure is developed to provide the strain field across the entire welded region.

To systematically address the above challenges, a novel experimental procedure based on HR-DIC and optical measurements of specimen geometry is developed, which allows the local material properties of the FSW to be determined. The purpose of the work described in the chapter is to validate the methodology on the FSW (SS-SS) joints, the production of which is described in chapter 4. Once the HR-DIC procedure has been validated in the elastic range on the FSW (SS-SS) joint, the procedure is adapted in Chapter 7 to study the behaviour of a range of materials subject to plastic deformation.

6.2 HR-DIC experimental set-up

Figure 6.1a shows the exact tensile specimen, presented generally in Figure 4.7 that was machined from the FSW (SS-SS) joint for the HR-DIC experimental methodology demonstration. The fine black speckled pattern required for the HR 2D-DIC analysis was created using an airbrush kit (Make: Clarke, Dunstable, UK; Model: CAB 3P) operated at 40 psi pressure with a 0.2 mm diameter nozzle on a white painted background specimen using Createx paint as shown in Figure 6.1b. The HR 2D-DIC experimental set-up and the region of interest (ROIs) for HR 2D-DIC strain measurements within the material elastic range are shown in Figure 6.2a and Figure 6.2b, respectively. As it was planned that the tests would be in the elastic region only the premise was that each region could be imaged separately and the loading repeated for each region.

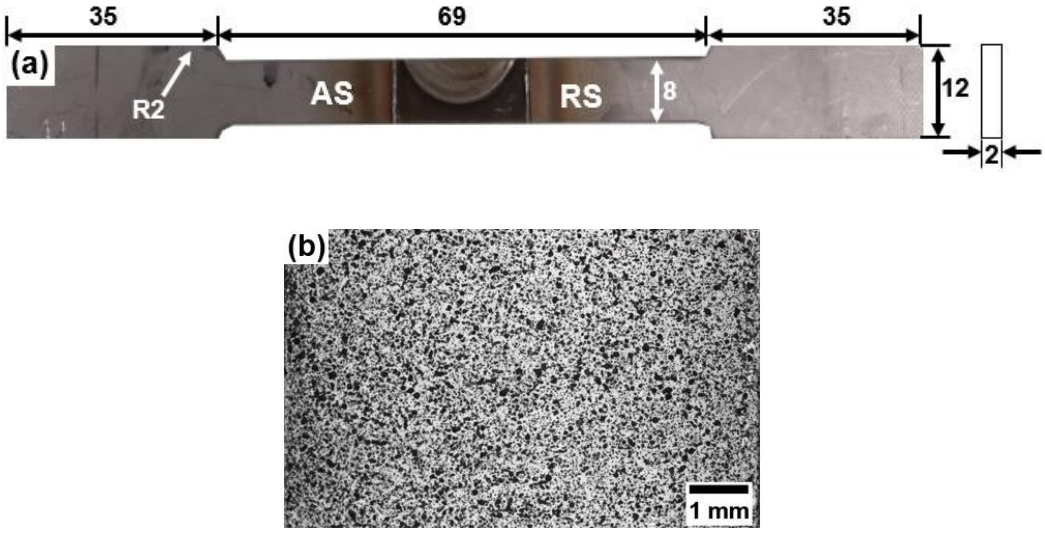

Figure 6.1 Specimen preparation for HR-DIC measurements: (a) FSW (SS-SS) specimen used to develop the HR-DIC methodology; (b) Fine speckle pattern produced through an airbrush [34]

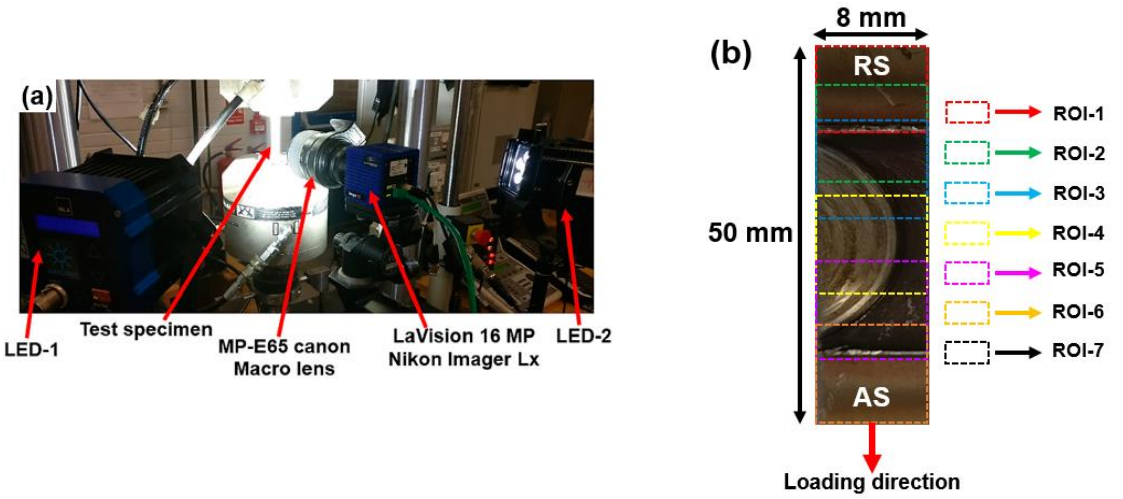

Figure 6.2 (a) The HR 2D-DIC experimental setup; (b) Region of interest (ROI) for the high-resolution (HR) 2D-digital image correlation (DIC) strain measurements on the FSW (SS-SS) joint [34]

It was decided for the initial HR-DIC set-up to use a 16 MP CCD camera (Make: LaVision, Gottingen, Germany; Model: Imager Lx) having a resolution of 4904 × 3280 pixels fitted with a Canon MP-E 65 mm focal length macro lens. Through these high-resolution optics, the images were captured at the spatial and strain resolution of 300 pixel/mm and 6.4390 × 10^{-5}, respectively. The illumination was provided throughout the test with a pair of 40 W LED lights, and all the images were recorded at a frame rate of 1 Hz. All the uniaxial tensile tests were performed in an Instron-8800 servo-hydraulic testing machine equipped with 5 kN load cell. The specimen was tested in the position control mode at a displacement rate of 0.1 mm/min. Load values for each image being captured were recorded using a separate Analog to Digital converter (ADC) channel data acquisition system. The specimen surface was maintained perpendicular to the camera sensor axis.

All the recorded images were processed using commercial data correlation software LaVision (DaVis 8.3.1, LaVision, Gottingen, Germany). This software uses the least square difference method (LSM) to compute the position of displacement vector fields and also employs a 6^{th} order spline interpolation to achieve sub-pixel displacement accuracy. All the HR-DIC data were processed using a subset size of 59 × 59 pixels and step size of 10 to increase the correlation accuracy and also to minimise noise in the strain maps. The DaVis system employs a central difference scheme to compute the strain values using a fixed strain window size of three data points. To maintain the same spatial resolution at different ROIs during the HR-DIC experiments, the cross-head of the servo-hydraulic test machine was moved at sequential stages instead of adjusting the position of the tripod where the HR-DIC optics were mounted. This procedure was adopted because of the narrow depth of field of HR-DIC optics to eliminate any need to adjust the optical stage on which the camera was mounted and hence, maintain a constant spatial resolution for each image. Thus, the position of HR-DIC optics was fixed

throughout the mechanical tests. It is important to note that the sequential loading approach can only be used for tests conducted in the material elastic region but is acceptable for the purposes of validating the HR-DIC procedure.

6.3 FSW (SS-SS) Weld Surface Geometry

It is clearly visible in Figure 6.3a that the cross-section of the weld nugget is thinner than the base material. The impact is that when the specimen is loaded in tension to perform the DIC, an offset loading will be experienced across the welded section causing a non-uniform strain through the thickness of the welded region. To avoid this, most DIC investigations [30, 32, 41] have been attempted on the FSW specimens that were machined to the reduced thickness of the weld nugget. However, it is necessary to establish the geometry change in the FSW (SS-SS) specimens.

This was carried out using an Alicona optical 3D measurement system. The Alicona 3D surface topography maps derived from the trial Alicona scans (vertical resolution: 4 μm) on the ROI-1 and ROI-2 of Figure 6.3a with respect to their reference position (height = 0 μm) are shown in Figure 6.3b and Figure 6.3c, respectively. From these maps, a sharply reduced thickness in the weld nugget is clearly evident. It is noteworthy that the thickness reduction is more predominant in the RS than the AS of the weld. The Alicona full-field measurements provide the specimen thickness measurements that are used to calculate the stress in the cross-section in the DIC stress-strain behaviour analysis.

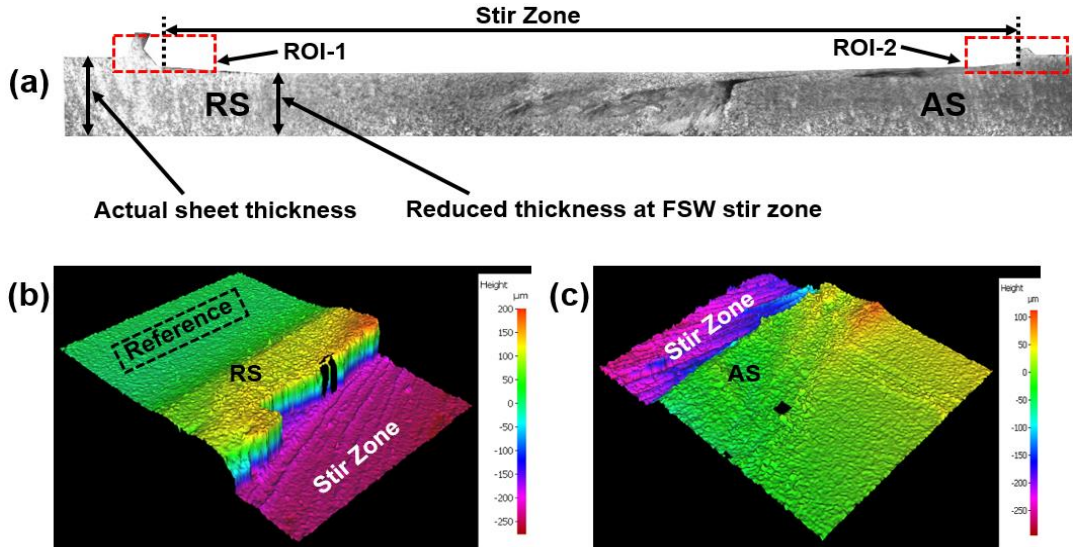

Figure 6.3 (a) ROIs (1, 2) for the Alicona profile measurements along the FSW (SS-SS) weld cross-section; (b) Alicona 3D surface topography of the ROI-1 located in (a); (c) Alicona 3D surface topography of the ROI-2 located in (a) [34]

A suitable ROI (Figure 6.4a) in the weld surface of a tensile specimen was chosen for the Alicona full-field surface measurements. Figure 6.4b shows the Alicona derived (vertical resolution: 1 μm)

whole weld geometry embedded with local thickness variation measurements. Here the large thickness reduction in the weld nugget and especially the shoulder affected region ("a" in Figure 6.4b) is evident. An additional thickness reduction in the region "a" was due to an extra dwell time spent by the tool shoulder while retracting the tool at the end of the FSW process. By post-processing the Alicona 3D data points, the average thickness reduced in the region "a", "b", and "c" are determined as 0.48 ± 0.042 mm, 0.34 ± 0.027 mm, and 0.40 ± 0.075 mm, respectively. The thickness variations across the horizontal lines (1, 2), as illustrated in Figure 6.4b are plotted as line profiles shown in Figure 6.4c. From Figure 6.4c, it is important to note that the outer boundaries of the weld nugget had a marginal increase in thickness (0.2 to 0.5 mm) with respect to the reference position because of extruded material depositions during the FSW process. Moreover, the line profiles also reveal the presence of minor deformation in the joint (<0.05 mm), which is removed when the specimen is subjected to tensile stress during the mechanical tests.

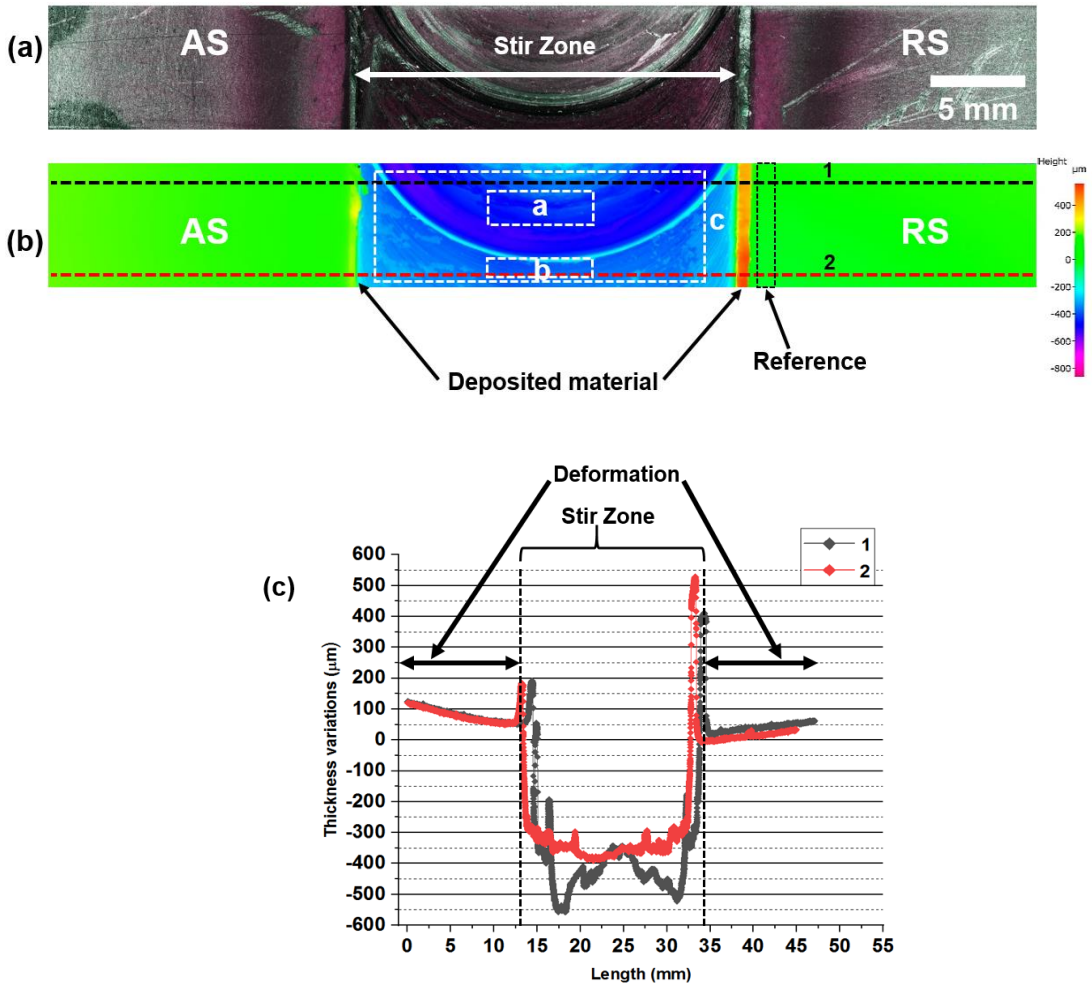

Figure 6.4 (a) Alicona ROI on the FSW (SS-SS) weld surface; (b) Alicona surface profile of the FSW (SS-SS) weld surface. (c) Line profiles showing the thickness variations along the horizontal lines (1, 2) as shown in (b) [34]

6.4 Image stitching procedure

As the HR-DIC measurements have a limited field of view, it is necessary to employ an image stitching algorithm to combine an array of DIC strain maps to obtain the full-field strain distributions over the entire welded region. Figure 6.5a shows the welded region divided into six ROIs for the HR-DIC strain measurements with their corresponding speckle patterns imaged using the HR-DIC optics. The grey scale DIC images from each ROI captured at the same load step were sequentially stitched through the Image-J (Fiji) software, as demonstrated in Figure 6.5b. The theory behind this stitching method has been explained elsewhere [99]; an overview of the procedure is given in Figure 6.5b.

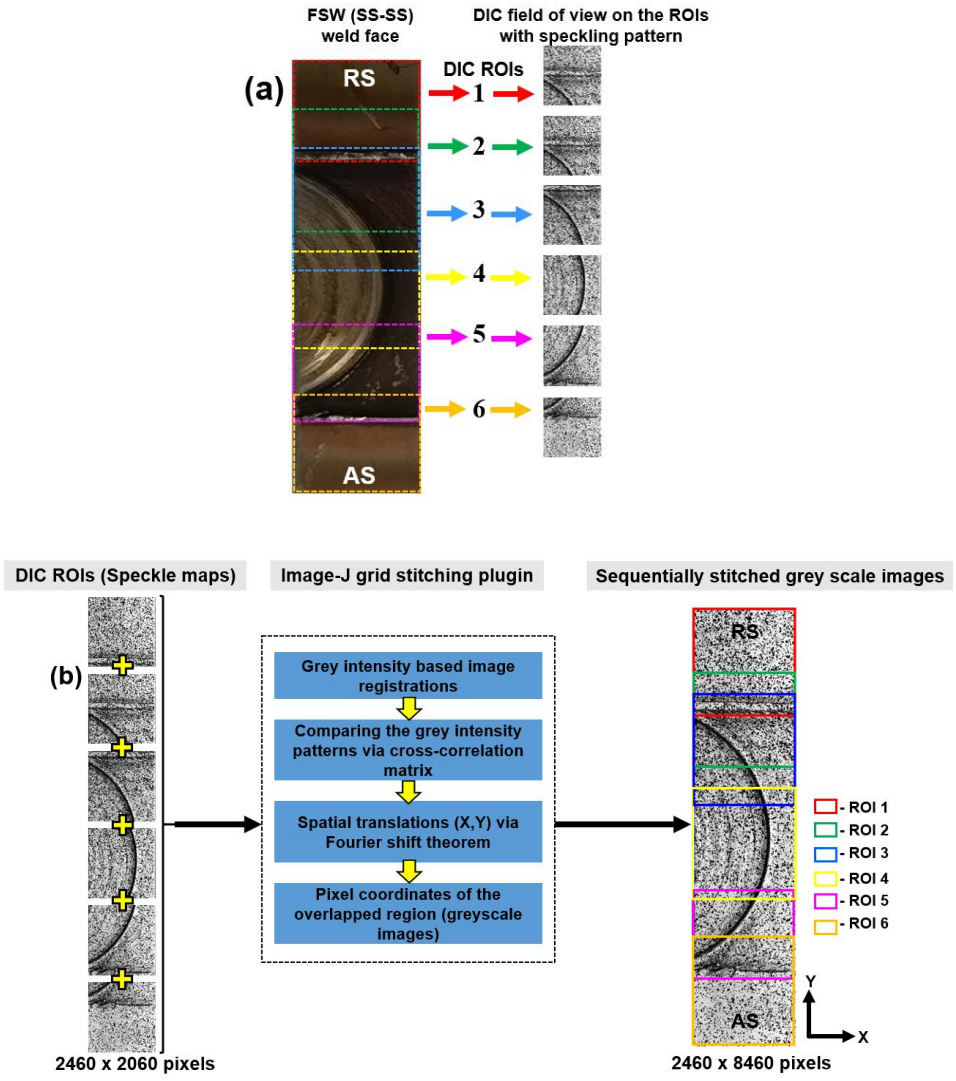

Figure 6.5 Sequential image stitching using ImageJ: (a) DIC speckle maps captured from the ROIs; (b) Image stitching procedures involved in Image-J to stitch DIC speckle maps (grey scale images) [34]

To summarise, the Image-J software uses a Fourier shift theorem based stitching algorithm that correlates the pixel grey level intensity values in the image so that the pixel coordinates in the overlap region can be obtained with sub-pixel accuracy [99]. Based on the computed pixel coordinates, the sequence of images is fused using a linear blending method, where the grey level intensity of the overlapped region is adjusted. The fidelity of the Image-J grid plugin for stitching the DIC strain maps has been tested [100] and clearly evidenced that this method has minimum interpolation error compared to other stitching methods.

Initially, DIC correlation was performed on the stitched images, but this resulted in a series of artefacts in the stitched region, as shown in Figure 6.6. This is due to an interpolation error caused by the different sub-pixel accuracy of the DIC correlation software and Image-J software. Additionally, an intensity smoothing made by the image stitching software at the overlapped region further amplifies the error during correlation through the DIC software, as mentioned in [100]. To further compound the difficulties, the procedure used to capture the images results in lighting fluctuations due to the close proximity of the lens to the test specimen. Hence to avoid the artefacts, the post-processed individual DIC strain maps were stitched to visualize the strain distribution over the entire field. As the Image-J stitching procedure works only on grey scale images, it is not straightforward to stitch the RGB colour format DIC strain maps. However, the pixel coordinates derived from the overlapped grey scale images can be used as reference points to stitch the corresponding DIC strain maps. Due to the step size of ten pixels in overlapping the subsets of DIC correlation, the resolution of the DIC strain map is 246 × 206, i.e., one-tenth of the pixel resolution of speckle map (2460 × 2060) as shown in Figure 6.7. To spatially stitch the strain data using the already computed overlap coordinates of the speckle maps, the overlap coordinates determined from the high spatial resolution speckle maps must be scaled to the resolution of the strain map. To achieve this, it is necessary to export TIF images of the strain map, which are compressed and hence, further image processing is required. Adobe Photoshop was used to adjust the spatial resolution of the strain maps to one-tenth of the greyscale images (246 × 206) captured by the camera by using a bicubic interpolation to generate strain maps as represented in Figure 6.8.

Figure 6.8 shows the procedures for stitching the RGB strain map images using the strain map coordinates determined from the grey scale images based on the overlap pixel coordinates. During the stitching process, the series of strain maps (RGB) are converted into their equivalent grey scale format, and the necessary spatial translations performed to align the images with the strain map coordinates of the overlapped region. All the spatially translated strain maps are fused at the overlapped region using a linear blending method. The finally stitched grey scale strain map is converted into its equivalent RGB colour format, as shown in Figure 6.8. The reliability of the stitching approach using the derived strain map coordinates of the overlap region is verified by extracting correlation coefficients using Image-J. The average correlation coefficient achieved by the final stitched strain maps was 0.93 ± 0.019, which shows a high degree of confidence in the accuracy

of the image stitching. The procedure provides only a visualization in the image form of the full field strain distribution. Therefore, it is necessary to devise a means of stitching the displacement/strain data so that further manipulation and interrogation of the data can take place. This would enable strain values at discrete points to be extracted and combined to allow, e.g., principal strain and stress maps to be produced.

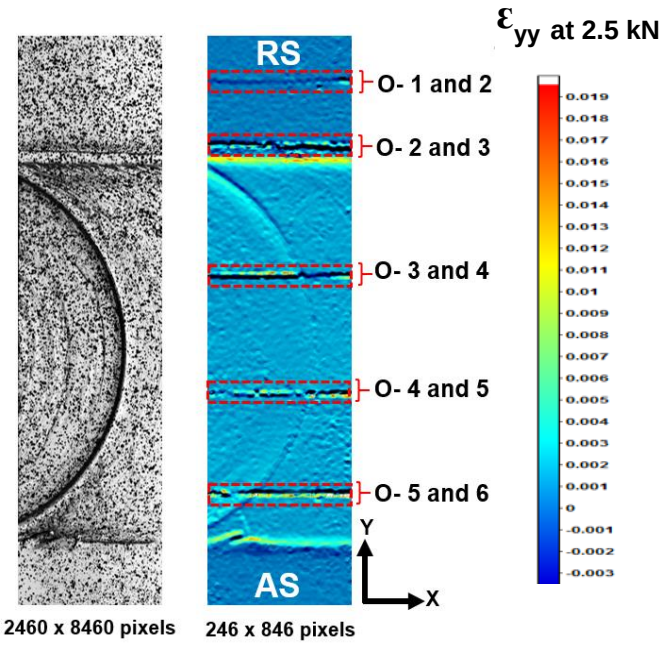

Figure 6.6 ε_{yy} strain map derived from the DIC correlation on the stitched speckle maps of the FSW (SS-SS) weld at 2.5 kN (O—Overlap between the images)

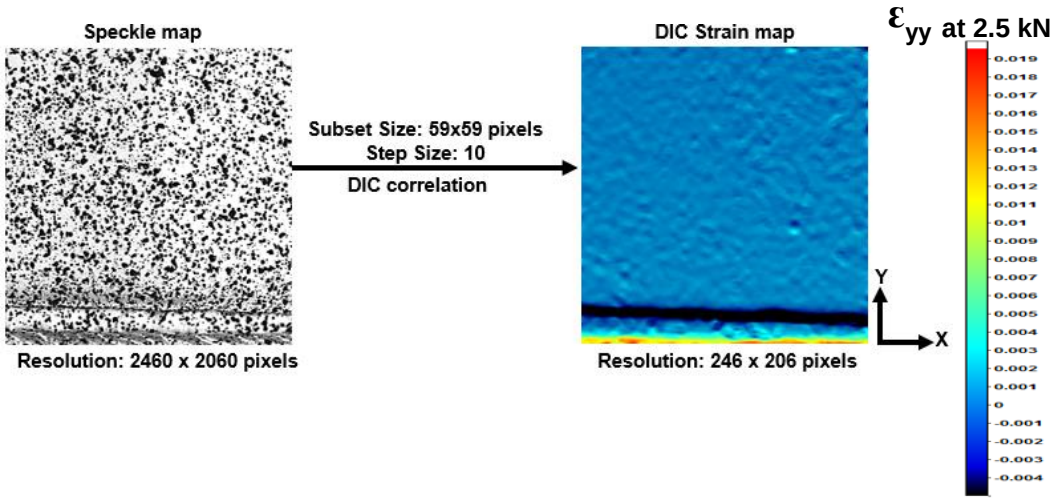

Figure 6.7 Speckle map and its corresponding DIC strain map at 2.5 kN [34]

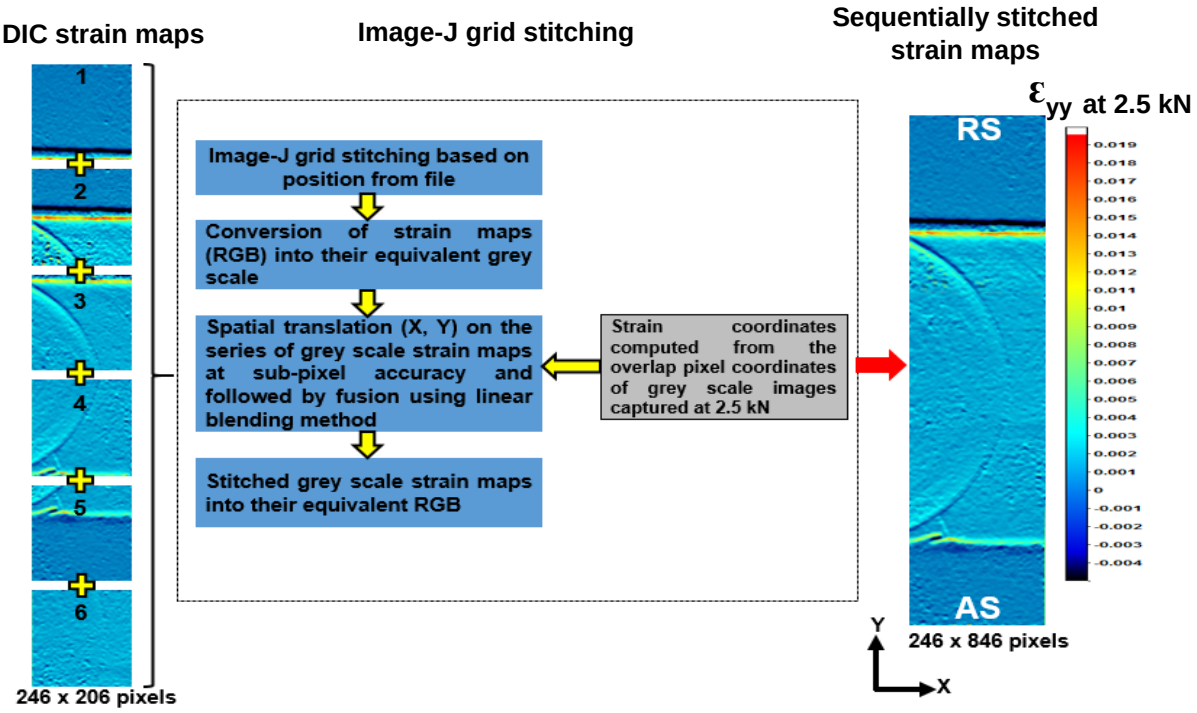

Figure 6.8 Image stitching procedures in Image-J to stitch strain maps (RGB) using reduced pixel coordinates determined from the stitched grey scale DIC speckle images [34]

6.5 HR-DIC strain data stitching procedure

To interrogate the stitched strain maps, it is necessary to devise a means of stitching the HR-DIC strain data implemented using the image processing functions of Image-J and MATLAB [100, 101]. Figure 6.9a shows the sequential steps involved, where each array of strain data obtained from the different ROIs was imported from DIC correlation software (DaVis) into Image J using a MATLAB script. By using the strain map overlap coordinates derived in the previous section, the appropriate spatial translations were made to align the strain data with sub-pixel accuracy. As in the previous section, the spatially translated data sets (grey scale) were fused in the overlap region using a linear blending method. Then MATLAB was used to convert the Image-J stitched strain data (grey scale) into a colour contour plot shown in Figure 6.9a, i.e., a full-field strain map where data interrogation is possible. To confirm the reliability of the stitching approach, the strain values along the vertical line shown in the colour contour plot were correlated with the manually aligned strain data sets shown in Figure 6.9b. In the manual method, the data in the overlap was aligned visually, and the average strain value taken from the two overlapping points. The data points plotted from these approaches are spatially overlap with one another. This agreement between the manual method and the MATLAB stitching confirms the accuracy of the stitching approach.

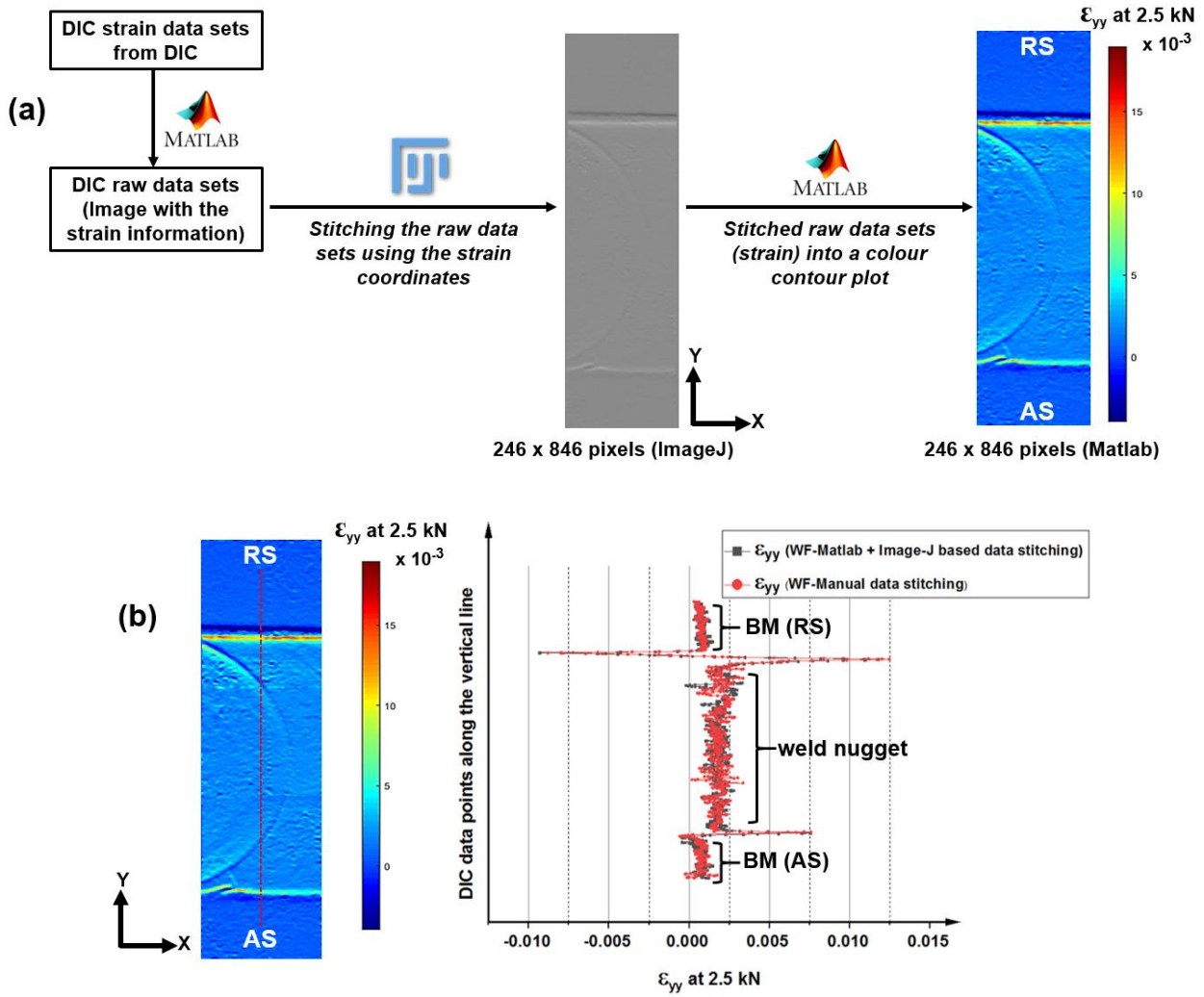

Figure 6.9 (a) MATLAB and Image-J based strain data stitching procedures; (b) Correlation between the stitched strain data and manually stitched data (right) along a vertical line as shown in the strain map (left) at 2.5 kN [34]

6.6 HR-DIC strain measurements and procedure for removing parasitic strains

Figure 6.10a shows the full-field stitched strain maps derived from the weld face (WF), weld root (WR) and weld cross-section (CS) at 2.5 kN tensile load. It is clear that both the base material regions (AS and RS) have more uniform strain distributions than the weld nugget (WF). Furthermore, the strain gradient is clearly evident across the weld nugget CS due to the specimen bending caused by the reduced thickness of the weld nugget. In Figure 6.10a, on the WR side of the specimen, there are two localized regions of high strain. One region is at the joint and is simply where the weld has not penetrated through the material, and the other is a small crack occurring close to the interface of the weld nugget. There is no indication of the crack in the weld CS image because the spatial resolution

is not sufficient to identify a crack. The cracks are visible in the high-resolution images of the specimen shown in Figure 6.10b.

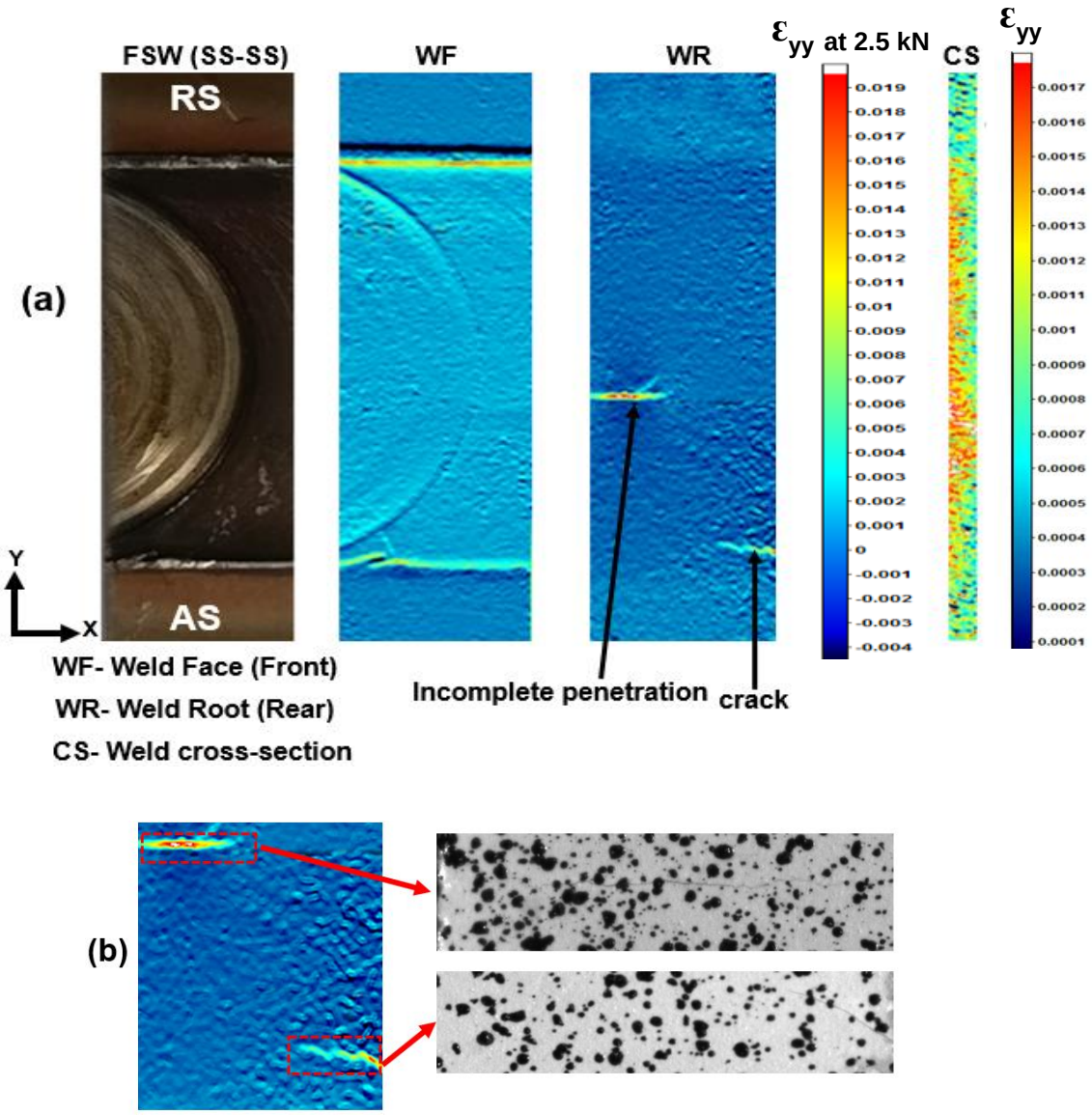

Figure 6.10 (a) ε_{yy} strain map of the FSW (SS-SS) weld along the weld face (WF), weld root (WR), and weld cross-section (CS) at 2.5 kN; (b) defect locations on the WR [34]

Figure 6.11b shows the strain measurements (WF and WR) plotted along the line, as shown in Figure 6.11a. There are large strains at the interface between the stir zone and the base material on the WF, which could be attributed to the inevitable stress concentration due to the rapid change in geometry. However, it should be considered that the build-up of material on the RS highlighted in the Alicona images (Figure 6.3b), would defocus the cameras, and may also produce some decorrelation. There is a clear increase in strain in the stir zone on the WF and a reduction on the WR; the average of the two values gives the same strain as that of the theoretical value of weld nugget (Figure 6.11c). This clearly shows that the specimen is bending as a result of the thinner cross-section in the stir zone; it

is noticeable in the line plots in Figure 6.11c that the strain away from the stir zone on both the WF and WR sides of the specimen have the same value as expected in theory. Figure 6.11c also shows the shear (ε_{xy}) and transverse (ε_{xx}) strain plots derived from the average of WF and WR, and these plots are also close to theory. Thus, the bending has led to out-of-plane displacements and additional bending strains, and therefore, additional parasitic strains caused by rigid body motion towards and away from the DIC optics, which are included in the DIC measured in-plane strains on the weld nugget. The theoretical strain value (ε_{yy} = 0.001) of the weld nugget at 2.5 kN is calculated based on its cross-section area measured through Alicona (13.04 mm^2) and known elastic modulus of the 304 SS (E = 200 GPa).

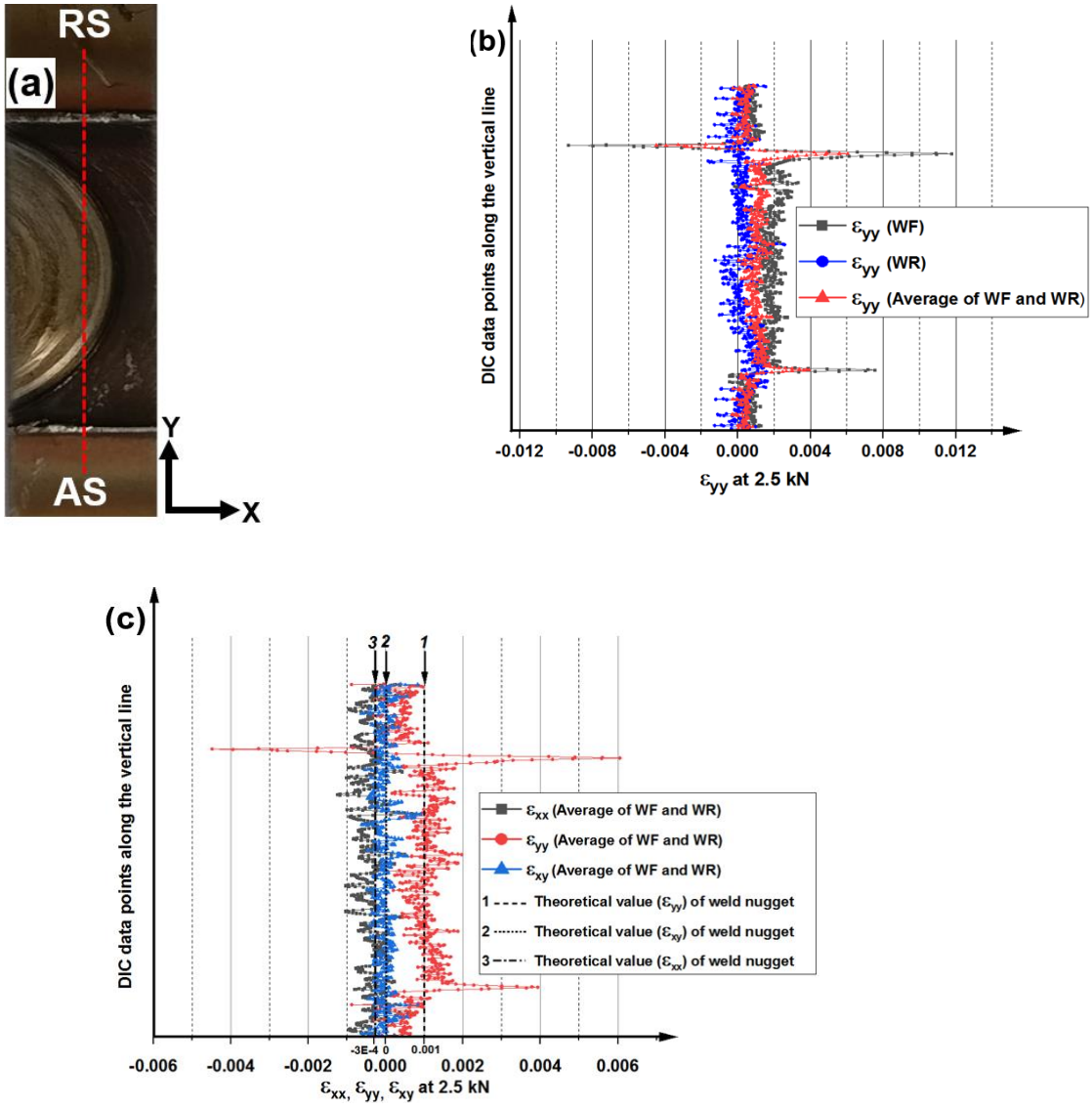

Figure 6.11 Strain distribution through the weld region: (a) DIC ROI; (b) strain distribution on the WF and WR along the vertical line shown in (a) at 2.5 kN load; (c) average strain (ε_{xx}, ε_{yy}, and ε_{xy}) distributions [34]

To validate the procedure, a stress-strain curve was developed for the data taken from the base metal, and weld nugget regions from both the WF and WR faces of the specimen, as shown in Figure 6.12a.

The stress was adjusted to take account of the reduction in cross-sectional area in the weld nugget region. The local stress-strain curves derived from the BM and weld nugget of WF and WR are shown in Figure 6.12b. The elastic modulus is determined from linear fitting the stress-strain curves in each region of interest indicated in Figure 6.12b. It is noted that both the BM regions (AS and RS) of WF and WR have an elastic modulus very close to the theoretical value. The elastic modulus derived for the weld nugget on the WF side was 100 ± 1 GPa, and for the weld nugget on the WR shows infinite stiffness, thus, providing an excellent illustration of the deleterious effect of the out-of-plane deformation on DIC measurements. Hence, as stereo DIC cannot be applied, there is a necessity to apply an appropriate correction procedure to remove the bending and parasitic strains from measured in-plane strains across the FSW weld nugget.

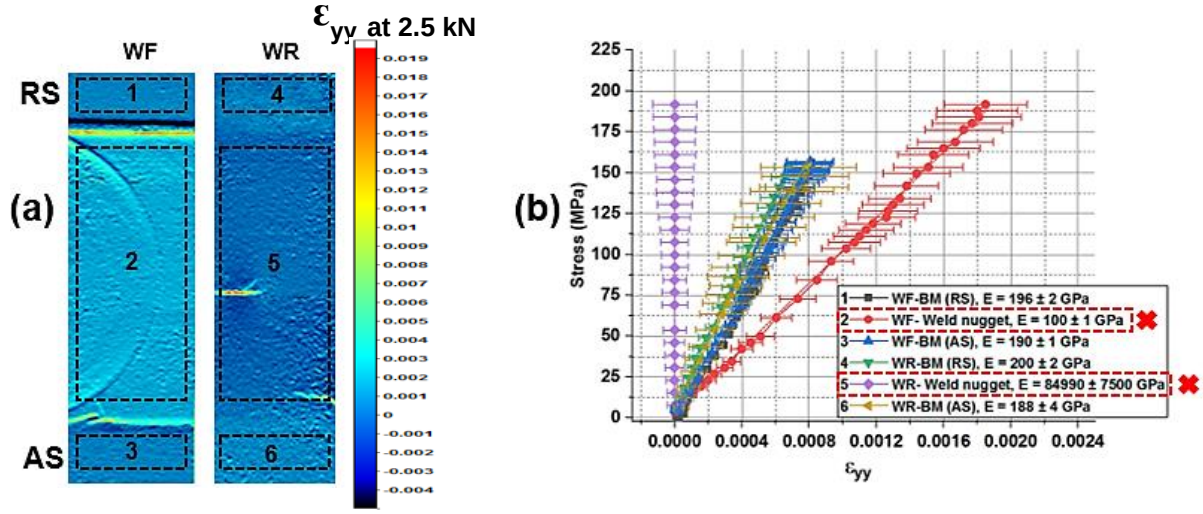

Figure 6.12 (a) ROIs on WF and WR for local stress-strain curves; (b) local stress-strain curves of WF and WR [34]

Although the average strains measured from the front and rear face of the weld nugget and base materials had the expected theoretical Young's modulus value, the strain value recorded is a combination of the strain caused by the out of plane displacement and the bending strain resulting from the offset load. It is useful therefore to establish the amount of bending strain expected and compare this to the estimate of the strain caused by the out of plane displacement as shown in the below equation [98]:

$$\varepsilon_{xx} = -\frac{\Delta Z}{Z} \quad \ldots 6.1$$

where ΔZ is the out-of-plane displacement and Z is the stand-off distance. The strain produced by the bending of the specimen is calculated from the total stress (σ) experienced by the actual FSWs is the combination of the axial tensile stress (σ_a) and bending stress (σ_b) as follows:

$$\sigma = \sigma_a \pm \sigma_b = \frac{P}{wt} \pm \frac{6Pe}{wt^2} \ldots 6.2$$

where P is the load, w is the width, t is the thickness, and e is the reduction in thickness caused by the FSW

Equation 6.2 is further simplified to give:

$$\sigma = \frac{P}{wt}\left(1 \pm \frac{6e}{t}\right) \ldots 6.3$$

This value is then divided by Young's modulus to give a theoretical bending strain which is then added to the strain caused by the out of plane displacement to give the parasitic strain caused by a combination of the bending and out-of-plane displacement as shown in Figure 6.3. Figure 6.3a and Figure 6.3b show the stress-strain response of the weld face (WF) and weld root (WR) respectively calculated using Equation 6.3 along with the DIC measured strains. Parasitic strains were obtained using Equation 6.1 with the known standoff distance. From Figure 6.3, it is noted that the DIC measured strain along the WF and WR at various load steps is the sum of axial, bending and parasitic strains (due to out-of-plane displacement). However, it is important to note that both the bending as well as parasitic strains can be removed if the DIC measurements from the WF and WR are averaged.

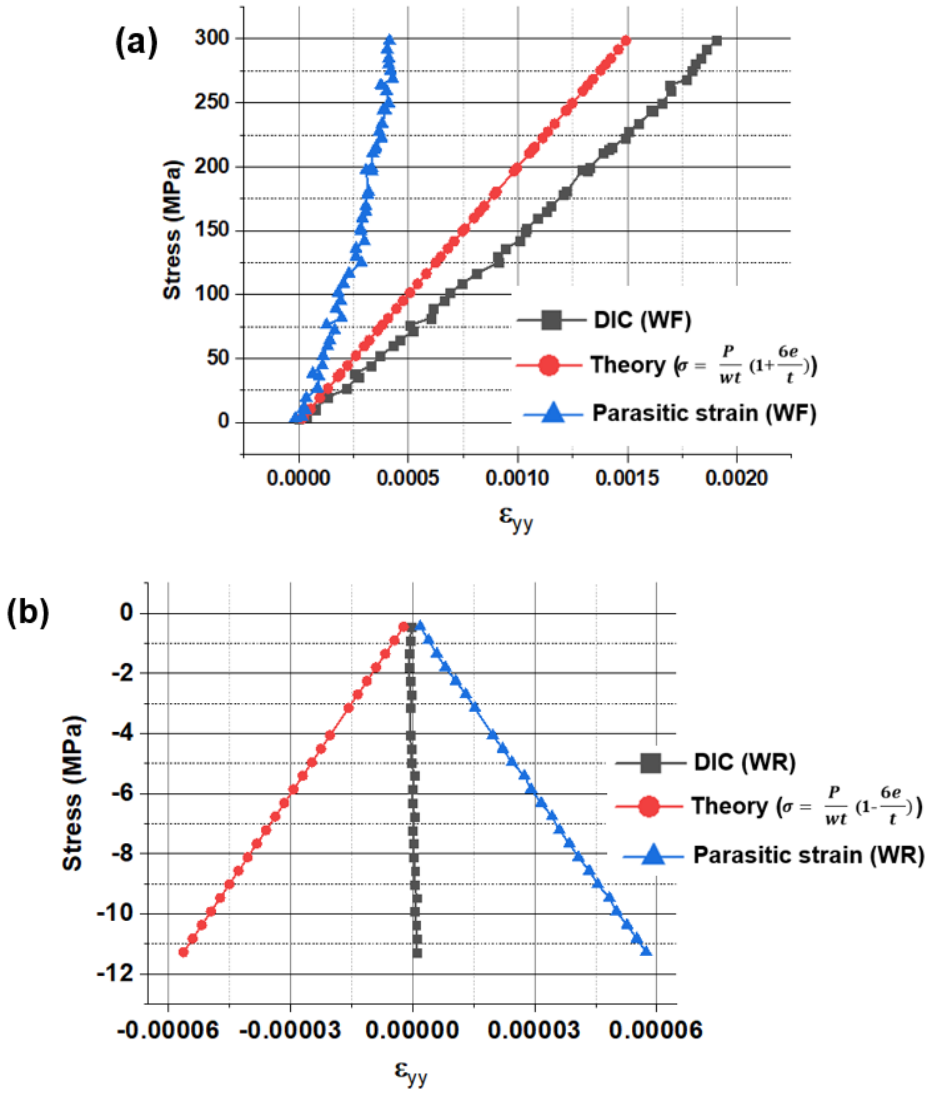

Figure 6.13 Stress-strain response of the FSW (SS-SS) weld nugget in the elastic limit (DIC measured Vs Theoretical bending): (a) Weld Face; (b) Weld Root

The out-of-plane displacement was evaluated from the DIC measurements carried out on the CS, as shown in Figure 6.14a. From this procedure, the average out-of-plane displacement (ΔZ) was measured on the weld nugget (CS) at different load values. An average parasitic strain ($\Delta Z/Z$) at a particular load value can be calculated by using the known stand-off distance (Z) and its corresponding (ΔZ) as given by equation 6.1. To measure the out of plane displacement (ΔZ) of the weld face, the HR-DIC experimental set-up was pointed towards the edge of the specimen. From the HR-DIC measurements, the x-displacement measured along the edge of the specimen during the uniaxial tensile test was considered as the out of plane displacement (ΔZ) of the weld face. Hence, the corrected strain at a particular load value was derived by eliminating the parasitic strains from the DIC measured strains. The modified stress-strain curves of the weld nugget (WF and WR) determined by applying the above correction procedure are shown in Figure 6.14b. After applying the correction procedure, Young's modulus of the weld nugget on the WF and WR faces were determined as 193 ± 2 GPa and 201 ± 3 GPa, respectively. These elastic moduli values are very close to the expected theoretical value (E = 200 GPa), which validates the reliability of this procedure. A simple check can be carried out by taking the average values from the uncorrected stress-strain curve of the weld nugget (WF, WR). This plot is also shown in Figure 6.14b, which shows excellent agreement between the average values and the theoretically obtained stress-strain curve. The procedure developed to determine the out-of-plane deformation confirms that the error is due to bending across the reduced cross-section of the weld nugget. Moreover, all the aforementioned vital findings prove that the HR-DIC erroneous strain measured on the weld nugget (WF, WR) is exclusively an outcome of combined tensile and bending effects evolved due to local variations in the FSW weld geometry. The principal outcome is that to conduct accurate HR-DIC measurements on such a specimen it is necessary to monitor the strains from both the front and back of the specimens to account for the out-of-plane deformation in the elastic region where the material behaves homogeneously. However, as the material in the weld has different thermomechanical histories post-yield the deformation is likely to be heterogeneous, and it will be necessary to measure the out-of-plane deformation in the edge of the specimen to properly account for the parasitic strains.

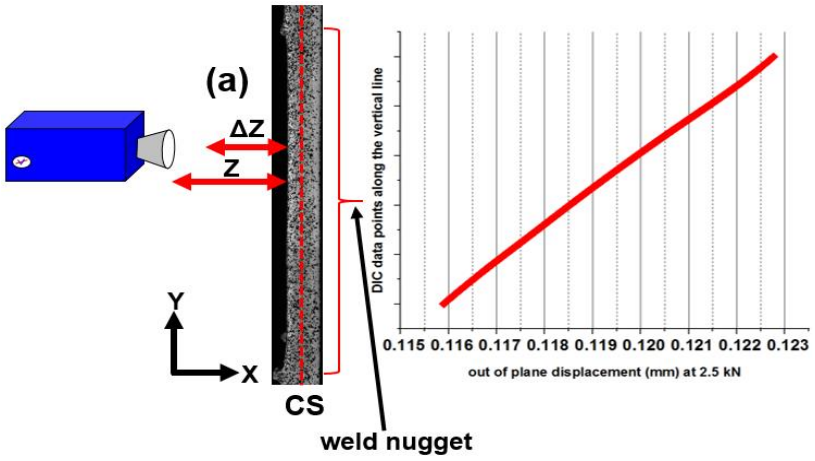

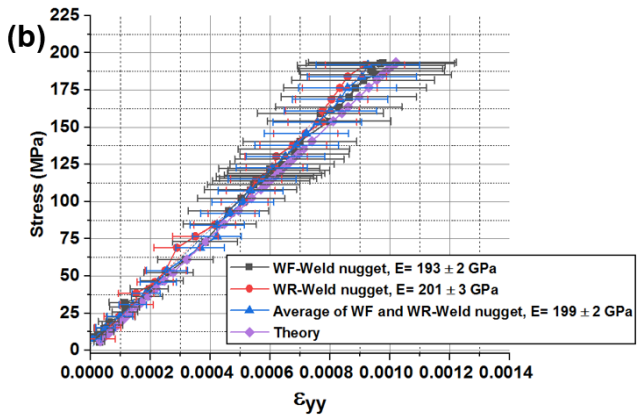

Figure 6.14 (a) Out-of-plane displacement measurements along the vertical line of weld cross-section at 2.5 kN; (b) correction factor applied stress-strain curves of the weld nugget [34]

6.7 Summary

The results obtained from the HR-DIC measurements in the elastic loading range of actual FSW (SS-SS) weld using a novel experimental methodology were presented and validated in this chapter. By using the experimental methodology, the parasitic strains caused by the FSW weld geometry were successfully removed from the HR-DIC measurements. However, this methodology is strictly applied only in the elastic loading range as the sequential loading procedures explained in this chapter cannot be used beyond the elastic range as the material will behave in a non-linear fashion. To avoid this limitation, a modified HR-DIC experimental procedure is developed and validated for FSW welds in both elastic and plastic regimes. The high-fidelity images obtained by the image stitching cannot be reproduced beyond the elastic limit of the material with any degree of accuracy. This would involve using a series of test specimens, loading each specimen into the plastic range whilst viewing one ROI and then stitching the images. It is clearly impractical based on the limited number of specimens available. Furthermore, aligning the images from each region of interest would be virtually impossible, as demonstrated by the difficulties described in the present chapter even though the specimen is not removed from the test machine. The work described in the Chapter has demonstrated the level of fidelity possible for DIC and has highlighted in detail the difficulties of conducting DIC on the FSWs. The shortcomings of the previous work [25, 29, 30, 41, 96, 97] have been addressed in the next chapter to enable DIC to be applied on specimens that are loaded into the material plastic region. Based on the findings of the present chapter, a modified HR-DIC experimental procedure is developed and validated for FSW welds in both elastic and plastic regimes, as explained in the next chapter of this PhD thesis.

Chapter 7 Development and validation of a HR-DIC methodology to characterise the stress-strain behaviour of FSWs loaded beyond the material elastic limit

7.1 Introduction

As stated in the previous chapter, it would be practically impossible to stitch the HR images obtained from individual regions during plastic deformation. The procedure would require several identical specimens to be loaded into the plastic region; only seven specimens of each type are available. Even though the specimens are manufactured together it is unlikely they would be identical because of variabilities in the FSW process. Furthermore, issues associated with lighting and camera position would make stitching the HR-DIC strain maps obtained from a series of ROIs, as done in chapter-6, impossible with any degree of accuracy. Therefore, it is necessary to develop a modified procedure based on the findings from chapter 6 that allows the entire weld region to be imaged at a suitable level of fidelity so that a single ROI for HR-DIC measurements is in the field of view.

In chapter 6 it was shown that the out of plane displacement had a significant effect on the measured strains and a way of correcting this was to take images from both front and back of the specimen. Hence an identical 16 MP camera was purchased from LA Vision so that the two camera methodology could be applied to all tests. Hence, a modified HR-DIC procedure is presented in this chapter based on two cameras, which is validated using for all three FSW (SS-SS, Cu-Cu, and Cu-SS) joints in the elastic loading range. The work then moves on to apply the modified HR-DIC methodology in the post-elastic deformation of the joints. A key part of the process is to identify the different yield strength of each region in the FSW, alongside the hardening behaviour. A detailed examination is performed both during loading and unloading of the specimens followed by the effect of repeated loading. Finally and most importantly, the HR-DIC results are correlated with micrographs to identify the FSW weld sub-regions to explain the post-yielding characteristics of the FSW sub-regions.

7.2 Modified HR-DIC experimental arrangement

For HR-DIC measurements, two tensile specimens machined from the FSW (SS-SS, Cu-Cu, and Cu-SS) joints named as S1 and S2 were tested. For S1, the HR-DIC strain measurements were performed on the Weld Face (WF) and Weld Root (WR) sides; for S2, the HR-DIC strain measurements were performed on the weld cross-sections (CS-1, CS-2). Figure 7.1 shows a photograph of the modified

HR-2D DIC experimental set-up, which has two identical high-resolution DIC set-ups observing the front and rear of the test specimen S1 at close stand-off distance. The main objective of using two HR DIC cameras is to perform HR-DIC strain measurements simultaneously on both sides (front and rear) of the FSW(SS-SS) specimen to remove the parasitic and bending strains caused by the out of plane displacements [34]. It is significant to note that this methodology can be applied both in the elastic and plastic loading range for S2 as the microstructure along the welding direction of an FSW weld can be considered uniform away from the start and finish positions. However, on the weld face and root surfaces (S1), this methodology can only be applied in the elastic range. This is because both the weld face and weld root regions have different microstructural features normal to the welding direction and hence have different yield points and subsequent hardening characteristics, so that as the material yields it cannot be expected a simple averaging of the strains from the WF and WR faces can accurately account for the out of plane deformation.

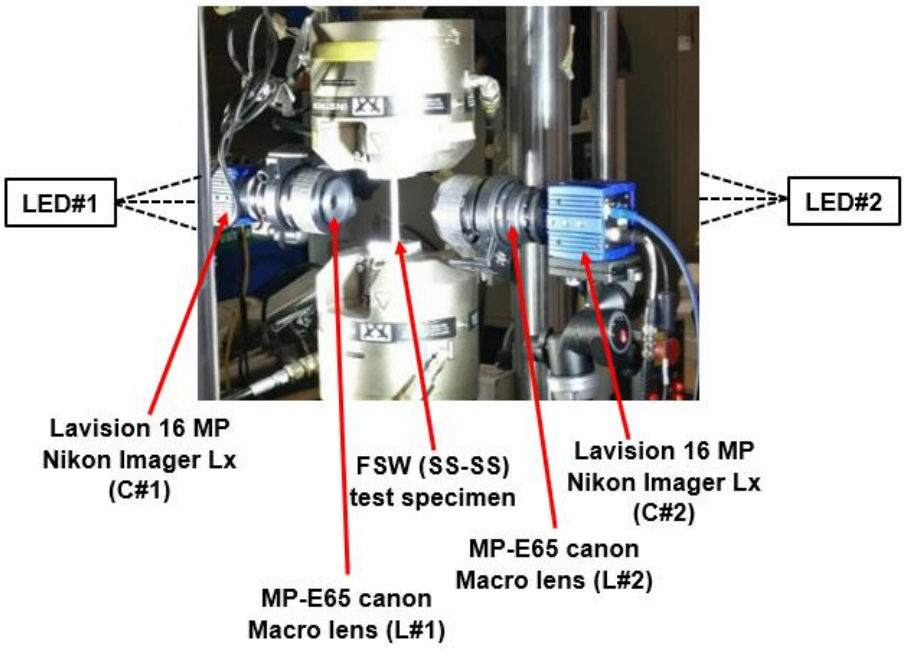

Figure 7.1 Modified HR 2D-DIC experimental setup

The HR 2D-DIC parameters used in this investigation are listed in Table 7.1. In the HR-DIC experimental set-up, the DIC optics consist of 16 MP CCD camera (Make: LaVision, Germany; Model: Imager Lx) having a pixel resolution of 4904 x 3280 pixels fitted with a Canon MP-E65 mm focal length macro lens. All the images were captured at a frequency of 0.5 Hz, and the lens magnification was fixed at 1x to achieve the maximum field of view. By using the high-resolution DIC optics at this magnification, the images were captured at a spatial and strain resolution of 200 pixels/mm and 6.4390 x 10^{-5} respectively. To achieve adequate illumination on both sides of the specimen, a pair of 40 W LED lights (Make: Nila; Model: Zaila) were used throughout the HR-DIC experiments. Load data for each image captured during the DIC was recorded using an Analog to Digital converter (ADC) channel (Make: National Instruments) synchronised with the DIC system.

During uniaxial tensile tests, the specimen surface was strictly maintained perpendicular to the DIC camera sensor axis. All the uniaxial monotonic tensile tests were performed in an Instron-8800 servo-hydraulic testing machine (Make: Instron, UK) equipped with 10 kN load cell at room temperature. During DIC imaging, both the specimens were subjected to loads beyond the material yield point by sequential loading/unloading cycles in a load step of 0.5 kN. All the recorded HR-DIC images were correlated using commercial data correlation software LaVision (DaVis 8.3.1, LaVision, Germany). All the HR-DIC data were processed using a subset size of 59 x 59 pixels and a step size of 20 to achieve an optimum trade-off between the spatial and strain resolution.

Table 7.1 HR 2D-DIC parameters

Technique used	2D-DIC
Camera (Front and Rear)	16 MP LaVision Imager Lx
Sensor and digitization	3280 x 4904, 12 bit
Lens (Front and Rear)	MP E-65 Canon Macro lens
Lens magnification	1x
Lens and Imaging distance	MP-E65 Macro lens, 0.08 m
ROI	16.4 mm x 24 mm
Correlation software	DaVis 8.3.1 (LaVision)
Subset, Step	59, 20
Interpolation, Shape functions, Correlation criterion	6^{th}order spline, 1^{st}order shape function, Least square difference
Camera Frequency	0.5 Hz
Spatial resolution	200 pixel/mm
Strain window	3 data points
Displacement resolution	0.047 pixels, 2.35 x 10^{-4} mm
Strain resolution	6.4390 x 10^{-5}

7.3 FSW (SS-SS)

7.3.1 Validation of the HR-DIC methodology in the elastic region

Figure 7.2 displays the HR-DIC strain maps of the FSW (SS-SS)-S1 specimen along the weld face (WF) and weld root (WR) captured in the elastic loading range. All the strain maps derived from the WF show strain concentration across the weld nugget due to the reduced thickness of the FSW weld nugget. This reduced thickness of the FSW (SS-SS) specimen usually leads to a significant out of plane displacement during the HR-DIC measurements, and generates parasitic strains, as explained

in chapter 6. HR-DIC strain maps captured from the WR show negative strain across the weld nugget, which indicates a clear bending of the specimen across the weld nugget during the uniaxial tensile loading. Importantly, the WR strain maps also show the strain concentration along the weld centreline, i.e. weld interface. This may be due to the incomplete solid-state material consolidation produced by FSW along the root side. Figure 7.2a also shows the ROIs (BM-AS, Weld nugget, and BM-RS) from which the local stress-strain curves were extracted. To remove the parasitic strains from the HR-DIC measurements, the strain measured from the WF and WR were spatially averaged with respect to the load value for all the ROIs. Figure 7.2b displays the local stress-strain curves plotted through the average strain versus the stress calculated from the actual area of cross-section of the ROIs. Although the strain maps of the WF and WR regions show non-uniform strain in their elastic range, from Figure 7.2b, it is confirmed that the Young's Modulus of the weld sub-regions calculated from the average strain is completely aligned with the theoretical value (E= 200 GPa). This finding again validates the methodology proposed in chapter-6 where the parasitic strains caused by the out of plane displacement were removed from the actual HR-DIC measurements by averaging the strains measured on the WF and WR regions in the material elastic region.

Figure 7.3a shows the strain maps captured within the elastic loading regime of the front (CS-1) and rear (CS-2) weld cross-sections, it is important to note that this is a different specimen to that described above. Here, the strain localisation due to the out-of-plane bending across the weld nugget is not as apparent. what is very clear is that, the strains are much larger in CS-1 than in CS-2 for the same load value. This could be caused by in-plane bending caused by a slight specimen rotation in the test machine grips, as explained in chapter 4. To assess if the differences could be due to in-plane bending of the specimen Equation 4.5 was used to calculate the stress at a different angle of misalignment varying from -1^{o} to 1^{o} when a 2 kN load is applied. The black lines in Figure 7.3b show the variation in the strain caused by the specimen rotation. By taking the value of the strain (average) from the base metal region from HR-DIC measurements from CS-1 and CS-2 and plotting these on Figure 7.3b as dotted vertical lines it can be seen that a small rotation of around 0.4^{o} and 0.5^{o} could be responsible for the difference in the strains, which is very small and difficult to avoid. Hence, it was decided to investigate if this difference could be accounted for by averaging the strain values from CS1 and CS2. Average values were determined for the three weld sub-regions of BM-AS (1, 2), weld nugget (3, 4), and BM-RS (5, 6) (shown in Figure 7.3a) to extract the local HR-DIC strain data. The local stress-strain curves are plotted in Figure 7.3c using the average strain values and stress values determined using the cross-sectional area of the weld sub-regions obtained from the Alicona measurements provided in chapter 6. Figure 7.3c shows that the elastic modulus of the weld nugget is very close the material theoretical value of 200 GPa. However, the elastic modulus of the BM-AS (E= 190 GPa) and BM-RS (E= 220 GPa) regions do not coincide from the theoretical value. It should be considered that only a small region of the base material could be imaged, close to the stress concentration caused by the change in section and this could explain the reason why these values do not correspond as well as those taken from the weld nugget. It should also be considered

that as only a small section of the BM (AS and RS) regions were covered the scatter in the readings due to the stress concentration becomes more dominant. Another point to note is that the effect of the out of plane bending is evident in Figure 7.3a with the strain values slightly greater on the CS-1 side than the CS-2 side. Averaging across the entire region will counteract the effect of the bending in the weld nugget.

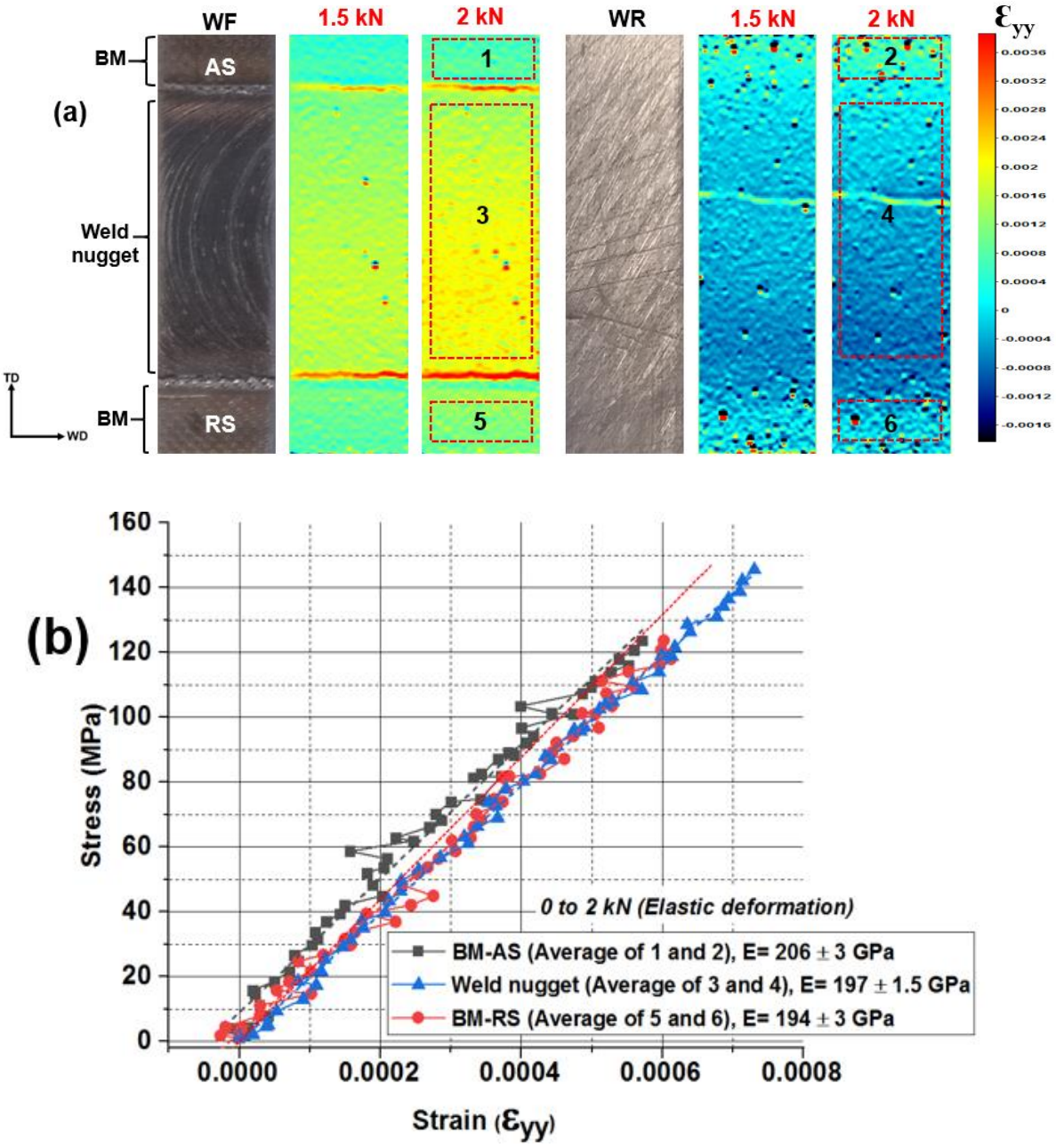

Figure 7.2 HR-DIC results: (a) HR-DIC strain maps (ε_{yy}) captured at 1.5 kN and 2 kN load values from the Weld Face (WF) and Weld Root (WR) of the FSW (SS-SS)-S1 specimen; (b) Local stress-strain curves extracted using average strain values from the corresponding ROIs shown in (a)

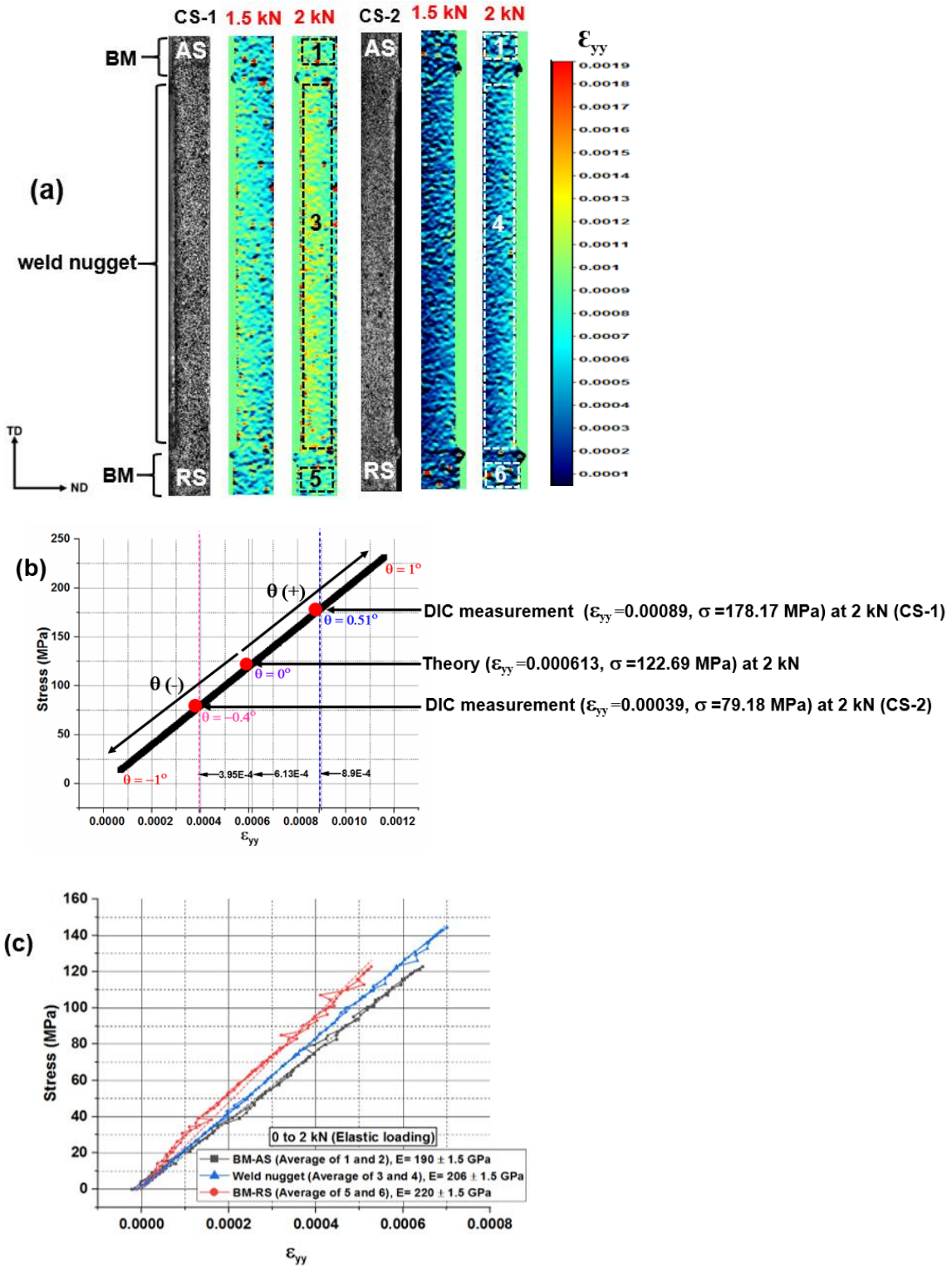

Figure 7.3 HR-DIC results from the FSW (SS-SS)-S2 specimen in the elastic loading range: (a) DIC strain maps (ε_{yy}) along the front weld cross-section (CS-1) and rear weld cross-section (CS-2) at 1.5 kN and 2 kN load values; (b) Stress-Strain plots calculated using Equation 4.5 and Equation 4.6 (Chapter-4) with respect to the FSW (SS-SS) tensile specimen misalignment at 2 kN (Theory Vs DIC measurements); (c) Local stress-strain curves derived from the specimen using average strain values from the corresponding ROIs shown in (a)

After conducting the above analyses, it was concluded that the DIC set-up was suitable to load the specimens into the elastic range. The consequences of small in-plane rotations the grips during clamping were understood, and that these were a limitation imposed by the FSW plate geometry that could be achieved by the facilities available. Thicker and wider specimens would be more desirable to counteract these effects but achieving a good FSW in stainless steel would require significant modifications to make the facility more robust and probably introduce other features in the final welded specimen. Hence it was decided to proceed with the tests into the plastic range using the specimens, as these would still reveal the effect of the different weld sub-regions on the stress-strain response and provide a better understanding of FSWs.

7.3.2 Local strain response of the FSW (SS-SS) joint during plastic deformation

Table 7.2 shows the loading and unloading cycles used for the HR-DIC measurements on FSW (SS-SS)-S1 and FSW (SS-SS)-S2 specimens. Figure 7.4a shows the strain maps (ε_{yy}) of weld face (WF) from S1 obtained at 5 and 6 kN. All strain maps derived from the WF show the increased strain across the stir zone due to the reduced thickness of the FSW weld nugget and bending, as explained in chapter 6. More importantly, it can be seen that the strain localisation is maximum at the outer boundary of the stir zone (TMAZ) at all load values due to the sharp change in the cross-sectional area. It is evident that at 5 kN, the strain is more pronounced on the TMAZ-RS than the TMAZ-AS; Mironova et al. [41] also found the same result in their investigation. Therefore, at the step-change in the area of cross-section at TMAZ-AS and TMAZ-RS regions, the displacement, and hence strain, are not the same due to the different amount of plastic work received in the AS and RS regions during the FSW process. It is clear that different hardening characteristics have resulted from the different grain morphology generated by the plastic work in each region. This finding is corroborated by the EBSD findings discussed in chapter 5 of the thesis. Additionally, at 5 kN, the stir zone of the WF shows several strain concentration regions, which appear to be aligned with the stir profiles of the WF. As the weld nugget has a considerable amount of tungsten particles from the tool wear identified in chapter 5, it is considered that the local strain concentrations in the stir zone of the WF at 5 kN result from the tungsten distributed in the weld nugget. At 6 kN, it is observed that the centre of the weld nugget along the WF shows a minimum strain in addition to the local strain concentration regions. This may be due to some crack propagation in the interface located in the weld root (WR). Figure 7.4b shows the DIC strain plots extracted along the vertical line of the specimen at various load values along the WF and both the base metal regions (AS and RS) show similar stress-strain characteristics within the elastic limit. In addition to this, the weld nugget had higher strain than the base metal regions due to the cross-section reduction and the offset loading. During plastic deformation (5 kN and 6 kN), a clear strain gradients is evident across the weld nugget due to more refined grains in the weld nugget region resulting in smaller strain as well as the strain hardening effects produced by the loading/unloading cycle alongside possible effects of the tungsten inclusions.

Table 7.2 Loading/unloading cycles used for HR-DIC measurements on FSW (SS-SS) joints

Cycle	Loading range (kN)	Unloading range (kN)
1	0 to 0.5 kN	0.5 to 0 kN
2	0 to 1 kN	1 to 0 kN
3	0 to 1.5 kN	1.5 to 0 kN
4	0 to 2 kN	2 to 0 kN
5	0 to 2.5 kN	2.5 to 0 kN
6	0 to 3 kN	3 to 0 kN
7	0 to 3.5 kN	3.5 to 0 kN
8	0 to 4 kN	4 to 0 kN
9	0 to 4.5 kN	4.5 to 0 kN
10	0 to 5 kN	5 to 0 kN
11	0 to 5.5 kN	5.5 to 0 kN
12	0 to 6 kN	6 to 0 kN

Figure 7.5a shows the strain maps (ε_{yy}) of weld root (WR) from S1 obtained at 5 and 6 kN. The effect of the localised bending resulting from the offset loading and the slight bend of the specimen has resulted in the negative strains in the strain maps. Importantly though, the WR strain maps show large strain concentrations along the weld centreline, i.e. the weld root. From both 5 and 6 kN, it is seen that some additional strain concentrations emerge at the weld root, which could be attributed to cracking. Figure 7.5b shows the strain plots extracted at various load values along the vertical line of the weld root (WR). All the line plots (2, 3, 4, and 5 kN) extracted from the WR confirm that the strain experienced by the weld sub-regions is very close to zero except at the weld interface. However, at 6 kN, the WR demonstrates a large strain gradient across the weld nugget as noticed along the WF (Figure 7.4b).

Figure 7.6 shows the HR-DIC results captured from S2 along the front (CS-1) and rear (CS-2) weld cross-sections at plastic deformation. At 5 kN, the stir zone has achieved two major strain gradients along both cross-sections (CS-1 and CS-2). From CS-1 perspective, firstly, region 4 located in the central region of stir zone as well as region 2 located along the AS have a smaller strain compared to the BM. Secondly, regions 3 and 5 located in the stir zone have a substantial increase in strain compared to regions 1 and 6. These DIC findings establish that regions 3 and 5 have reached their yield point at a lower load than regions 2 and 4. All these key observations from the 5 kN strain map are also confirmed at the same locations in the strain map captured at 6 kN. Figure 7.6b and Figure 7.6c show the strain distribution at different load values along the vertical line of CS-1 and CS-2 regions (as shown in greyscale images), respectively. Both these figures show a similar trend where

the strain distribution until 4 kN is found to be uniform along the vertical line that includes all the major weld sub-regions such as BM, TMAZ and weld nugget. However, after 4 kN, the specimen strains vary across along the line due to the plastic deformation. It is noteworthy that at larger loads resulting plastic deformation the RS had higher strain than the AS. In similar to the observation from HR-DIC strain maps (Figure 7.6a), a sharp reduction in the strain is also noticed at the centre of the weld nugget.

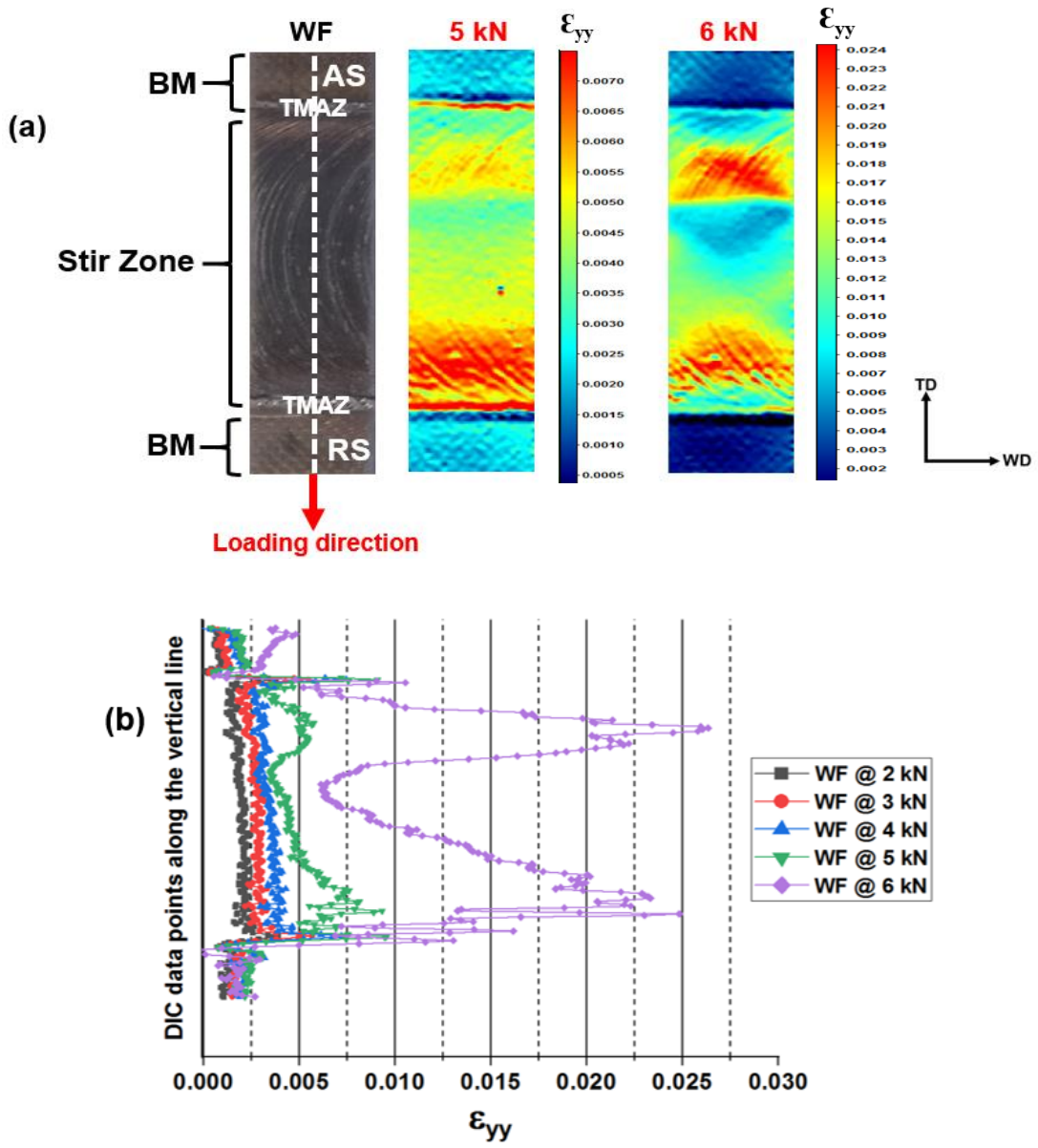

Figure 7.4 DIC results of the FSW (SS-SS)-S1 specimen along the Weld face (WF): (a) DIC strain maps (ε_{yy}) captured at 5 kN and 6 kN; (b) Strain plots along the vertical line of the WF as shown in (a) at different load values

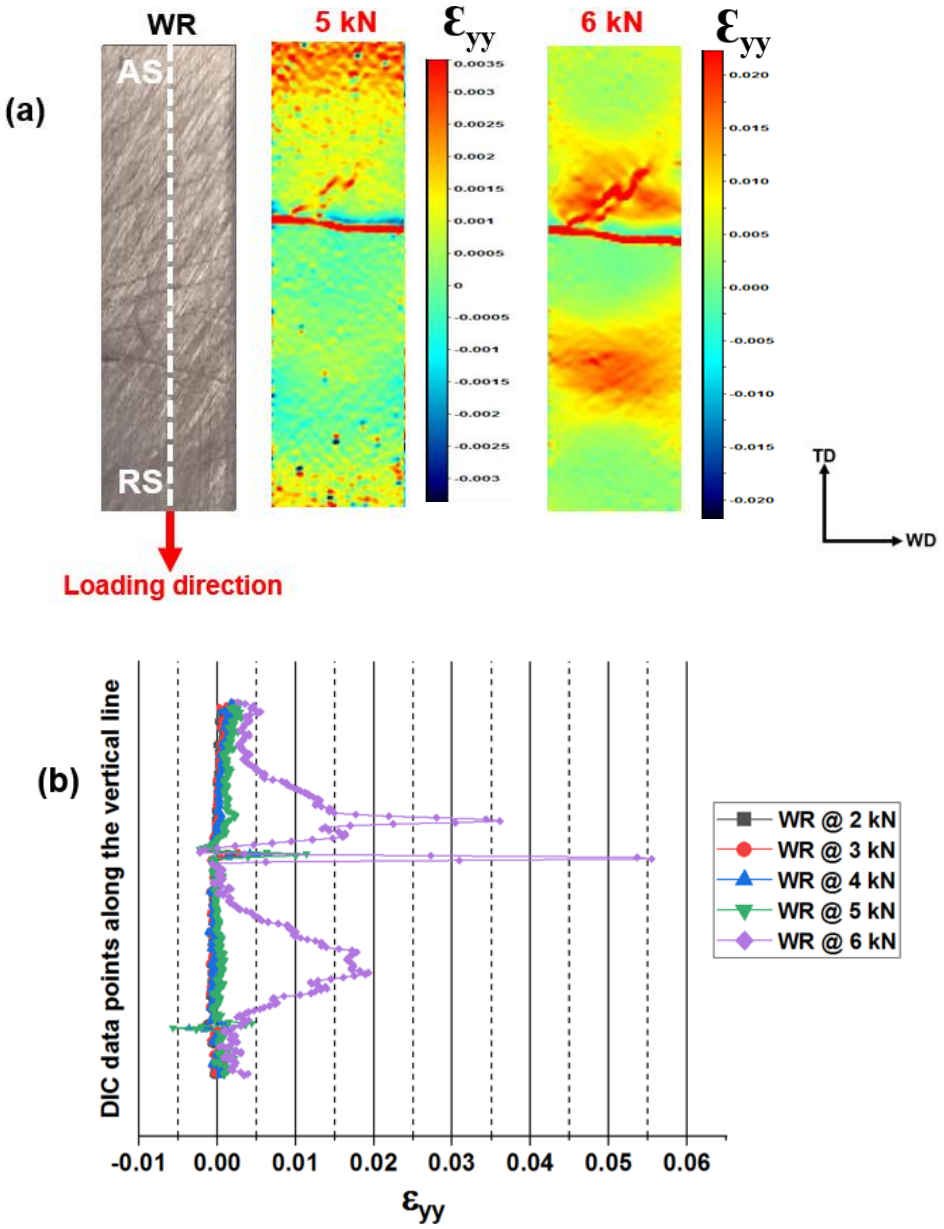

Figure 7.5 DIC results of the FSW (SS-SS)-S1 specimen along the Weld Root (WR): (a) DIC strain maps (ε_{yy}) captured at 5 kN and 6 kN; (b) Strain plots along the vertical line of the WR as shown in (a) at different load values

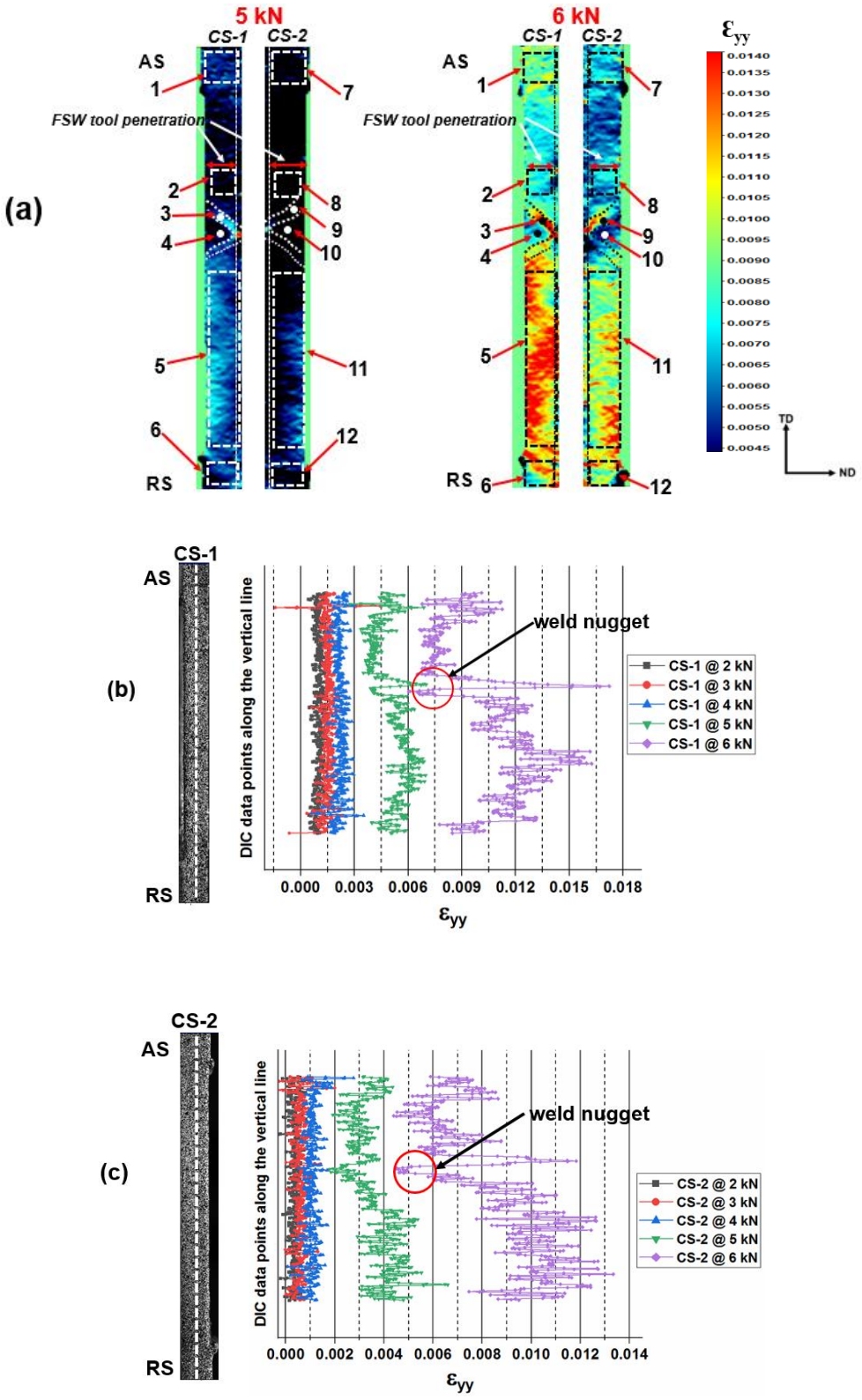

Figure 7.6 DIC results of the FSW (SS-SS)-S2 specimen along the front weld cross-section (CS-1) and rear weld cross-section (CS-2) at plastic deformation: (a) DIC strain maps (ε_{yy}) captured at 5 kN and 6 kN; (b) Strain plots along the vertical line of the CS-1 at different load values; (c) Strain plots along the vertical line of the CS-2 at different load values

7.3.3 Microstructure-property correlation of the FSW (SS-SS) joint

From Chapter-5, it is found that the effect of high frictional heat and severe plastic deformation of the FSW process led to the generation of weld sub-regions such as weld nugget, TMAZ and HAZ in the vicinity of the weld. These weld sub-regions have distinct microstructural features based on the intensity of frictional heat and mechanical deformation received from the FSW process. As the mechanical behaviour of a material is strongly linked to its microstructural features especially the grain size, it is highly expected that the local mechanical behaviour of these weld sub-regions will be heterogeneous [71]. Therefore, to achieve a better understanding of the locally varying post-yield behaviour across the stir zone, the strain map derived at plastic deformation (6 kN) is correlated against the optical micrograph as displayed in Figure 7.7. This optical micrograph was captured from the reference specimen (not the same specimen used for the HR-DIC measurements) machined from the same FSW (SS-SS) joint used for HR-DIC measurements. From Figure 7.7a and Figure 7.7c, it is confirmed that the reduced strain observed in region 4 (Figure 7.7a) is due to the presence of onion ring pattern occupied with densely populated fine grains. Furthermore, the high hardness achieved at the centre region of the weld (as discussed in chapter-4) also facilitated a high resistance of region-4 to the applied plastic deformation during tensile loading. It is noteworthy that the entire weld nugget (stir zone) has not achieved reduced strain. In general, the entire stir zone of an FSW nugget usually achieves homogeneous fine recrystallized grains from the plastic work developed in the FSW process. However, the FSW (SS-SS) weld investigated in this study has wider range of fine grains across the stir zone due to the effect of FSW process parameters and tool geometry. Therefore, the reduced strain is observed only in region 2 and 4 that have a high intensity of fine recrystallized grains, which make the strain distribution much more heterogeneous over the stir zone. High strain concentration in region 3 may be due to the rich mixture of coarse and fine grains. Much coarser grains located in region 5 compared to region 2 is the reason for strain localisation along the RS. As clearly explained in chapter-4, it is confirmed that the microstructural differences observed on the AS and RS regions are completely associated with the gradients of frictional heat and plastic deformation generated during the FSW process. Overall, a wide range of grain size variations achieved across the stir zone has enabled a good correlation between the local microstructural morphology and the corresponding strain response.

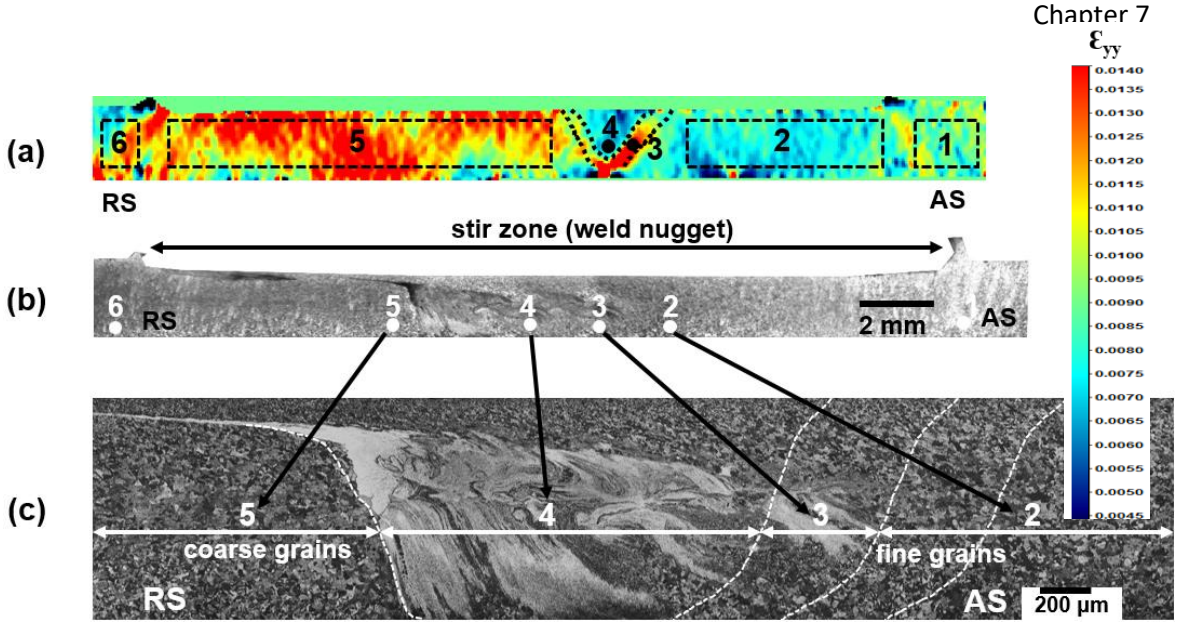

Figure 7.7 Microstructure-property correlation: (a) Ɛyy strain map of the FSW (SS-SS)-S2 along the weld cross-section at 6 kN; (b) Macrograph of the FSW (SS-SS) weld cross-section-S2; (c) Optical micrograph of the FSW (SS-SS) weld cross-section-S2 on the location shown in (b)

7.3.4 Local stress-strain curves of the FSW (SS-SS) joint

Figure 7.8 displays the local stress-strain curves extracted from the weld cross-section at different load levels from the ROIs, as shown in the HR-DIC strain maps. It is important to note that the HR-DIC strain data measured on the particular ROI that corresponds to both CS-1 and CS-2 regions were averaged to reduce the effects of in-plane displacement on DIC measurements and therefore, only the average strain value is considered in all the local stress-strain curves. Additionally, the reduced thickness of the weld nugget is accounted for all the local stress-strain curves. Three major weld sub-regions such as BM-AS, weld nugget, and BM-RS are considered as the ROIs for the local stress-strain curves extracted in the 0 to 4 kN loading range (Figure 7.8a). In addition to this, the entire stir zone is considered as the weld nugget in this loading range. At 0 to 4 kN, all the weld sub-regions have yielded at different stress values, as displayed in Figure 7.8a, which shows that the yield strength of the weld nugget is higher than the BM. The local stress-strain curves derived at 0 to 5 kN and 0 to 6 kN loading range includes the TMAZ, TMAZ-AS, and TMAZ-RS regions as the ROIs in addition to the BM and weld nugget regions. Furthermore, as there is a different grain structure across the weld nugget that respond differently during plastic deformation, these stress-strain curves include the ROIs (4 and 10) corresponding to CS-1 and CS-2 respectively as the weld nugget instead of the entire stir zone.

From Figure 7.8b, it is determined that both the BM-AS and BM-RS regions have achieved similar stress-strain characteristics with the yield strength of 272 MPa. Weld nugget (Region-4 and 10) and TMAZ-AS (Region-2 and 8) have achieved the highest yield strength of 326 MPa and minimum strain among other weld sub-regions due to a large number of fine grains located in these regions. It

is interesting to note that the stress-strain response of TMAZ, TMAZ-AS, and TMAZ-RS are entirely different from one another due to their widely varying grain morphology. The local stress-strain curves derived at 0 to 6 kN loading range (Figure 7.8c) also agree with the above observations, but slightly at a higher stress level due to the strain hardening effects. Hence the local stress-strain curves extracted from the weld sub-regions confirm their structure-property relationships especially the weld nugget (region-4) where it has achieved superior yield strength than the BM because of the high density of grain boundaries. The fine grain boundaries located in the region-4 have enhanced the deformation resistance of the material following yielding and resulted in superior mechanical properties. The local high yield strength achieved by the regions across the stir zone proved the capability of the FSW process in producing over-matching stainless steel welds. Furthermore, the local stress-strain curves also provide a solid evidence about the thermo-mechanical effect of FSW on producing distinct local yielding and straining behaviours across the weld nugget. Figure 7.9 schematically represents the post-elastic material properties such as yield strength and residual plastic strain in a typical loading/unloading stress-strain curve. Here the post-yield hardening characteristic is captured by taking the tangent to the stress-strain curve after yielding and is denoted as tangent modulus, E_t.

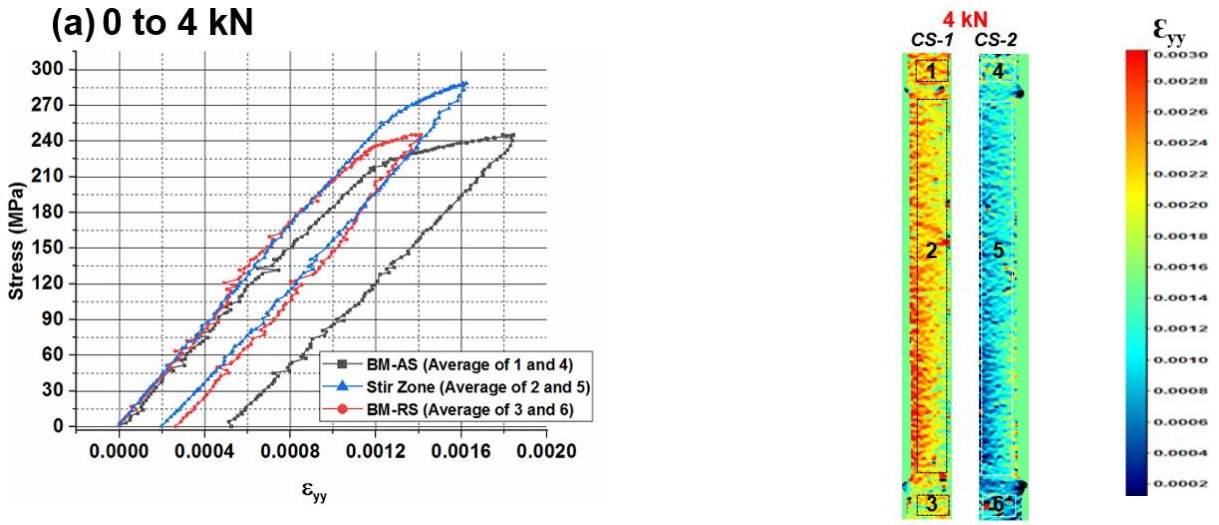

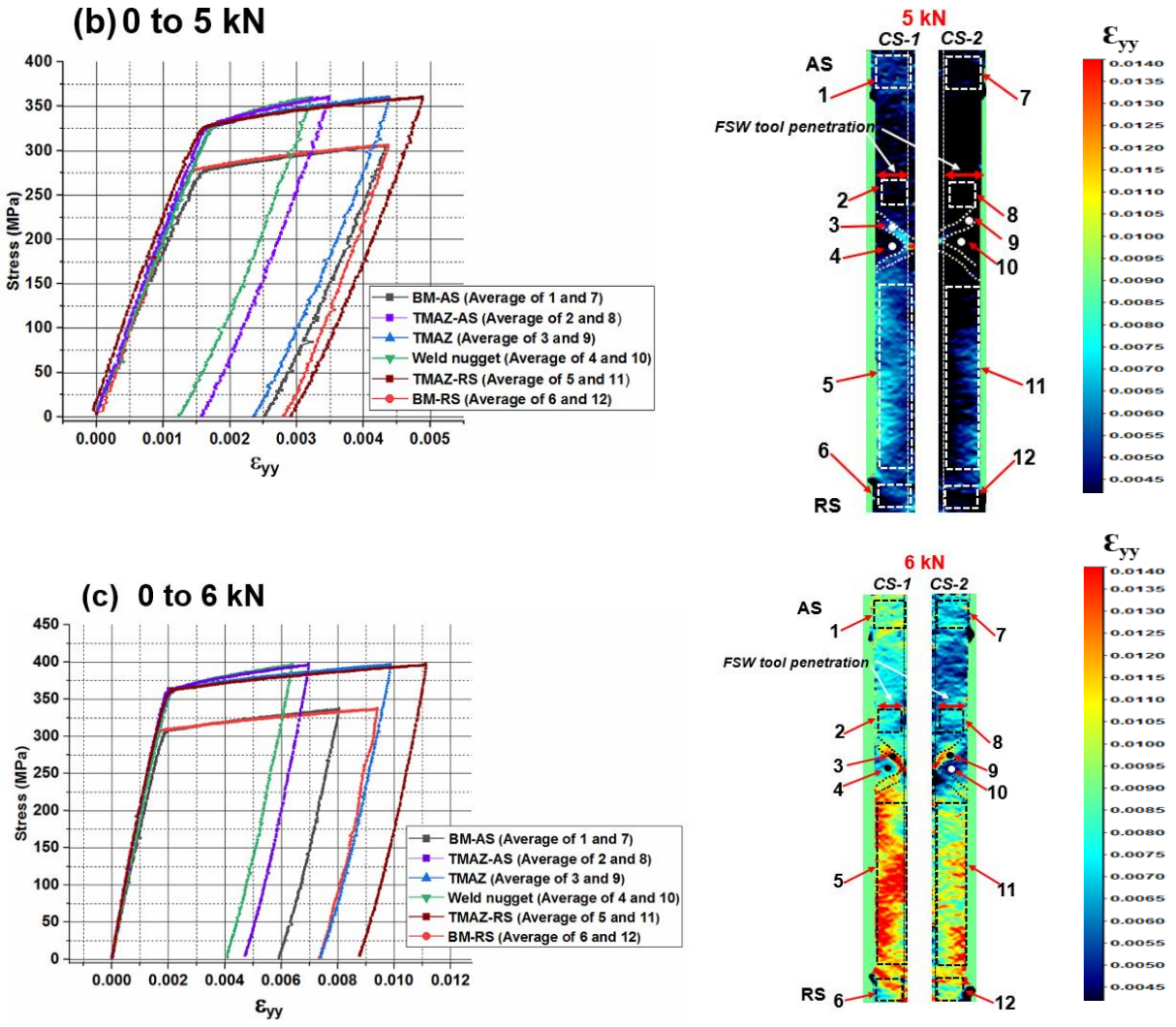

Figure 7.8 Local stress-strain curves of the FSW (SS-SS)-S2 weld sub-regions at plastic deformation: (a) 0 to 4 kN; (b) 0 to 5 kN; (c) 0 to 6 kN

Table 7.3 lists the post-elastic mechanical properties derived from the corresponding local stress-strain curves extracted at various loading range shown in Figure 7.8. From Table 7.3, it is again confirmed that the FSW weld nugget has achieved the highest yield strength and less strain compared to other FSW(SS-SS) weld sub-regions at all loading range due to a high degree of grain refinement. Although the values given in Table 7.3 are for a very particular set of welding parameters, it demonstrates the material properties that could be extracted for the procedure and inserted into models of welded structure to better understand how differences in the welded material influence the overall structural performance.

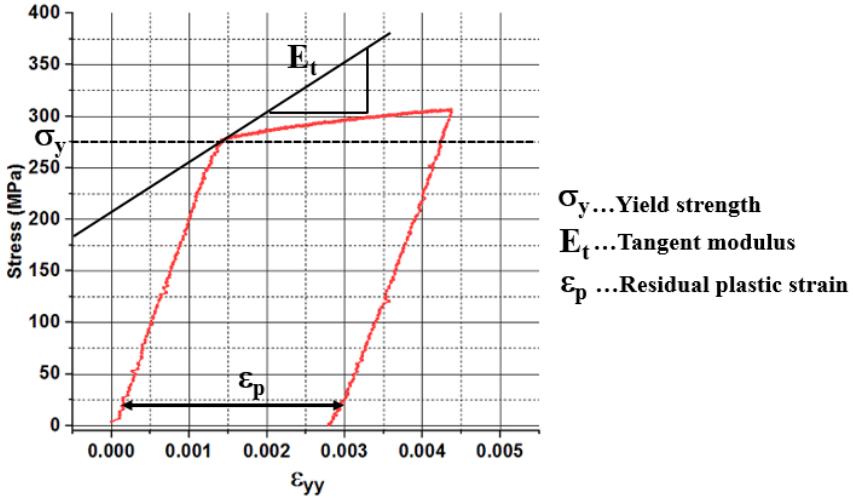

Figure 7.9 Schematic representation of Yield strength, Tangent modulus and residual plastic strain in a typical loading-unloading stress-strain curve

Table 7.3 Local material properties derived at post-elastic deformation of the FSW (SS-SS) weld sub-regions

Load range	Weld sub-region	Yield strength (MPa)	Residual plastic strain (ε_p)	Tangent modulus (E_t) GPa
0 to 4 kN	BM-AS	216	0.00052	84
	Stir zone	257	0.00019	171.87
	BM-RS	228	0.00026	128.24
0 to 5 kN	BM-AS	272	0.00252	49.20
	TMAZ-AS	326	0.00157	111.66
	TMAZ	319	0.00235	104
	Weld nugget	326	0.00124	122
	TMAZ-RS	322	0.00291	65
	BM-RS	272	0.00279	60
0 to 6 kN	BM-AS	307	0.00590	32.50
	TMAZ-AS	360	0.00471	60
	TMAZ	357	0.00741	32

Weld nugget	357	0.00408	55
TMAZ-RS	360	0.00877	32.50
BM-RS	303	0.00734	38

7.4 FSW (Cu-Cu)

7.4.1 Validation of the HR-DIC methodology in the elastic region

The first step in the work is to evaluate the shape of the final weld cross-section. Hence Figure 7.10b and Figure 7.10c show the Alicona 3D surface topography maps obtained from the Alicona surface measurements on location 1 and location 2 (shown in Figure 7.10a), respectively, which show a significant thickness reduction produced across the weld nugget.

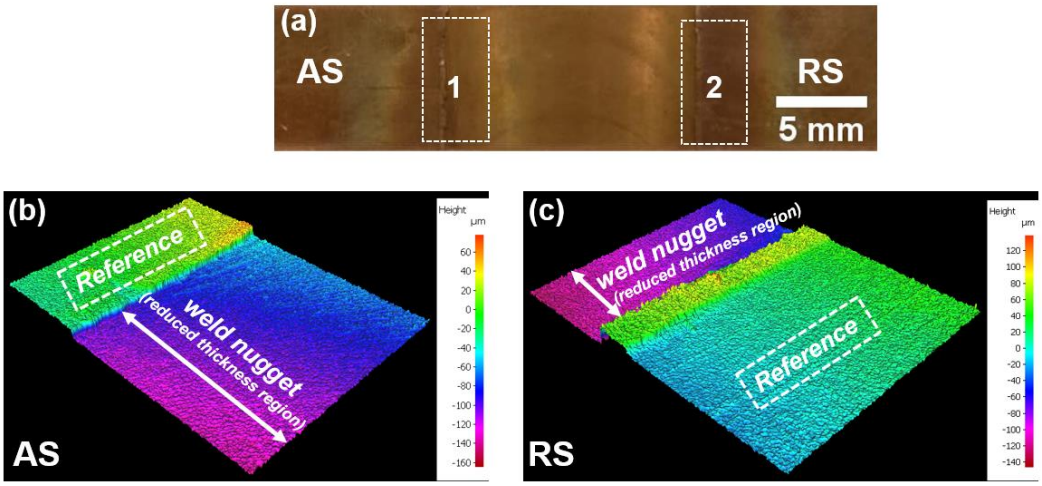

Figure 7.10 Alicona measurements: (a) ROIs (1, 2) for the Alicona profile measurements along the FSW (Cu-Cu) weld cross-section; (b) Alicona 3D surface topography of the ROI-1 located in (a); (c) Alicona 3D surface topography of the ROI-2 located in (a)

The average thickness reduction of the weld nugget measured from the full-field Alicona surface measurements is 0.1 ± 0.021 mm. It is noteworthy that the thickness reduction produced in the FSW (Cu-Cu) joint is much less than the FSW (SS-SS) joint as the copper is generally softer than the steel, and therefore it requires less frictional force and plastic deformation during the FSW process compared to steel.

HR-DIC strain maps captured within the elastic loading range on the weld face (WF) and weld root (WR) of the FSW (Cu-Cu) joint-S1 are shown in Figure 7.11a. From the strain maps obtained along the WF, it is confirmed that both the BM (AS and RS) regions have same strain at all load values (1

kN and 1.5 kN). Additionally, a clear strain localisation is evident across the weld nugget at these load values due to the minor reduction in the thickness of the weld nugget. As observed on the FSW (SS-SS) joint, the WR of the FSW (Cu-Cu) shows minimum strain than that of the WF at all load values. From the previous work on the FSW (SS-SS) joint, the difference in the strains on the WF and WR faces is because of out of plane bending caused by offset loading of the weld nugget. Although a visual inspection of the WR of the FSW (Cu-Cu) did not show any weld defects, all the WR strain maps have a sharp strain concentration at the weld interface, which can only be attributed to incomplete bonding in the weld root region. To eliminate the parasitic strains from the HR-DIC measurements of the WF and WR regions, the modified HR-DIC methodology was applied using the same procedure as demonstrated in the FSW (SS-SS) joint. The area of cross-section of the weld nugget (15.248 mm^2) is calculated by accounting its reduced thickness. Figure 7.11b shows the local stress-strain curves plotted from the average strain value of WF and WR regions calculated from the corresponding ROIs shown in Figure 7.11a. From the stress-strain curves, it is found that the elastic modulus derived from the FSW (Cu-Cu) weld sub-regions after applying the methodology is very close to their theoretical value (E=110 GPa). From this finding, it is confirmed once again that the strain localisation observed across the FSW (Cu-Cu) weld nugget is due to the parasitic strain caused by out of plane displacement.

Figure 7.12a shows the strain maps captured on the front (CS-1) and rear (CS-2) weld cross-sections of the FSW (Cu-Cu) joint-S2 in the elastic range. In contrast to the findings obtained from the FSW (SS-SS) joint, the strain distribution due to the bending across the weld nugget is not evident. This is because, the FSW (Cu-Cu) joint had only a minor reduction in the thickness compared to the FSW (SS-SS) joint and therefore the out of plane displacement produced from a minor thickness reduction is very small. However, as with the FSW (SS-SS), the CS-1 strains appear to be larger than the CS-2 strains. This is attributed to the in-plane bending effect caused by specimen rotation in the grips. To investigate this, an identical procedure to that of the FSW (SS-SS) joint was carried out. Figure 7.12b shows the effect of in-plane bending, and by using the measured strains it can be seen that the misalignment is around 0.26^o to 0.41^o degrees. Also, as for the FSW (SS-SS) specimens, the average strain values from CS1 and CS2 were extracted from the ROIs shown in Figure 7.12a to give the local stress-strain curves in Figure 7.12c. Similar to the WF and WR of the FSW (Cu-Cu) joint, the local stress-strain curves extracted from the average strain value of CS-1 and CS-2 of the joint have also confirmed that the elastic modulus of all the weld sub-regions is close to their theoretical value (E=110 GPa). Hence it is evident that the HR-DIC experimental methodology successfully removes the parasitic strains from the actual HR-DIC measurements obtained from the weld face and cross-section of the FSW (Cu-Cu) joint in the elastic loading range. It should be noted that in comparison to the FSW (SS-SS) joints a much larger BM area was imaged as the weld nugget region is much smaller, which could account for the better correlation as more data away from the strain concentration is available and also that the strain concentration is smaller than that of the FSW (SS-SS) joint.

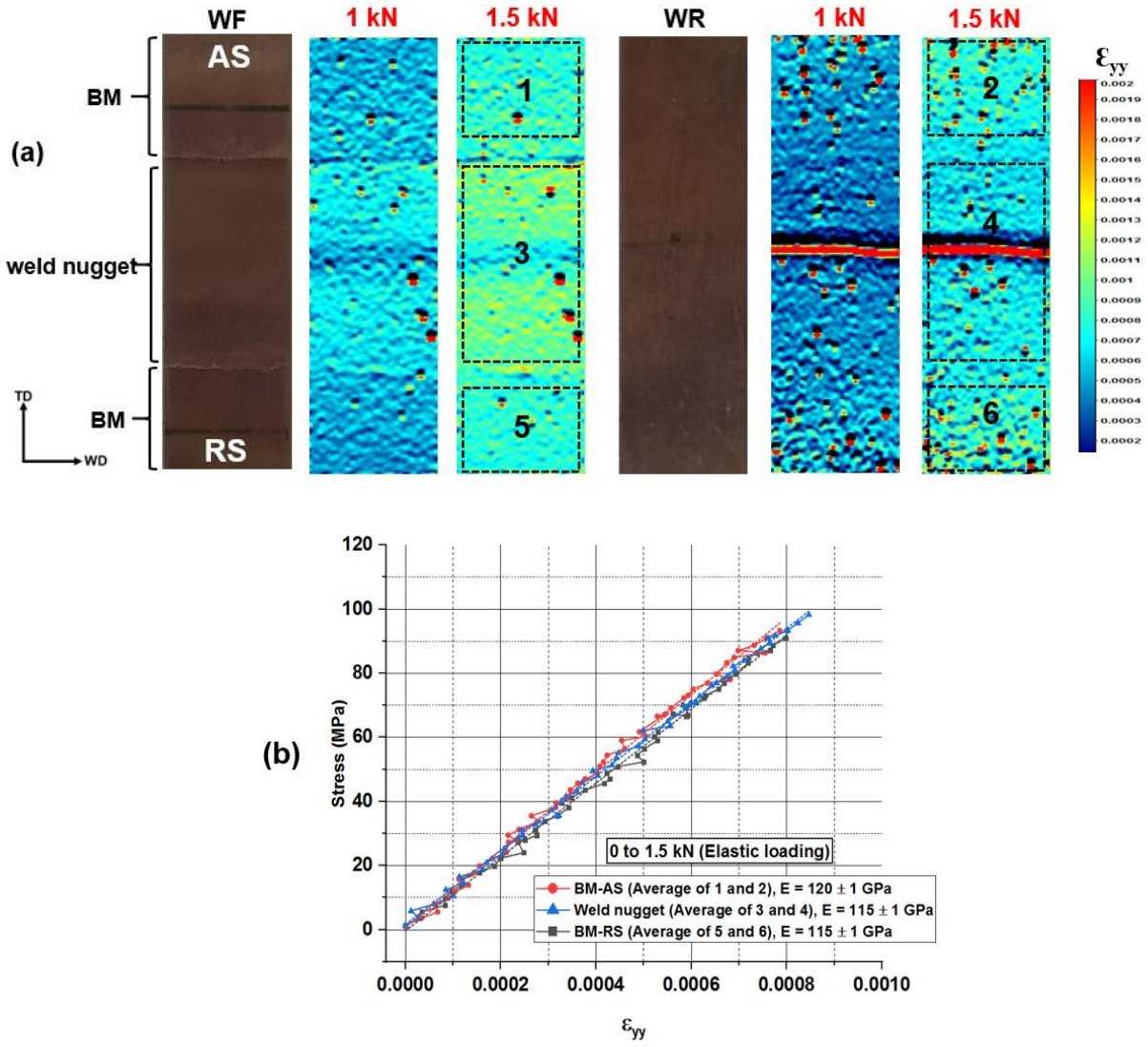

Figure 7.11 HR-DIC results: (a) HR-DIC strain maps (Ɛyy) captured at 1 kN and 1.5 kN load values from the Weld Face (WF) and Weld Root (WR) of the FSW (Cu-Cu)-S1 specimen; (b) Local stress-strain curves extracted using average strain values from the corresponding ROIs shown in (a)

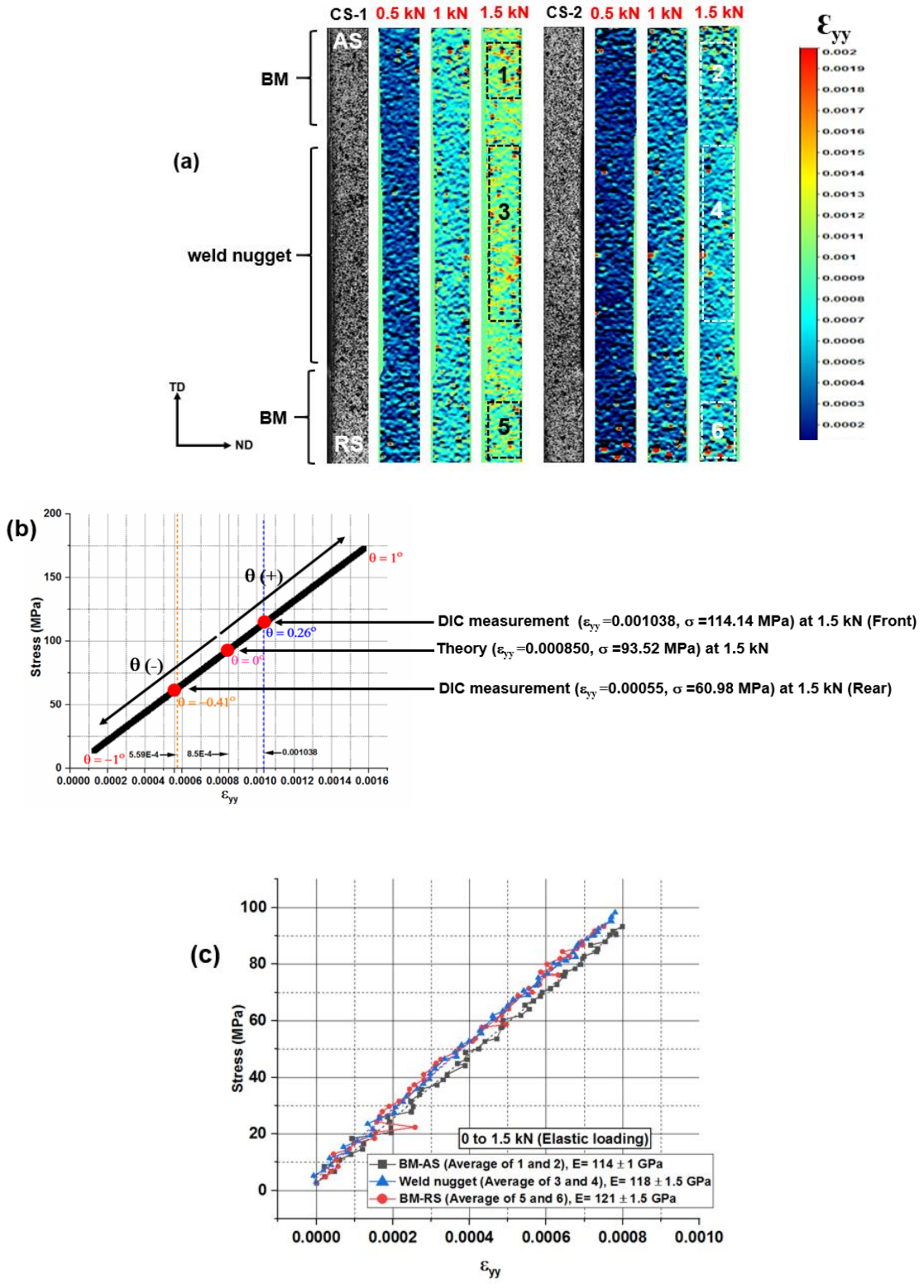

Figure 7.12 HR-DIC results from the FSW (Cu-Cu)-S2 specimen in the elastic loading range: (a) DIC strain maps (ε_{yy}) along the CS-1 and CS-2; (b) Stress-Strain plots calculated using Equation 4.5 and Equation 4.6 with respect to the FSW (Cu-Cu) tensile specimen at 1.5 kN; (c) Local stress-strain curves derived using average strain values from the corresponding ROIs shown in (a)

7.4.2 Local strain response of the FSW (Cu-Cu) joint during plastic deformation

Table 7.4 shows the loading and unloading cycles used for the HR-DIC measurements on FSW (Cu-Cu)-S1 and FSW (Cu-Cu)-S2 specimens. Figure 7.13a shows the HR-DIC strain maps (Ɛyy) of the weld face (WF) from FSW (Cu-Cu)-S1 obtained at 2 kN and 3 kN load values. The strain map captured at 2 kN indicates the presence of strain concentration across the weld nugget, and also both the BM regions have achieved similar strain. However, at 3 kN, the entire specimen contains a non-uniform strain distributions with three clear strain concentrations. Firstly, the strain concentration location is shifted towards the BM-RS and also the strain in the weld nugget is less compared to the BM regions (AS and RS). In addition to the presence of high density of fine recrystallized grains, the strain hardening effect produced by the sequential loading/unloading cycles is also responsible for minimising the strain that can be carried in the weld nugget. Secondly, there is a crack propagating in the region close to the centre of the weld nugget where the strain concentration is also clearly localised. Thirdly, the weld nugget contains a small strain in the centre region. This indirectly confirms a significant bending along the rear side (weld root) of the specimen caused by the reduced thickness of the specimen. Figure 7.13b shows the strain distribution at different load values (1.5 kN, 2 kN, and 3 kN) along the vertical line, as shown in Figure 7.13a. During loading in the elastic range (1.5 kN and 2 kN), both the AS and RS base material regions achieved similar strain distributions, and also the weld nugget shows comparatively higher strain than the base material regions. However, during plastic deformation (3 kN), the weld nugget has highly heterogeneous strain response due to the local microstructural effects of the FSW (Cu-Cu) weld sub-regions. Additionally, the BM (RS) had higher strain than the BM(AS) as exactly noticed in the FSW (SS-SS) joint.

Table 7.4 Loading/unloading cycles used for HR-DIC measurements on FSW (SS-SS) joints

Cycle	Loading range (kN)	Unloading range (kN)
1	0 to 0.5 kN	0.5 to 0 kN
2	0 to 1 kN	1 to 0 kN
3	0 to 1.5 kN	1.5 to 0 kN
4	0 to 2 kN	2 to 0 kN
5	0 to 2.5 kN	2.5 to 0 kN
6	0 to 3 kN	3 to 0 kN

Figure 7.14a shows the HR-DIC strain maps (Ɛyy) along the weld root (WR) obtained at 2 kN and 3 kN load values. HR-DIC strain maps captured along the WR provide a solid evidence on the specimen bending at the centre of the weld nugget where it shows negative strain. As noticed in the elastic loading regime, the strain concentration is evident at the weld interface. Although both the WF and WR strain maps captured at 3 kN have achieved the same features, a step-change in the strain distribution at the outer boundary of the weld nugget (along the RS) is much clearly evident

along the WR side. Figure 7.14b shows the strain distribution at different load values along the vertical line, as shown in Figure 7.14a. There is a large spike in the strain distribution at the centre of the weld interface that confirms the incomplete joining and possibly the presence of a crack. In addition to this, at 3 kN it is clearly evident that the BM-RS had higher strain than the BM-AS as similar to the WF.

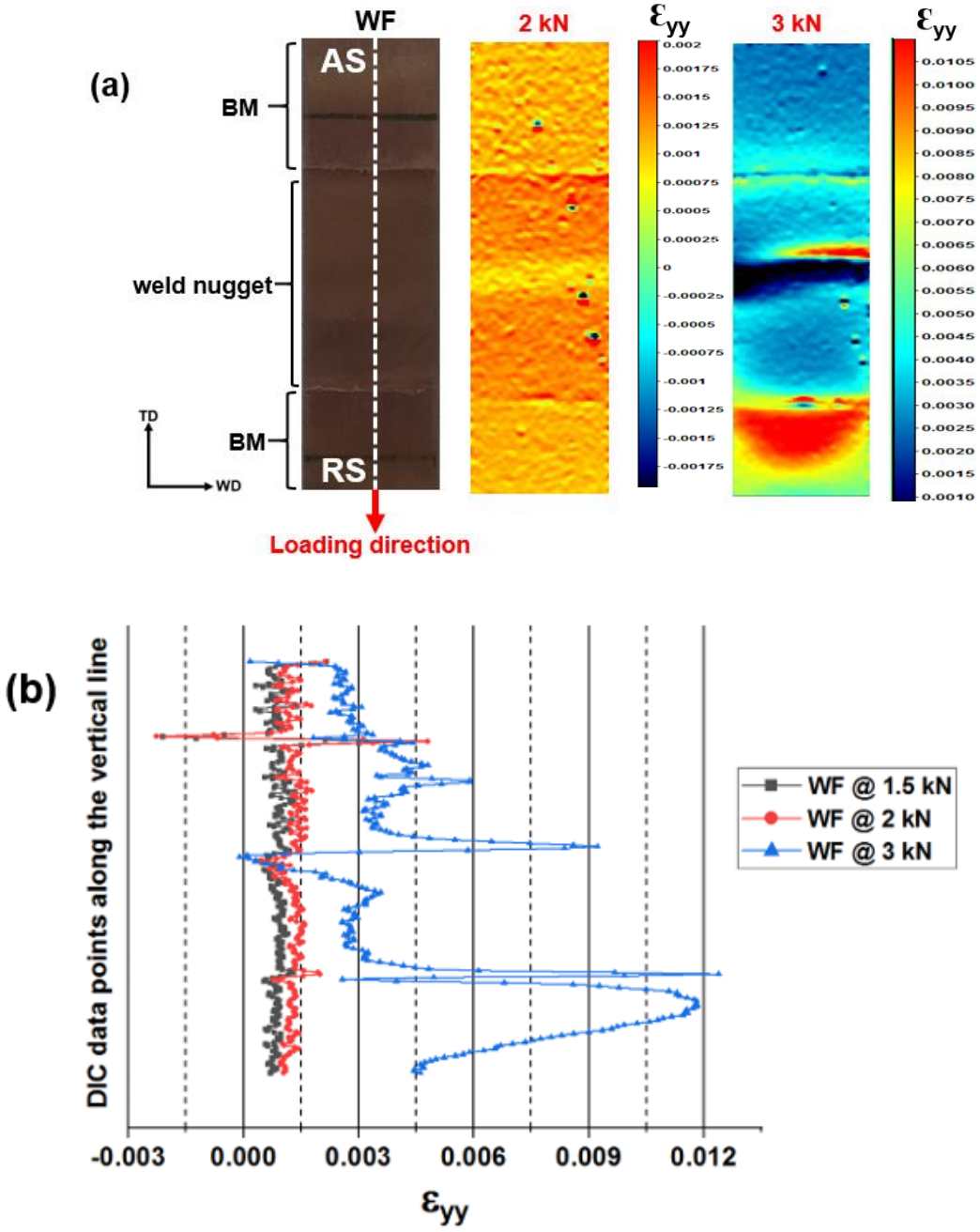

Figure 7.13 DIC results of the FSW (Cu-Cu)-S1 specimen along the Weld face (WF): (a) DIC strain maps (ε_{yy}) captured at 2 kN and 3 kN; (b) Strain plots along the vertical line of the WF as shown in (a) at different load values

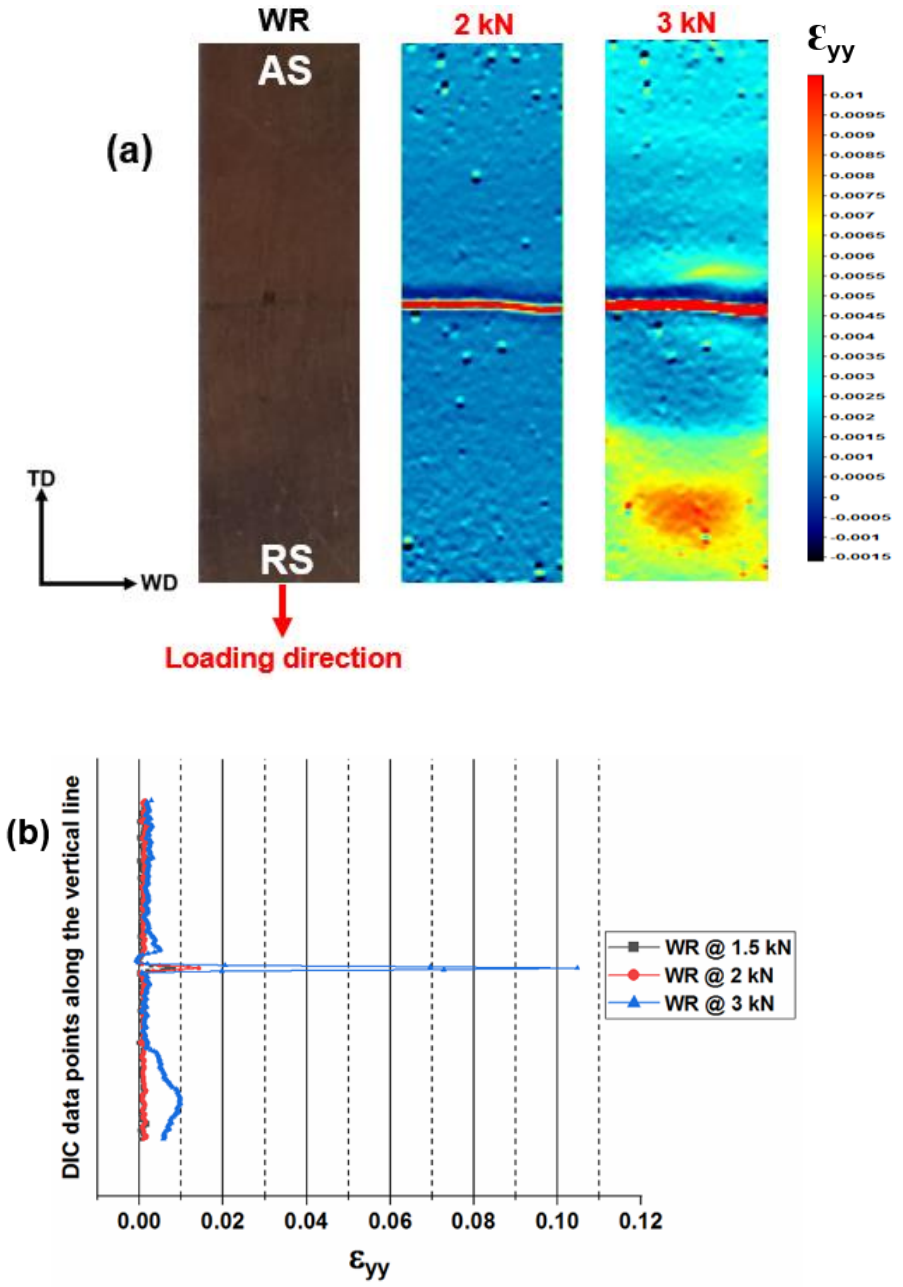

Figure 7.14 DIC results of the FSW (Cu-Cu)-S1 specimen along the Weld Root (WR): (a) DIC strain maps (ε_{yy}) captured at 2 kN and 3 kN; (b) Strain plots along the vertical line of the WR at different load values

Figure 7.15 displays the HR-DIC strain maps captured from the front (CS-1) and rear (CS-2) weld cross-sections of the FSW (Cu-Cu) joint-S2. HR-DIC strain maps captured at 2 kN, and 3 kN load values show uniform strain distribution along both the weld cross-sections. Due to the grain refinement achieved by the FSW process, it is expected that the FSW weld nugget should have higher yield strength than the other weld sub-regions (as per the Hall-Petch relationship). The strain maps obtained at higher load values (3.314 kN, 3.379 kN, and 3.489 kN) are in line with this phenomenon

where the weld nugget has achieved a significant reduced strain than that in the base metal regions. These strain maps also established that the BM-RS has higher strain than the BM-AS along the front (Figure 7.15a) and rear (Figure 7.15b) weld cross-sections. Although the optical micrographs observed from the weld cross-section of the FSW (Cu-Cu) joint do not show any sign of weld defects, two strain concentration spots noticed on the centre region of the weld nugget. This indicates the presence of FSW weld defects. All the HR-DIC findings obtained from the front weld cross-section at different load values spatially agree with their corresponding rear weld cross-section. Figure 7.16a and Figure 7.16b show the strain distribution at different load values along the vertical line of CS-1 and CS-2 regions (as shown in grey scale images), respectively. As noticed in the HR-DIC strain maps, both these figures confirm the strain reduction across the weld nugget and also the BM-RS had the highest strain than other weld sub-regions during plastic deformation (3.5 kN).

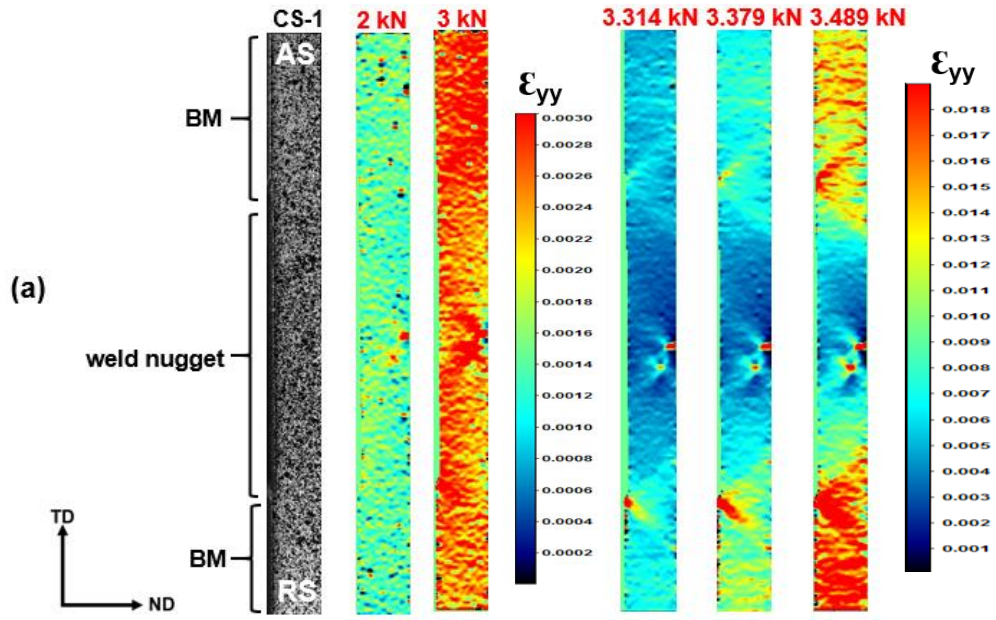

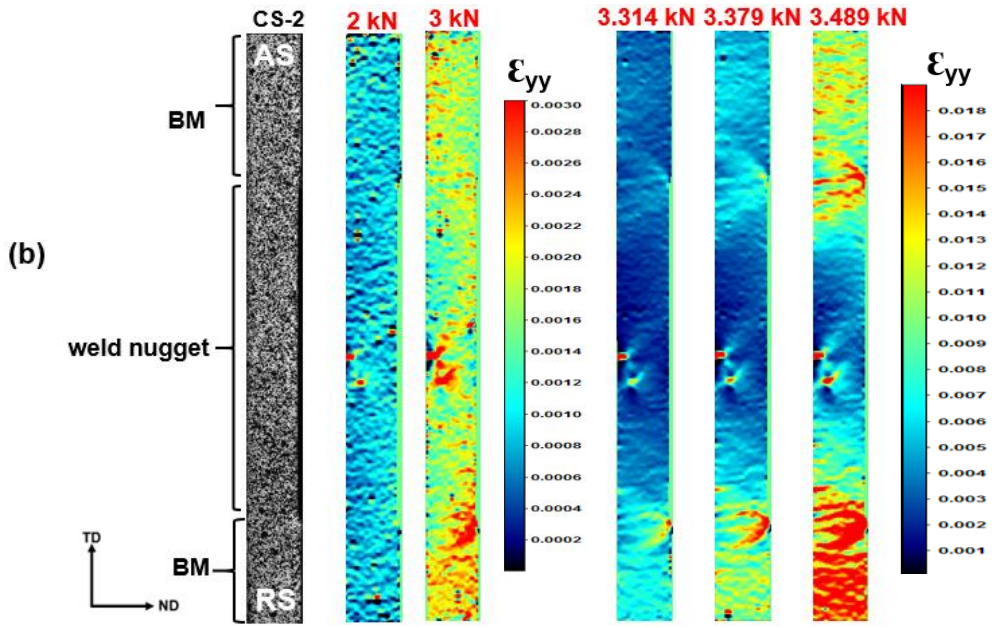

Figure 7.15 DIC results of the FSW (Cu-Cu)-S2 specimen at different load values: (a) Front weld cross-section (CS-1); (b) Rear weld cross-section (CS-2)

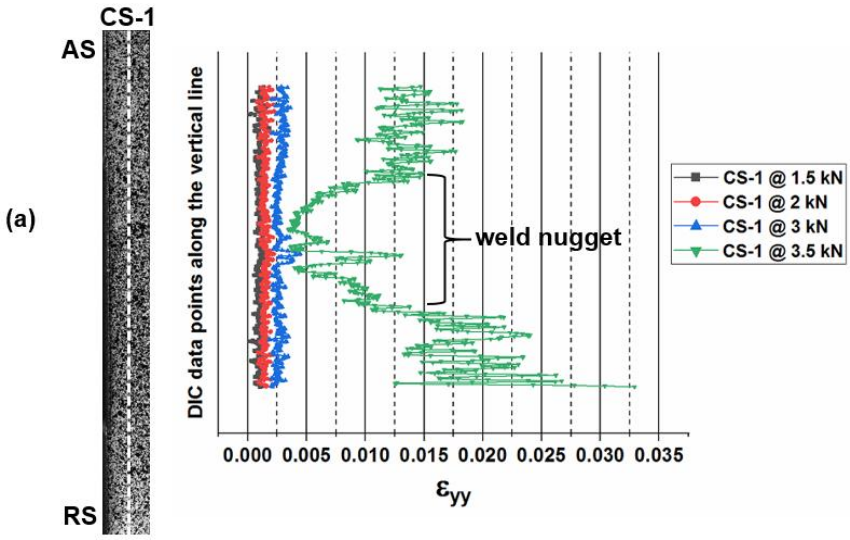

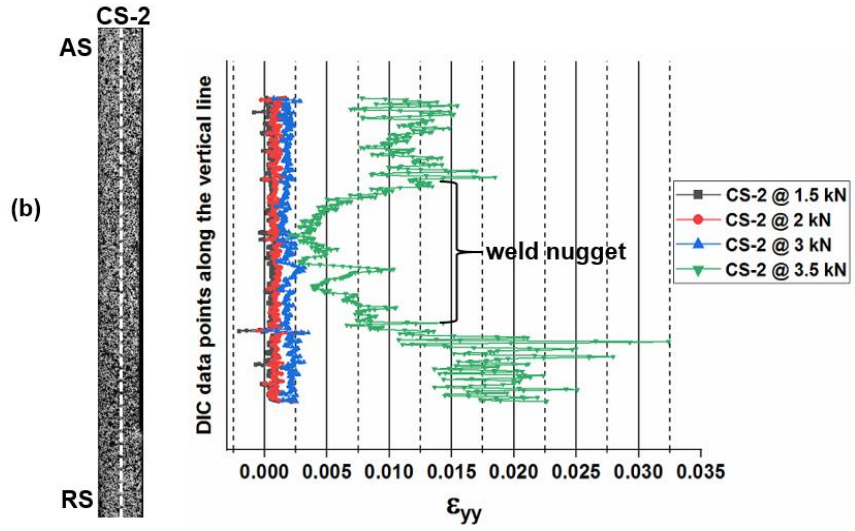

Figure 7.16 DIC results of the FSW (Cu-Cu)-S2 specimen: (a) Strain plots along the vertical line of the CS-1 at different load values; (b) Strain plots along the vertical line of the CS-2 at different load values

7.4.3 Microstructure-property correlation of the FSW (Cu-Cu) joint

To achieve a clear insight into the structure-property relationships of the FSW (Cu-Cu) weld sub-regions, both DIC and microscopy findings are spatially correlated, as shown in Figure 7.17. Figure 7.17a shows the HR-DIC strain map captured at 3.5 kN from the front weld cross-section (CS-1). Figure 7.17b exhibits the macrostructure of the FSW (Cu-Cu) weld cross-section. Figure 7.17c and Figure 7.17d display the optical micrographs observed from the corresponding locations, as shown in Figure 7.17b. The weld sub-regions (from 1 to 5) are plotted on the DIC strain map (Figure 7.17a) based on the correlation between the DIC strain map and optical micrographs. From this correlation, it is confirmed that the minimum strain observed across the entire region of the weld nugget (region 3) is due to the presence of ultrafine recrystallized grains. From Figure 7.17a, it is clearly evident that both the weld nugget (region 3) and TMAZ (region 2 and region 4) regions have achieved a distinct strain response in the plastic loading regime. As the TMAZ usually possesses a mixture of both fine and elongated grains as evidenced in the optical micrographs (Figure 7.17c and Figure 7.17d), both the TMAZ-RS (region 2) and TMAZ-AS (region 4) regions exhibit comparatively higher strain than the weld nugget. From the optical micrographs, it is revealed that the grains located close to the BM-RS (region 1) are slightly coarser than the BM-AS (region 5). Due to this reason, the BM-RS (region 1) had contained greater strain concentration than the BM-AS (region 5), as shown in Figure 7.17a. In addition to this, there is no major strain variation evident in the region between the TMAZ and BM. Therefore, both the optical microscopy and DIC findings point to the absence of HAZ.

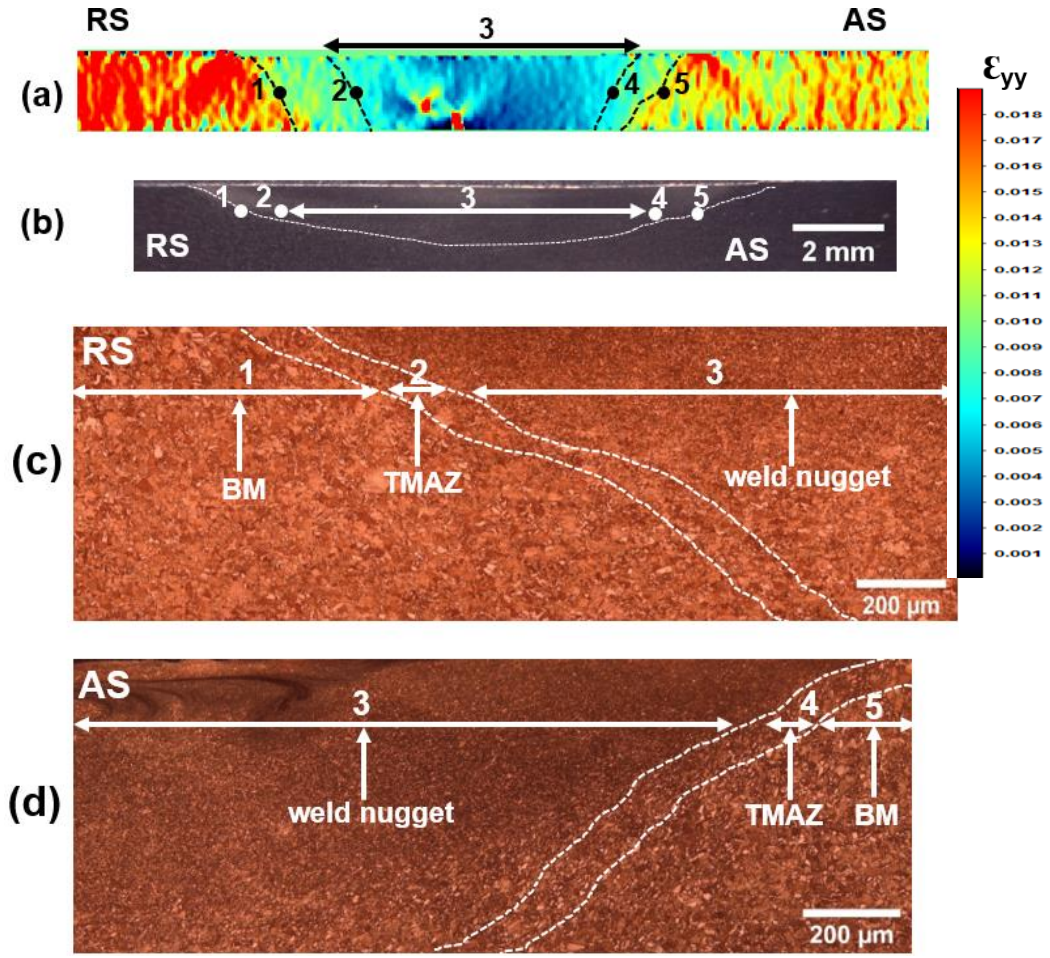

Figure 7.17 Microstructure-property correlation: (a) Ɛyy strain map of the FSW (Cu-Cu)-S2 along the weld cross-section at 3.5 kN; (b) Macrograph of the FSW (Cu-Cu) weld cross-section; (c) Optical micrograph of the FSW (Cu-Cu) weld cross-section along the RS; (d) Optical micrograph of the FSW (Cu-Cu) weld cross-section along the AS

7.4.4 Local stress-strain curves of the FSW (Cu-Cu) joint

To investigate the post-yielding characteristics of the FSW (Cu-Cu) weld sub-regions, local stress-strain curves are derived from the weld sub-regions, as shown in Figure 7.18. Based on the correlation between the microscopy and DIC results, the ROIs were chosen to extract the local stress-strain curves. All the stress-strain curves are plotted using the average DIC strain data obtained from the CS-1 and CS-2 regions and also using the actual area of cross-section of the weld sub-regions. At 0 to 2 kN (Figure 7.18a), all the weld sub-regions such as BM-AS, weld nugget, and BM-RS show similar stress-strain characteristics. However, Figure 7.18b (0 to 3 kN) clearly demonstrates the yielding of the BM and weld nugget regions. Additionally, it is shown that the weld nugget strains less and has a higher yield strength than the base material. The local stress-strain curves extracted from the 0 to 3.5 kN loading range (Figure 7.18c) show that the weld sub-regions such as BM-AS, TMAZ-RS and BM-RS have a similar yield strength of 189 MPa alongside with the different plastic

strain; TMAZ-RS does not strain as much as both base material regions (AS and RS). Both the weld nugget and TMAZ-AS regions have attained a similar yield strength of 200 MPa. It is confirmed that the weld nugget has experienced the least plastic strain among all the weld sub-regions of the FSW (Cu-Cu) joint due to the grain refinement produced by the FSW process. The local material properties derived at post-elastic deformation of the FSW (Cu-Cu) weld sub-regions are shown in Table 7.5. From the local stress-strain curves (Figure 7.18) as well as from Table 7.5, it is clearly revealed that each weld sub-region has different post-yielding material responses aligned with the corresponding microstructural features. Furthermore, the FSW weld nugget has achieved superior mechanical properties than other weld sub-regions.

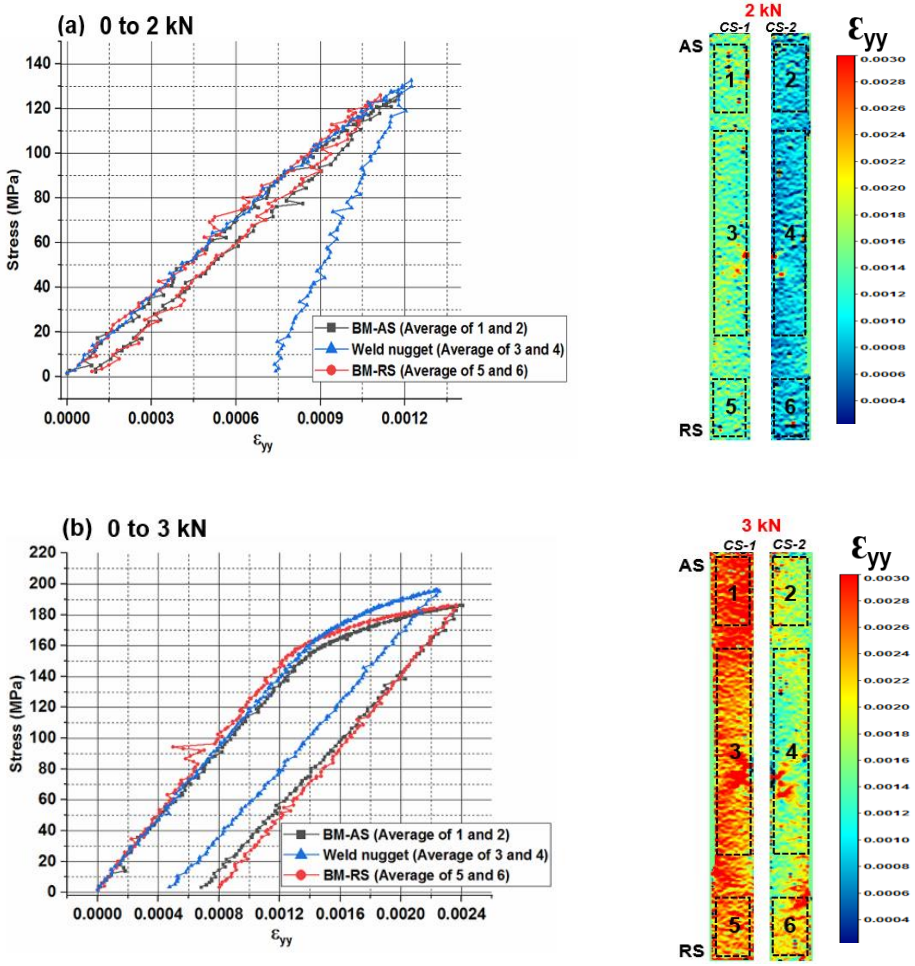

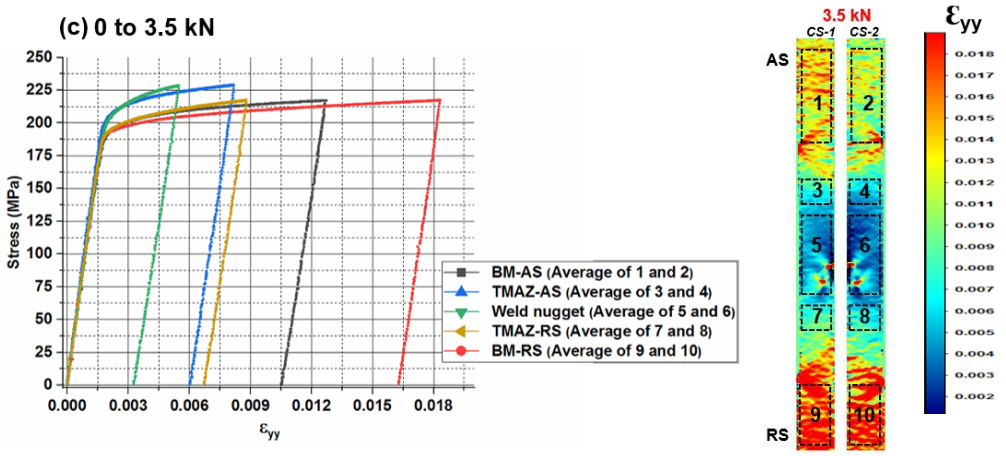

Figure 7.18 Local stress-strain curves of the FSW (Cu-Cu)-S2 weld sub-regions at plastic deformation: (a) 0 to 2 kN; (b) 0 to 3 kN; (c) 0 to 3.5 kN

Table 7.5 Local material properties derived at post-elastic deformation of the FSW (Cu-Cu) weld sub-regions

Load range	Weld sub-region	Yield strength (MPa)	Residual plastic strain (ε_p)	Tangent modulus (E_t) GPa
0 to 3 kN	BM-AS	159	0.000681	72.22
	Weld nugget	161	0.000473	95.56
	BM-RS	160	0.000805	87.22
0 to 3.5 kN	BM-AS	189	0.01050	52.50
	TMAZ-AS	200	0.006052	65.00
	Weld nugget	200	0.003268	53.33
	TMAZ-RS	189	0.006743	53.33
	BM-RS	189	0.016278	55.55

7.5 FSW (Cu-SS) joint

7.5.1 Validation of the HR-DIC methodology in the elastic region

As with the previous investigations, it was essential to establish an accurate profile of the weld geometry. Therefore, Figure 7.19b and Figure 7.19c show the Alicona 3D surface topography maps of the FSW (Cu-SS) joint measured from the corresponding location 1 and location 2, as shown in Figure 7.19a. As the FSW tool was offset towards the copper side during the FSW process, there is a greater thickness reduction towards the copper side (Figure 7.19b) compared to the stainless steel side (Figure 7.19c). The average thickness reduction of the weld nugget measured from the full-field Alicona surface measurements is 0.3 ± 0.045 mm.

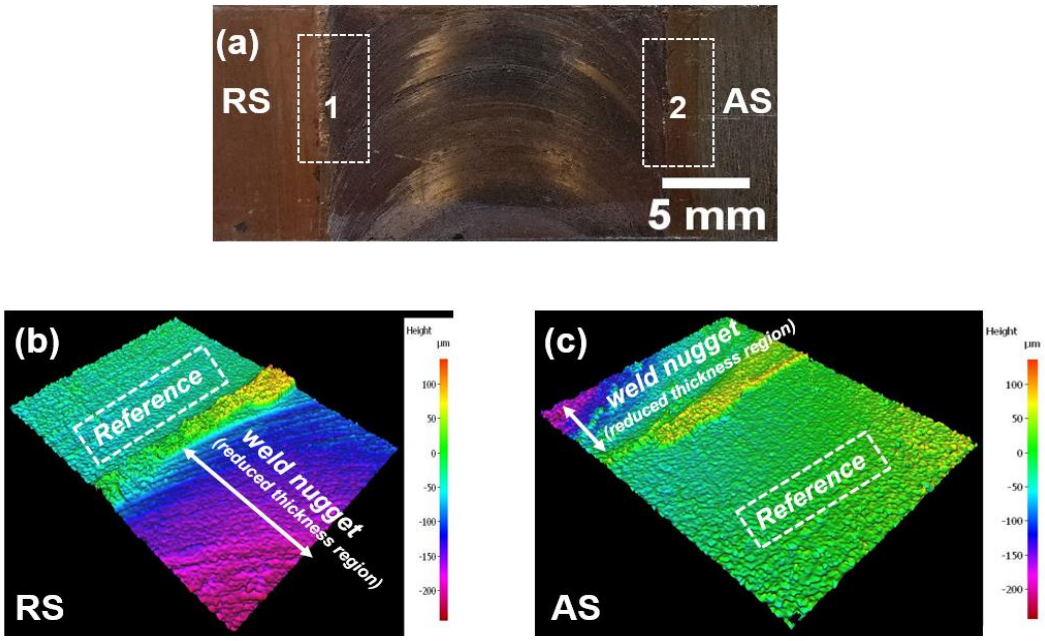

Figure 7.19 Alicona measurements: (a) ROIs (1, 2) for the Alicona profile measurements along the FSW (Cu-SS) weld cross-section; (b) Alicona 3D surface topography of the ROI-1 located in (a); (c) Alicona 3D surface topography of the ROI-2 located in (a)

Figure 7.20a shows the HR-DIC strain maps captured along the weld face and weld root of the FSW (Cu-SS) joint at different load values within the elastic range of both materials. Along the Weld Face (WF) (1 kN and 1.5 kN), it is observed that both the SS and Cu base materials have totally different strain distributions corresponding with their distinct stiffness characteristics. As expected, the weld nugget of the FSW (Cu-SS) joint shows strain localisation across the weld nugget due to the significant reduction in the thickness. During the entire elastic loading range, the SS base metal strains less than the Cu. However, the weld nugget has complex local strain gradients due to the presence of both Cu and SS elements located across the weld nugget. As evident in the HR-DIC strain maps of the FSW (SS-SS) joint, the outer boundary of the FSW (Cu-SS) weld nugget contains

a large strain localisation along the advancing and retreating sides due to the step-change in the weld geometry. Along the Weld Root (WR), some local regions of the stainless steel contain strains close to zero, which indicates that the specimen was subjected to bending during the uniaxial tensile test. The strain map captured at 1.5 kN shows a sharp change in the strain distribution between the copper and stainless steel regions. In contrast to the HR-DIC results derived from the FSW (Cu-Cu) joint, there is no evidence of a strain concentration at the weld interface along the root side of the joint. This indicates that good bonding without any major weld defects was achieved between the copper and stainless steel materials through the FSW process.

To validate the HR-DIC methodology on the FSW (Cu-SS) joint, three ROIs such as SS-BM, weld nugget, and Cu-BM were chosen along the WF and WR regions as shown in Figure 7.20a to average the strain data from these regions. Figure 7.20b shows the local stress-strain curves plotted from the average strain data along using the area of cross-section of the weld sub-regions (SS-BM, weld nugget, and Cu-BM)obtained from the Alicona. The elastic modulus of the SS and Cu BM regions determined from the local stress-strain curves is found to be exactly equivalent to their expected theoretical value (SS=200 GPa, Cu=110 GPa). It is important to note that the elastic modulus of the dissimilar weld nugget (151 ± 1 GPa) is higher than the Cu-BM (112 ± 1 GPa). This shows that the weld nugget has a higher proportion of stainless steel than copper, which enhanced the stiffness of the weld nugget. As previously by averaging the strain data from the weld face and weld root regions the parasitic strains resulting from the offset loading of the weld nugget are removed.

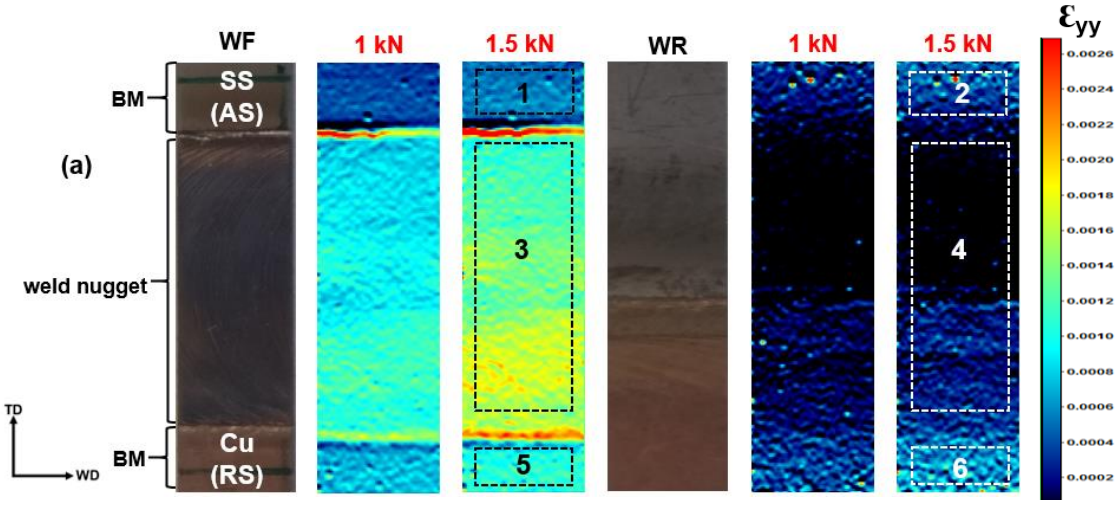

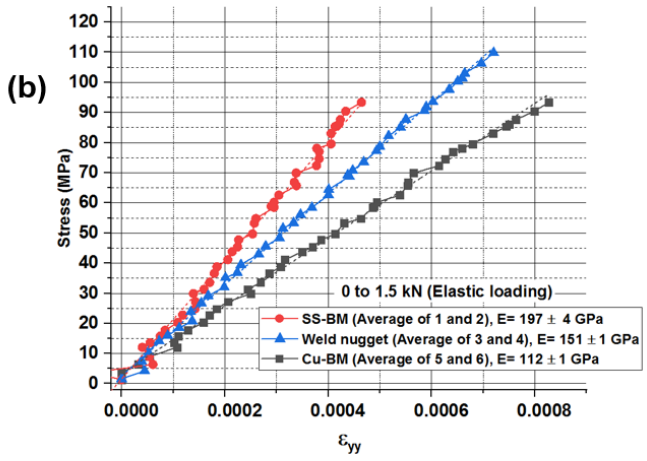

Figure 7.20 HR-DIC results: (a) HR-DIC strain maps (Ɛyy) captured at 1.5 kN and 2 kN load values from the Weld Face (WF) and Weld Root (WR) of the FSW (Cu-SS)-S1 specimen; (b) Local stress-strain curves extracted using average strain values from the corresponding ROIs shown in (a)

Figure 7.21a shows the DIC strain maps captured from the front (CS-1) and rear (CS-2) weld cross-sections of the FSW (Cu-SS) joint at a range of load values within the materials elastic range. The strain maps from the weld cross-sections show similar results as observed on the WF and WR regions; copper as a soft material experiences more strain than the stainless steel. There is clearly some in-plane bending occurring, by using the procedure described previously Figure 7.21b shows that the angle of misalignment for the SS-BM is around 0.70°. Along the Cu side, the angle of misalignment looks to be much smaller, 0.11° to 0.14° respectively, as shown in Figure 7.21c. This result cannot be true and indicates that there is some overall deformation occurring in a non-uniform fashion between the dissimilar materials. It might be expected that the copper would deform more as the Young's modulus is small, however the cross section of the steel in the weld is smaller. It is evident that the specimen is not loaded ideally and that any conclusions should take this into account.

To investigate if taking average values of the strains from CS1 and CS2 could account for the strain differences noted above, three ROIs comprised of SS-BM, weld nugget, and Cu-BM were chosen to extract the local DIC strain data at a range of load values (as shown in Figure 7.21a). The local stress-strain curves (Figure 7.22) are extracted from these ROIs by using the average strain between the front (CS-1) and rear (CS-2) weld cross-sections in the corresponding ROIs. The elastic modulus of the SS and Cu base metal regions obtained from the local stress-strain curves is again very close to their theoretical value. Furthermore, the local stress-strain curves extracted along the weld surface and weld cross-section provided the same value for the elastic modulus of the weld nugget, which further validates the high fidelity of the HR-DIC methodology. Hence the devised HR-DIC methodology can be applied successfully in all three FSW welds (SS-SS, Cu-Cu, and Cu-SS) and the effect of the in-plane bending can be accounted for by using this procedure.

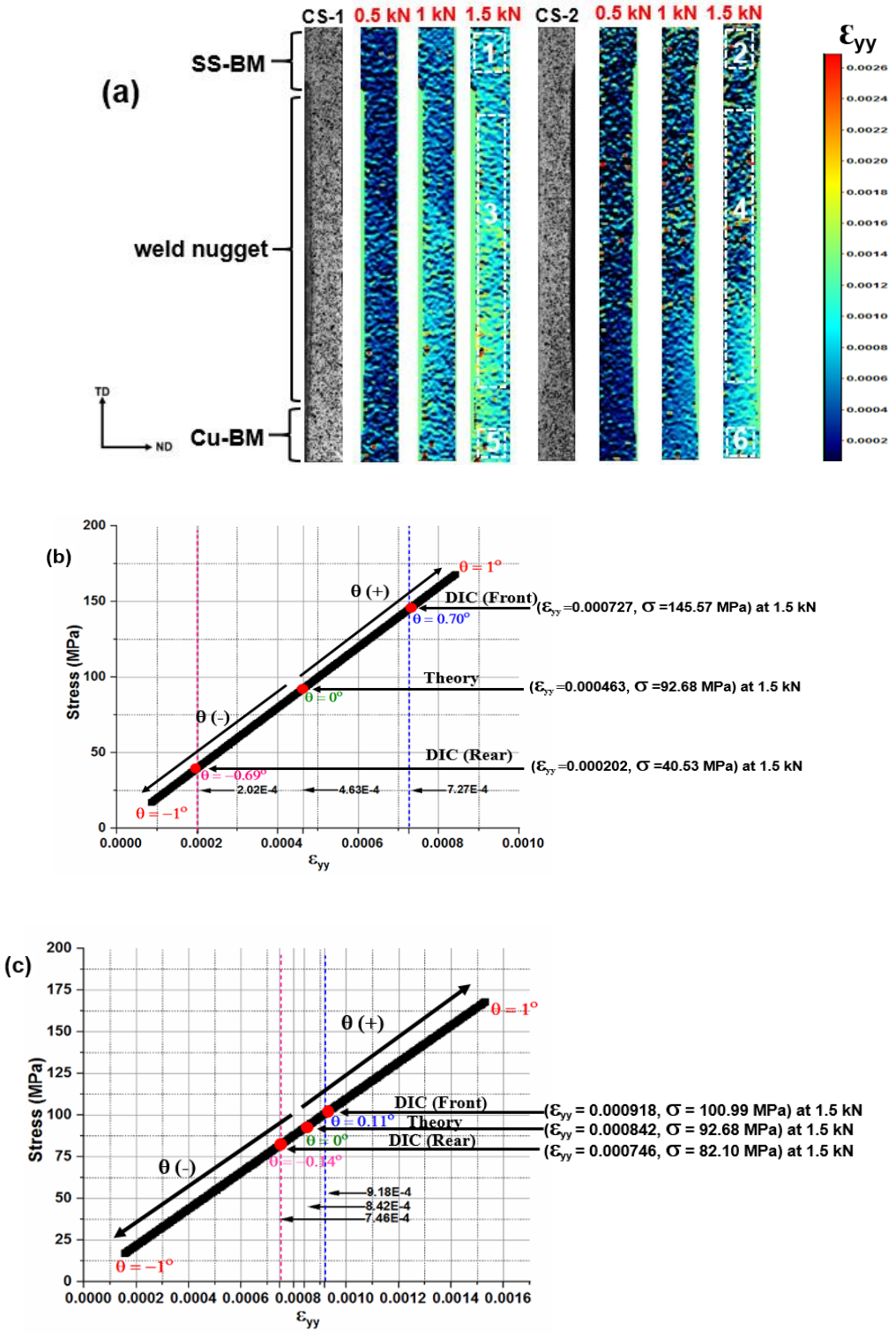

Figure 7.21 HR-DIC results from the FSW (Cu-SS)-S2 specimen: (a) DIC strain maps (ε_{yy}) along the (CS-1) and (CS-2) at different load values; (b) Stress-Strain plots of SS-BM calculated using Equation 4.5 and Equation 4.6 (Chapter-4) with respect to the FSW (Cu-SS) tensile specimen at 1.5 kN; (c) Stress-Strain plots of Cu-BM calculated using Equation 4.5 and Equation 4.6 (Chapter-4) with respect to the FSW (Cu-SS) tensile specimen at 1.5 kN

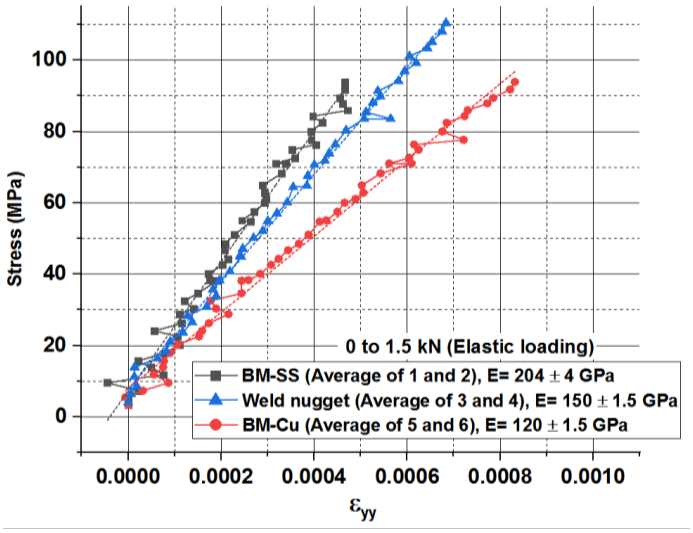

Figure 7.22 Local stress-strain curves extracted using average strain values from the corresponding ROIs shown in Figure 7.21 (a)

7.5.2 Local strain response of the FSW (Cu-SS) joint during plastic deformation

Table 7.6 shows the loading and unloading cycles used for the HR-DIC measurements on FSW (Cu-SS)-S1 and FSW (Cu-SS)-S2 specimens.

Table 7.6 Loading/unloading cycles used for HR-DIC measurements on FSW (Cu-SS) joints

Cycle	Loading range (kN)	Unloading range (kN)
1	0 to 0.5 kN	0.5 to 0 kN
2	0 to 1 kN	1 to 0 kN
3	0 to 1.5 kN	1.5 to 0 kN
4	0 to 2 kN	2 to 0 kN
5	0 to 2.5 kN	2.5 to 0 kN
6	0 to 3 kN	3 to 0 kN

Figure 7.23a shows the strain maps obtained at various load steps along the weld face. At 2.5 kN and 3 kN load values, the weld nugget has achieved clear strain gradients in according with the spatial distribution of copper and stainless steel across the weld nugget. It is noteworthy that a part of the weld nugget close to the stainless steel has achieved the material response exactly equivalent to the stainless steel base material, and the remaining part has achieved the material response of the copper base material. This finding highlights that the plastic response of the FSW (Cu-SS) weld nugget depends on the spatial distribution of copper and stainless steel elements located across the weld

nugget. At 2.5 kN, the WF has achieved a sharp change in the strain distribution at the centre region of the weld nugget where the weld interface between the stainless steel and copper is located. As the stainless steel has higher stiffness than the copper, the copper base metal contains a higher strain than the stainless steel. At 3 kN, the centre of the weld face has attained a highly heterogeneous strain profile that is produced by the inhomogeneous mixture of stainless and copper elements located in this region. Figure 7.23b shows the strain distribution plots extracted at different load values along the vertical line (as shown in Figure 7.23a) of the WF. This figure clearly differentiates the elastic and post-elastic strain response of the dissimilar weld nugget.

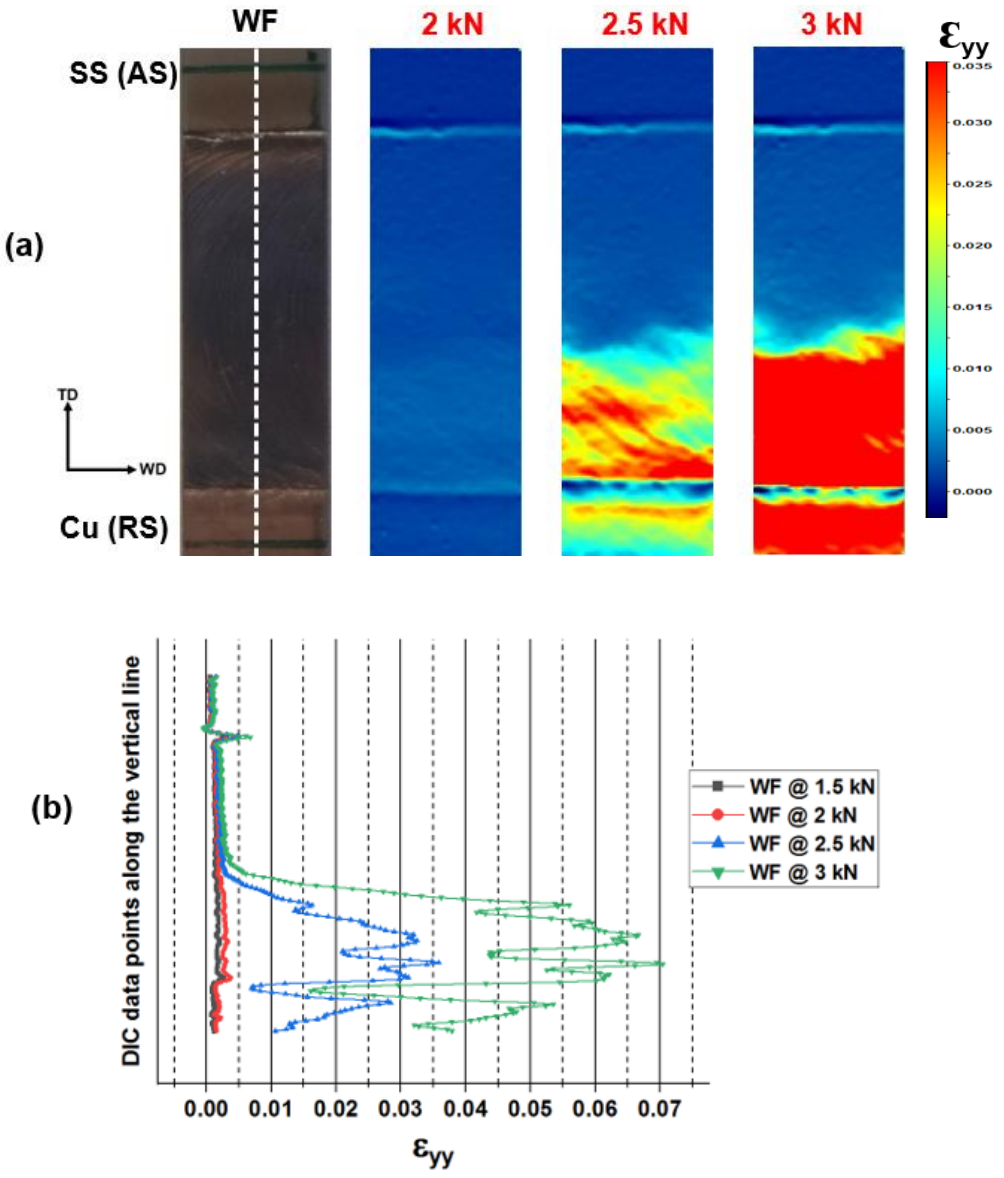

Figure 7.23 DIC results of the FSW (Cu-SS)-S1 specimen along the Weld face (WF): (a) DIC strain maps (ε_{yy}) captured at plastic deformation; (b) Strain plots along the vertical line of the WF as shown in (a) at different load values

At 1.5 kN and 2 kN load values, both the dissimilar base materials (Cu and SS) and the weld nugget show their distinct elastic strain response. It is interesting to note that even at higher load values (2.5 kN and 3 kN), the SS-BM as well as the upper half of the weld nugget, are still in the elastic region due to major distribution of SS. However, the lower half of the weld nugget has plastically deformed at these load values due to the high population of Cu elements.

Figure 7.24a shows the strain maps obtained at various load steps along the weld root (WR). The strain map captured at 2.5 kN along the root side again demonstrates the strain concentration in the copper region. In addition to this, most of the scattered strain concentration profiles along the copper side are exactly aligned with the direction of material flow, as the FSW tool was more offset towards the copper side during the FSW process. Figure 7.24b shows the strain distribution plots extracted at different load values along the vertical line (as shown in Figure 7.24b) of the WR. This figure confirms the similar trend as noticed along the WF, where the lower half of the weld nugget has a non-uniform strain distribution due to the mixture of Cu and SS. Furthermore, the lower half of the weld nugget also achieved significant strain compared to other weld sub-regions during plastic deformation due to the higher proportion of Cu than the SS.

The HR-DIC strain maps captured on the front (CS-1) and rear (CS-2) weld cross-sections of the FSW (Cu-SS)-S2 joint at different load steps are shown in Figure 7.25a and Figure 7.25b respectively. As noticed along the WF and WR, the strain maps captured at 2.5 kN clearly show a non-homogeneous strain distribution across the weld nugget. In comparison to the copper base metal, a significant strain reduction is evident at the centre of the weld nugget, which is in line with the shape of the weld nugget as well as the depth of FSW tool penetration. The strain reduction is entirely due to grain refinement occurring in the FSW process. However, this region has strained more than the stainless steel base material, indicating that the centre of the FSW (Cu-SS) weld nugget is dominated by stainless steel rather than copper. It is noteworthy that the strain reduction occurs over a small area at the centre of the weld nugget instead across the entire weld nugget. Furthermore, the HR-DIC strain maps clearly captured the step change in the strain distribution along the copper and stainless steel interfaces in the region close to the centre of the weld nugget. Similarly to the observations noticed on the WF and WR regions, the copper shows high strain concentration compared to the stainless steel along the weld cross-section. Figure 7.25c and Figure 7.25d show the strain distribution plots at different load values along the vertical line (as shown in greyscale images) of CS-1 and CS-2 regions, respectively. Both these figures again confirm the strain reduction region at the centre of the weld nugget during plastic deformation (2.5 kN and 3 kN) is due to the presence of fine recrystallized grains. Similar to the observations derived from the WF and WR, during plastic loading, both the CS-1 and CS-2 regions also show large scatter in the strain distribution along the lower half of the weld nugget due to the mixture of Cu and SS elements.

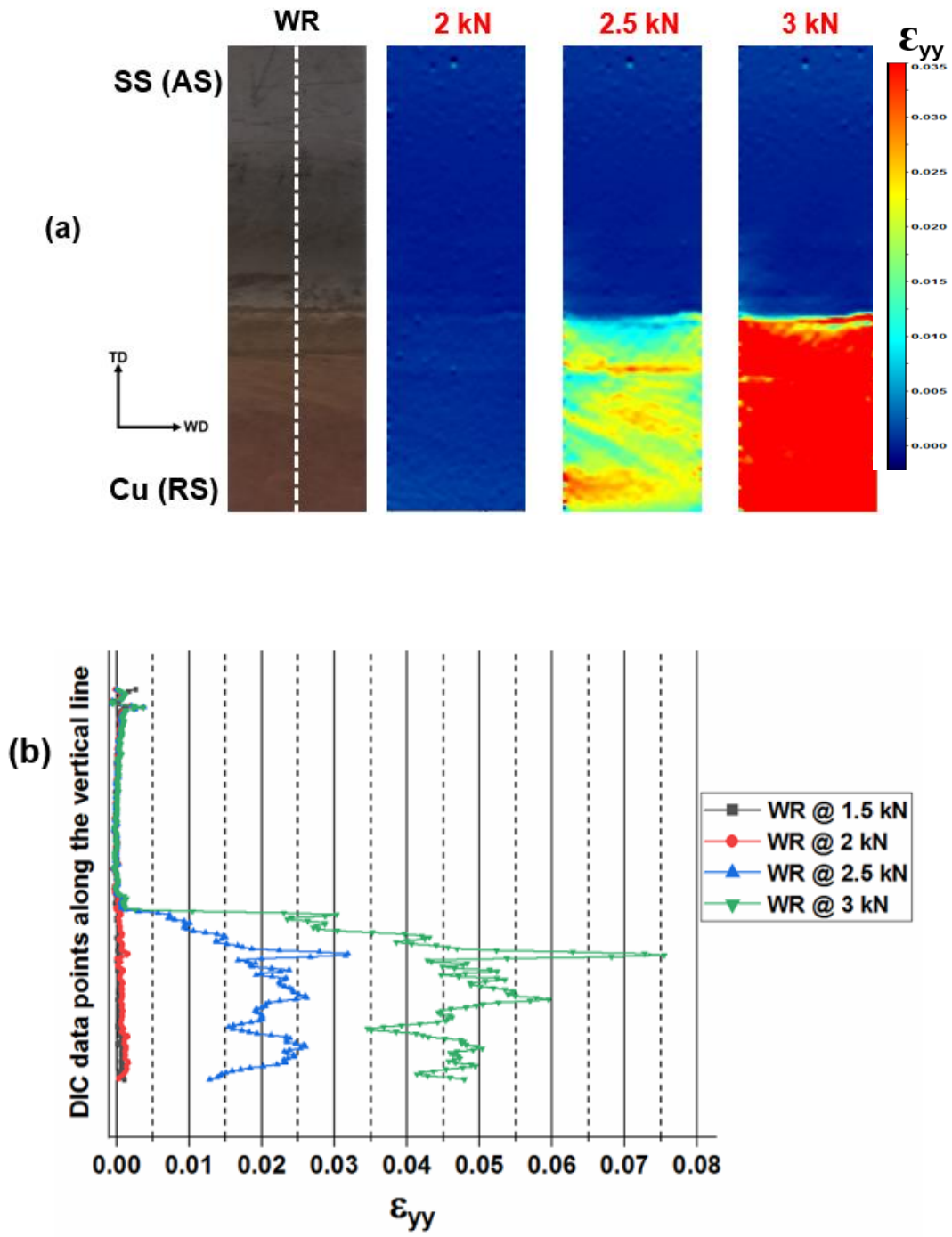

Figure 7.24 DIC results of the FSW (Cu-SS)-S1 specimen along the Weld Root (WR): (a) DIC strain maps (ε_{yy}) captured at plastic deformation; (b) Strain plots along the vertical line of the WR as shown in (a) at different load values

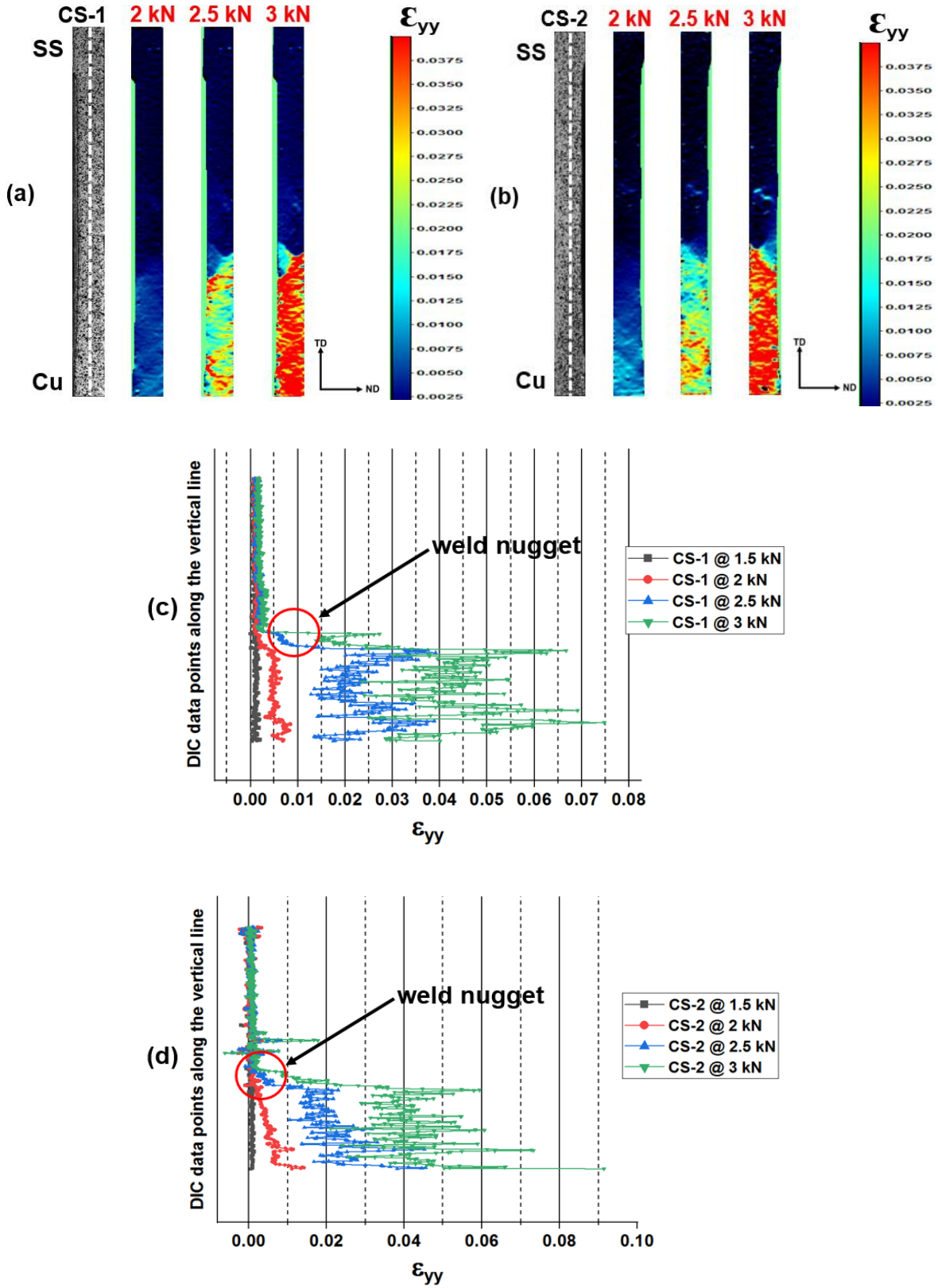

Figure 7.25 DIC results of the FSW (Cu-SS)-S2 specimen at plastic deformation: (a) Front weld cross-section (CS-1); (b) Rear weld cross-section (CS-2); (c) Strain plots along the vertical line of the CS-1 at different load values; (d) Strain plots along the vertical line of the CS-2 at different load values

7.5.3 Microstructure-property correlation of the FSW (Cu-SS) joint

To further understand the HR-DIC results obtained from the FSW (Cu-SS) specimen, the findings from the HR-DIC are correlated with the optical and SEM/SEM-EDS micrographs given in Figure 7.26. The weld sub-regions (1, 2, and 3) are located in the strain map based on the change in the strain distributions (Figure 7.26a) as well as correlation with the optical micrographs. These same weld sub-regions also located in the macrograph of the FSW (Cu-SS) weld cross-section (Figure 7.26b). By correlating the HR-DIC strain map and macrograph, it is found that region 1, region 2, and region 3 are copper-weld interface, weld nugget, and steel-weld interface respectively. The optical and SEM-EDS micrographs captured on these weld sub-regions are shown in Figure 7.26c and Figure 7.26d, respectively. By correlating the HR-DIC strain map and optical micrographs, it is confirmed that the strain reduction at the centre region of the weld nugget (region 2) is due to the presence of fine recrystallized grains. Although the weld nugget had fine recrystallized grains generated from the FSW process, it has contained a higher strain than the stainless steel base material. The reason for this phenomenon can be revealed by correlating the HR-DIC strain map with optical and SEM-EDS micrographs where it clearly evidenced the presence of both copper and stainless steel elements located across the dissimilar weld nugget. Due to the presence of both copper and stainless steel elements, the local strain response of this region is clearly affected by the population density of these elements located in the dissimilar FSW weld nugget.

7.5.4 Local stress-strain curves of the FSW (Cu-SS) joint

The local stress-strain curves extracted from the weld sub-regions along the weld cross-section at different loading ranges are shown in Figure 7.27. At 0 to 2 kN, three ROIs include BM-SS, weld nugget, and BM-Cu are chosen (as shown in Figure 7.27a) to extract the local stress-strain curves based on the average strain measured from the CS-1 and CS-2 regions. From this figure, it is observed that the copper base metal has achieved its yield point in advance of the weld nugget, although the stainless steel base metal is still in the elastic range. The local stress-strain curves extracted from 0 to 2.5 kN loading range include the ROIs TMAZ-Cu and TMAZ-SS regions in addition to the dissimilar base metals and weld nugget, as shown in Figure 7.27b. From these strain-strain curves, it is evident that both the TMAZ-SS and weld nugget have an almost similar stress-strain response. As the weld nugget has achieved a complete grain refinement than the TMAZ, the weld nugget exhibits less plastic strain than the TMAZ-SS. As the weld nugget is completely dominated by the stainless steel elements, the TMAZ associated with the Cu side also achieved higher yield strength than the copper base metal. Additionally, the stainless-steel base metal still remains elastic in this loading range (0 to 2.5 kN). Among all the weld sub-regions, the copper base metal has achieved maximum plastic strain. The stress-strain characteristics of the weld sub-regions at 0 to 3 kN loading range (Figure 7.27c) also confirm the above findings at a higher stress-strain level due to the strain hardening effects. Table 7.7 shows the local material properties derived at post-elastic deformation

of the FSW (Cu-SS) weld sub-regions. From the key findings obtained from the post-yielding local stress-strain curves as well as from Table 7.7, it is found that the FSW (Cu-SS) weld sub-regions have heterogeneous stress-strain characteristics in their plastic loading range and also the weld nugget has achieved superior yield strength than the copper.

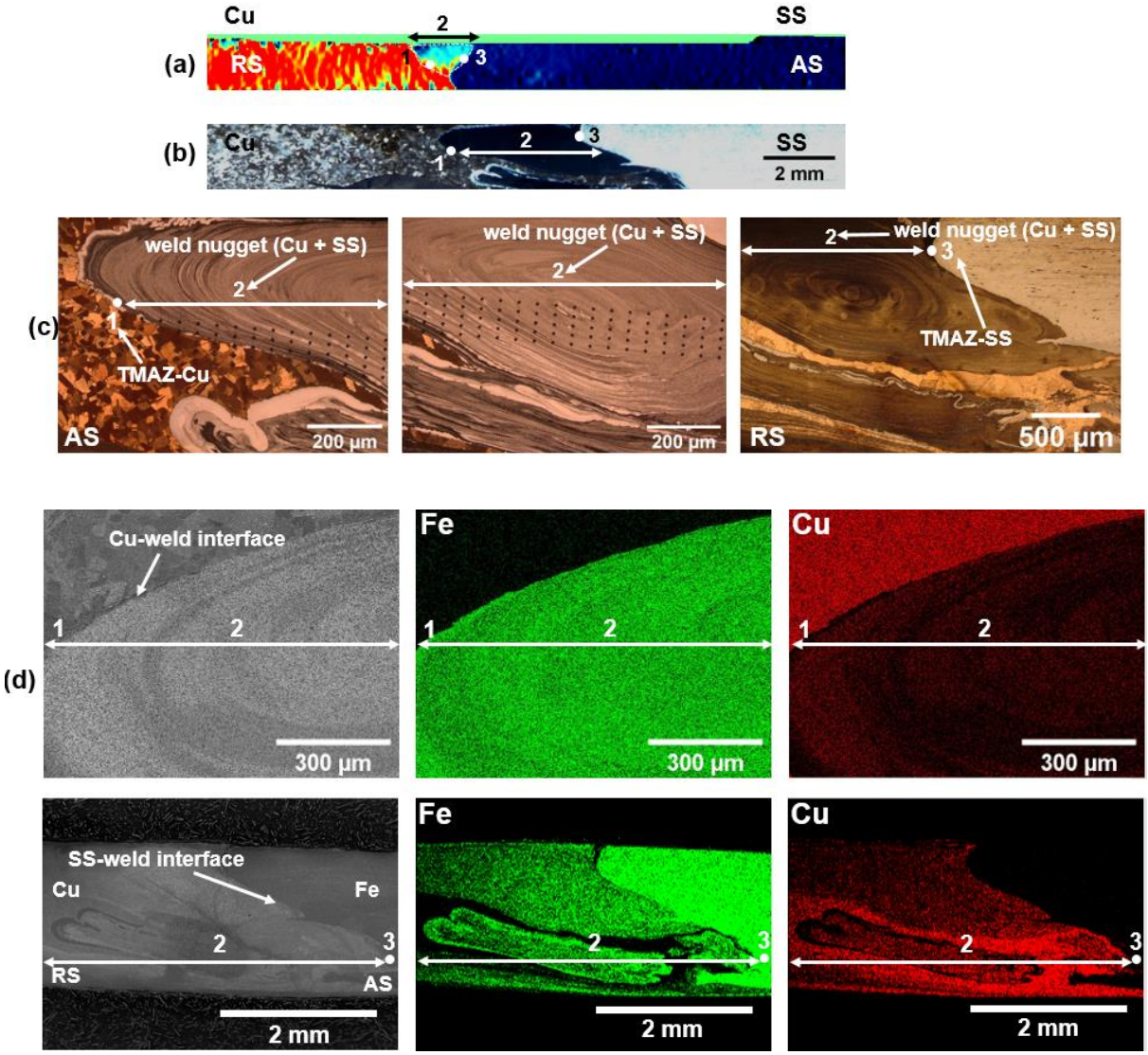

Figure 7.26 Microstructure-property correlation: (a) Ɛyy strain map of the FSW (Cu-SS)-S2 along the weld cross-section at 3 kN; (b) Macrograph of the FSW (Cu-SS) weld cross-section; (c) Optical micrograph of the FSW (Cu-SS) weld cross-section; (d) SEM-EDS micrographs of the FSW (Cu-SS) weld cross-section

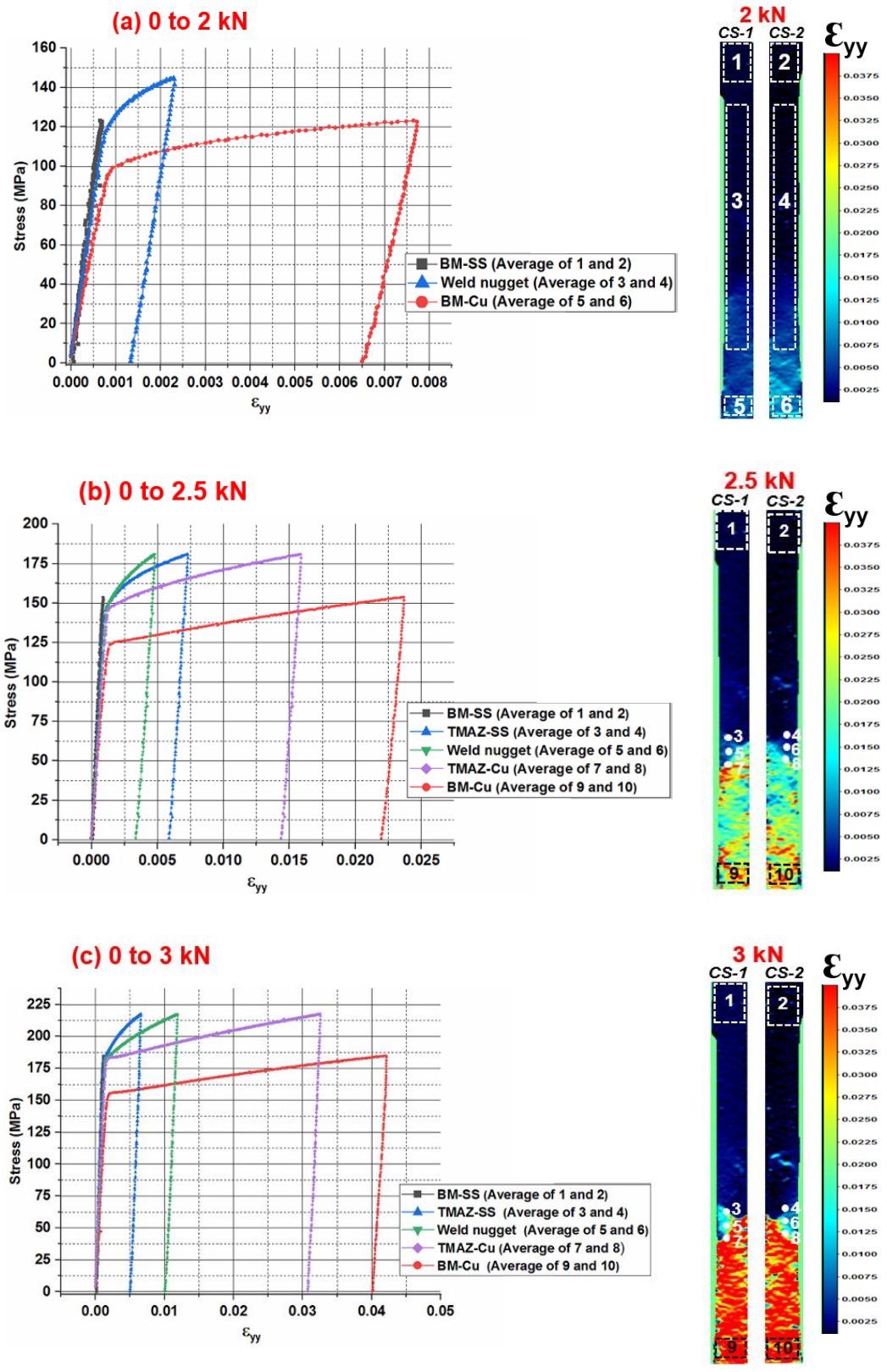

Figure 7.27 Local stress-strain curves of the FSW (Cu-SS)-S2 weld sub-regions at plastic deformation: (a) 0 to 2 kN; (b) 0 to 2.5 kN; (c) 0 to 3 kN

Table 7.7 Local material properties derived at post-elastic deformation of the FSW (Cu-SS) weld sub-regions

Load range	Weld sub-region	Yield strength (MPa)	Residual plastic strain (ε_p)	Tangent modulus (E_m) GPa
0 to 2 kN	BM-SS	NA	0.000055	NA
	Weld nugget	117	0.001333	111.11
	BM-Cu	97	0.006643	44.44
0 to 2.5 kN	BM-SS	NA	0.000047	NA
	TMAZ-SS	148	0.005964	54.44
	Weld nugget	145	0.003352	77.77
	TMAZ-Cu	145	0.014446	22.22
	BM-Cu	121	0.022203	18.33
0 to 3 kN	BM-SS	NA	0.000158	NA
	TMAZ-SS	180	0.005075	83.33
	Weld nugget	180	0.010245	43.33
	TMAZ-Cu	178	0.030755	16.33
	BM-Cu	154	0.040100	18.33

7.6 Summary

The results obtained from the simultaneous front and rear HR-DIC measurements using the modified novel experimental methodology on the actual FSW (SS-SS, Cu-Cu, and Cu-SS) welds were presented and discussed. By using the 2D-DIC methodology established in Chapter 6, the parasitic strains produced from the out of plane displacements were removed along the through-thickness plane both in elastic and plastic loading regimes of the FSW (SS-SS) joint. Additionally, the same experimental methodology was successfully applied as well as validated in the other two weld combinations (Cu-Cu, and Cu-SS). High-fidelity structure-property relationships of the weld sub-regions were established through the spatial correlation of the DIC and microscopy results. The local

stress-strain curves extracted from the DIC results represent that all the weld sub-regions (BM, TMAZ, and weld nugget) have achieved different yield strengths aligned with the microstructural features received from the outcome of the FSW process. In both similar FSW (SS-SS and Cu-Cu) weld combinations, the grain refinement region located in the FSW weld nugget had superior mechanical properties than the corresponding base material. For the FSW (Cu-SS) weld, the mechanical properties derived from the weld nugget were superior to the copper base metal, but inferior to the stainless steel base metal as both dissimilar elements stirred into the weld nugget. It is noteworthy that the entire stir zone of the FSW (Cu-Cu) joint has achieved strain reduction; however, in the case of FSW (SS-SS) and FSW (Cu-SS) joints only the centre of the stir zone had strain reduction. Although the key findings derived through the correlation between DIC and microscopy results have achieved a clear insight into the structure-property relationships of the weld sub-regions, the reason for the local strain concentration achieved on the FSW weld nugget is not completely known. In addition to this, the strain distribution aligned with the FSW material flow is not precisely correlated using the DIC results and optical micrographs. From the HR-DIC results, it is also confirmed that the FSW welds have some defects. Therefore, to accurately map the spatial location of weld defects and also to relate the FSW material flow with the corresponding DIC results, the next stage in the investigation is to employ an X-ray CT characterisation in the plastically deformed specimens used for the HR-DIC measurements. The results obtained from the X-ray CT characterisation on the FSW (SS-SS, Cu-Cu, and Cu-SS) weld combinations are discussed in the next chapter.

Chapter 8 X-ray CT, DIC and Optical microscopy results correlation

8.1 Introduction

The SEM-EDS findings presented in chapter 5 from the FSW (SS-SS) joint confirmed the distribution of tungsten particles across the weld nugget, which is likely to be due to the effect of FSW tool wear. However, the spatial distribution of W particles over the entire weld nugget in 3D cannot be quantitatively revealed using SEM-EDS. To investigate the effect of W particles on the local strain response of the FSW weld sub-regions and in the FSW (Cu-SS) joint the effect of the spatial distribution of Fe and Cu elements across the weld nugget, it is necessary to understand the heterogeneous material composition of the joint. Therefore, an X-ray CT characterisation technique has been adopted to probe the spatial distribution of these various heterogeneous elements over the entire *volume* of the weld nugget, this will also help to achieve a clearer understanding of the complex material flow across the weld. The findings obtained from the X-ray CT are compared with the DIC results and micrographs, which provides a more holistic understanding of the local strain gradients produced in various observed planes of the FSW welds. The spatial distributions of Fe, Cu, and W located in the FSW welds can be resolved through an X-ray CT approach in 3D as all these elements have different X-ray attenuation rates, which will produce contrast in the tomographs.

8.2 X-ray CT experimental set-up

The X-ray CT scan parameters used in this investigation are listed in Table 8.1. All CT scans on the FSW (SS-SS, Cu-Cu, and FSW (Cu-SS) joints were performed using a custom Nikon XTEK XTH 225 KV micro-focus CT system at the voxel resolution of 7.1 x 7.1 x 7.1 μm^3. The operating voltage and X-ray beam current used during the CT scans were 220 kV and 110 μA, respectively. The CT data captured at an exposure time of 0.177 sec was reconstructed from 8 frames and 2201 projections, which were evenly spaced over 360^o. All the reconstructed CT 3D data sets were post-processed using the commercial software called Avizolite 9.3 to allow 3D volume rendering analysis.

8.3 X-ray CT results

8.3.1 FSW (SS-SS)

Figure 8.1 shows the CT scan results from the ROIs (Figure 8.1a) of the FSW (SS-SS) specimen in a 3D representation. To better visualise the spatial distribution of different phases present in the reconstructed CT images, the grey level histogram of all the CT data is compared with the

corresponding colour histogram (green) where the intensity range was fixed close to the maximum grey intensity value. From Figure 8.1b and Figure 8.1c, it can be seen that both the AS and RS reconstructed images show different greyscale intensities on their surface. In these images, the brighter spots demonstrate the regions of higher X-ray absorption rate than seen in the darker regions. It is noteworthy that the majority of these brighter spots concentrated on the surface of the stir zone are closely aligned with the stir profiles of the FSW (SS-SS) specimen. Along the through-thickness cross-sections, the brighter areas are overlapping with the onion ring pattern. The brighter and darker areas in the CT images are associated with the spatial distribution of tungsten (W) and iron (Fe), respectively. All the above observations confirm the presence of W in the regions that had the expected major impact of FSW tool wear due to the severe frictional contact with the tool shoulder and pin. It is also observed that the tool shoulder affected region (weld surface) has a higher W level distribution than the through-thickness cross-section. Figure 8.2 correlates the DIC strain map of the weld face captured at 5 kN with the corresponding X-ray CT reconstructed image obtained after the plastic deformation of the specimen. From this correlation, it is clearly revealed that the strain localisation observed in the HR-DIC strain map (Figure 8.2b) is closely linked to the localised spatial distribution of tungsten (Figure 8.2a). The correlation also reveals that the larger strain on the RS compared to the AS of the FSW (SS-SS) weld face is likely to be due to the heterogeneous distribution of scattered tungsten particles in the SS. Tungsten has a greater stiffness than the stainless steel, but the inclusion of the particle simply deposited has resulted in the strain localisation effects on the RS. Furthermore, no significant strain localisation is observed on the centre of the weld face compared to the AS and RS regions, and it should be noted that there is no evidence of tungsten in the centre of the FSW (SS-SS) weld face.

Table 8.1 X-ray CT scan parameters used for FSW welds

Parameter	In-house (Nikon/X-tek HMX)
Sample thickness (mm)	2
Acceleration voltage (kV)	200
Beam current (μA)	110
Voxel resolution (μm)	7.1
Detector dimensions (pixels)	2000 x 2000
Scan time (hours)	~0.8
Number of projections	2201 (360^{o} rotation)
Number of frames	8
Exposure time (second)	0.177

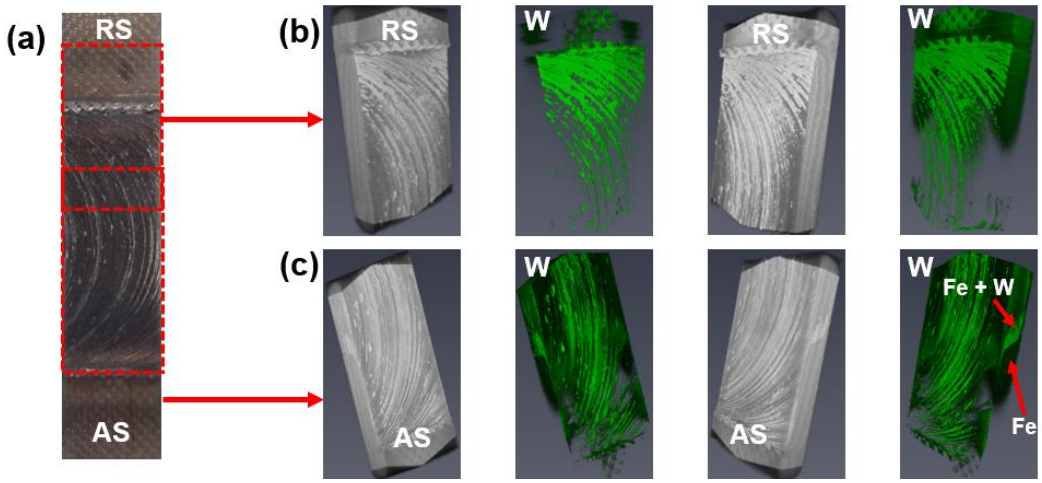

Figure 8.1 X-ray CT scan results of the FSW (SS-SS) specimen: (a) ROIs for X-ray CT scan; (b) X-ray reconstructed image along the RS; (c) X-ray reconstructed image along the AS

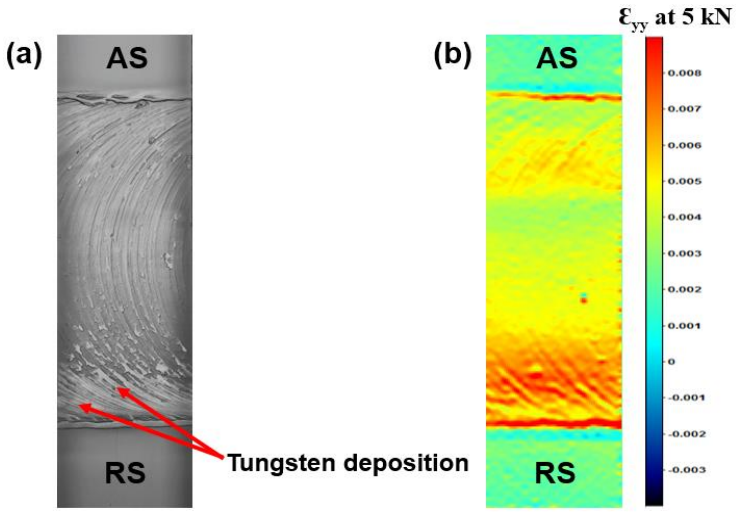

Figure 8.2 Correlation between HR-DIC strain map and X-ray CT reconstructed image (after plastic deformation) of the FSW (SS-SS) weld face: (a) X-ray CT reconstructed image; (b) HR-DIC strain map (ε_{yy}) at 6 kN

Figure 8.3 correlates the HR-DIC strain map of the weld root captured at 5 kN with the corresponding X-ray CT reconstructed image obtained after the plastic deformation of the specimen. The crack that can be observed along the weld root (Figure 8.3b) correlates with the strain localisation observed in Figure 8.3a. Furthermore, the CT image also reveals a series of cracks located on the AS, and these cracks were responsible for additional strain localisation spots in the weld root. In contrast to the FSW (SS-SS) weld face, the weld root does not show evidence of any tungsten particles in the X-ray CT image, this is to be expected as it is the weld face that usually experiences the most plastic deformation and is in contact with the FSW tool.

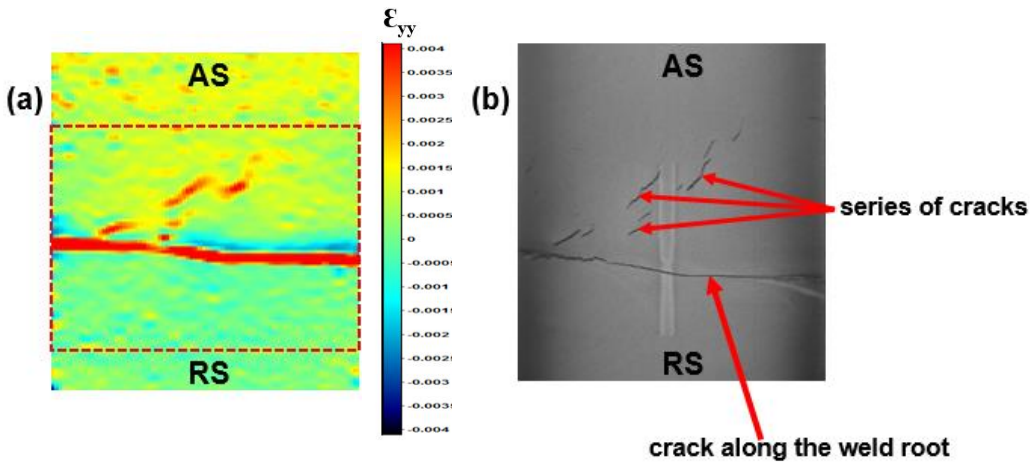

Figure 8.3 Correlation between HR-DIC strain map and X-ray CT reconstructed image (after plastic deformation) of the FSW (SS-SS) weld root: (a) DIC strain map (ε_{yy}) at 6 kN; (b) X-ray CT reconstructed image

Figure 8.4 correlates the X-ray CT findings with the optical microscopy and DIC results of the FSW (SS-SS) weld cross-section. From Figure 8.4c and Figure 8.4d, it is clearly seen that the through-thickness cross-section of the weld has a tungsten distribution that exactly covers the whole onion ring pattern. But only a reduced strain is observed in region-4 (Figure 8.4a). Therefore, the high degree of grain refinement located in the weld cross-section effectively prevented significant strain localisation effects from the heterogeneous tungsten distribution. By correlating DIC result (Figure 8.4a) with X-ray CT (Figure 8.4d), it can also be seen that the strain localisation observed in region 5 of the weld cross-section is due to an excessive amount of W deposition in the form of material flow along the RS. It is noteworthy that during the FSW process the material on the RS usually receive more friction from the FSW tool compared to the AS, as the tool movement is against the rotating direction. Therefore, the tool wear (W particles) is more significant in the RS. Another possible reason for the accumulation of W particles in the RS may be due to accidental tool offset towards the RS during the FSW process. Although the collaborator, who manufactured the specimens, has not reported any tool offset during the welding of similar materials (SS-SS and Cu-Cu), there is a possibility where the FSW tool can slightly deviate from the butt interface and offset towards the RS[102]. Overall, the effect of W on the strain distribution is more pronounced on the weld surface than in the through-thickness cross-section as the weld surface had a low degree of grain refinement than the cross-section. The expected effect of the higher stiffness and strength tungsten particles is to reduce the localised plastic strain in the surrounding matrix, the higher mechanical strength produced by the finer grains in the weld cross-section has counter-acted the adjacent material increased strain effects induced by load transfer from the tungsten. The use of correlation between the X-ray CT, Optical microscopy, and HR-DIC results elucidates both the local effects of tungsten on the spatial strain distribution and also links this to the structure-property relationships of the local weld sub-regions.

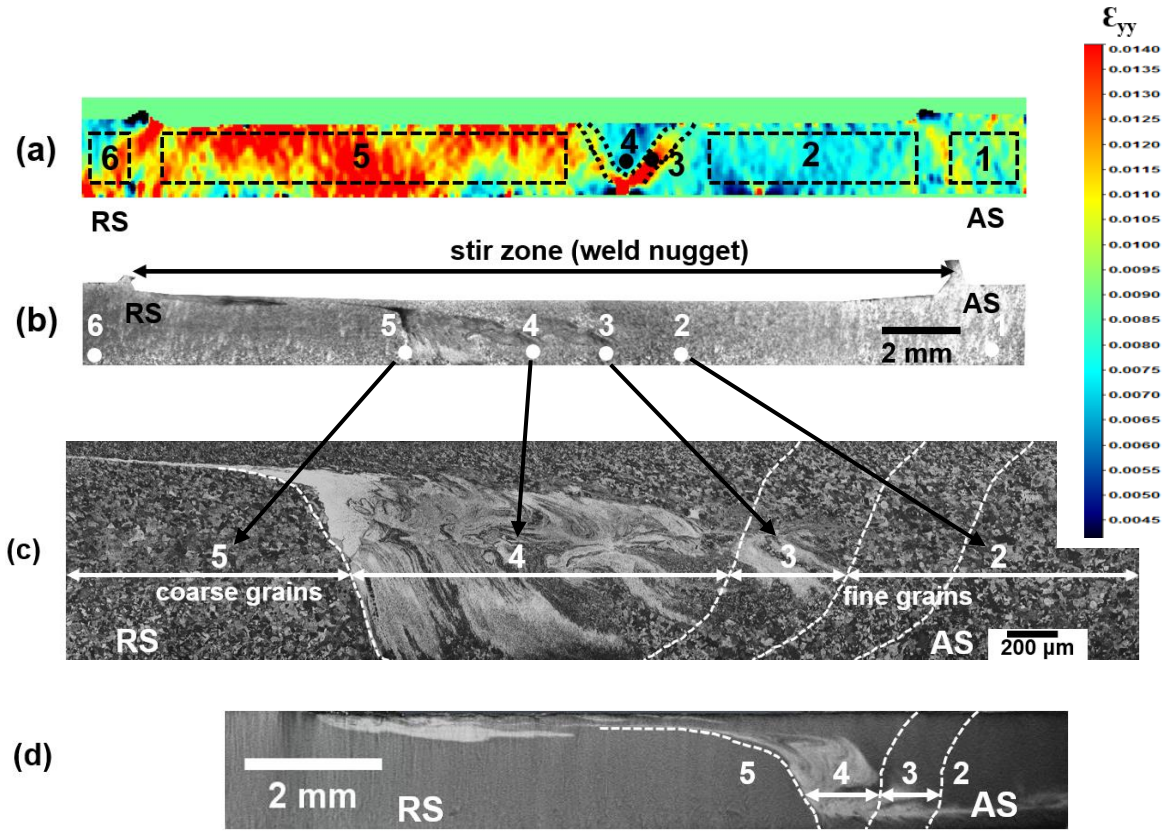

Figure 8.4 DIC strain map correlation with optical micrograph and X-ray CT results: (a) ε_{yy} strain map of the FSW (SS-SS)-S2 along the weld cross-section at 6 kN; (b) Macrograph of the FSW (SS-SS) weld cross-section; (c) Optical micrograph of the FSW (SS-SS) weld cross-section; (d) X-ray CT reconstructed image of the FSW (SS-SS) weld cross-section-S2

8.3.2 FSW (Cu-Cu)

Figure 8.5 correlates the HR-DIC strain map of the FSW (Cu-Cu) weld root with the corresponding X-ray CT reconstructed image captured during the plastic deformation of the specimen. The DIC strain map (Figure 8.5a) of the weld root captured at 2.5 kN shows the strain concentration exactly at the weld interface. By correlating the DIC strain map with its corresponding X-ray CT result (Figure 8.5b), it is clearly revealed that the strain concentration occurred due to crack propagation along the welding direction. Figure 8.6 shows the correlation between the HR-DIC and X-ray CT results of the FSW (Cu-Cu) weld cross-section under plastic deformation of the tensile specimen. This correlation effectively demonstrates that the two strain localisation spots (1 and 2) observed in the strain map (Figure 8.6a) are due to the presence of porosity and minor crack propagation respectively (Figure 8.6b). In contrast to the observation received from the FSW (SS-SS) weld cross-section, the X-ray CT result of the FSW (Cu-Cu) weld cross-section (Figure 8.6b) confirms the absence of any tungsten particles across the entire weld cross-section, indicating the absence of tool wear during the FSW of copper, and thus that there is no influence of tungsten on the HR-DIC strain

measurements of the FSW (Cu-Cu) specimens. Correlating the HR-DIC and X-ray CT results of the FSW (Cu-Cu) specimen has clearly mapped the location of weld defects and their associated strain response during plastic deformation.

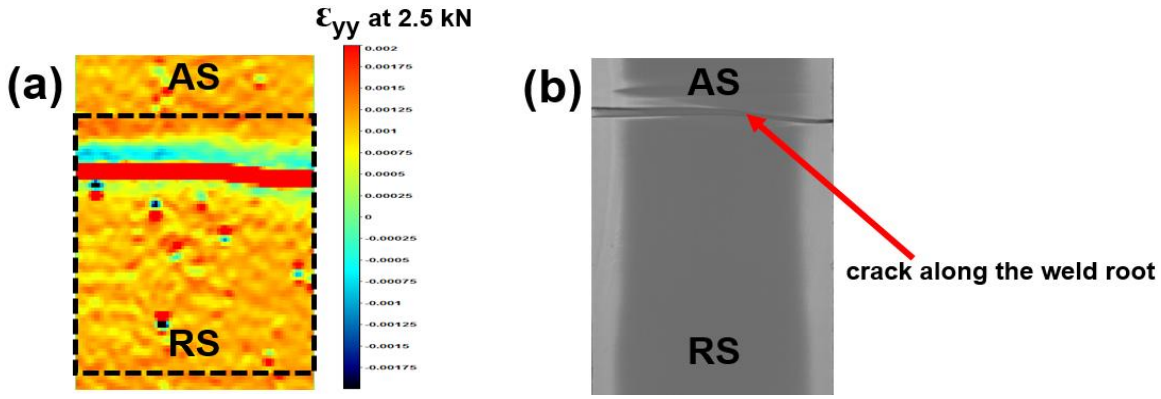

Figure 8.5 Correlation between DIC strain map and X-ray CT reconstructed image (after plastic deformation) of the FSW (Cu-Cu) weld root: (a) DIC strain map (ε_{yy}) at 2.5 kN; (b) X-ray CT reconstructed image

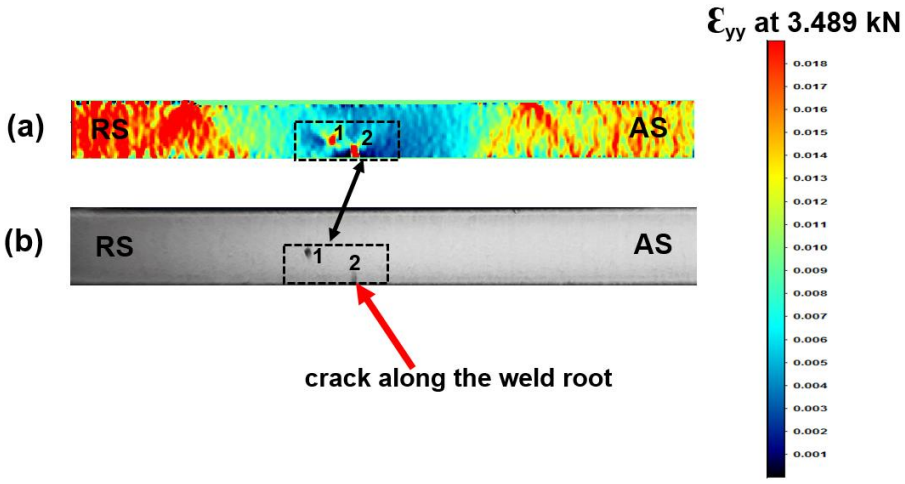

Figure 8.6 Correlation between DIC strain map and X-ray CT reconstructed image (after plastic deformation) of the FSW (Cu-Cu) weld cross-section: (a) DIC strain map (ε_{yy}) at 3.489 kN; (b) X-ray CT reconstructed image

8.3.3 FSW (Cu-SS)

Figure 8.7 shows the correlation between the HR-DIC and X-ray CT results derived from the FSW (Cu-SS) weld face. Based on the X-ray absorption rate, the distribution of Cu and SS elements across the weld nugget are mapped as bright and dark features, respectively in the X-ray CT reconstructed image (Figure 8.7a). As the tool was offset towards the Cu, the weld nugget does not have any apparent scattered tungsten particles (Figure 8.7a), and this indicates no tool wear occurred during

the FSW of Cu to SS. Figure 8.7a shows the X-ray CT image where the lower half of the FSW (Cu-SS) weld nugget has achieved a richer mixture of Cu and SS than the upper half, indicating the material movement during the FSW process has been from the AS to the RS. This finding is aligned with the HR-DIC result where the lower half of the weld nugget has experienced complex strain gradients due to the migration of SS towards the Cu. In contrast to this observation, the upper half of the weld nugget shows a uniform strain distribution with the absence of local strain concentrations due to the dense population of SS with a negligible amount of any Cu. Figure 8.7b shows a clear relationship between the HR-DIC and X-ray CT results along the FSW (Cu-SS) weld root. Both the HR-DIC strain map and X-ray CT reconstructed image show a sharp interface at the centre of the dissimilar welded joint. As observed in the weld face, the X-ray CT image captured from the weld root also shows the distribution of SS and Cu elements as dark and bright features, respectively. In line with the weld face, the lower half of the weld root clearly shows a wide range of strain gradients due to the heterogeneous composition of Cu and SS achieved through the stirring action of the FSW. Additionally, the correlation between the HR-DIC strain map and X-ray CT results achieved from the weld root also shows that the location of the major strain localisation regions are spatially aligned with the stir profiles as well as heterogeneous composition spots located on the Cu side. Similarly to the weld face, the upper half of the weld root shows a more homogeneous strain distribution due to the predominant presence of SS along with the apparent absence of Cu elements. Figure 8.8 shows the X-ray CT reconstructed image of the FSW (Cu-SS) weld in 3D using the same methodology, as explained in Figure 8.1. The X-ray CT image (Figure 8.8a) represented in grey scale shows the spatial distribution of Cu and SS elements both along the surface and the through-thickness weld cross-section. The colour histogram image (Figure 8.8b) represents the spatial distribution of copper as a dark green colour. From these figures, it is evident that the FSW (Cu-SS) weld surface possesses a mixture of both Cu and SS. However, the distribution of Cu is much more dense along the lower half of the weld nugget. This finding can be demonstrated through Figure 8.8b where both the Cu BM and lower half of the weld nugget have the same colour intensity indicating the spatial distribution of Cu. Compared to the weld face, the weld cross-section (Figure 8.8a) shows a complex mixture of both Cu and SS with an extensive migration of SS towards Cu.

Figure 8.9 shows the correlation between the HR-DIC and the X-ray CT results of the FSW (Cu-SS) weld. These results are further correlated with the optical micrographs derived from the reference specimen of the FSW (Cu-SS) weld. Based on the position of the dissimilar weld interface and weld nugget, the local regions (1, 2, and 3) are mapped in Figure 8.9a-c. HR-DIC (Figure 8.9a) and X-ray CT results (Figure 8.9b) show the relationship between the strain distribution with the corresponding elemental distribution. Furthermore, the shape of the weld nugget (Region-2) as well as the dissimilar weld interfaces (Region-1 and 3) determined from the DIC strain map are in agreement with the X-ray CT result. From the key findings derived from a range of material characterisation techniques on the same ROI (as shown in Figure 8.9), it is clearly determined that the strain reduction observed at the centre of the weld nugget (Region-2) is due to the presence of a high proportion of SS as well as

a high density of fine recrystallized grains. This correlation further emphasises that the presence of both Cu and SS in region-2 has led to strain gradients as noticed in the DIC strain map (Figure 8.9a). Overall the findings through a range of material characterisation techniques (HR-DIC, X-ray CT, and Optical microscopy) from the local regions (1, 2, and 3) are well aligned with one another.

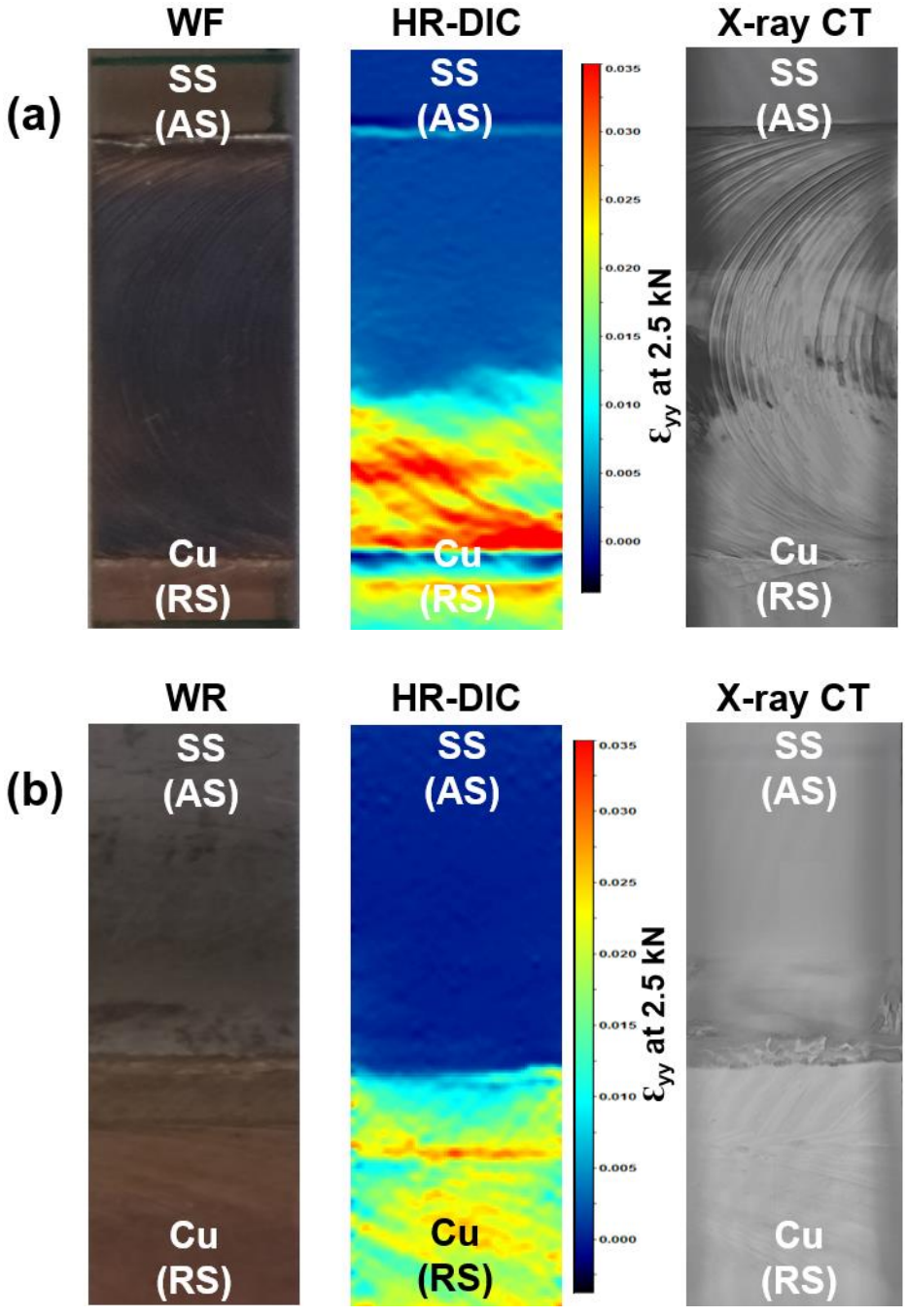

Figure 8.7 Correlation between DIC strain map and X-ray CT reconstructed image (after plastic deformation) of the FSW (Cu-SS) joint: (a) Weld Face; (b) Weld Root

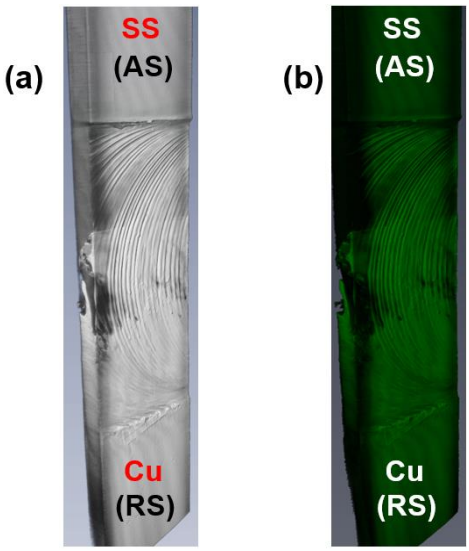

Figure 8.8 X-ray CT scan results of the FSW (Cu-SS) specimen: (a) X-ray reconstructed image in grey scale; (b) X-ray reconstructed image shows the distribution of Cu in dark green colour

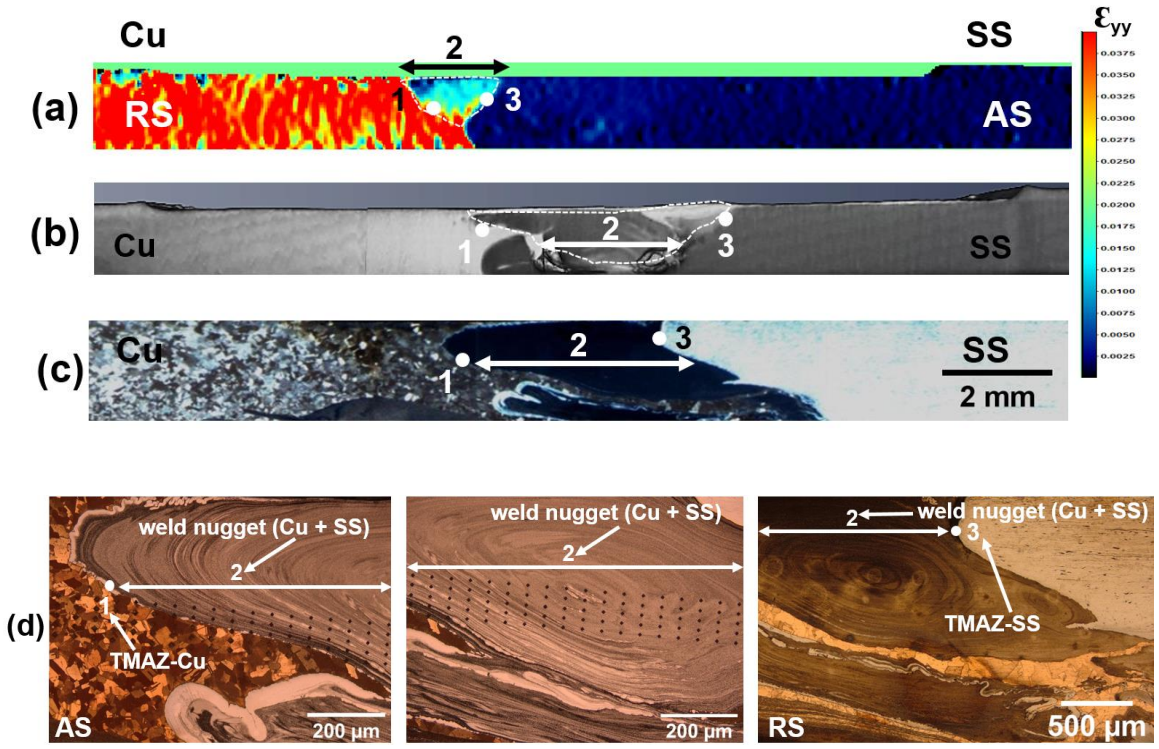

Figure 8.9 DIC strain map correlation with optical micrograph and X-ray CT results: (a) ε_{yy} strain map of the FSW (Cu-SS)-S2 along the weld cross-section at 3 kN; (b) X-ray CT reconstructed image of the FSW (Cu-SS)-S2 weld cross-section; (c) Macrograph of the FSW (Cu-SS) weld cross-section; (d) Optical micrographs of the FSW (Cu-SS) weld cross-section

8.4 Summary

The results obtained from the X-ray CT scans on the FSW (SS-SS, Cu-Cu, and Cu-SS) joints were effectively correlated with their corresponding HR-DIC results and optical micrographs to achieve a clear insight into the microstructure-property relationships of the local weld sub-regions. Based on the above results and discussion, the following conclusions are drawn:

- The FSW (SS-SS) weld nugget had a significant amount of scattered tungsten particles due to the effect of FSW tool wear. The spatial location of tungsten particles was determined from the X-ray CT reconstructed image in 3D and correlated with the corresponding HR-DIC and Optical microscopy results. Although the presence of tungsten was confirmed both in the weld face and cross-section, strain localisation effects due to the presence of the scattered tungsten particles, which was much more pronounced on the weld face than in the cross-section. This has been linked to the refined grain structure in the cross-section increasing the local resistance to plastic deformation of the SS.
- X-ray CT results of the FSW (Cu-Cu) joint confirmed the absence of FSW tool wear as no significant presence of tungsten particles was observed across the weld nugget. However, the weld nugget had some minor defects that led to strain localisation along the through-thickness cross-section.
- HR-DIC and X-ray CT results correlation of the FSW (Cu-SS) joint evidenced the severe migration of SS elements towards the Cu side, which lead to higher strain gradients on the RS than the AS of the weld nugget. Along the through-thickness cross-section, the centre of the weld nugget had a lower strain than the Cu base metal due to the dense population of SS.
- To further summarise from the above key conclusions, the X-ray CT characterisation of the FSW welds and post-processing the X-ray CT data established a methodology to confirm FSW tool wear by spatially mapping the distribution of tungsten particles in the weld nugget. For dissimilar FSW joints, the same methodology can be used to map the distribution of dissimilar elements (with different X-ray attenuations) located across the weld nugget. The correlation between the surface HR-DIC results with the corresponding 3D X-ray CT data and optical micrographs has provided a more holistic understanding of the complex microstructure-mechanical property relationships of the local weld sub-regions.

Chapter 9 Conclusions and Future work

9.1 Conclusions

The overall aim of this PhD research was to develop high-fidelity imaging procedures to establish the relationship between the microstructure and material properties developed locally in the weld sub-regions during the FSW procedure. Both similar and dissimilar welds were studied, i.e. SS-SS, Cu-Cu, and Cu-SS joints. A wide range of microscopy techniques were used to evaluate the microstructure and a novel HR-DIC experimental methodology was devised to study the local behaviour of the weld subregions under elastic and plastic deformation. The microscopy and DIC findings were spatially correlated in a unique way, which allowed the mechanical behaviour of each weld sub-region to be linked directly to the corresponding microstructure. These results were also correlated with X-ray CT. The main conclusions of the thesis are summarised as follows:

- The microscopy results showed that the FSW process produced a major grain refinement across the weld nugget.
    - From the microscopy results of all FSWs it was clear that the most refined grains occurred in the weld nugget.
    - The TMAZ of FSW (SS-SS) and FSW (Cu-Cu) had elongated and partially recrystallized ultrafine grains. However, the TMAZ of FSW (Cu-SS) joint was not clearly evident in micrographs.
    - In all FSWs, there was no significant HAZ measured across the weld nugget.
    - Both the AS and RS of FSWs weld sub-regions have achieved different microstructural features.
    - All FSWs had a significant non-uniform thickness reduction across the weld nugget.
    - Tool wear in the form of tungsten particles was evident in the weld nugget of FSW (SS-SS) joint.
- High fidelity DIC strain measurements were performed on actual FSWs in a high resolution through a novel experimental methodology.
    - A novel image stitching approach was devised to stitch the HR strain maps captured from the ROIs across the FSWs.
    - The minor thickness reduction of the FSW weld nugget was accurately measured for the first time to account for the reduced area of cross-section.
    - The out-of-plane displacement evolved from the complex FSW weld geometry was measured.
    - Parasitic strains produced due to the out of plane displacement resulting from offset loading of the weld nugget during the HR-DIC measurements were removed through a novel DIC experimental approach.

- It was shown for the similar welds that the Young's modulus of the weld nugget was the same as the base material hence the HR-DIC procedure was validated in the elastic loading range.

- The novel HR-DIC approach allowed the mechanical properties for the weld sub-regions to be identified in the plastic loading range without modifying the actual thickness of FSWs.
  - The novel HR-DIC approach also applied in the plastic deformation of the FSWs cross-section to extract the post-yielding characteristics of the heterogeneous weld sub-regions.
  - HR-DIC results were correlated with micrographs to link the microstructure-mechanical property relationships of the FSW weld sub-regions with a high degree of confidence.
  - In similar FSWs, the weld nugget had the highest yield strength and lower strain compared to the base materials at all load steps. In case of FSW (Cu-SS) joint, the weld nugget had higher yield strength than the copper base metal but lesser than the stainless steel base metal.
- Correlation between the DIC and X-ray CT findings derived from FSWs has offered a wide range of key findings.
  - Presence of FSW tool wear by means of spatial distribution of tungsten particles was confirmed in the SS-SS joint. However, the FSW tool wear was not evident in the FSW (Cu-Cu) and FSW (Cu-SS) joints.
  - Correlation between the HR-DIC and X-ray CT characterisation results of the FSW (SS-SS) joint has confirmed the effects of tungsten distribution on the formation of strain localisation.
  - In case of FSW (Cu-SS) joint, the weld nugget had the major density of stainless steel than the copper.

9.2 Future work

- The results presented in this thesis were achieved through high-fidelity experimental procedures performed on similar and dissimilar FSW joints. Even though this PhD investigation has successfully established the microstructure-property relationships of the FSW weld sub-regions by interlinking the microscopy and HR-DIC findings on the same ROI, these findings have not been obtained from the same specimen. Instead, this investigation has assumed that the microstructure of the FSW joint along the welding direction would be homogeneous. Hence, all the FSW weld micrographs reported in the thesis were obtained from the specimen dedicated for microstructural characterisations. This specimen was not the same specimen that had HR-DIC strain measurements. Therefore, the correlation of microscopy and HR-DIC findings reported in this investigation is not the exact

representation of the structure-property relationships of the FSW weld sub-regions, which is identified as the main limitation of this PhD investigation. As the FSW process usually produces high thermal gradients and plastic deformation, there is a possibility where a typical FSW joint will achieve highly heterogeneous microstructures along its through-thickness welding direction. Therefore, there is a definite scope in the future to investigate the structure-property relationship of an FSW joint with a higher degree of confidence by performing the microscopy and HR-DIC characterisations on the same FSW specimen with the same ROI. This will lead to achieve a clear understanding of the microstructural based local strain response of the FSW weld sub-regions without any prior assumption.

- The fractured specimens produced during a tensile test can be characterised further through SEM observations to study the surface fracture morphology and identify the failure processes and in which microstructural features they have occurred.
- In-situ SEM-DIC measurements have been considered as the more advanced characterisation technique to assess the local material response down to the resolution of grain size. To date, no in-situ SEM-DIC work has been reported in dissimilar FSW welds. Establishing a high-fidelity experimental procedure to perform an In-situ SEM-DIC investigation on FSW welds is also considered as a challenging area of investigation in the future.
- The novel HR-DIC experimental procedure reported in the PhD investigation was successfully used to perform more accurate strain measurements on the reduced thickness of FSW welds. However, there is a strong necessity to correlate the DIC results derived from the actual FSW Vs machined FSW specimens to understand the effect of weld geometry on the high-resolution strain measurements. There is also a scope to further expand the application and validation of the procedure to other welded joints that have complex weld geometry.
- This PhD investigation has determined the post-elastic material response of the FSW weld sub-regions along the weld cross-section. It would also be of interest to perform HR-DIC measurements simultaneously on the weld cross-section as well as the surface during plastic deformation to account for the out of plane displacement from the specimen edge. This will evaluate the local material response of the weld surface in addition to the cross-section. However, this experimental task on actual FSW welds would involve many high-resolution optics and therefore is not entirely feasible until the cost of optics will become more economical.
- Another challenging area readily available for investigation is to analyse the thermoelastic response of dissimilar FSW welds under cyclic loading using a full-field technique such as Thermoelastic Stress Analysis (TSA). To date, no such work has been attempted. By using TSA, local principal stress of the dissimilar FSW weld sub-regions can be determined, and it would be correlated with their respective microstructures to derive a new relationship between microstructure and thermoelastic response.

- Developing an experimental methodology to image the fatigue response of FSW welds using a full-field experimental approach is also considered as a novel research area for future investigation. In addition to this, investigating the fatigue crack initiation and growth mechanisms of dissimilar FSW welds in 3D through X-ray CT characterisation have been considered as the potential research areas for further investigation.
- X-ray CT data obtained from the FSW welds can be transformed into a numerical model through software packages such as Abaqus, and therefore a finite element analysis could be performed on the complex FSW weld geometry at uniaxial tensile loading condition. The results offered by the numerical analysis will provide a clear insights into the stress concentration effects caused by the corresponding FSW weld geometry (i.e. reduced thickness across the weld nugget).
- Although this investigation attempted an SEM-EBSD characterisation on similar and dissimilar FSW welds, a clear distinction between the FSW weld sub-regions based on their grain size was not clearly observed along the weld cross-section. Therefore, there is a definite need to move towards a high-resolution EBSD characterisation technique in the future to capture the principal differences in the microstructure of FSW weld sub-regions. Furthermore, high-resolution EBSD will also offer more reliable average grain size information of the FSW weld sub-regions.
- From this PhD investigation, it is clearly seen that both the SEM and SEM-EBSD characterisations do not have sufficient spatial resolution to characterise the microstructure of the dissimilar FSW (Cu-SS) weld nugget. This is because the FSW (Cu-SS) weld nugget had ultrafine recrystallized grains and also the mixture of Cu and SS elements. Therefore, it is worthwhile to perform the TEM (Transmission Electron Microscopy) characterisation on dissimilar FSW welds in the future to understand the detailed phase formations of the FSW weld sub-regions.

Appendix A (Chapter-4)

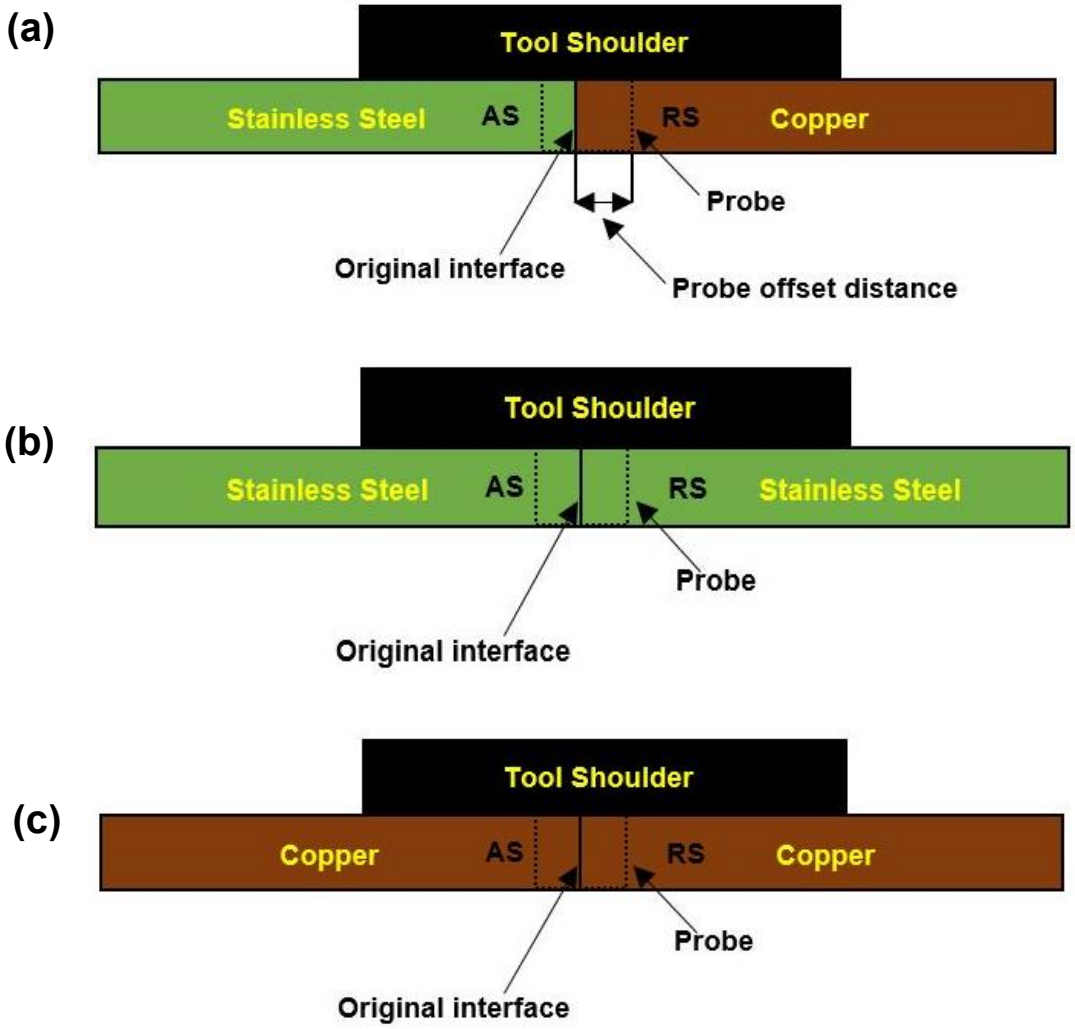

Figure A.1 A schematic representation of the tool offset position (a) FSW (Cu-SS) process (b) FSW (SS-SS) process c) FSW (Cu-Cu) process

Appendix B (Chapter-5)

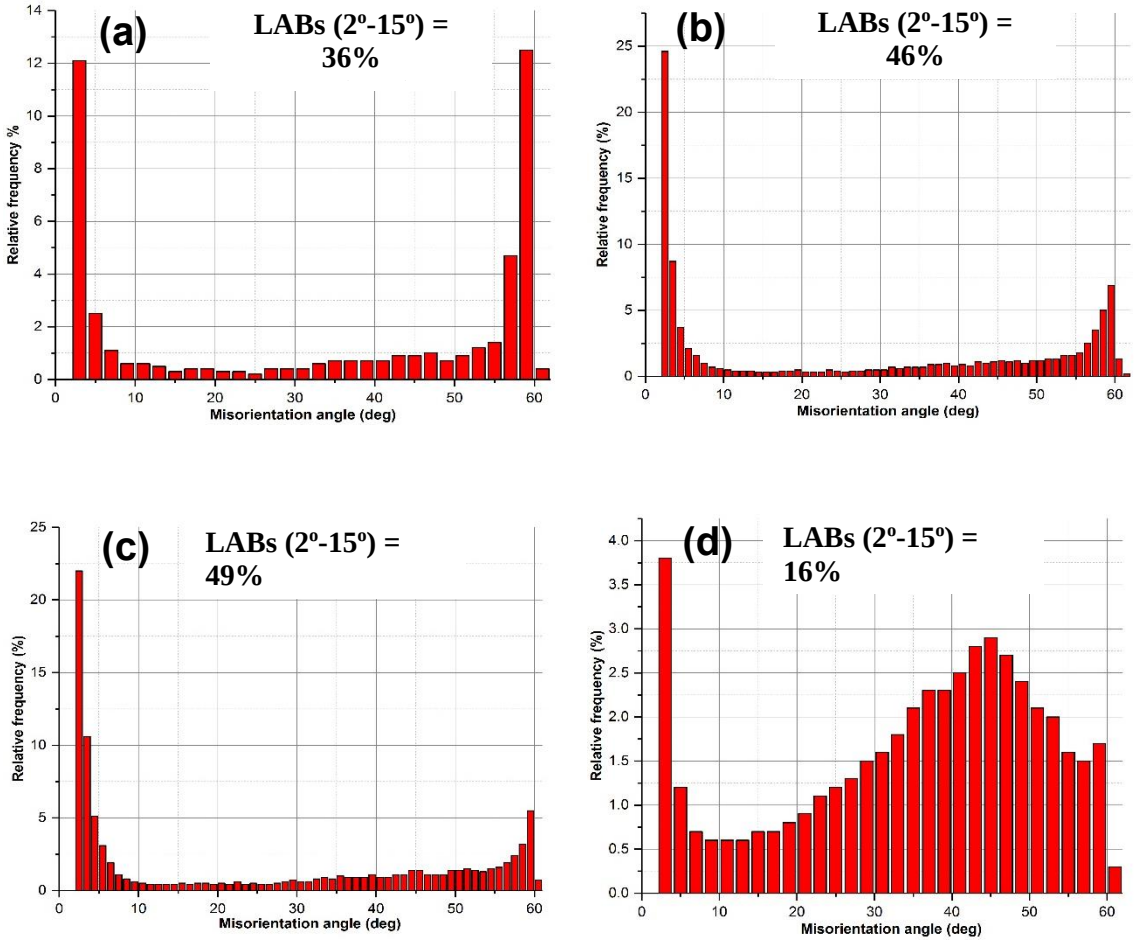

Figure B.1 Misorientation angle distributions of the FSW (Cu-SS) received from the EBSD: (a) Cu Base metal; (b) SS Base metal; (c) SS-TMAZ; (d) Weld nugget

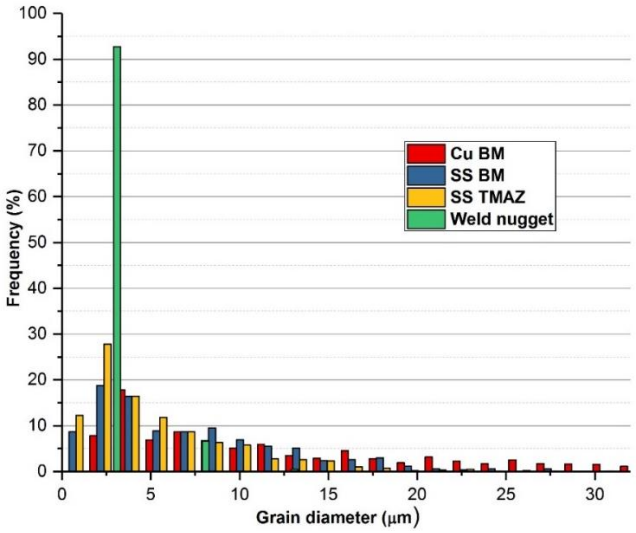

Figure B.2 Grain size statistics of the local weld zones of the FSW (Cu-SS) joint received from the EBSD

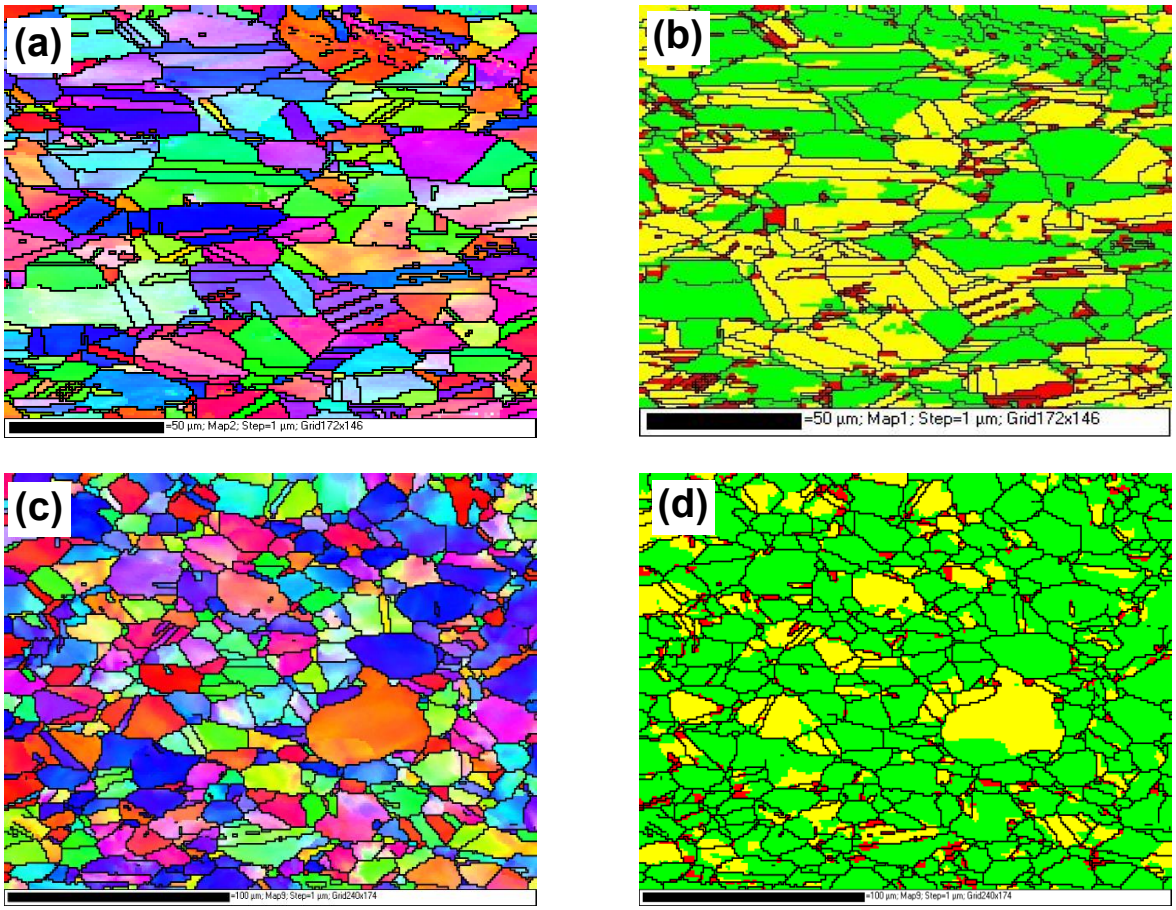

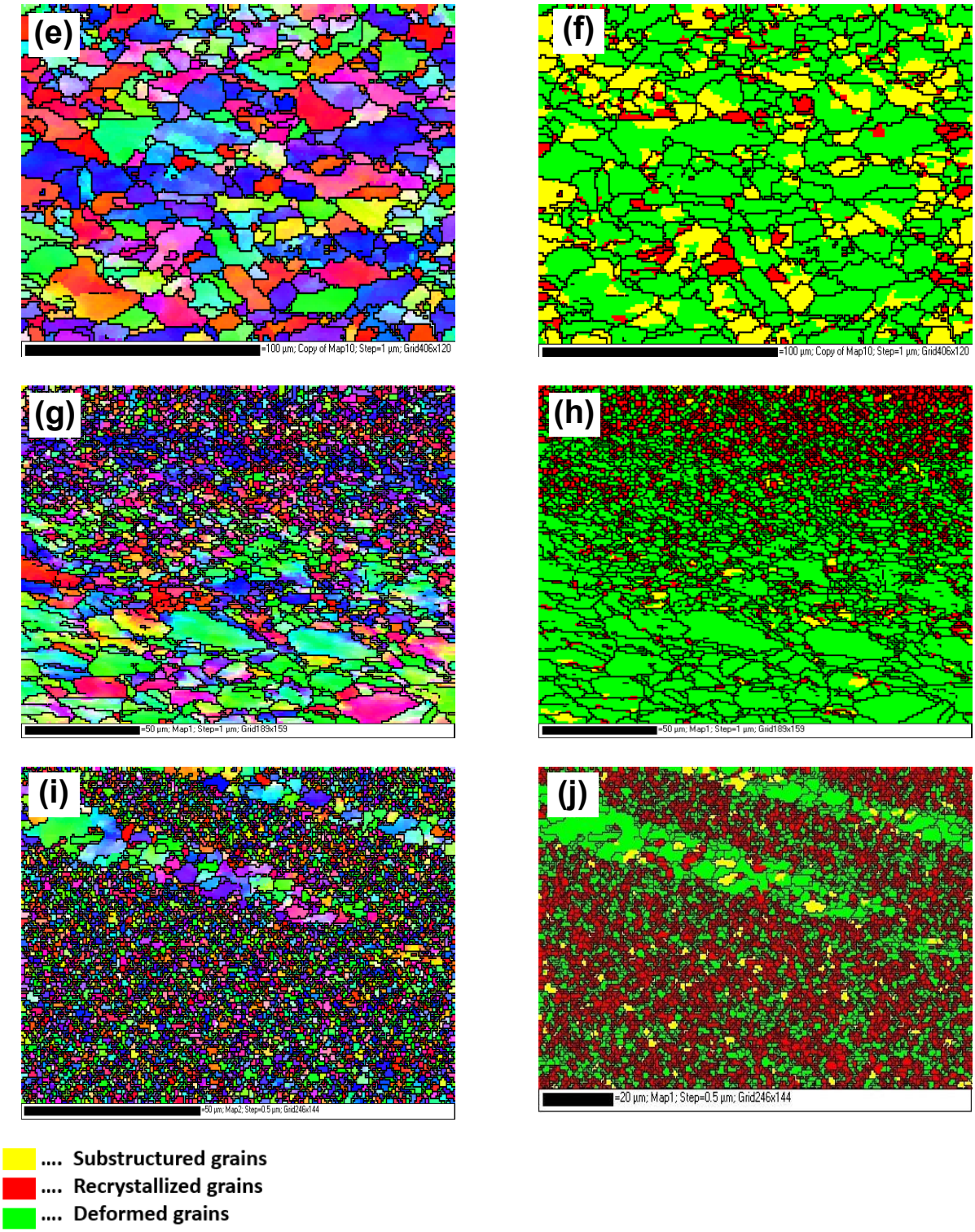

Figure B.3 IPF and its respective Grain morphology map of the various zones of the FSW (Cu-SS) (a) (b) Cu base metal; (c) (d) SS base metal; (e) (f) TMAZ; (g) (h) TMAZ/Weld interface; (i) (j) Weld nugget

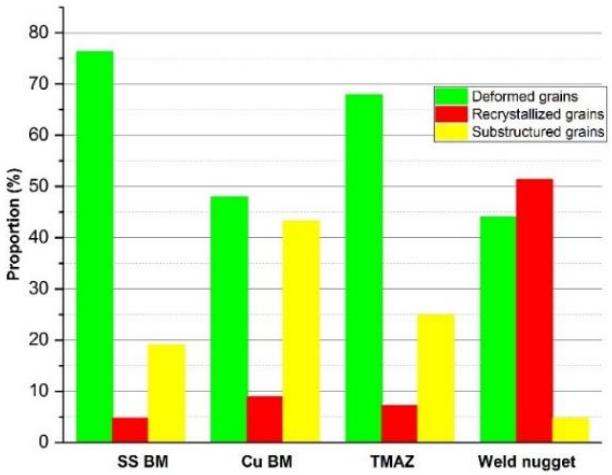

Figure B.4 Proportion of deformed, substructured and recrystallized grains at different zones of the FSW (Cu-SS) weld

Table B.1 Average grain size, the proportion of different types of grains and grain boundaries across various zones of the FSW (Cu-SS) weld

Region	**Average grain size (μm)**	**Proportion of deformed grains (%)**	**Proportion of recrystallized grains (%)**	**Proportion of substructured grains (%)**	**Proportion of HAGBs (%)**	**Proportion of LAGBs (%)**
SS-BM	7.28 ± 6.63	76.266	4.652	19.080	54	46
Cu-BM	14.81 ± 3.61	47.881	8.852	43.266	64	36
TMAZ	5.48 ± 5.57	67.910	7.190	24.899	51	49
Weld nugget	2.91 ± 37.46	44.022	51.284	4.693	84	16

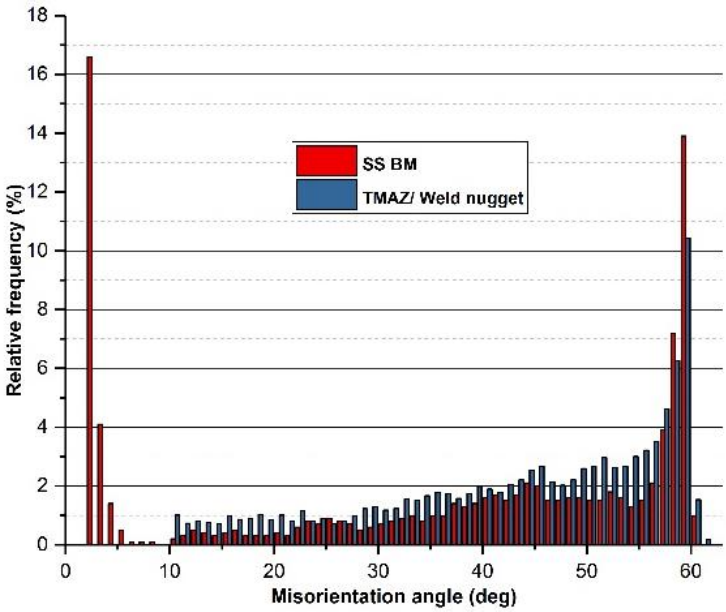

Figure B.5 Grain misorientation angle distribution received from the EBSD characterisation on the FSW (SS-SS)

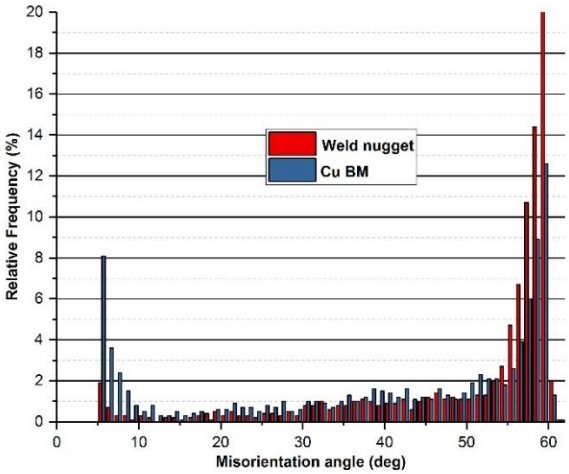

Figure B.6 Grain misorientation angle distribution received from the EBSD characterisation on the FSW (Cu-Cu)

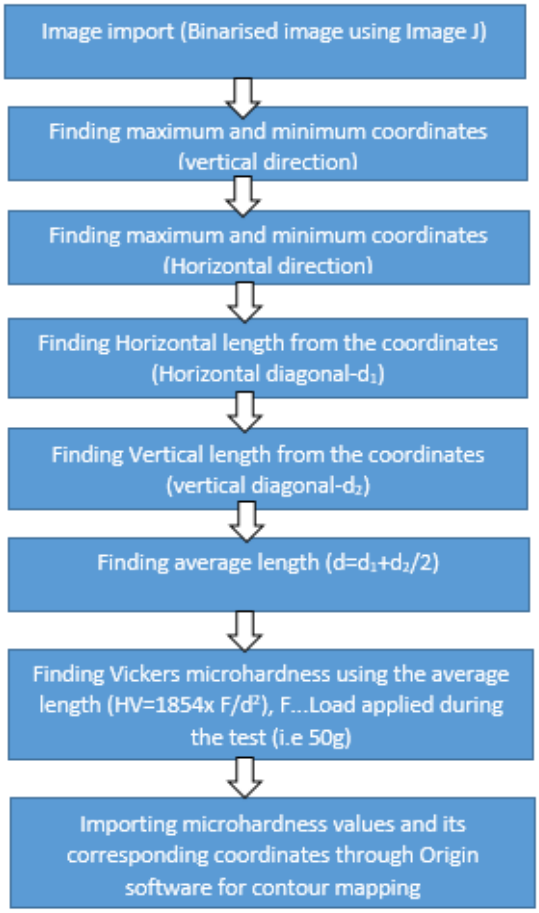

Figure B.7 Processing steps involved in the ImageJ/ Matlab assisted microhardness measurements

Matlab program used for microhardness measurements

```
clear all
%Resolution
resolution=2.9367; %Pixels / um
resolution=1/resolution; %um / pixel
%User promt to open image and select region
[FileName, Path] = uigetfile ('*.tif;','Select the secret
image');
secretImg = FileName;
 I=imread(FileName);
%I=imcrop(I);
 imshow(I); hold on;
% Generate boundaries for this
B=bwboundaries(I);
 [m,n]=size(B);
data=zeros(m,1);
for i=1:m %Start for loop
 %Find vertical max and min
[M,Min]=min(B[68](:,1));
x1=B[102](Min,1);
```

```
y1=B{i,1}(Min,2);
[M,Max]=max(B{i,1}(:,1));
x2=B{i,1}(Max,1);
y2=B{i,1}(Max,2);
  % plot(x1, y1, 'r*');
% plot(x2, y2, 'r*');
 %Find length
vert_length=sqrt(((x1-x2)^2)+((y1-y2)^2));
 %horizontal length
[M,Min]=min(B{i,1}(:,2));
x1=B{i,1}(Min,1);
y1=B{i,1}(Min,2);
[M,Max]=max(B{i,1}(:,2));
x2=B{i,1}(Max,1);
y2=B{i,1}(Max,2);
 % plot(x1, y1, 'r*');
% plot(x2, y2, 'r*');
 %Find length
hor_length=sqrt(((x1-x2)^2)+((y1-y2)^2));
 %Find average length
avg_length=((vert_length+hor_length)/2)*resolution;
 % plot(B{1,1(:,1),B{1,1}(:,2))
 %Write your data
data(i,1)=avg_length;
 end %end for loop
```

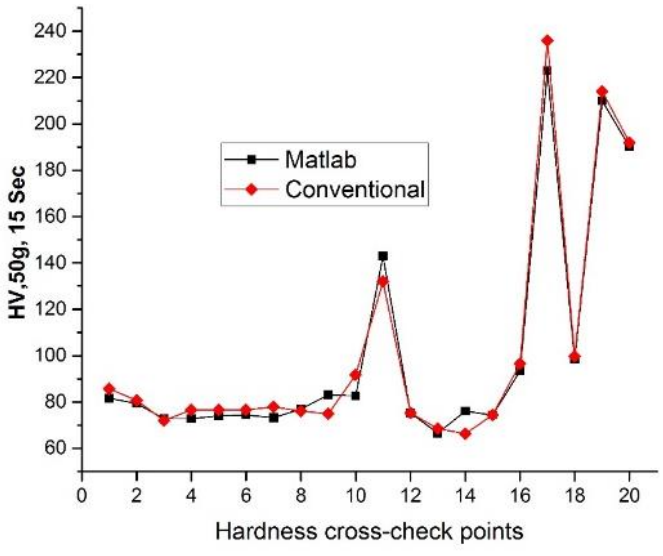

Figure B.8 Microhardness measurements (Matlab Vs Conventional measurements)

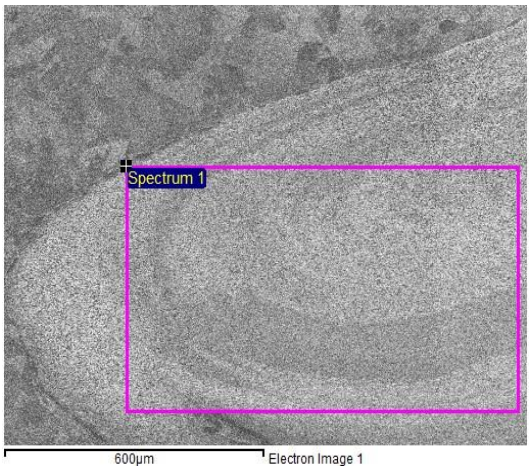

Element	Weight%	Atomic%
C K	0.01	0.80
Cr K	1.51	19.34
Mn K	0.06	0.70
Fe K	6.00	71.41
Ni K	0.57	6.42
Cu L	0.11	1.10
Zn L	0.02	0.23
Totals	8.29	100

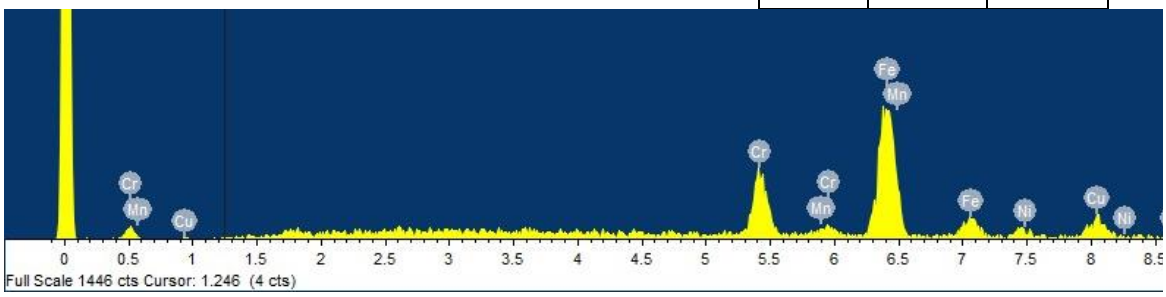

Figure B.9 SEM-EDS (area mapping) analysis on the weld nugget of FSW (Cu-SS) joint

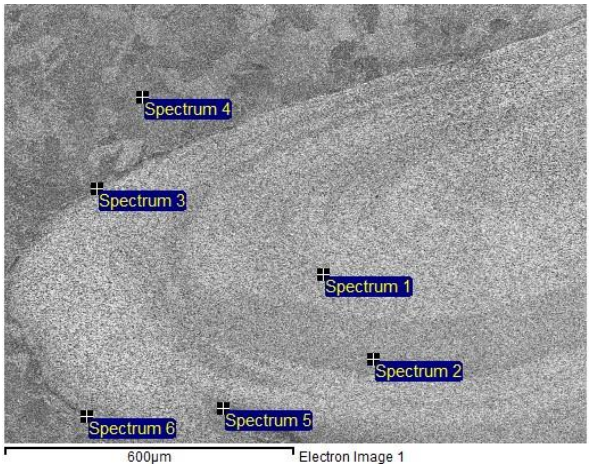

Spectrum	Cr (atm%)	Fe (atm%)	Cu (atm%)	Zn (atm%)	Total (atm%)
Spectrum 1	20.49	78.17	1.11	0.23	100
Spectrum 2	21.90	77.91	0.14	0.05	100
Spectrum 3	20.60	78.53	0.85	0.02	100
Spectrum 4	-	-	100	-	100
Spectrum 5	22.46	77.91	-0.24	-0.14	100
Spectrum 6	21.37	78.87	-0.02	-0.22	100

Figure B.10 SEM-EDS point spectrum analysis on the weld nugget of FSW (Cu-SS) joint

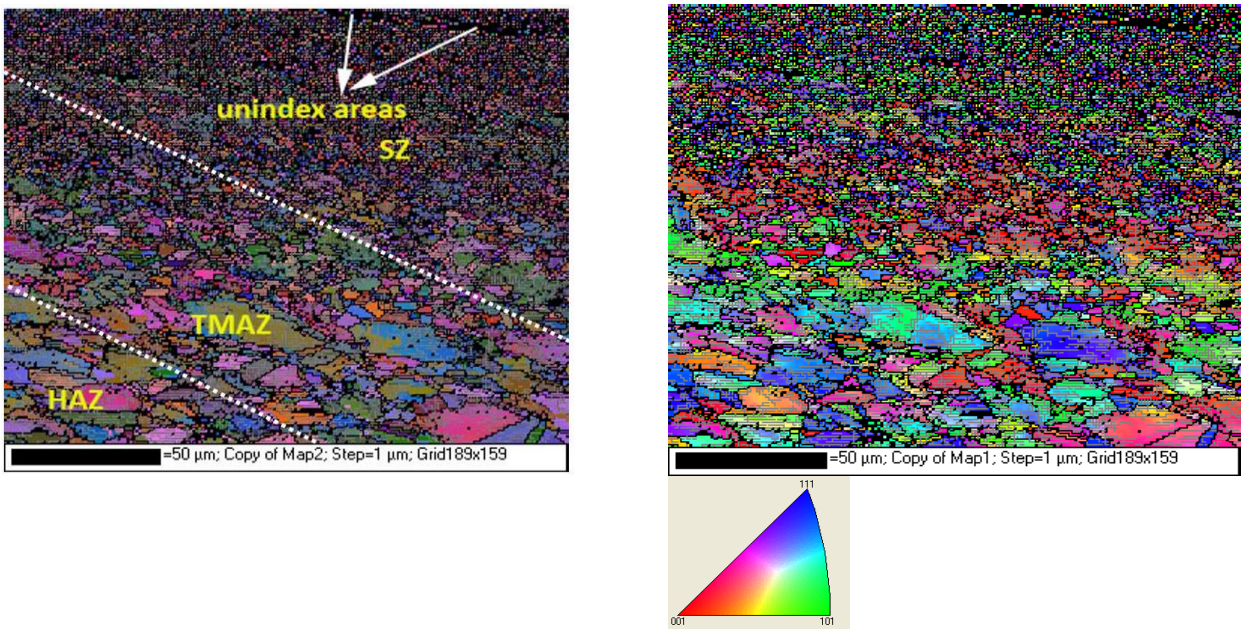

Figure B.11 EBSD Analysis at the TMAZ and Weld nugget of FSW (Cu-SS) joint

Appendix C (Chapter-6)

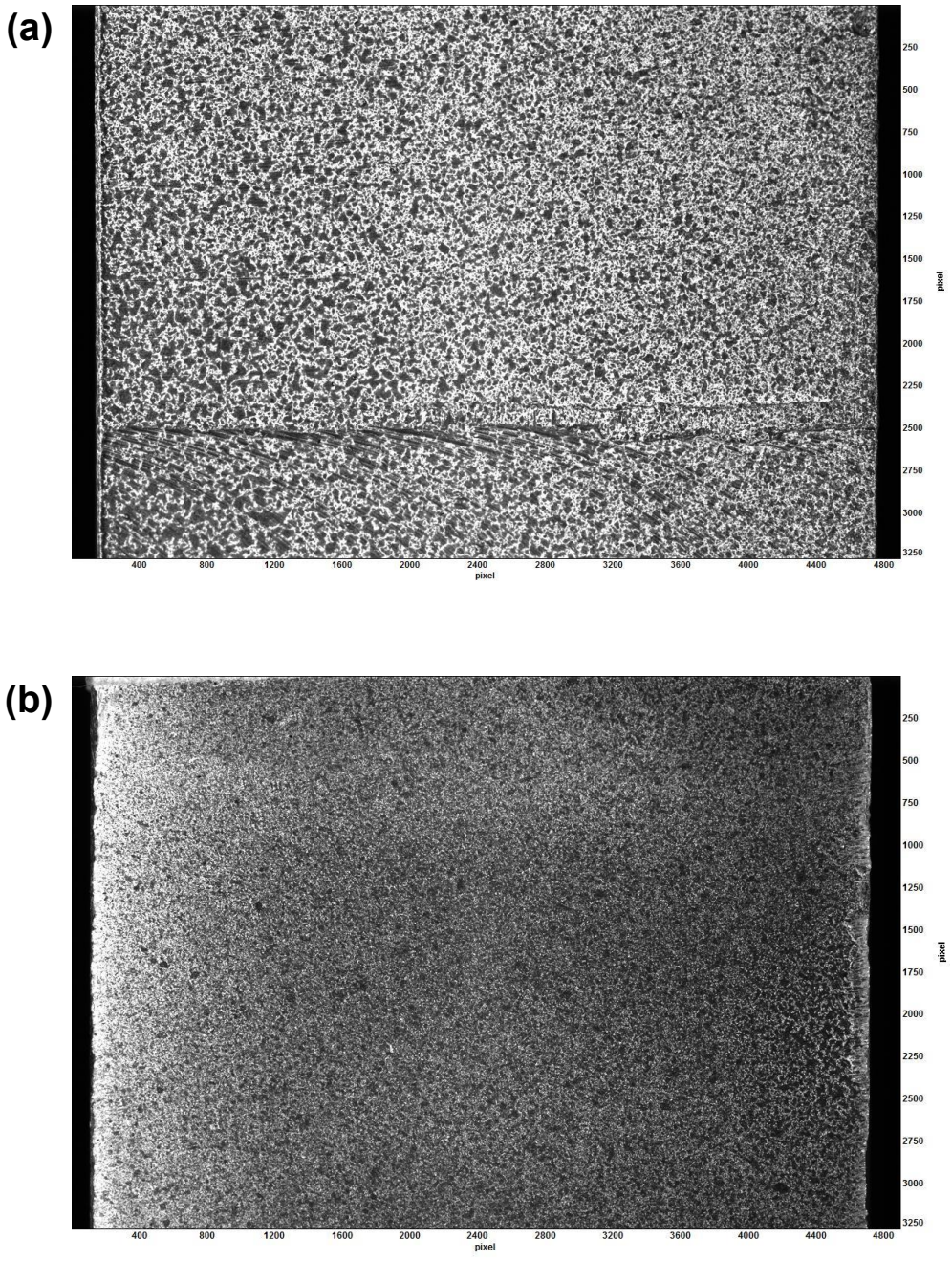

Figure C.1 Speckle patterns for HR-DIC measurements: (a) Produced using an aerosol spray paint; (b) Produced using an airbrush

Matlab code used for stitching HR-DIC strain data

```
clear all
 % Read in data from 1.dat
 A=importdata('1.dat');
 d= 246;
w= 206;
 data_A=zeros(w,d);
 for i=1:w
    for j=1:d
       data_A(i,j)=A.data((i-1)*d+j,3);

    end
end
 B=importdata('2.dat');
data_B=zeros(w,d);
for i=1:w
    for j=1:d
       data_B(i,j)=B.data((i-1)*d+j,3);

    end
end
 C=importdata('3.dat');
data_C=zeros(w,d);
for i=1:w
    for j=1:d
       data_C(i,j)=C.data((i-1)*d+j,3);

    end
end
D=importdata('4.dat');
data_D=zeros(w,d);
for i=1:w
    for j=1:d
       data_D(i,j)=D.data((i-1)*d+j,3);

    end
end
 E=importdata('5.dat');
data_E=zeros(w,d);
for i=1:w
    for j=1:d
       data_E(i,j)=E.data((i-1)*d+j,3);

    end
end
 F=importdata('6.dat');
data_F=zeros(w,d);
for i=1:w
    for j=1:d
```

```
        data_F(i,j)=F.data((i-1)*d+j,3);

    end
end
 %%
 % imagesc(data_A);
%export data as a raw file
fileID = fopen('1_206x246.raw','w');
fwrite(fileID,data_A,'float32');
fclose(fileID);
 fileID = fopen('2_206x246.raw','w');
fwrite(fileID,data_B,'float32');
fclose(fileID);
 fileID = fopen('3_206x246.raw','w');
fwrite(fileID,data_C,'float32');
fclose(fileID);
 fileID = fopen('4_206x246.raw','w');
fwrite(fileID,data_D,'float32');
fclose(fileID);
 fileID = fopen('5_206x246.raw','w');
fwrite(fileID,data_E,'float32');
fclose(fileID);
 fileID = fopen('6_206x246.raw','w');
fwrite(fileID,data_F,'float32');
fclose(fileID);
%C=imfuse(data_A, data_B);
fid = fopen('final_stitched_255x846.raw', 'r');
if fid == -1
  error('Cannot open file: %s', FileName);
end
data = fread(fid, 255*846, 'float32','b');
fclose(fid);
data = reshape(data, [255, 846]);
data=flipdim(data,2);
data=rot90(data);
% % contour plot
clims=[-0.004 0.019];
imagesc(data,clims);
set(gca,'dataAspectRatio',[1 1 1])
% % strain along y axis and write the values in a table
% plot(data(:,112))
% T=table(data(:,112))
% xlswrite('T.xls',data(:,112))
% M=mean(data,2);
% T=table(M)
% % print contour plot in higher resolution
% print('contour','-dtiff','-r500')
% % to remove axis
axis off;
```

Appendix D (Chapter-7)

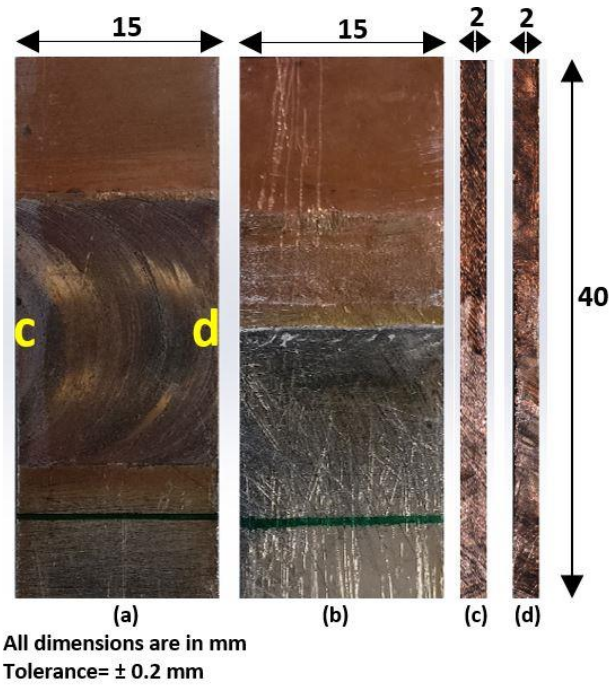

Figure D.1 Dimensions of FSW (Cu-SS) strip: (a) Weld face (WF), (b) Weld root (WR), (c) Cross-section-c as located in (a), (d) Cross-section-d as located in (a)

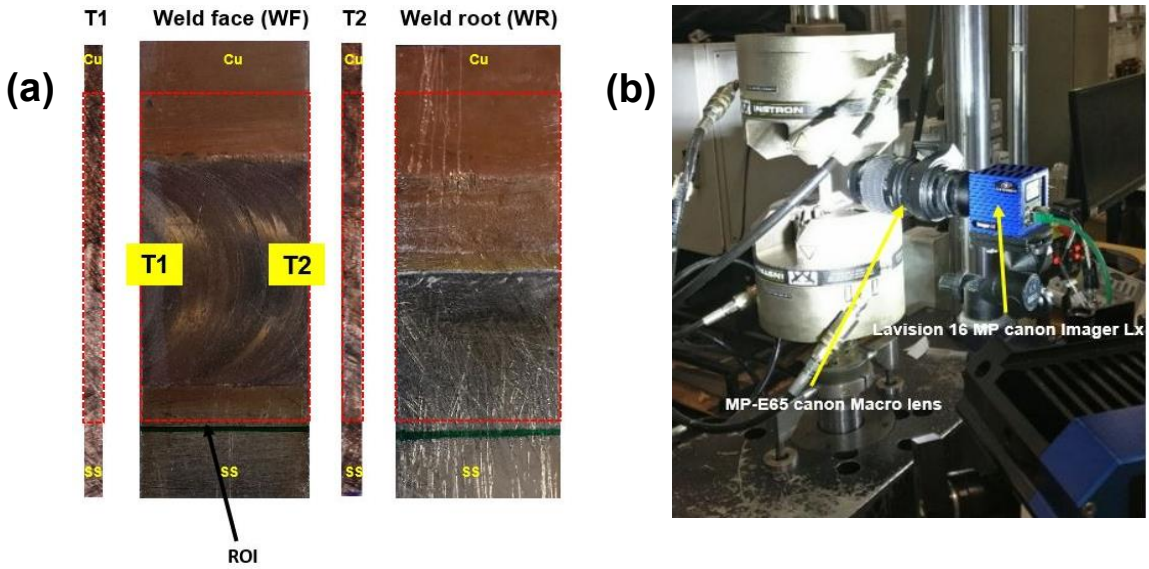

Figure D.2 (a) ROI for the HR 2D-DIC strain measurements; (b) The HR 2D-DIC experimental setup

Table D.1 Average Ɛyy strain values at zero load (Noise)

Subset size= 121 x 121 pixels, Step size= 60		
Region	Mean	Standard deviation
Weld face	1.5233E-6	1.60465E-5
Weld root	1.73432E-5	1.75375E-5
Thickness (T1)	1.89726E-5	2.20315E-5
Thickness (T2)	5.19361E-6	7.9215E-6

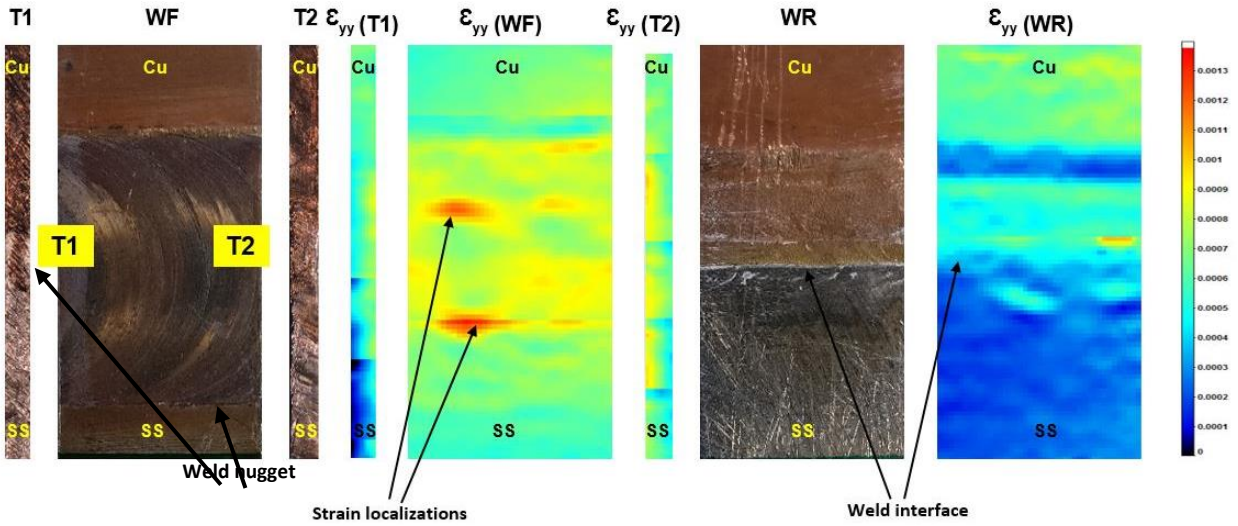

Figure D.3 HR-DIC trial experiments: HR 2D-DIC strain maps captured at 1.6 kN along the Weld Face (WF), Weld Root (WR) and through-thickness cross-sections (T1, T2)

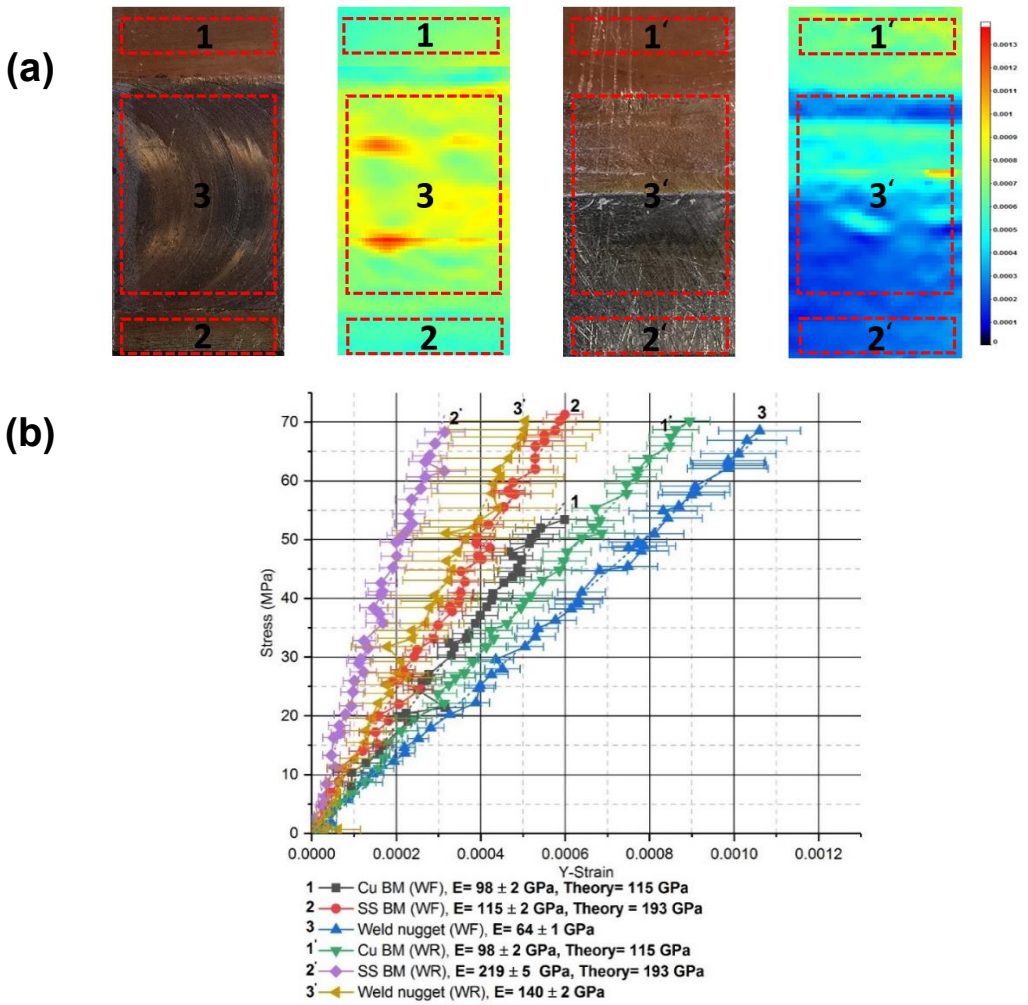

Figure D.4 (a) HR-DIC strain maps of the WF and WR of the FSW (Cu-SS) joint at 1.6 kN; (b) Local Stress-strain curves

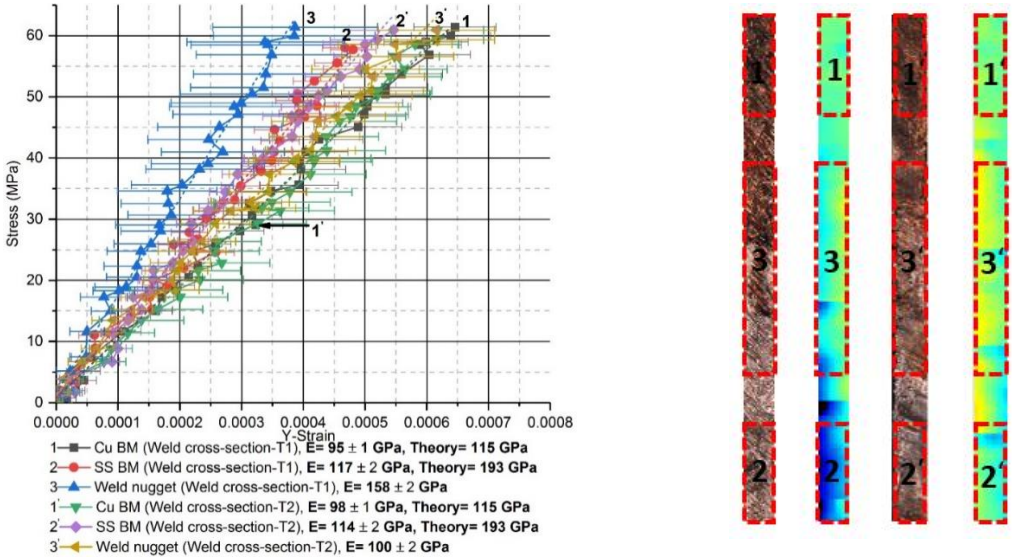

Figure D.5 (a) HR-DIC strain maps of the T1 and T2 of the FSW (Cu-SS) joint at 1.6 kN (c) Local Stress-strain curves

Appendix E (List of Publications)

E.1 Journal Publication

1. **Ramachandran, S**.; Lakshminarayanan, A.K.; Reed, P.A.S.; Dulieu-Barton, J.M. (2019) "Development of High-Fidelity Imaging Procedures to Establish the Local Material Behavior in Friction Stir Welded Stainless Steel Joints". Metals, 9, 592, https://doi.org/10.3390/met9050592.

E.2 Conference Papers

1. **Ramachandran, S**.; Lakshminarayanan, A.K.; Reed, P.A.S.; Dulieu-Barton, J.M, "Application of high-resolution DIC to assess the weld region of Friction Stir Welded (FSW) joints", *SEM Annual Conference on Experimental and Applied Mechanics*, Reno, Nevada, USA, June 2019, 1-3.

2. **Ramachandran, S**.; Reed, P.A.S.; Dulieu-Barton, J.M, "Application of high-resolution DIC to assess the weld region of Friction Stir Welded (FSW) joints", *BSSM 4th Postgraduate Experimental Mechanics Conference Glasgow*, UK, December 2018, 1-1.

3. **Ramachandran, S**.; Reed, P.A.S.; Dulieu-Barton, J.M, "An approach towards a high fidelity imaging the local material behaviour of Friction Stir Welded (FSW) 304 stainless steel joints", *BSSM 13th International Conference on Advances in Experimental Mechanics*, Southampton, UK, August 2018, 1-2.

4. **Ramachandran, S**.; Lakshminarayanan, A.K.; Reed, P.A.S.; Dulieu-Barton, J.M, *"*A combined high-resolution full-field imaging and metallography approach to assess the local properties of FSW (Cu-SS) joints", *SEM Annual Conference on Experimental and Applied Mechanics*, Greenville, South Carolina, USA, June 2018, 1-3.

5. **Ramachandran, S**.; Reed, P.A.S.; Dulieu-Barton, J.M, *"*A combined high-resolution full-field imaging and metallography approach to assess the local properties of FSW (Cu-SS) joints" *BSSM 3rd Postgraduate Experimental Mechanics Conference*, London, UK, November 2017, 1-1.

6. **Ramachandran, S**.; Lakshminarayanan, A.K.; Reed, P.A.S.; Dulieu-Barton, J.M, *"*A combined high-resolution full-field imaging and metallography approach to assess the local properties of FSW (Cu-SS) joints", *BSSM 12th International Conference on Advances in Experimental Mechanics*, Sheffield, UK, August 2017, 1-1.

E.3 Journal paper in preparation

1. **Ramachandran, S**.; Lakshminarayanan, A.K.; Reed, P.A.S.; Dulieu-Barton, J.M. (2020) "Application of imaging techniques to determine the post-yield behaviour of the heterogeneous microstructure of friction stir welds". Journal: Materials Science and Engineering-A.

E.4 Planned Publications

1. **Ramachandran, S**.; Lakshminarayanan, A.K.; Reed, P.A.S.; Dulieu-Barton, J.M. (2020) "Application of imaging techniques to determine the post-yield behaviour of the heterogeneous microstructure of friction stir welded copper joints". Journal: Materials Science and Engineering-A.
2. **Ramachandran, S**.; Lakshminarayanan, A.K.; Reed, P.A.S.; Dulieu-Barton, J.M.; Wajira Mirihanage.; Haigh SJ. (2020) "High fidelity full-field imaging the post-yield behaviour of the heterogeneous microstructure of dissimilar friction stir welded copper to stainless steel joints". Journal: Acta Materialia.

List of References (Numbered)

1. Velu, M. and S. Bhat, Metallurgical and mechanical examinations of steel–copper joints arc welded using bronze and nickel-base superalloy filler materials. Materials & Design, 2013. 47: p. 793-809.

2. DebRoy, T. and H.K.D.H. Bhadeshia, Friction stir welding of dissimilar alloys – a perspective. Science and Technology of Welding and Joining, 2013. 15(4): p. 266-270.

3. Nandan, R., T. Debroy, and H. Bhadeshia, Recent advances in friction-stir welding – Process, weldment structure and properties. Progress in Materials Science, 2008. 53(6): p. 980-1023.

4. Martinsen, K., S.J. Hu, and B.E. Carlson, Joining of dissimilar materials. CIRP Annals - Manufacturing Technology, 2015. 64(2): p. 679-699.

5. Nilesh Kumar, W.Y., Rajiv S. Mishra, Friction Stir Welding of Dissimilar Alloys and Materials. 2015: Butterworth-Heinemann. 1-134.

6. Phanikumar, G., et al., Characterization of a continuous CO2 laser-welded Fe-Cu dissimilar couple. Metallurgical and Materials Transactions A, 2005. 36(8): p. 2137-2147.

7. Chen, S., et al., Influence of processing parameters on the characteristics of stainless steel/copper laser welding. Journal of Materials Processing Technology, 2015. 222: p. 43-51.

8. Srinivas, K., et al., Zone Wise Properties of Friction Stir Welded Copper – Stainless Steel Joints Using Digital Image Correlation. Applied Mechanics and Materials, 2015. 787: p. 485-489.

9. Lakshminarayanan, A.K., et al., Characteristics of friction welded AZ31B magnesium–commercial pure titanium dissimilar joints. Journal of Magnesium and Alloys, 2015. 3(4): p. 315-321.

10. Guo, S., et al., Effect of beam offset on the characteristics of copper/304stainless steel electron beam welding. Vacuum, 2016. 128(Supplement C): p. 205-212.

11. Roy, C., et al., Characterization of Metallurgical and Mechanical Properties of Commercially Pure Copper and AISI 304 Dissimilar Weldments. Procedia Materials Science, 2014. 5(Supplement C): p. 2503-2512.

12. Tomashchuk, I., et al., Evolution of microstructures and mechanical properties during dissimilar electron beam welding of titanium alloy to stainless steel via copper interlayer. Materials Science and Engineering: A, 2013. 585: p. 114-122.

13. Yang, T., et al., Interface behavior of copper and steel by plasma-MIG hybrid arc welding. Acta Metallurgica Sinica (English Letters), 2013. 26(3): p. 328-332.

14. Jothi, S., et al., Localized microstructural characterization of a dissimilar metal electron beam weld joint from an aerospace component. Materials & Design, 2016. 90: p. 101-114.

15. Yao, C., et al., Interface microstructure and mechanical properties of laser welding copper–steel dissimilar joint. Optics and Lasers in Engineering, 2009. 47(7-8): p. 807-814.

16. Meng, Y., et al., Microstructures and mechanical properties of laser-arc hybrid welded dissimilar pure copper to stainless steel. Optics & Laser Technology, 2019. 111: p. 140-145.

17. Jafari, M., et al., Microstructures and mechanical properties of friction stir welded dissimilar steel-copper joints. Journal of Mechanical Science and Technology, 2017. 31(3): p. 1135-1142.

18. Xu, W.-f. and Z.-l. Zhang, Microstructure and mechanical properties of laser beam welded TC4/TA15 dissimilar joints. Transactions of Nonferrous Metals Society of China, 2016. 26(12): p. 3135-3146.

19. Velu, M. and S. Bhat, Experimental investigations of fracture and fatigue crack growth of copper–steel joints arc welded using nickel-base filler. Materials & Design, 2015. 67: p. 244-260.

20. Ramirez, A.J., Benati,D.M., Effect of Tool Offset on Dissimilar Cu-AISI 316 Stainless Steel Friction Stir Welding. Proceedings of the Twenty-first (2011) International Offshore and Polar Engineering Conference, 2011: p. 548-552.

21. Lusch, C., et al., Qualification of electron-beam welded joints between copper and stainless steel for cryogenic application. IOP Conference Series: Materials Science and Engineering, 2015. 102(1): p. 012017.

22. Mai, T.A. and A.C. Spowage, Characterisation of dissimilar joints in laser welding of steel–kovar, copper–steel and copper–aluminium. Materials Science and Engineering: A, 2004. 374(1-2): p. 224-233.

23. Mishra, R.S. and Z.Y. Ma, Friction stir welding and processing. Materials Science and Engineering: R: Reports, 2005. 50(1-2): p. 1-78.

24. Murr, L.E., A Review of FSW Research on Dissimilar Metal and Alloy Systems. Journal of Materials Engineering and Performance, 2010. 19(8): p. 1071-1089.

25. Lockwood, W.D. and A.P. Reynolds, Simulation of the global response of a friction stir weld using local constitutive behavior. Materials Science and Engineering: A, 2003. 339(1): p. 35-42.

26. Ambriz, R.R., et al., Local mechanical properties of the 6061-T6 aluminium weld using micro-traction and instrumented indentation. European Journal of Mechanics - A/Solids, 2011. 30(3): p. 307-315.

27. Saranath, K.M. and M. Ramji, Local zone wise elastic and plastic properties of electron beam welded Ti–6Al–4V alloy using digital image correlation technique: A comparative study between uniform stress and virtual fields method. Optics and Lasers in Engineering, 2015. 68: p. 222-234.

28. Saranarayanan, R., A.K. Lakshminarayanan, and B. Venkatraman, A combined full-field imaging and metallography approach to assess the local properties of gas tungsten arc welded copper–stainless steel joints. Archives of Civil and Mechanical Engineering, 2019. 19(1): p. 251-267.

29. Leitão, C., et al., Determination of local constitutive properties of aluminium friction stir welds using digital image correlation. Materials & Design, 2012. 33: p. 69-74.

30. Reynolds, A.P.D., F.,, Digital image correlation for determination of weld and base metal constitutive behaviour. Welding Research Supplement, 1999. 78(10): p. 355-360.

31. Crammond, G., S.W. Boyd, and J.M. Dulieu-Barton, Evaluating the localised through-thickness load transfer and damage initiation in a composite joint using digital image correlation. Composites Part A: Applied Science and Manufacturing, 2014. 61: p. 224-234.

32. Wang, T., et al., Towards Obtaining Sound Butt Joint Between Metallurgically Immiscible Pure Cu and Stainless Steel Through Friction Stir Welding. Metallurgical and Materials Transactions A, 2018. 49(7): p. 2578-2582.

33. Texier, D., et al., Near-surface mechanical heterogeneities in a dissimilar aluminum alloys friction stir welded joint. Materials & Design, 2016. 108: p. 217-229.

34. Ramachandran, S., et al., Development of High-Fidelity Imaging Procedures to Establish the Local Material Behavior in Friction Stir Welded Stainless Steel Joints. Metals, 2019. 9(5): p. 592.

35. Thomas W M, N.E.D., Needham J C, Temple-Smith P, Kallee S W and Dawes C J, Friction Stir Welding, in UK patent publication, U. patent, Editor. 1995: UK.

36. Zhang, H., et al., Achieving ultra-high strength friction stir welded joints of high nitrogen stainless steel by forced water cooling. Journal of Materials Science & Technology, 2018. 34(11): p. 2183-2188.

37. Li, H., et al., Microstructure evolution and mechanical properties of friction stir welding super-austenitic stainless steel S32654. Materials & Design, 2017. 118: p. 207-217.

38. Bhadeshia, H.K.D.H. and T. DebRoy, Critical assessment: friction stir welding of steels. Science and Technology of Welding and Joining, 2013. 14(3): p. 193-196.

39. Park, S.H.C., et al., Microstructural characterisation of stir zone containing residual ferrite in friction stir welded 304 austenitic stainless steel. Science and Technology of Welding and Joining, 2005. 10(5): p. 550-556.

40. Guo, R., et al., Microstructures and mechanical properties of thin 304 stainless steel sheets by friction stir welding. Journal of Adhesion Science and Technology, 2018. 32(12): p. 1313-1323.

41. Mironov, S., et al., Microstructure and tensile behavior of friction-stir welded TRIP steel. Materials Science and Engineering: A, 2018. 717: p. 26-33.

42. Lakshminarayanan, A.K., Enhancing the properties of friction stir welded stainless steel joints via multi-criteria optimization. Archives of Civil and Mechanical Engineering, 2016. 16(4): p. 605-617.

43. Miyazawa, T., et al., Friction stir welding of 304 stainless steel using Ir based alloy tool. Science and Technology of Welding and Joining, 2012. 17(3): p. 207-212.

44. Heidarzadeh, A., et al., Effect of stacking fault energy on the restoration mechanisms and mechanical properties of friction stir welded copper alloys. Materials & Design, 2019. 162: p. 185-197.

45. Shen, J.J., H.J. Liu, and F. Cui, Effect of welding speed on microstructure and mechanical properties of friction stir welded copper. Materials & Design, 2010. 31(8): p. 3937-3942.

46. Sun, Y.F. and H. Fujii, Investigation of the welding parameter dependent microstructure and mechanical properties of friction stir welded pure copper. Materials Science and Engineering: A, 2010. 527(26): p. 6879-6886.

47. Hwang, Y.M., P.L. Fan, and C.H. Lin, Experimental study on Friction Stir Welding of copper metals. Journal of Materials Processing Technology, 2010. 210(12): p. 1667-1672.

48. Xue, P., et al., Effect of Heat Input Conditions on Microstructure and Mechanical Properties of Friction-Stir-Welded Pure Copper. Metallurgical and Materials Transactions A, 2010. 41(8): p. 2010-2021.

49. Xu, N., Q. Song, and Y. Bao, Investigation on microstructure development and mechanical properties of large-load and low-speed friction stir welded Cu-30Zn brass joint. Materials Science and Engineering: A, 2018. 726: p. 169-178.

50. Xie, G.M., Z.Y. Ma, and L. Geng, Development of a fine-grained microstructure and the properties of a nugget zone in friction stir welded pure copper. Scripta Materialia, 2007. 57(2): p. 73-76.

51. Liu, H.J., et al., Effect of tool rotation rate on microstructure and mechanical properties of friction stir welded copper. Science and Technology of Welding and Joining, 2009. 14(6): p. 577-583.

52. Cavaliere, P., et al., Effect of welding parameters on mechanical and microstructural properties of AA6056 joints produced by Friction Stir Welding. Journal of Materials Processing Technology, 2006. 180(1): p. 263-270.

53. Shiri, S.G., et al., Gas tungsten arc welding of CP-copper to 304 stainless steel using different filler materials. Transactions of Nonferrous Metals Society of China, 2012. 22(12): p. 2937-2942.

54. Shokri, V., A. Sadeghi, and M.H. Sadeghi, Effect of Friction Stir Welding Parameters on Microstructure and Mechanical Properties of DSS–Cu Joints. Materials Science and Engineering: A, 2017.

55. Imani, Y., M.K. Besharati Givi, and M. Guillot, Improving Friction Stir Welding between Copper and 304L Stainless Steel. Advanced Materials Research, 2011. 409: p. 263-268.

56. Aval, H.J., Microstructural evolution and mechanical properties of friction stir-welded C71000 copper–nickel alloy and 304 austenitic stainless steel. International Journal of Minerals, Metallurgy, and Materials, 2018. 25(11): p. 1294-1303.

57. Chuang, Y.-Y., R. Schmid, and Y.A. Chang, Thermodynamic analysis of the iron-copper system I: The stable and metastable phase equilibria. Metallurgical Transactions A, 1984. 15(10): p. 1921-1930.

58. Sutton, M.A., et al., Recent Progress in Digital Image Correlation: Background and Developments since the 2013 W M Murray Lecture. Experimental Mechanics, 2016. 57(1): p. 1-30.

59. Pan, B. and Z. Wang, Recent progress in digital image correlation, in Application of Imaging Techniques to Mechanics of Materials and Structures, Volume 4: Proceedings of the 2010 Annual Conference on Experimental and Applied Mechanics, T. Proulx, Editor. 2013, Springer New York: New York, NY. p. 317-326.

60. Saranath, K.M., A. Sharma, and M. Ramji, Zone wise local characterization of welds using digital image correlation technique. Optics and Lasers in Engineering, 2014. 63: p. 30-42.

61. Boyce, B.L., P.L. Reu, and C.V. Robino, The constitutive behavior of laser welds in 304L stainless steel determined by digital image correlation. Metallurgical and Materials Transactions A, 2006. 37(8): p. 2481-2492.

62. Dannemann, K.A., et al., Application of Digital Image Correlation for Comparison of Deformation Response in Fusion and Friction Stir Welds. Journal of Dynamic Behavior of Materials, 2016. 2(3): p. 347-364.

63. Boroński, D., et al., Mechanical properties of explosively welded AA2519-AA1050-Ti6Al4V layered material at ambient and cryogenic conditions. Materials & Design, 2017. 133: p. 390-403.

64. Corigliano, P., et al., Fatigue analysis of marine welded joints by means of DIC and IR images during static and fatigue tests. Engineering Fracture Mechanics, 2017. 183(Supplement C): p. 26-38.

65. Reu, P., Introduction to Digital Image Correlation: Best Practices and Applications. Experimental Techniques, 2012. 36(1): p. 3-4.

66. Sutton, M.A., J.J. Orteu, and H. Schreier, Image Correlation for Shape, Motion and Deformation Measurements. 2009: Springer US.

67. Crammond, G., S.W. Boyd, and J.M. Dulieu-Barton, Speckle pattern quality assessment for digital image correlation. Optics and Lasers in Engineering, 2013. 51(12): p. 1368-1378.

68. LaVan, D.A., MICROTENSILE PROPERTIES OF WELD METAL. Experimental Techniques, 1999. 23(3): p. 31-34.

69. Sutton, M.A., et al., Banded microstructure in 2024-T351 and 2524-T351 aluminum friction stir welds: Part II. Mechanical characterization. Materials Science and Engineering: A, 2004. 364(1): p. 66-74.

70. Li, H., Q.L. Dai, and Q.Y. Shi, Experimental Study on the Heterogeneity of Mechanical Properties of Friction Stir Welded Joints with the Digital Image Correlation Method. Strength of Materials, 2015. 47(1): p. 80-86.

71. Leitao, C., et al., Mechanical behaviour of similar and dissimilar AA5182-H111 and AA6016-T4 thin friction stir welds. Materials & Design, 2009. 30(1): p. 101-108.

72. Leal, R.M., et al., Material flow in heterogeneous friction stir welding of thin aluminium sheets: Effect of shoulder geometry. Materials Science and Engineering: A, 2008. 498(1): p. 384-391.

73. Mehta, K.P. and V.J. Badheka, A Review on Dissimilar Friction Stir Welding of Copper to Aluminum: Process, Properties, and Variants. Materials and Manufacturing Processes, 2016. 31(3): p. 233-254.

74. Hamilton, C., et al., A Coupled Thermal/Material Flow Model of Friction Stir Welding Applied to Sc-Modified Aluminum Alloys. Metallurgical and Materials Transactions A, 2013. 44(4): p. 1730-1740.

75. Properties of C21000 Copper alloy. [cited 2017 01.11.2017]; Available from: http://www.matweb.com/search/datasheet.aspx?matguid=e97c544724cb429eaf877d35ceca469a&ckck=1.

76. ASTM E3 - 11(2017), Standard Guide for Preparation of Metallographic Specimens, ASTM International, West Conshohocken, PA, 2017, www.astm.org. 2017.

77. Bjerregaard, L., Struers Metalog Guide, ISBN 87-987767-0-3.

78. ASTM E407-07(2015)e1, Standard Practice for Microetching Metals and Alloys, ASTM International, West Conshohocken, PA, 2015, www.astm.org. 2015.

79. Maitland, T. and S. Sitzman, Backscattering Detector and EBSD in Nanomaterials Characterization, in Scanning Microscopy for Nanotechnology: Techniques and Applications, W. Zhou and Z.L. Wang, Editors. 2007, Springer New York: New York, NY. p. 41-75.

80. Abbasi, M., et al., Investigation of Fe-rich fragments in aluminum-steel friction stir welds via simultaneous Transmission Kikuchi Diffraction and EDS. Acta Materialia, 2016. 117: p. 262-269.

81. Buehler. MetaDi Supreme, Poly, 3µm Fine, 8oz. 2017 [cited 2017 07/11/2017]; Available from: https://shop.buehler.com/metadi-supreme-poly-susp-3-mic-fine-8oz.

82. Forsström, A., et al., Strain localization in copper canister FSW welds for spent nuclear fuel disposal. Journal of Nuclear Materials, 2019. 523: p. 347-359.

83. Prangnell, P.B. and C.P. Heason, Grain structure formation during friction stir welding observed by the 'stop action technique'. Acta Materialia, 2005. 53(11): p. 3179-3192.

84. Krishnan, K.N., On the formation of onion rings in friction stir welds. Materials Science and Engineering: A, 2002. 327(2): p. 246-251.

85. Goldstein, J.I., et al., Scanning Electron Microscopy and X-Ray Microanalysis. 2018: Springer-Verlag New York.

86. Britton, T.B., et al., Tutorial: Crystal orientations and EBSD — Or which way is up? Materials Characterization, 2016. 117: p. 113-126.

87. Chen, H., L. Fu, and P. Liang, Microstructure, texture and mechanical properties of friction stir welded butt joints of 2A97 AlLi alloy ultra-thin sheets. Journal of Alloys and Compounds, 2017. 692: p. 155-169.

88. Liu, X.C., Y.F. Sun, and H. Fujii, Clarification of microstructure evolution of aluminum during friction stir welding using liquid CO2 rapid cooling. Materials & Design, 2017. 129: p. 151-163.

89. Song, Z., et al., Influence of probe offset distance on interfacial microstructure and mechanical properties of friction stir butt welded joint of Ti6Al4V and A6061 dissimilar alloys. Materials & Design, 2014. 57: p. 269-278.

90. Wang, B., et al., EBSD study on microstructure and texture of friction stir welded AA5052-O and AA6061-T6 dissimilar joint. Materials & Design, 2015. 87: p. 593-599.

91. Nakata, K., Friction stir welding of copper and copper alloys. Welding International, 2005. 19(12): p. 929-933.

92. Tan, C.W., et al., Microstructural evolution and mechanical properties of dissimilar Al–Cu joints produced by friction stir welding. Materials & Design, 2013. 51: p. 466-473.

93. Watanabe, T., H. Takayama, and A. Yanagisawa, Joining of aluminum alloy to steel by friction stir welding. Journal of Materials Processing Technology, 2006. 178(1-3): p. 342-349.

94. Uzun, H., et al., Friction stir welding of dissimilar Al 6013-T4 To X5CrNi18-10 stainless steel. Materials & Design, 2005. 26(1): p. 41-46.

95. Galvão, I., et al., Formation and distribution of brittle structures in friction stir welding of aluminium and copper: Influence of shoulder geometry. Intermetallics, 2012. 22: p. 122-128.

96. Mironov, S., et al., Tensile behavior of friction-stir welded AZ31 magnesium alloy. Materials Science and Engineering: A, 2017. 679: p. 272-281.

97. Wang, Y.-F., et al., Ultrafine-Grained Microstructure and Improved Mechanical Behaviors of Friction Stir Welded Cu and Cu–30Zn Joints. Acta Metallurgica Sinica (English Letters), 2018. 31(8): p. 878-886.

98. Sutton, M.A., et al., The effect of out-of-plane motion on 2D and 3D digital image correlation measurements. Optics and Lasers in Engineering, 2008. 46(10): p. 746-757.

99. Preibisch, S., S. Saalfeld, and P. Tomancak, Globally optimal stitching of tiled 3D microscopic image acquisitions. Bioinformatics, 2009. 25(11): p. 1463-1465.

100. Carroll, J., et al., An experimental methodology to relate local strain to microstructural texture. Review of Scientific Instruments, 2010. 81(8): p. 083703.

101. Chen, Z., et al., High-Resolution Deformation Mapping Across Large Fields of View Using Scanning Electron Microscopy and Digital Image Correlation, in Experimental Mechanics. 2018. p. 1407-1421.

102. Kumar, K. and S.V. Kailas, Positional dependence of material flow in friction stir welding: analysis of joint line remnant and its relevance to dissimilar metal welding. Science and Technology of Welding and Joining, 2013. 15(4): p. 305-311.